AD NUMBER
AD461864
NEW LIMITATION CHANGE
TO Approved for public release, distribution unlimited
FROM Distribution authorized to U.S. Gov't. agencies and their contractors; Administrative Operational Use; Feb 1965. Other requests shall be referred to Air Force Materials Lab, Research and Technology Div, Air Force Systems Command, Wright-Patterson AFB, OH 45433.
AUTHORITY
USAF ltr, 22 Aug 1974

RTD-TDR-63-4096
Part II

INVESTIGATION OF BORIDE COMPOUNDS FOR VERY HIGH TEMPERATURE APPLICATIONS

Larry Kaufman
Edward V. Clougherty

ManLabs, Inc.

TECHNICAL DOCUMENTARY REPORT NO. RTD-TDR-63-4096, Part II
February 1965

Air Force Materials Laboratory
Research and Technology Division
Air Force Systems Command
Wright-Patterson Air Force Base, Ohio

NOTICES

When Government drawings, specifications, or other data are used for any purpose other than in connection with a definitely related Government procurement operation, the United States Government thereby incurs no responsibility nor any obligation whatsoever; and the fact that the Government may have formulated, furnished, or in any way supplied the said drawings, specifications, or other data, is not to be regarded by implication or otherwise as in any manner licensing the holder or any other person or corporation, or conveying any rights or permission to manufacture, use, or sell any patented invention that may in any way be related thereto.

This report not releasable to (CFSTI) Clearing House for Federal Scientific and Technical Information formerly (OTS) Office of Technical Services. Qualified users may obtain copies of this report from the Defense Documentation Center (DDC), (formerly ASTIA), Cameron Station, 5010 Duke Street, Alexandria Virginia. The distribution of this report is limited because it contains technology identifiable with items on the Mutual Defense Assistance Control List excluded from export under U.S. Export Control Act of 1949, as implemented by AFR 400-10.

Copies of this report should not be returned to the Research and Technology Division unless return is required by security considerations, contractual obligations, or notice on a specific document.

RTD-TDR-63-4096
Part II

INVESTIGATION OF BORIDE COMPOUNDS FOR VERY HIGH TEMPERATURE APPLICATIONS

Larry Kaufman
Edward V. Clougherty

ManLabs, Inc.

MATERIALS RESEARCH AND DEVELOPMENT

ManLabs, Inc.
21 ERIE STREET
CAMBRIDGE 39
MASSACHUSETTS

FOREWORD

This report was prepared by the Research Division, ManLabs, Inc., with the assistance of the following subcontractors: Arthur D. Little, Inc., Lexington Laboratories, Inc., and the University of Cincinnati, under U.S.A.F. Contract No. AF33(657)-8635. This contract was initiated under Project No. 7350 "Refractory Inorganic Non-Metallic Materials" Task 735001 "Non-Graphitic". The work was administered under the direction of the A.F. Materials Laboratory, Research and Technology Division with J. D. Latva acting as project engineer.

This report covers the period of work from October 1963 to November 1964.

ManLabs personnel participating in this study included, L. Kaufman, E. V. Clougherty, R. Pober, M. Hyman, J. Elling, C. Gallagher, S. Wallerstein, R. Gould, W. Lindonen and C. Ayer.

The manuscript of this report was released by the authors December 1964 for publication as an RTD Technical Documentary Report.

This technical documentary report has been reviewed and is approved.

W. G. Ramke
Chief, Ceramics and Graphite Branch
Metals and Ceramics Division
A. F. Materials Laboratory

ABSTRACT

The earlier prediction of this program that metal rich diboride compounds would exhibit superior oxidation resistance was investigated and verified. Studies were made of high pressure hot pressed hafnium and zirconium diborides, which are the most oxidation resistant diborides, at boron/metal ratios between 1.7 and 2.1. Measurements between 1200 and 2200°K at partial pressures of 7 to 40 torr oxygen and flowrates of 100 to 200 cm^3/min. were performed. At 1900°K $HfB_{1.88}$ has a parabolic rate constant which is 50 times smaller than $HfB_{2.12}$. The parabolic rate constants for hafnium diboride oxidation are about ten times smaller than the corresponding zirconium diboride rate constants. Silicon additions were found to improve oxidation resistance below 1600°K but not at higher temperatures. Additional work is in progress to investigate larger silicon and aluminum additions. Measurements of vapor deposited $ZrB_{1.85}$ and Boride Z have been performed for comparison purposes. At present, our best "pure" diboride is $HfB_{1.7}$ which exhibits a parabolic rate constant for oxygen pickup of 10^{-3} gm^2/cm^4 min. at 2200°K corresponding to a diboride/dioxide conversion of 20 mils in one hour at this temperature. Sintering studies on ZrB_2 indicate that densification proceeds by grain boundary diffusion and that $ZrB_{1.89}$ can be sintered to 96% theoretical density in four hours at 2100-2200°C without discontinuous grain growth. Additions of zirconium to $ZrB_{1.7}$ permitted densification at 1800°C. Silicon and ZrC additions did not inhibit discontinuous grain growth at high temperatures. Preliminary studies indicate that hafnium diboride sinters at slower rates than ZrB_2. Measurements of the thermal conductivity and emissivity of TiB_2, ZrB_2, HfB_2 and TaB_2on dense polycrystalline samples between 1200° and 2000°K are presented. Studies of the electrical resistivity of ZrB_2 and HfB_2 have been extended to 1500°C and are presented as a function of porosity and impurity phases. Comparisons have been made of computed Zr-B and Hf-B phase diagrams with experimental phase equilibria in these systems and permit estimates to be made of the free energies of formation of the monoborides. Theoretical methods for predicting the relative oxidation resistance of the pure diborides, off-stoichiometric compounds and ternary diborides have been developed. This description predicts the correct sequence of oxidation resistance and the enhanced oxidation resistance of metal rich diboride. An additional inference is that ternary alloying elements substituting on the boron sublattice will enhance oxidation properties.

TABLE OF CONTENTS

		Page
I.	INTRODUCTION AND SUMMARY	1
	A. Summary of Results	1
II.	PROGRAM MANAGEMENT	4
	A. Introduction	4
	B. Subcontracting Laboratories	4
	C. Publications	4
III.	PROCUREMENT AND CHARACTERIZATION OF STARTING MATERIALS	6
	A. Introduction	6
	B. Characterization	6
	1. Hafnium Diboride and Zirconium Diboride	6
	2. Metals and Boron	11
	3. Attempted Purification of HfB_2(2)	12
	C. Discussion	12
IV.	CHARACTERIZATION OF SPECIMENS FOR OXIDATION STUDIES	14
	A. Introduction	14
	B. Experimental Procedures	14
	1. Fabrication by High Pressure Hot Pressing	14
	C. Materials for Oxidation	16
	1. Boron Rich Hafnium Diboride	16
	2. Metal Rich Hafnium Diboride	16
	3. Stoichiometric Hafnium Diboride	17
	4. Metal Rich Hafnium Diboride with Silicon Additive	17
	5. Metal Rich Zirconium Diboride	29

TABLE OF CONTENTS (CONT.)

				Page
		6.	Boron Rich Zirconium Diboride	29
		7.	Metal Rich Zirconium Diboride with Silicon Additive	29
		8.	Boride Z	29
		9.	Pyrolytic Zirconium Diboride	29
V.	SINTERING CHARACTERISTICS OF ZrB_2			30
	A.	Introduction and Summary		30
	B.	Experimental		31
		1.	Powder Preparation	31
		2.	Pressing	33
		3.	Sintering	33
	C.	Results		33
	D.	Discussion		55
VI.	OXIDATION CHARACTERISTICS			60
	A.	Introduction		60
	B.	Experimental Results		60
		1.	General Discussion	60
		2.	Experimental Materials and Techniques	61
		3.	Results	61
			3.1 Long Term Oxidation of Hafnium Diboride	61
			3.2 The Effect of Water Vapor on the Oxidation of Diborides	72
			3.3 The Effect of Stoichiometry on the Oxidation of HfB_2	72
			3.4 The Effect of Stoichiometry on the Oxidation of ZrB_2	84

TABLE OF CONTENTS (CONT.)

Page

3.5 Gas Phase Diffusion Limited Oxidation and Effects of Flow Rate on Oxidation of HfB_2 and ZrB_2 92

3.6 Effect of Silicon Additions on the Oxidation of ZrB_2 and HfB_2 92

3.7 Oxidation of Boride Z and Pyrolytic $ZrB_{1.85}$ 99

C. The Effects of Alloying Additions on Oxidation Behavior 99

1. Applications of the Wagner-Hauffe Theory 99

1.1 The Parabolic Rate Law 99

1.2 Wagner-Hauffe Mechanism-General Considerations 100

1.3 Wagner-Hauffe Mechanism-Derivation of Equations 100

1.4 Wagner-Hauffe Mechanism Applied to HfB_2 103

2. Preferential Formation of the Oxide of the Alloying Element 103

3. Formation of a Ternary Oxide 104

4. Stabilization of a More Protective Oxide 104

5. Formation of a Metal or Internal Oxide Barrier . 105

D. Thermodynamics of Oxidation 105

1. The Influence of B_2O_3 Volatility on Diboride Oxidation 105

2. Calculation of the Pressure of B_2O_3 at the Oxide/Boride Interface 106

E. Conclusions 109

VII. PHYSICAL PROPERTIES 111

A. Introduction 111

TABLE OF CONTENTS (CONT.)

			Page
	B.	Thermal Conductivity	111
		1. Experimental Procedure	111
		2. Characterization of Specimens	112
		3. Results	118
	C.	Electrical Resistivity	121
		1. Experimental Procedures	121
		2. Sample Characterization	121
		3. Results	125
VIII.	PHASE EQUILIBRIA		128
	A.	Introduction	128
	B.	Calculation of Phase Diagrams	129
		1. Computation of Diboride/Liquid Equilibria	129
		2. Computation of the Pure Metal/Liquid and Pure Boron/Liquid Equilibria	134
		3. Location of the Diboride/Boron and (Metastable) Diboride/Metal Eutectics	135
		4. Computation of Monoboride/Liquid Equilibria	135
		5. Location of the Monoboride/Metal Eutectics	137
		6. Locations of the Congruently Vaporizing Composition within Diboride Phase Field	137
	C.	Experimental	139
		1. Diffusion Couples	139
		2. Equilibration Experiments	140
		2.1 Zone Refined Specimens	140
		2.2 High Pressure Hot Pressed Specimens	141

TABLE OF CONTENTS (CONT.)

Page

2.3 Cold Pressed Compacts of Zirconium and Boron 141

2.4 Arc Melted Specimens 141

3. Heating Procedures 142

4. Heating Conditions and Evaluations 142

5. Results and Discussion 142

IX. THERMODYNAMICS OF STABILITY 156

A. Introduction 156

B. Consideration of the Boron Activity Gradient Across the Metal Oxide Formed During Diboride Oxidation 156

C. Calculation of the Effects of Ternary Additions on the Thermodynamic Properties of Diborides 159

1. Ternary (Me, Mé) B_2 Diborides 162

2. Ternary Me $(B, X)_2$ Diborides 167

3. Evaluation of the Calculated Thermodynamic Effect of Ternary Additions on the Boron Activity 171

D. Comparison of the Volumes of HfB_2 vs. HfO_2 and ZrB_2 vs. ZrO_2 172

References 176

Appendix - Chemical and Spectroscopic Analyses of Samples Fabricated by High Pressure Hot Pressing 179

ILLUSTRATIONS

Figure		Page
1	Boron Rich Hafnium Diboride Fabricated from HfB_2(2), B/Me = 2.12. Characterization No. 29-2 Oxidation No. XVIII - 45	18
2a	Metal Rich Hafnium Diboride Fabricated from HfB_2(2A), B/Me = 1.88. Characterization No. 38-4 Oxidation No. XVIII - 49	19
2b	Metal Rich Hafnium Diboride Fabricated from HfB_2(2) + Hf, B/Hf = 1.70. Characterization No. A16-3 Oxidation No. XXI - 11	19
3	Stoichiometric Hafnium Diboride Fabricated from HfB_2(2) + Hf, B/Hf = 2.0. Characterization No. A4-1 Oxidation No. XIX - 38	20
4	Metal Rich Hafnium Diboride with Silicon Additive Fabricated from HfB_2(2) + Hf + Si, $HfB_{1.7}Si_{0.25}$ Characterization No. A19-5 - Oxidation No. XXI-1 . . .	21
5	Metal Rich Zirconium Diboride Fabricated from ZrB_2(1), B/Zr = 1.89. Characterization No. 30-3 Oxidation No. XVIII-28	22
6	Metal Rich Zirconium Diboride Fabricated from ZrB_2(P), B/Zr = 1.97. Characterization No. P5-5 Oxidation No. XX-17	23
7	Metal Rich Zirconium Diboride Fabricated from ZrB_2(1) + Zr, B/Zr = 1.70. Characterization No. A17-2 Oxidation No. XX-47	24
8	Boron Rich Zirconium Diboride Fabricated from ZrB_2(1) + B, B/Zr = 2.1, Characterization No. A22-1, Oxidation No. XXII-9	25
9	Metal Rich Zirconium Diboride with Silicon Additive Fabricated from ZrB_2(1) + Zr + Si, $ZrB_{1.7}Si_{0.25}$ Characterization No. A21-3 - Oxidation No. XXI-17 . .	26
10	Boride Z, Zirconium Diboride Composite Supplied by Carborundum Company	27
11	Pyrolytic Zirconium Diboride, B/Zr = 1.85 Supplied by Raytheon Company	28

Figure		Page
12	Fluid Energy Milled Zirconium Diboride Powder	32
13	Relative Density vs. Time for $ZrB_{1.89}$ as a Function of Temperature and for $ZrB_{1.96}$ at 2100°C	39
14	Relative Density vs. Time for Various Materials Compared with $ZrB_{1.89}$ at 2000° to 2300°C	41
15	Grain Size vs. Time $^{1/3}$ for $ZrB_{1.89}$	42
16a	FEM $ZrB_{1.89}$ Fired at 2300°C for 32 Minutes; (400X, Unetched)	43
16b	FEM $ZrB_{1.89}$ Fired at 2300°C for 32 Minutes; (400X, Etched 1 Hf, 1 HNO_3, 3 Lactic)	43
17a	FEM $ZrB_{1.89}$ Fired at 2100°C for 1/2 Hour, 400X, Unetched	44
17b	FEM $ZrB_{1.89}$ Fired at 2100°C for 1/2 Hour, 400X, Etched 1 HF: 2 HNO_3: $2H_2O$	44
18a	FEM $ZrB_{1.89}$ Fired at 2100°C 1 Hour, 400X, Unetched .	45
18b	FEM $ZrB_{1.89}$ Fired at 2100°C 1 Hour, Etched 1 HF: $2HNO_3$: $2H_2O$	45
19a	FEM $ZrB_{1.89}$ Fired at 2100°C 2 Hours, 400X, Unetched	46
19b	FEM $ZrB_{1.89}$ Fired at 2100°C 2 Hours, 400X, Etched 1 HF: $2HNO_3$: $2H_2O$	46
20a	FEM $ZrB_{1.89}$ Fired at 2100°C 6 Hours, 400X, Unetched	47
20b	FEM $ZrB_{1.89}$ Fired at 2100°C 6 Hours, 400X, Etched 1 HF: $2HNO_3$: $2H_2O$	47
21a	FEM $ZrB_{1.89}$ Fired at 2200°C for 4 Hours 400X, Unetched	48
21b	FEM $ZrB_{1.89}$ Fired at 2200°C for 4 Hours 400X, Etched 1 HF: $2HNO_3$: $2H_2O$	48
22a	FEM $ZrB_{1.89}$ Fired at 2000°C for 16 Hours 400X, Unetched	49
22b	FEM $ZrB_{1.89}$ Fired at 2000°C for 16 Hours 400X, Etched 1 HF: $2HNO_3$: $2H_2O$	49

Figure		Page
23a	A.R. $ZrB_{1.96}$ Fired at 2100°C for 6 Hours 400X, Unetched	50
23b	A.R. $ZrB_{1.96}$ Fired at 2100°C for 6 Hours 400X, Etched 1HF: $2HNO_3$: $2H_2O$	50
24a	$ZrB_{1.7}$ Fired at 1800°C for 2 Hours 400X, Unetched . .	51
24b	$ZrB_{1.7}$ Fired at 1800°C for 2 Hours 400X, Etched $1HNO_3$: $1H_2SO_4$: $2H_2O$	51
25a	A.R. HfB_2 Fired at 2100°C for 4 Hours 400X, Unetched .	52
25b	A.R. HfB_2 Fired at 2100°C for 4 Hours 400X, Etched $1HF:2HNO_3:2H_2O$	52
26a	$Zr(B, Si)_{1.89}$ Fired at 1500°C for 2 Hours 400X, Unetched	53
26b	$Zr(B, Si)_{1.89}$ Fired at 1500°C for 2 Hours 400X, Etched $1HF:2HNO_3:2H_2O$	53
27	$ZrB_{1.89}$ + 1 wt. %-ZrC Fired at 2200°C for 4 Hours, Etched $1HF:2HNO_3:2H_2O$	54
28	(Relative Density)$^{3/2}$ vs. t/G.S.^{4} for $ZrB_{1.89}$	58
29	Long Term Oxidation of HfB_2, 1758°K, p_{O_2} = 40.7 Torr .	71
30	Oxidation of HfB_2	73
31	Oxidation of HfB_2	74
32	Pellet XXII - 1, $HfB_{1.70}$, After Oxidation for 133 Minutes at 2020°K and 111 Minutes at 2120°K. Initial Height = 98 Mils, Final Height = 43 Mils, Depth of Conversion 27.5 Mils	77
33	Pellet XXII - 16, Pyrolytic $ZrB_{1.85}$, After Oxidation at 1897°K. Initial Height 86 Mils, Final Height 70 Mils, Depth of Conversion = 8 Mils	78
34	Pellet XXII - 16, Pyrolytic $ZrB_{1.85}$, After Oxidation at 1897°K. Initial Diameter 292 Mils, Final Diameter 275 Mils, Depth of Conversion = 8.5 Mils	79
35	Pellet XX - 36, $HfB_{1.70}$ After Oxidation at 1900°K . . .	80

Figure		Page
36	Pellet XXI - 11, $HfB_{1.70}$ After Oxidation at 2178°K . . .	81
37	Pellet XXI - 11, $HfB_{1.70}$ After Oxidation at 2178°K . . .	82
38	Pellet XIX - 38, $HfB_{2.0}$ After Oxidation at 2109°K . . .	83
39	Pellet XXI - 11, $HfB_{1.70}$, Matrix Structure	85
40	Pellet XXI - 11, $HfB_{1.70}$, Matrix Structure, After Oxidation at 2178°K	85
41	Pellet XVIII - 49, $HfB_{1.88}$, Matrix Structure	86
42	Pellet XVIII - 49, $HfB_{1.88}$, Matrix Structure, After Oxidation at 1852°K	86
43	Pellet XIX - 31, $HfB_{1.88}$, Matrix Structure	87
44	Pellet XIX - 31, $HfB_{1.88}$, Matrix Structure, After Oxidation at 2179°K	87
45	Pellet XXI - 37, $HfB_{1.88}$, Matrix Structure, After Oxidation at 2164°K	88
46	Pellet XVIII - 45, $HfB_{2.10}$, Matrix Structure	89
47	Pellet XVIII - 45, $HfB_{2.10}$, Matrix Structure, After Oxidation at 2118°K	89
48	Oxidation of ZrB_2	90
49	Oxidation of ZrB_2	91
50	Pellet XX - 42, $ZrB_{1.75}$, Matrix Structure	93
51	Pellet XX - 42, $ZrB_{1.75}$, Matrix Structure After Oxidation at 1898°K	94
52	Pellet XX - 47, $ZrB_{1.75}$, Matrix Structure, After Oxidation at 2170°K	94
53	Pellet XX - 17, $ZrB_{1.97}$, Matrix Structure	95
54	Pellet XX - 17, $ZrB_{1.97}$, Matrix Structure, After Oxidation at 2118°K	95
55	Pellet XXI - 19, $ZrB_{2.10}$, Matrix Structure	96
56	Pellet XXI - 19, $ZrB_{2.10}$, Matrix Structure, After Oxidation at 1898°K	96

ILLUSTRATIONS (CONT.)

Figure		Page
57	Pellet XXI - 17, $ZrB_{1.7}Si_{0.25}$, After Oxidation at 1899°K	97
58	Pellet XXI - 17, $ZrB_{1.7}Si_{0.25}$, After Oxidation at 1899°K	97
59	Pellet XXI - 17, $ZrB_{1.7}Si_{0.25}$, Matrix Structure	98
60	Pellet XXI - 17, $ZrB_{1.7}Si_{0.25}$, Matrix Structure, After Oxidation at 1899°K	98
61	Titanium Diboride Thermal Conductivity Material	114
62	Zirconium Diboride Thermal Conductivity Material	115
63	Hafnium Diboride Thermal Conductivity Material	116
64	Niobium Diboride Thermal Conductivity Material	117
65	Variation of Thermal Conductivity of Polycrystalline Diborides with Temperature	120
66	Zirconium Diboride Resistivity Specimen	122
67	Hafnium Diboride Resistivity Specimen	123
68	Resistivity of Zone Refined, Dense Polycrystalline and Porous Polycrystalline Zirconium Diboride as a Function of Temperature	126
69	Resistivity of Dense and Porous Polycrystalline Hafnium Diboride as a Function of Temperature	127
70	Calculated Zr-B Phase Diagram	130
71	Calculated "ZrB_2" Phase Field	131
72	Calculated Hf-B Phase Diagram	132
73	Calculated "HfB_2" Phase Field	133
74	Zone Refined Two Phase Alloy Specimen: Boron Rich ZrB_2 + 2nd Phase	146
75	High Pressure Hot Pressed Specimen: ZrB_2(1) Powder and Zr Metal, B/Zr = 1.5	147

ILLUSTRATIONS (CONT.)

Figure		Page
76	Cold Pressed Compact Specimen: $Hf_{0.93}B_{0.07}$	148
77	Arc Melted Specimen: $Zr_{0.14}B_{0.86}$	149
78	Arc Melted Specimen: $Hf_{0.4}B_{0.6}$	150
79	Arc Melted Specimen: $Zr_{0.4}B_{0.6}$	151
80	Zirconium-Boron System	153
81	Hafnium-Boron System	154
82	Schematic Illustration of the Effect of Diboride Composition on the Boron Activity Gradient Between MeB_2 and B_2O_3	158
83	Computed Ratio of Boron Activity in Stoichiometric Diborides (a_B^{η} [x = 2/3]) and B_2O_3 (a_B^{λ}) as a Function of Temperature	161
84	Comparison of ZrB_2/ZrO_2 and HfB_2/HfO_2 Volumes . . .	175

TABLES

Table		Page
1	Chemical Analyses of Hafnium Diboride and Zirconium Diboride	7
2	Pycnometric Density of Diboride Powders	9
3	X-ray Analysis of Diboride Powders	9
4	Calculated Assay of Matrix Diboride Material for Different Stoichiometries	10
5	Characterization of Metal and Boron Powder Qualitative Results (Range w/o)	11
6	Preparation and Characterization of Oxidation Specimens	15
7	Effect of Low Density Impurities on the Apparent Characterization Properties of Fabricated Material	17
8	Analysis of ZrB_2 Powder Samples and Fired Specimens	34
9	Properties of Diboride Sintering Specimens	35
10	Selected Data from Sintering and Grain Growth Curves	57
11	Diffusion Coefficients Calculated from Sintering Data on $ZrB_{1.89}$	57
12	Summary of Experimental Results	62
13	Identification of Specimens and Summary of Dimensional Changes During Oxidation	69
14	Pressures of $B_2O_3(g)$ in Equilibrium with $MeO_y(c)$ and $Me_{1-x}B_x$	108
15	Characterization of Thermal Conductivity Specimens	113
16	Thermal Conductivity and Total Emissivity of Polycrystalline TiB_2, ZrB_2, HfB_2 and NbB_2	118
17	Specimen Characterization and Resistivity Results	124

TABLES (CONT.)

Table		Page
18	Summary of Computed Thermodynamic Properties of HfB and ZrB	138
19	Heating Conditions and Evaluations for Phase Diagram Study	143
20	Comparison of Observed and Calculated Phase Boundaries in the Zr-B and Hf-B Systems	155
21	Tabulation of Free Energies of Formation Required in Model Calculations	160
22	Comparison of Diboride and Oxide Volumes at 25°C . .	173

I. INTRODUCTION AND SUMMARY

Transition metal diborides offer a number of attractive features as future high-strength, high temperature materials. The combination of high bond strength with low relative masses of TiB_2, ZrB_2, HfB_2, NbB_2 and TaB_2 leads to a unique series of compounds which offer the possibility of refractoriness, oxidation resistance and high strength to weight ratios. Realization of the full potential of borides as future high temperature materials requires a thorough knowledge of their properties and behavior under diverse conditions of temperature, environment and stress states. Although application of these compounds may require alloying or composite structures, a rational basis for such departures requires a thorough knowledge of the properties of the pure compounds. In order to determine the factors which control the behavior of these materials, an integrated research program has been designed and implemented. Phase I of this program was completed in September 1963 and resulted in the distribution of RTD-TDR-63-4096 "Investigation of Boride Compounds for Very High Temperature Applications, Part I" (December 1963). This document, in addition to a number of technical publications (see Section II) provides a good working description of the chemical, physical and thermodynamic properties of pure diborides relevant to their behavior in high temperature oxidizing environments. The information included in the above mentioned reports contains the results of studies on expansion coefficient, electrical resistivity, hot hardness, specific heat, vapor pressure, thermodynamic stability, oxidation characteristics and methods for preparation of pure, high density boride compounds.

On the basis of the background data generated by the Phase I study, it was predicted that metal-rich HfB_2 and ZrB_2 would exhibit superior oxidation properties and that additions of tantalum, yttrium and silicon appeared as the most promising candidates for confering additional increments of oxidation resistance. Since this latter property imposes severe limitations on the performance of refractory compounds at elevated temperatures, the efforts of the Phase II study reported here have been directed toward verification of this prediction. Other activities include studies of sintering kinetics, measurements of thermal conductivity, electrical resistivity and phase equilibria and a thermodynamic analysis of the effects of ternary additions on the stability of diboride compounds.

A. Summary of Results

In accordance with the Phase I study, high density specimens of ZrB_2 and HfB_2 covering a range of B/Me ratios have been prepared by high pressure-hot pressing and characterized by X-ray, metallographic, pycnometric and chemical analysis. Oxidation measurements on metal-rich and boron-rich ZrB_2, metal-rich and boron-rich HfB_2, metal-rich HfB_2 and ZrB_2 with silicon additions have been performed at 40 Torr oxygen in helium up to 2200° K. In addition, oxidation measurements on pyrolytic ZrB_2 prepared by Raytheon Co. and Carborundum's "Boride Z" have been carried out. The results obtained on specimens of varying stoichiometry support the predictions i.e., at 1900°K, HfB_2 prepared from a powder having B/Me = 1.88 exhibits a parabolic rate constant which is 50 times smaller than HfB_2 prepared from a powder having B/Me = 2.12. Moreover, it has been shown that hafnium additions to the B/Me = 2.12 powder in quantities sufficient to reduce B/Me to 1.70 reduce the rate constant to a level comparable with the B/Me ≈ 1.88. Similarly, in the case of ZrB_2, at 1900°K, it was found that the rate constant for B/Me = 1.89 was ten times smaller than B/Me ≈ 2.1. The results reported here together with those of the Part I "December 1963" (1*) report indicate that the rate constants for HfB_2 are approximately one order of magnitude lower than for ZrB_2 which in turn is five to ten times better than TiB_2 and TaB_2. Niobium diboride is the poorest of this family in that it exhibits break-away and linear oxidation kinetics. The preliminary results with silicon additions are encouraging since a $HfB_{1.7}Si_{0.25}$ formulation was found to exhibit a rate constant fifty times smaller than $HfB_{1.7}$ at 1600°K. However, this advantage vanished above 1800°K presumably due to loss of silicon. On the basis of research reported by General Telephone and Electronic Laboratories (2, 3) which indicated that yttrium additions to zirconium and hafnium degraded the oxidation resistance and that Al_2O_3 was the oxide most impervious to oxygen diffusion at 2000°C, plans to make yttrium additions have been postponed in favor of aluminum additions. The best material at present, metal-rich HfB_2, has a parabolic rate constant of about $10^{-3} gms^2 cm^{-4} min^{-1}$ at 2200°K corresponding to a conversion rate (diboride to dioxide) of 20 mils/hr. Lowering the rate constant by a factor of fifty (which would result in a conversion rate of about 3 mils/hr) by alloying would constitute a significant advance and is our goal for the next phase of this program.

Sintering studies on high purity ZrB_2 provide data which support a grain boundary diffusion model for the densification. The observed behavior for ZrB_2 differs from that observed for TiB_2 because unlike the latter, vaporization does not effect the sintering kinetics nor control the limiting densities. Samples of as received ZrB_2 with B/Zr = 1.89 were sintered to 96% relative density at 2100°-2200°C in the absence of discontinuous grain growth; the addition of zirconium metal to adjust B/Zr to 1.70 increased the sintering rate and material with 98% relative density could be prepared at 1800°C. Silicon and zirconium carbide additives to ZrB_2 inhibited the sintering rate; in the range where investigated. None of the selected additions inhibited discontinuous grain growth. Preliminary results for HfB_2 indicate slightly reduced sintering rates relative to ZrB_2 at 2100°C; the specimens did not exhibit discontinuous grain growth.

Measurements of the thermal conductivity and emissivity of TiB_2, ZrB_2, HfB_2 and NbB_2 have been performed on polycrystalline samples between 1200° and 2000°K. The results show a linear increase in thermal conductivity with temperature for all the borides examined. The available data in the literature and the characterization data for the measured samples provide a correlation of structure and composition for the thermal conductivity of these materials.

*Underscored numbers in parentheses indicate References given at end of this report.

The electrical resistivity data for ZrB_2 and HfB_2 have been extended to 1400°C and 1500°C respectively for polycrystalline samples. These results confirm the previously reported linear increase of resistivity with temperature. The variation of resistivity and the temperature coefficient of resistivity with porosity and impurity phases are discussed.

Phase diagrams for the Zr-B and the Hf-B systems have been calculated from the available thermodynamic descriptions of the diborides and the metal and boron; this calculation provided an estimate of the free energy of formation of the monoborides, ZrB and HfB. The computed diagrams are compared with the previously reported phase diagrams and with the results obtained in the experimental program in this area. The latter program included solidus determinations and phase boundary experiments in the range 1000° to 2200°C in both systems.

Theoretical methods for predicting the relative oxidation resistance of the pure diborides and the off-stoichiometric compositions based on minimizing the B_2O_3 pressure or the boron activity gradient across the oxide layer are presented. These idealized descriptions, together with considerations of oxide stability, oxide-boride volume coherency and a thermodynamic treatment of ternary diborides have been performed in order to guide the alloying program. An interesting result of the latter analysis is that elements which substitute on the boron sublattice will depress the boron activity more effectively than those which enter on the metal lattice.

II. PROGRAM MANAGEMENT

A. Introduction

In view of the diverse nature of the present study, it is being performed as a group effort in which ManLabs, Inc. functions as prime contractor with Larry Kaufman serving as principal investigator and Edward V. Clougherty as group leader. In this capacity, ManLabs provides management responsibility in addition to performing "in-house" research. Several other laboratories are participating in this study and are identified below.

During the two year period since the inception of this study three semi-annual reports (prior to the present report) and one summary report have been prepared and distributed. In addition, several technical papers are in preparation and in print.

B. Subcontracting Laboratories

Arthur D. Little, Lexington Laboratories, and the University of Cincinnati are the principal subcontractors in the present study. The research performed by these groups is reported in Sections V, VI, and VII of this document and is identified accordingly. In addition, analytical services have been provided by Donald Gurnsey, Department of Metallurgy M.I.T., Jarrell Ash Co. of Newtonville, Mass. and Advanced Metals Research Corp. of Somerville, Mass.

C. Publications

Technical Documentary Report No. RTD-TDR-63-4096 summarizing the results of the first eighteen months of this study was prepared and distributed in December 1963. At present nine papers based largely on the results reported in our first summary report are in print or in various stages of preparation. We anticipate that the nature of our studies will continue to qualify future research on this program for inclusion in the technical literature. Published papers as well as those presently submitted for publication include:

L. Kaufman, "Thermodynamic Properties of Transition Metal Diborides", A.I.M.E. Symposium on Compounds of Interest in Nuclear Reactor Technology, Boulder, Colorado (1964)-Edited by J. T. Waber and P. Chiotti, Edwards Brothers, Ann Arbor, Michigan.

L. Kaufman and E. V. Clougherty, "Investigation of Boride Compounds for High Temperature Applications", Proceedings of an International Symposium on Materials for the Space Age, Metallwerk Plansee Reutte, Austria, (1964), (Proceedings to be published).

E. V. Clougherty and R. L. Pober, "Physical and Mechanical Properties of Transition Metal Diborides", A.I.M.E. Symposium on Compounds of Interest in Nuclear Reactor Technology, Boulder, Colorado (1964) -Edited by J. T. Waber and P. Chiotti, Edwards Brothers, Ann Arbor, Michigan.

H. Bernstein, "Debye Temperature Measurements and Thermodynamic Properties of HfB_2, ZrB_2, HfC and ZrC", A.I.M.E. Symposium on Compounds of Interest in Nuclear Reactor Technology, Boulder, Colorado (1964) -Edited by J. T. Waber and P. Chiotti, Edwards Brothers, Ann Arbor, Michigan.

J. B. Berkowitz-Mattuck, "Oxidation Characteristics of HfB_2 and ZrB_2" in preparation for publication in Jnl of Electrochemical Society.

P. Blackburn, "Vaporization of NbB_2" in preparation for Jnl of Physical Chemistry.

E. F. Westrum, Jr., and G. Clay, "$NbB_{1.963}$: The Heat Capacity and Thermodynamic Properties from 5 to 350°K", Jnl of Physical Chemistry (1963) 67 2385.

C. K. Jun and M. Hoch, "The Thermal Conductivity of TiB_2, ZrB_2, HfB_2 and NbB_2 at Elevated Temperatures" submitted for inclusion in the Proceedings of the International Conference on Thermal Conductivity held July 1964 at the National Physical Laboratory, Teddington, Middlesex, England.

E. F. Westrum, Jr. and G. Clay, "Specific Heat of TaB_2 and TiB_2" in preparation for Jnl of Chemical Engineering Data.

III. PROCUREMENT AND CHARACTERIZATION OF STARTING MATERIALS*

A. Introduction

Although a portion of the oxidation studies in the continuing investigation of the diborides of hafnium and zirconium involves the deliberate modification of pure starting material by the introduction of various additives, the procurement of high purity, well characterized starting materials is still required for the overall objectives of this program. In particular, the analysis of the results obtained from specimens with additives in the above mentioned oxidation studies is based in large part on the characterization of the test specimens and starting materials. Hence, there is a continuing requirement for high purity starting materials to minimize experimental variables and to maximize probability for reproducibility in the preparation of test specimens. In addition, fabricated samples of "as-received" hafnium diboride and zirconium diboride were prepared for other oxidation studies and for thermal conductivity and electrical resistivity measurements. High purity materials including diborides, metals and boron were used for phase boundary experiments.

B. Characterization

Diboride powders were characterized by quantitative chemical analysis for metal, boron, carbon, nitrogen, oxygen and iron, by qualitative spectrographic analysis for trace impurities, and by X-ray diffraction and powder densitometry for the presence of extraneous phases. Metals and elemental boron were characterized by qualitative spectrographic analysis for minor impurities. The evaluation of the dense material fabricated by high pressure hot pressing and the interpretation of the results obtained in the oxidation studies could not be performed with any degree of confidence unless the starting materials and the fabricated test specimens were well characterized.

1. Hafnium Diboride and Zirconium Diboride

In the course of this program fifteen pounds of hafnium diboride powder were purchased and received. This procurement included an initial five pound shipment, hereafter referred to as $HfB_2(1)$, a second one pound shipment, $HfB_2(2A)$, and a final nine pound shipment, $HfB_2(2)$. All the results pertaining to HfB_2 presented in RTD-TDR-63-4096 were obtained with $HfB_2(1)$. The procurement of zirconium diboride was accomplished in the previous investigation(1**). The initial ten pound shipment, hereafter referred to as $ZrB_2(1)$ was complemented by a small quantity of up-graded material, $ZrB_2(P)$ supplied under a purification subcontract(4) by U. S. Borax Research Corporation.

A summary of the results of chemical analyses is presented in Table 1. In the evaluation of samples of ZrB_2 and HfB_2 fabricated by high pressure hot pressing it became apparent (see Section IV) that the density of the "as-received" hafnium diboride powder was less than the calculated X-ray density. This was particularly noticeable for the material designated as $HfB_2(2)$. Accordingly, pycnometric procedures were used to obtain the powder density of $HfB_2(2)$ and $ZrB_2(1)$. The density was measured in several solvents; the

---

* E. V. Clougherty, ManLabs, Inc.
** Underscored numbers in parentheses designate References given at end of report.

TABLE 1

CHEMICAL ANALYSES OF HAFNIUM DIBORIDE AND ZIRCONIUM DIBORIDE

Averaged Quantitative Results (w/o)*

Material	M	B	B/Me	C	N	O	Fe
ZrB_2(1)	80.67	18.05	1.89	0.33	0.19	0.53	0.06
ZrB_2(P)	80.46	18.82	1.97	0.16	0.05	0.47	0.03
HfB_2(1)	89.0	10.6	1.97	0.14	0.017	0.10	0.083
HfB_2(2A)	88.4	10.07	1.88	0.28	0.02	0.10	0.07
HfB_2(2)	87.33	11.2	2.12	0.37	0.01	0.05	0.26

* Chemical analyses by D. Gurnsey, Metallurgy Dept., M.I.T. except for ZrB_2(P) for which analytical data are summarized in Reference 4.

Qualitative Results (Range w/o)
(Jarrell Ash Co., Newtonville, Mass.)

Material	0.10	0.01-0.10	0.001-0.01	0.001
ZrB_2(1)	--	Ca, Cr, Ti	Na, Mg, Co, Ni, Mo	Be, Nb, Ag Mn, Al, Cu
ZrB_2(P)	--	Ti, Si	--	Cu
HfB_2(1)	--	--	Al, Ti, Mn	Cu, Mg, Cr.
HfB_2(2A)	--	Fe, Zr	Si	Na, Mg, Al Ti, Mn, Cu
HfB_2(2)	--	Al, Zr, Mn	--	Na, Mg, Si, Ca, Ti

precision of the measurement was better for ZrB_2 than for HfB_2. The results are presented in Table 2. X-ray techniques were used to identify extraneous phases in the starting materials and to measure the lattice parameters for boron rich HfB_2(2), metal rich HfB_2(2A), and for near stoichiometric ZrB_2(P). The apparatus and the procedure for precise lattice parameter measurements were described in a recent report (5). Previous X-ray characterizations data and the results obtained for the above mentioned materials are presented in Table 3.

The characterization data in Tables 1 through 3 indicate that the materials designated as HfB_2(2A) and HfB_2(2) are quite dissimilar. Complementary evidence obtained by metallographic techniques on dense fabricated specimens (see Section IV) confirm these findings. The different materials were used to advantage in the present program.

Additional characterization data was obtained from the many chemical analyses that were performed on these two samples of high purity, commercially available hafnium diboride. The analytical procedure for the determination of hafnium in hafnium diboride (6) requires the dissolution of the sample in a solution of sulfuric acid and hydrogen peroxide. When HfB_2(2) and HfB_2(2A) were treated in this manner, insoluble residues (2.18 and 0.8 weight percent respectively) were obtained; HfB_2(1) was completely dissolved in this solution. The apparent low powder density of HfB_2(2) indicates the presence of a low density impurity and the X-ray results suggest the presence of HfB_{12}; the chemical analyses indicate excess boron and a relatively high carbon content. A check on a sample of B_4C showed that this low density material was insoluble in the above solvent. The effect of low density impurities on the measured density of fabricated specimens of moderately high density material (e.g., ZrB_2, $\rho = 6.09$ g/cc) and on high density material (e.g., HfB_2, $\rho = 11.20$ g/cc) is considered in detail in Section IV.

Further characterization was obtained from the available chemical analysis results by computing the weight percent of the matrix diboride material for given stoichiometries. The calculation was performed by assuming that the boron content controlled the metal composition for the metal rich powders and vice versa for the boron rich powders. The results presented in Table 4 provide a measure of powder purity which agrees with the other characterization data and with the results obtained for dense fabricated samples of these materials.

TABLE 2

PYCNOMETRIC DENSITY OF DIBORIDE POWDERS

Liquid	Liquid Density (g/cc)	Powder Density (g/cc)*	
		HfB_2(2)	ZrB_2(1)
Trichloro-ethylene	1.451	--	6.02
Toluene	0.858	10.39(2)	5.97
Xylene	0.861	10.27(4)	6.08(3)
Methanol	0.784	10.47(2)	6.09
	Average Density (g/cc)	10.38	6.04
	X-ray Density (g/cc)	11.20	6.09
	% X-ray Density	92.7	99.2

* The number in parentheses which follow tabulated averaged powder density values for a given solvent is the number of individual density measurements for that solvent.

TABLE 3

X-RAY ANALYSIS OF DIBORIDE POWDERS

Material	Atomic Ratio B/Me	Extraneous Phases*	Lattice Parameters		Radiation**
			a_o(Å)	c_o(Å)	
ZrB_2(1)	1.89	Zr(C, B)	3.171 3.169	3.527 3.532	M-Cu Un-Cu
ZrB_2(P)	1.97	ZrO_2	3.169	3.532	Un-Cu
HfB_2(1)	1.96	Hf(C, B)	3.1410	3.4761	M-Cu
HfB_2(2A)	1.88	Hf(C, B) HfO_2	3.1401	3.4761	M-Cu
HfB_2(2)	2.12	HfB_{12} HfO_2	3.1400	3.4758	Un-Cu

* The phases tabulated as Me(C, B) are the monoborides or carbides with the NaCl structure. The stabilization of the cubic monoboride by carbon is discussed in Section VIII. The identification of these phases is based in the assignment of one extraneous X-ray diffraction line, the known overall composition of the powders, and the methods for preparing these materials.

** M-Cu indicates monochromated Cu radiation (cf. Ref. 3); Un-Cu, unfiltered Cu radiation.

TABLE 4

CALCULATED ASSAY OF MATRIX DIBORIDE MATERIAL FOR DIFFERENT STOICHIOMETRIES

Matrix Material	Experimental (w/o)				Calculated Weight % of		
	Me	B	Me+B	B/Me	$MeB_{1.95}$	$MeB_{2.00}$	$MeB_{2.05}$
ZrB_2(1)	80.67	18.05	98.72	1.89	96.1	94.2	--
ZrB_2(F)	80.46	18.82	99.28	1.97	100.1	98.1	--
HfB_2(1)	89.0	10.6	99.6	1.97	100.1	98.4	--
HfB_2(2A)	88.4	10.07	98.47	1.88	95.1	93.0	--
HfB_2(2)	87.33	11.2	98.53	2.12	--	98.0	98.2

2. Metals and Boron

The characterization of the elemental powders used in the additive program for oxidation studies and in the phase boundary studies was limited to a qualitative spectrographic analysis. The results in Table 5 support the contention that further characterization is not necessary at this time.

TABLE 5

CHARACTERIZATION OF METAL AND BORON POWDER

QUALITATIVE RESULTS (RANGE w/o)

(Jarrell Ash Co., Newtonville, Mass.)

Element	0.1-1	0.01-0.1	0.001-0.01	0.0001-0.001
Hf	--	Fe, Zr	Mg, Na, Si	Al, B, Ca, Co, Mn, Cu
Zr	Ti*	Fe, Sr, B	Na, Al, Cr, Zn	Mg, Ca, Mn, Ni, Cu, Ag, Sn, Ba, Pb
Na	--	--	--	Na, Fe, Ni, Cu, Zn
Nb	--	Ni	Fe, Sn	Na, Mg, Al Si, Cu, Pb
Si	Al*		Ti, Cr, Mn, Fe, Ni, Cu	V
B	Mn,* Si*	Mg, Al, Fe,	Ca, Ti,	Ba, Pb, Cu Ag, Ni, Sn

*Quantitative spectrographic analyses for the elements marked with an asterisk (*) showed: 0.005 w/o Ti in Zr
0.40 w/o Mn and 0.72 w/o Si in B
0.53 w/o Al in Si

3. Attempted Purification of $HfB_2(2)$

One attempt was made to up-grade the large shipment of hafnium diboride, $HfB_2(2)$, by an acid leaching process similar to that successfully applied to ZrB_2 by the U. S. Borax Co. (4). The $HfB_2(2)$ was leached in 6N aqueous HF at $0^{o}C$ for four hours. This procedure did not effect a purification, rather most of the sample dissolved. The residue showed X-ray evidence for B_4C and HfB_2.

Special purification studies on hafnium diboride are not within the scope of the present program but the above rather simple procedure was attempted with the hope that it might prove helpful. The identification of B_4C in the residue supplied additional characterization data. The techniques discussed in Section IV and the results in Section VI show that the $HfB_2(2)$ material can be of significant value in this program without purification experiments, i.e., this material is boron rich HfB_2.

C. Discussion

The elaboration of details of the characterization for one material, namely, hafnium diboride, purchased as a high purity item from one manufacturer (on a "best effort basis" because at the time no other arrangements could be negotiated) demonstrates one of the many problems encountered in carrying out careful investigations with this type of material. In the course of these evaluations it was learned that the original material $HfB_2(1)$ was prepared from HfO_2 and crystalline boron. The $HfB_2(2A)$ was also prepared similarly. The $HfB_2(2)$ was prepared by firing a mixture of HfO_2, B_2O_3, and graphite. This alternate procedure was selected because reliable sources of crystalline boron could not be found at the particular time.

The combined knowledge of the manufacturing procedures, the chemical analyses, the X-ray diffraction results, the powder densitometry, the attempted purification studies, and the metallographic analyses and the pycnometric densities of the fabricated specimens lead to the following conclusions:

(a) $ZrB_2(1)$ is a metal rich powder with $B/Me \approx 1.89$; the powder contains a second phase which X-ray results indicate is a cubic material probably a carbon stabilized monoboride. The powder density is 6.04 g/cc, 99.2% of the X-ray density of ZrB_2. The powder contains from 94 to 96 weight percent of the diboride.

(b) $ZrB_2(P)$ is a metal rich powder with $B/Me \approx 1.97$; the powder contains a second phase which X-ray results indicate as ZrO_2. Metallographic results in Section IV indicate that the amount of second phase is reduced in this material relative to $ZrB_2(1)$. The powder contains from 98 to 100 weight percent of the diboride.

(c) $HfB_2(1)$ is a metal rich powder with $B/Me \approx 1.97$; the powder contains a second phase which X-ray results indicate is a cubic material probably a carbon stabilized monoboride. The earlier(1) metallographic results indicated that the amount of second phase was minimal. The powder contains from 98 to 100 weight percent of the diboride.

(d) $HfB_2(2A)$ is a metal rich powder with $B/Me \approx 1.88$; the powder contains a second phase which X-ray results indicate is a cubic material probably a carbon stabilized monoboride. There is also some X-ray evidence for a small amount of HfO_2. The metallographic results in Section IV indicate that this material has more of the second phase than $HfB_2(1)$ but less than $HfB_2(2)$. The powder contains from 93 to 95 weight percent of the diboride.

(e) $HfB_2(2)$ is a boron rich powder with $B/Me \approx 2.12$; the powder contains a phase which has a relatively low density and contains carbon and boron. This major contaminant is probably B_4C. There is some X-ray evidence to suggest the presence of HfO_2 and HfB_{12}. There is no X-ray evidence to suggest the cubic phase which appears in the metal rich ZrB_2 and HfB_2. The powder density is 10.38 g/cc, 92.7% of the X-ray density. The powder contains 98 weight percent of the diboride and approximately 2 weight percent of the impurity phase which may be B_4C.

(f) The lattice parameter results do not show any significant difference between the metal rich $HfB_2(2A)$ and the boron rich $HfB_2(2)$; previous results (5) for NbB_2 which is stable over a wide range of composition did show a significant variation in both parameters. However, the identification of the different second phases in these two materials does support the conclusions that $HfB_2(2A)$ is metal rich and $HfB_2(2)$ is boron rich. It is possible that the range of stability of HfB_2 is not sufficiently wide to change the lattice parameters. The two metal rich zirconium diboride powders, $ZrB_2(1)$ and $ZrB_2(P)$ have identical lattice parameters.

IV. CHARACTERIZATION OF SPECIMENS FOR OXIDATION STUDIES*

A. Introduction

High pressure hot pressing was used to prepare dense specimens for oxidation studies and for electrical resistance and thermal conductivity measurements. The characterization data presented for specimens of TiB_2, ZrB_2 and HfB_2 in the summary report (1) demonstrated that high density material could be prepared without significant contamination. Oxidation studies revealed that this material was at least equivalent to single crystals in oxidation resistance. The measured density of the fabricated material was generally at least 95% of the X-ray density. Metallographic analyses confirmed the relatively high density.

B. Experimental Procedures

1. Fabrication by High Pressure Hot Pressing

The general characteristics of the fabricating procedure and the experimental condition required to produce dense material were presented in the previous report (1). Temperature calibration studies performed in a fundamental investigation (7) of the mechanism of densification by this procedure have revealed that the temperatures employed are between 1800° and $2000^{\circ}C$. These temperatures are significantly lower than those previously reported (1). Selected experimental conditions used to fabricate some of the samples prepared in the present study are collected in Table 6.

The general procedure for preparing oxidation specimens required the fabrication of a bar 1.0 in. long by 0.40 in. diameter. Diamond impregnated tools were used to machine right circular cylinders 0.30 in. diameter and to cut specimen discs 0.110 in. thick. The samples were then polished metallographically and after examination, representative samples were selected for X-ray and chemical analyses. When the metallographic analyses indicated a need for homogenization of materials fabricated from mixtures of as-received powders and the various additives, the specimens were heated for 24 hours at $1500^{\circ}C$ in argon prior to oxidation. Additional metallographic analyses followed the homogenization.

The initial fabrications in the present program were performed with ZrB_2(1). A series of high density (>98% of X-ray density) bars were prepared. The second material selected for fabrication was HfB_2(2). In contrast to the apparent success for ZrB_2(1), material with more than 92% of the X-ray density could not be prepared. Metallographic analysis of the latter revealed the presence of a second phase; the apparent porosity was

---

* E. V. Clougherty and R. L. Pober, ManLabs, Inc.

TABLE 6

PREPARATION AND CHARACTERIZATION OF OXIDATION SPECIMENS*

Characterization No.	Material	Oxidation No.	Fabricating Conditions + Temp. (°C)	Time (min)	Figure	B/Me
29-2	HfB_2(2)	XVIII-45	2000	11	1	2.12
38-4	HfB_2(2A)	XVIII-49	2000	9	2a	1.88
A16-3	HfB_2(2) + Hf	XXI-11	1940	6	2b	1.70
A 4-1	HfB_2(2) + Hf	XIX-38	2000	5	3	2.0
A19-5	HfB_2(2) + Hf + Si	XXI-1	1850	14	4	1.95
30-3	ZrB_2(1)	XVIII-28		4	5	1.89
P 5-5	ZrB_2(P)	XX-17	1920	5	6	1.97
A17-2	ZrB_2(1) + Zr	XX-47	1820	7	7	1.70
A22-1	ZrB_2(1) + B	XXII-9	1850	15	8	2.1
A21-3	ZrB_2(1) + Zr + Si	XXI-17	1850	15	9	1.95
--	Boride Z**	--	--	--	10	--
--	Pyrolytic ZrB_2**	--	--	--	11	1.85

* Qualitative spectroscopic analyses and quantitative chemical analyses detailed in Appendix I coupled with the complete metallographic analyses show no evidence of significant contamination of the starting materials in the fabricating process.

** The metallographic results on Boride Z and pyrolytic ZrB_2 shown in Figures 10 and 11 are applicable to the respective materials in general and not to a specific sample. Accordingly, an Oxidation No. can not be assigned to a specific photomicrograph.

\+ The materials were heated for the indicated intervals at pressures ranging from 170,000 to 250,000 psi.

minimal. Additional fabrications were performed with ZrB_2(P), ZrB_2(1) + Zr, ZrB_2(1) + Zr + Si, ZrB_2(1) + B, and with HfB_2(2A), HfB_2(2) + Hf, HfB_2(2) + Hf + Si, HfB_2(2) + Ta. These materials afforded specimens with densities of 95% or more of the powder density. Metallographic analysis revealed the definite presence of a 2nd phase in ZrB_2(1) and in HfB_2(2) and a definite reduction in the amount of the second phase in ZrB_2(P) and in HfB_2(2A). Considerable reduction in the amount of the 2nd phase in HfB_2(2) was also observed in material fabricated from HfB_2(2) with added hafnium metal to adjust the B/Me ratio to 2.0 and to 1.70. The samples prepared with silicon and boron additions were two phase.

Before discussing each material, it is instructive to consider the effect of low density impurities (e.g., C, B, B_4C) on those properties of fabricated materials which are usually measured for purposes of characterization. A calculation of several properties of ZrB_2 and HfB_2 were performed for a given volume percentage of an impurity with a density of 3.0 g/cc. The densities of C, B and B_4C are 2.3, 2.2 and 2.5 g/cc. respectively. The calculated quantities are presented in Table 7. The volume percentage of the impurity is the same as the area percentage of the impurity. This property is reflected in the metallographic analysis. The calculated density corresponds to the measured density of the fabricated specimens and the powders. The percentage of the X-ray density is the usually calculated quantity when the powder density is not known. The weight percentage of the matrix is the percentage of the powder present as ZrB_2 or HfB_2; this quantity was calculated from the chemical analyses for different stoichiometrics in Table 4.

The characterization data for actual oxidation specimens tested in Section VI are presented in Table 6. Photomicrographs presented in Figures 1 through 11 show the principle features of the basic materials which were evaluated in this study; specific comments are provided below.

C. Materials for Oxidation

1. Boron Rich Hafnium Diboride

Material fabricated from HfB_2(2) as received with B/Hf = 2.12 provided dense two phase specimens, boron rich diboride and a second phase which comprised approximately eight percent of the surface area and two percent by weight of the sample. Some of the fabricated materials were characterized by large grain structures. The latter apparently formed in the presence of a liquid phase in grain boundaries during hot pressing. A representative photomicrograph is shown in Figure 1.

2. Metal Rich Hafnium Diboride

Material fabricated from HfB_2(2A) as received with B/Hf = 1.88 provided dense two phase specimens, metal rich diboride and a second phase which comprised five weight percent of the sample. This metal rich hafnium diboride showed a specific etching characteristic as illustrated in Figure 2a. Some specimens showed significant grain growth, others did not.

TABLE 7

EFFECT OF LOW DENSITY IMPURITIES ON THE APPARENT CHARACTERIZATION PROPERTIES* OF FABRICATED MATERIAL

Matrix	Volume % Impurity	Calculated Density (g/cc.)	% X-ray Density	Weight % Matrix
HfB_2	0.0	11.20	100.00	100.00
	1.0	11.12	99.28	99.73
	2.0	11.04	98.57	99.45
	3.0	10.95	97.76	99.17
	4.0	10.87	97.05	98.99
	5.0	10.79	96.33	98.60
	6.0	10.71	95.62	98.31
	7.0	10.63	94.91	98.02
	8.0	10.55	94.19	97.73
ZrB_2	0.0	6.09	100.0	100.0
	1.0	6.06	99.5	99.5
	2.0	6.03	99.0	99.0
	3.0	6.00	98.5	98.6
	4.0	5.97	98.0	98.0
	5.0	5.94	97.5	97.5

* The quantities: Calculated Density, % X-ray Density, and Weight % Matrix were calculated for the tabulated Volume % Impurity with an assumed density of 3/gcc. mixed with the matrix material.

Material fabricated from HfB_2(2) with initial B/Hf = 2.12 and added Hf to adjust the overall B/Hf = 1.70 provided dense two phase specimens, metal rich diboride and a cubic phase material. Representative photomicrographs in Figure 2b reveal the absence of the above etching effect; virtually no grain growth was observed.

3. Stoichiometric Hafnium Diboride

Material fabricated from HfB_2(2) with initial B/Hf = 2.12 and added Hf to adjust the overall B/Hf = 2.20 provided dense specimens of the stoichiometric diboride. Grain growth was not observed. A representative photomicrograph is shown in Figure 3.

4. Metal Rich Hafnium Diboride with Silicon Additive

Material fabricated from HfB_2(2) with initial B/Hf = 2.12 and added Hf and Si to adjust the overall B + Si/Hf = 1.95 ($HfB_{1.7}Si_{0.25}$), provided dense two phase specimens. X-ray diffraction indicated the absence of elemental silicon and the presence of the diboride. Several unexplained lines were noted. A representative photomicrograph is shown in Figure 4.

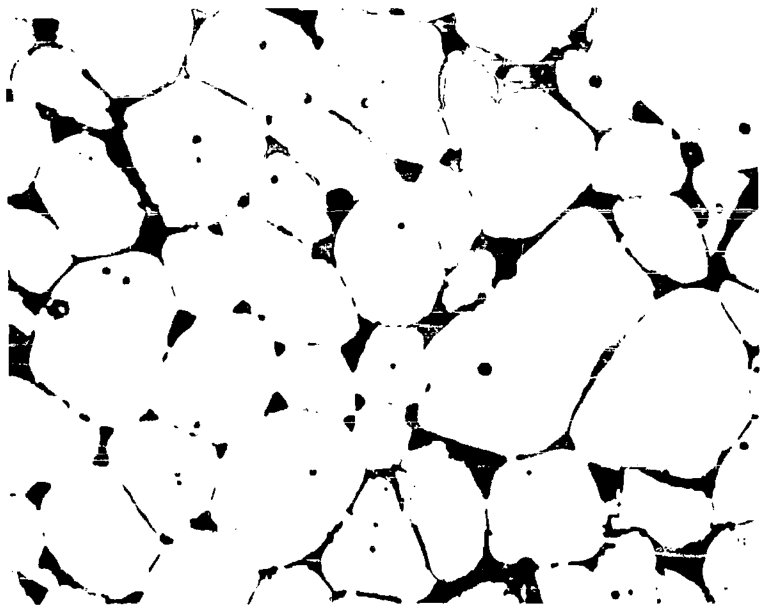

Etched X500
Etchant: Modified Aqua Regia

Figure 1 - Boron Rich Hafnium Diboride Fabricated from HfB_2(2), B/Me = 2.12. Characterization No. 29-2 Oxidation No. XVIII - 45

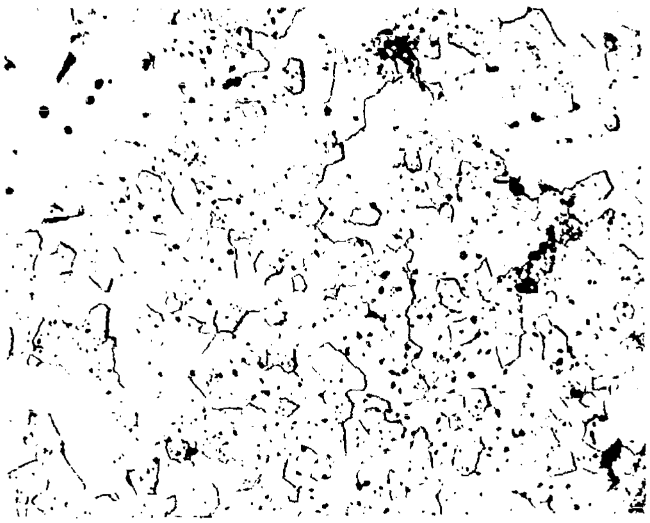

Etched X500
Etchant: Modified Aqua Regia
Note: Etching Effect Characteristic of this Metal Rich HfB_2.

Figure 2a - Metal Rich Hafnium Diboride Fabricated from HfB_2(2A), B/Me = 1.88. Characterization No. 38-4 Oxidation No. XVIII - 49

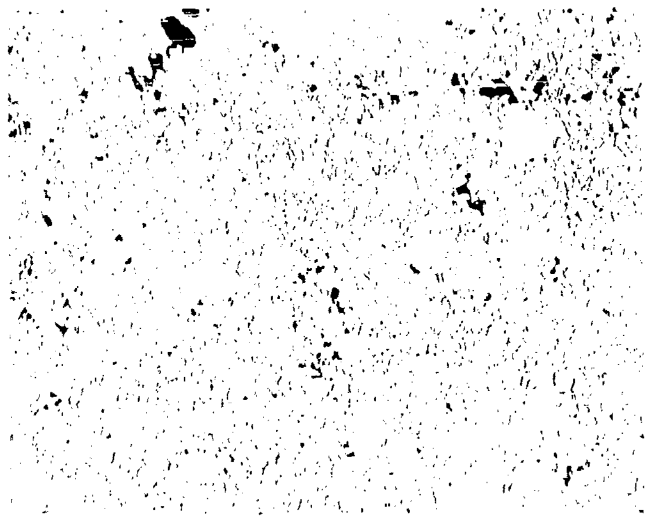

As Polished X500

Figure 2b - Metal Rich Hafnium Diboride Fabricated From HfB_2(2) + Hf, B/Hf = 1.70. Characterization No. A16-3 Oxidation No. XXI - 11

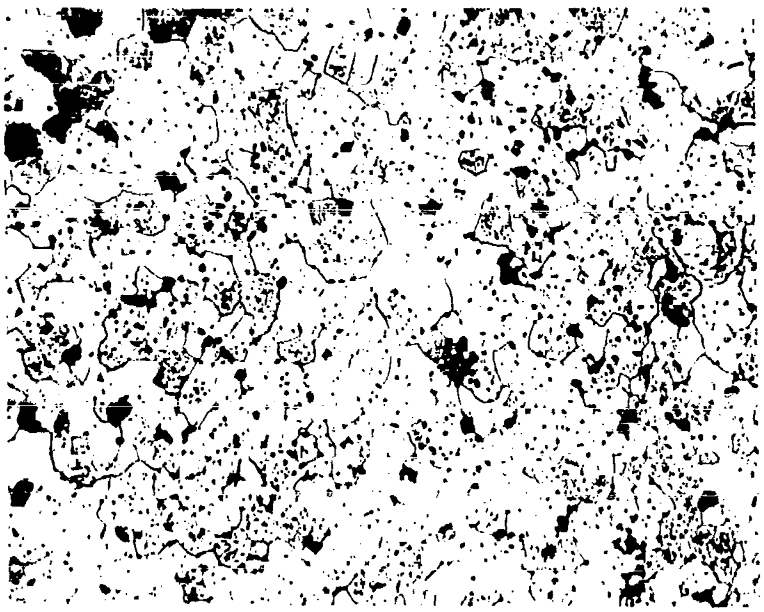

Etched X500
Etchant: Modified Aqua Regia

Figure 3 - Stoichiometric Hafnium Diboride Fabricated From HfB_2(2) + Hf, B/Hf = 2.0 Characterization No. A4-1 Oxidation No. XIX - 38.

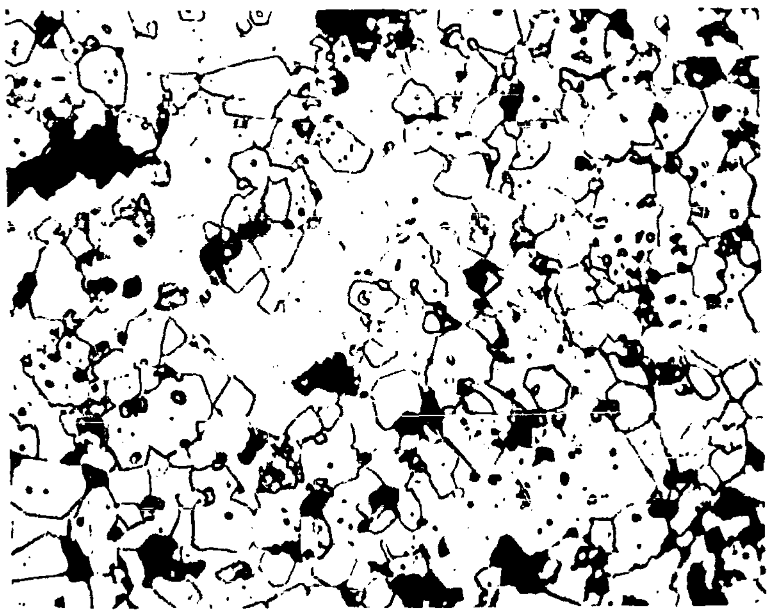

Etched X500

Etchant: 10cc glycerine, 10cc HNO_3, 2cc HCL, 0.1cc HF

Figure 4 - Metal Rich Hafnium Diboride With Silicon Additive Fabricated From $HfB_2(2)$ + Hf + Si, $HfB_{1.7}Si_{0.25}$
Characterization No. A19-5 Oxidation No. XXI-1

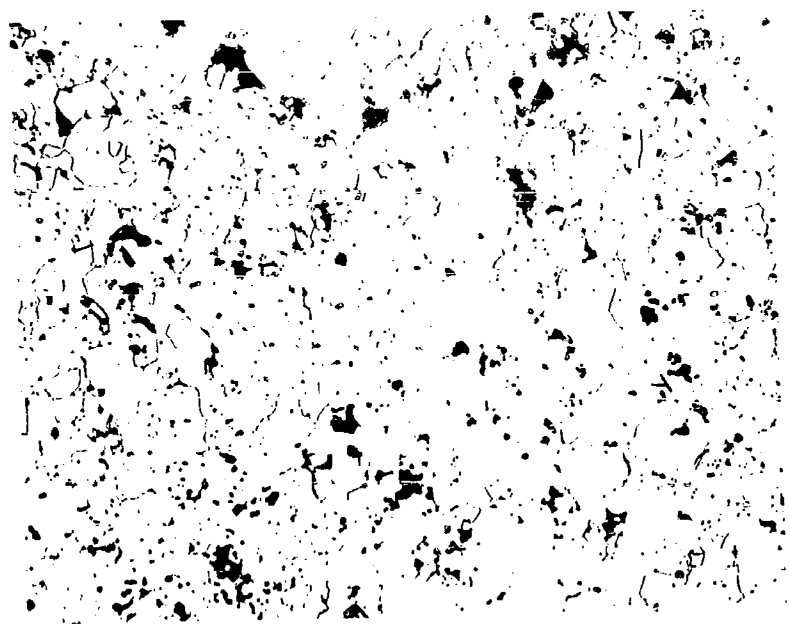

Etched X500
Etchant: Modified Aqua Regia

Figure 5 - Metal Rich Zirconium Diboride Fabricated From ZrB_2(1), $B/Zr = 1.89$. Characterization No. 30-3 Oxidation No. XVIII-28

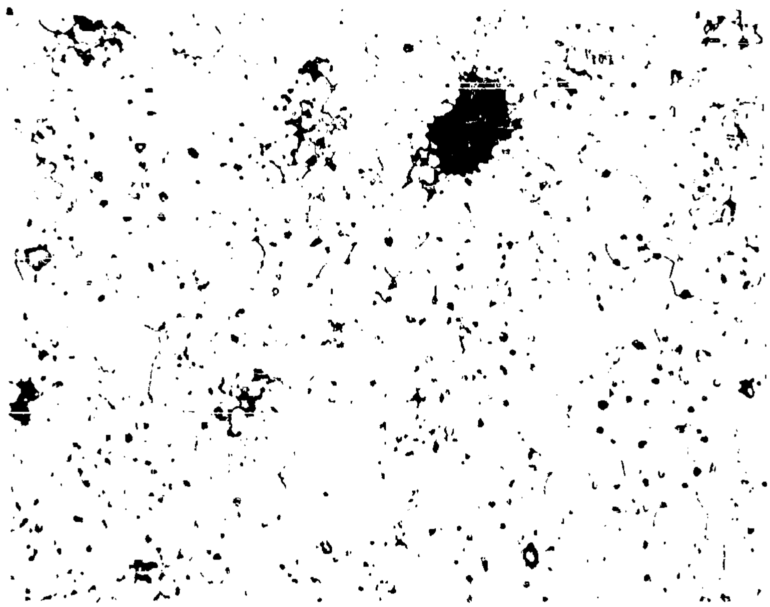

Etched X500
Etchant: Modified Aqua Regia

Figure 6 - Metal Rich Zirconium Diboride Fabricated From ZrB_2(P), B/Zr = 1.97 Characterization No. P5-5 Oxidation No. XX-17

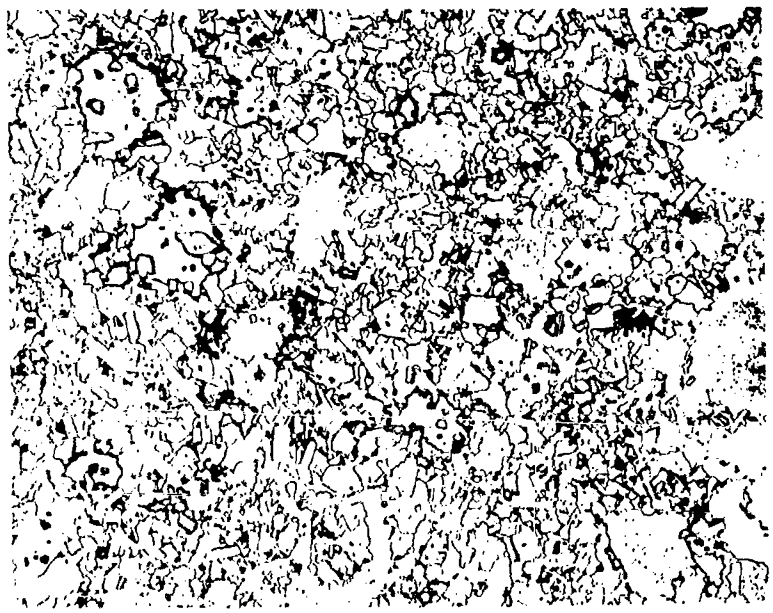

Etched X500

Etchant: 10cc glycerine, 10cc HNO_3, 2cc HCL, 0.1cc HF

Figure 7 - Metal Rich Zirconium Diboride Fabricated From ZrB_2(l) + Zr, B/Zr = 1.70. Characterization No. A17-2 Oxidation No. XX-47

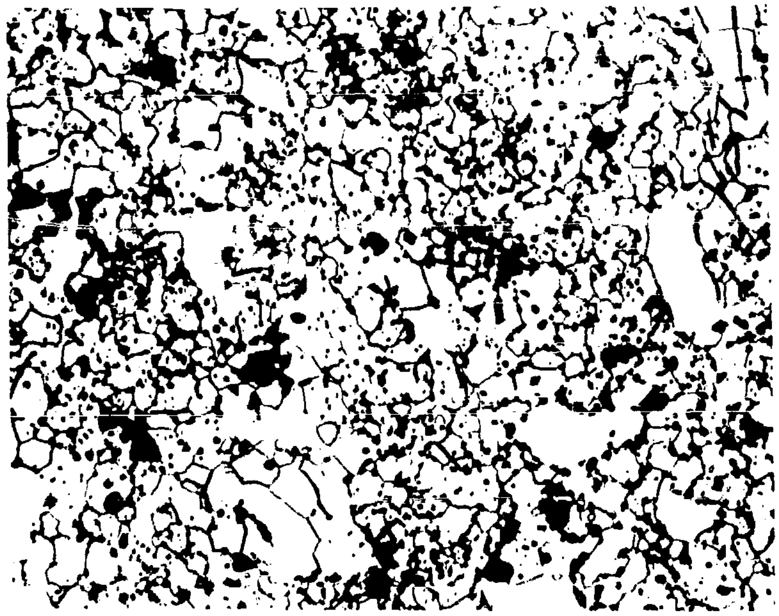

Etched X500
Etchant: 10cc glycerine, 10cc HNO_3
2cc HCL, 0.1cc HF

Figure 8 - Boron Rich Zirconium Diboride Fabricated From ZrB_2 (1) + B, B/Zr = 2.1, Characterization No. A22-1, Oxidation No. XXII-9.

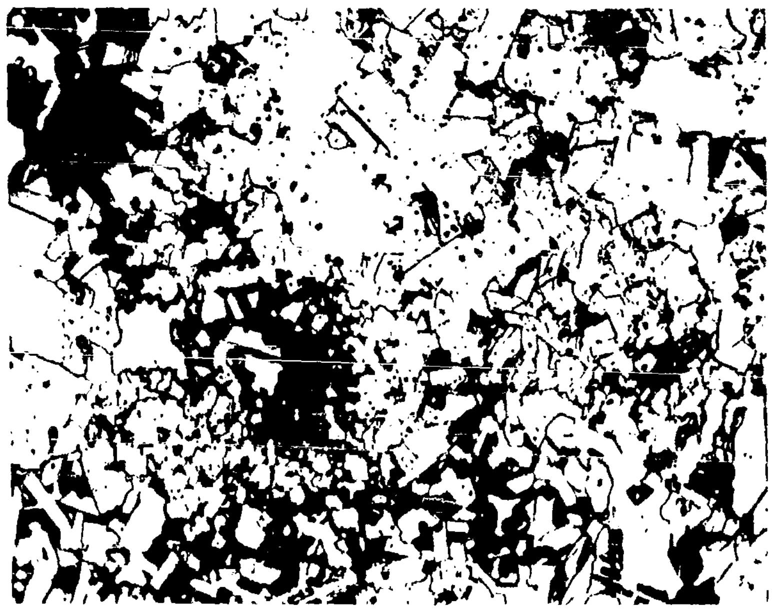

Etched X500
Etchant: 10cc glycerine, 10cc HNO_3
2cc HCL, 0.1cc HF

Figure 9 - Metal Rich Zirconium Diboride With Silicon Additive
Fabricated From $ZrB_2(1) + Zr + Si$, $ZrB_{1.7}\ Si_{0.25}$
Characterization No. A21-3 Oxidation No. XXI-17.

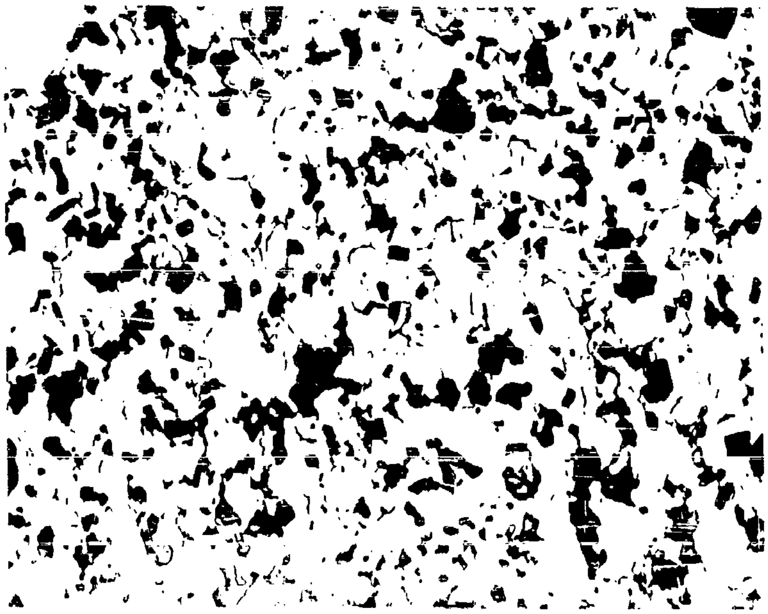

Typical Area

As Polished X500

Figure 10 - Boride Z, Zirconium Diboride Composite Supplied by Carborundum Company.

Top Layer

Initial Layer

Perpendicular Cross Section to Deposited Layer
Etched X500

Parallel Center Section of Top Layer to Deposited Layer
Etched X200

Parallel Center Section of Initial Layer to Deposited Layer
Etched X200

Etchant: 10 glycerine, 10cc HNO_3, 2cc HCL, 0.1cc HF

Figure 11 - Pyrolytic Zirconium Diboride, B/Zr = 1.85 Supplied by Raytheon Company.

5. Metal Rich Zirconium Diboride

Material fabricated from ZrB_2(1) as received with B/Zr = 1.89 provided dense two phase specimens, metal rich diboride and less than four weight percent of a cubic phase material. Grain growth was not observed. A representative photomicrograph is shown in Figure 5.

Material fabricated from ZrB_2(P) as received with B/Zr = 1.97 provided dense specimens which were primarily metal rich diboride with less than one weight percent ZrO_2. A fine grain specimen is shown in Figure 6.

Material fabricated from ZrB_2(1) with initial B/Zr = 1.89 with added Zr to adjust the overall B/Zr = 1.70 provided dense, fine grain, two phase specimens, metal rich diboride and a cubic phase material. A representative photomicrograph is shown in Figure 7.

6. Boron Rich Zirconium Diboride

Material fabricated from ZrB_2(1) with an initial B/Zr = 1.88 with added boron to adjust the overall B/Zr = 2.1 provided dense two phase specimens, boron rich diboride and free boron in the as hot pressed condition. Considerable difficulty was encountered in attempting to pre-mix the powders. The resulting structure is shown in Figure 8.

7. Metal Rich Zirconium Diboride with Silicon Additive

Material fabricated from ZrB_2(1) with initial B/Zr = 1.89 and added Zr and Si to adjust the overall B + Si/Zr = 1.95 ($ZrB_{1.7}Si_{0.25}$), provided dense two phase specimens. X-ray diffraction indicated the absence of elemental silicon and the presence of the diboride. Several unexplained lines were noted. A representative photomicrograph is shown in Figure 9.

8. Boride Z

Boride Z supplied by the Carborundum Company is manufactured as a hot pressed composite. X-ray examination indicated a slightly expanded zirconium diboride lattice and silicon carbide. Spectroscopic analysis showed the presence of Zr, B, Si and a small amount of Mo.; metallographic examination revealed the presence of two phases. The above characterization indicate that Boride Z (as received from Carborundum in this shipment) is a two phase composite. The major component is zirconium diboride with a small amount of molybdenum in solid solution and the minor component is silicon carbide. A representative photomicrograph is shown in Figure 10.

9. Pyrolytic Zirconium Diboride

The Raytheon Company, Research Division, Waltham, Mass. supplied a sheet of pyrolytically deposited ZrB_2. This dense, crack-free material was examined metallographically and several chemical analyses were obtained. The averaged results showed 80.5 w/o Zr, 17.8 w/o B, B/Zr = 1.85. Representative photomicrographs are shown in Figure 11.

V. SINTERING CHARACTERISTICS OF ZrB_2*

A. Introduction and Summary

The initial study of the sintering behavior of zirconium diboride followed the assumption that experimental behavior would be similar to that observed for titanium diboride (8). The objectives of the study were to collect suitable data for interpreting the sintering mechanism and to examine the treatments required to achieve high sintered densities. The data show that ZrB_2 differs from TiB_2 because vaporization does not affect the sintering kinetics nor control the limiting densities.

As received zirconium diboride, ($ZrB_{1.89}$), was the principal material used in the investigation; additional compositions were examined. Also, $ZrB_{1.89}$ samples with silicon and zirconium carbide were prepared and sintered. It was anticipated that the additives would provide (1) a liquid phase during sintering, and (2) an inert solid phase for inhibiting discontinuous grain growth. Hafnium diboride was sintered at two temperatures to determine if its behavior approximated that of zirconium diboride.

Sintering of $ZrB_{1.89}$ at the highest temperature (2300°C) resulted in tungsten contamination in some of the specimens. The contamination produced a liquid phase which caused more rapid sintering than would be predicted by extrapolation of rates observed at lower temperatures. Also, the interaction between zirconium diboride and tungsten caused early failure of the tungsten heating elements; short firing times were governed by element failure.

The highest sintered densities in $ZrB_{1.89}$ were in the range of 98% of theoretical density. The incorporation of excess zirconium to form a liquid phase permitted sintering to densities in the range of theoretical at temperatures lower than those required in undoped samples. Silicon and zirconium carbide additives in zirconium diboride effectively inhibited the sintering rate with the additions investigated. Discontinuous grain growth was not inhibited by any of the selected additions. Density was limited to 96% of theoretical in the absence of discontinuous grain growth.

Most of the sintered specimens of $ZrB_{1.89}$ contain a second phase. From examination of the photomicrographs, it is concluded that the second phase forms a liquid at the sintering temperatures. Therefore, the sintering behavior is interpreted in terms of the grain boundary diffusion model, which is applicable in the case where the volume fraction of a liquid second phase is small.

---

*R. L. Coble and H. A. Hobbs, Lexington Laboratories, Inc.

Zirconium diboride with a boron to zirconium ratio of 1.96 and a higher purity than the 1.89 ratio material was found to exhibit grain growth and densification essentially identical to $ZrB_{1.89}$. The addition of zirconium metal to $ZrB_{1.89}$ to give a boron to zirconium ratio of 1.70 increased the rate of densification. This observation is consistent with the much lower melting point of zirconium than that of the other phases suspected to be present in $ZrB_{1.89}$. Samples with excess zirconium were sintered to high density at 1800°C in 2 hours.

The occurrence of a boundary diffusion mechanism and the applicability of a boundary diffusion model to the sintering data are supported in the following discussion. The plots of relative density on a linear scale versus the logarithm of the sintering time for $ZrB_{1.89}$ show essentially linear behavior. For a lattice diffusion mechanism, linear time dependence has been observed for the sintering of aluminum oxide (9) when the grain size varies with time to the 1/3 power. This explanation is valid if the grain size versus time to the 1/3 power curves extrapolate back through zero at zero time. For the collected data, the grain size is linear with $t^{1/3}$ and extrapolates back through the initial particle size of 5 microns at zero time. However, the simple direct application of the 1/3 power time dependence for a lattice diffusion process should not lead to the observed linear relative density versus log time plots. For the data collected on $ZrB_{1.89}$, the occurrence of a boundary diffusion mechanism is supported by a linear relation between relative density (to the 3/2 power) versus linear time over the grain size to the fourth power. The calculated diffusion coefficients appear to be high; however, the effective width of the grain boundary in this material is uncertain since knowledge about the volume fraction liquid phase present at sintering temperatures is minimal. Our conclusion that zirconium diboride $ZrB_{1.89}$ sinters by boundary diffusion model is tentative because the data are barely sufficient to calculate diffusion coefficients and independent data are not available for comparison.

Hafnium diboride specimens were found to undergo densification at 2100°C, giving relative densities only slightly less than those achieved in zirconium diboride at equivalent times of sintering. The hafnium diboride contained more second phase than did the zirconium diboride, and, for the heat treatments employed, did not exhibit discontinuous grain growth. The excess second phase inhibits normal grain growth, as well. After firing for 4 hours at 2100°C, the average grain size of hafnium diboride is approximately two-thirds the size observed in zirconium diboride.

B. Experimental

1. Powder Preparation

Samples were prepared from both as-received, A.R., zirconium diboride and fluid-energy-milled, F.E.M., zirconium diboride. A photomicrograph of the fluid-energy-milled powder is shown in Figure 12.

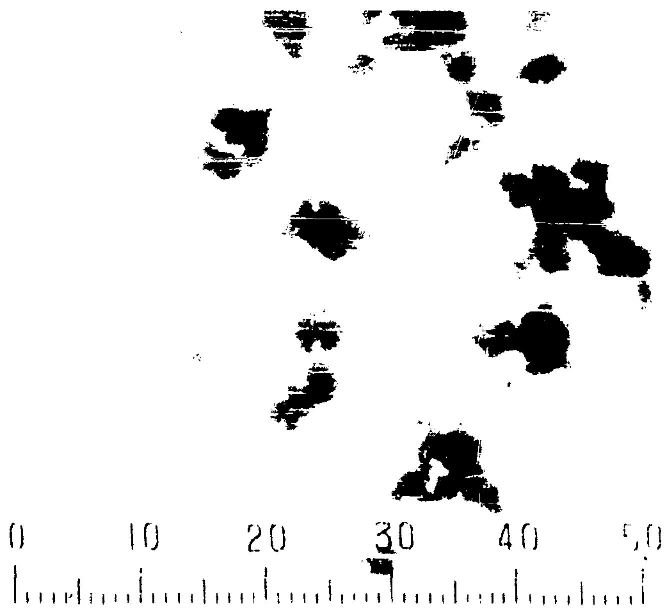

Figure 12. Fluid Energy Milled Zirconium Diboride Powder. 750X

The average particle size from this dispersion is 5 microns. The analysis of this powder is presented in Table 8 , where zirconium, boron, tungsten, nitrogen, oxygen, and carbon contents are shown. After firing, the carbon and oxygen contents are reduced although the oxygen content in the fired fluid-energy-milled sample is three times that in fired as-received samples. The B/Zr ratios do not change significantly after grinding or firing.

The preparation of $ZrB_{1.7}$ was achieved by adding metallic zirconium to $ZrB_{1.89}$. For the samples containing silicon, excess zirconium was added, giving a net formula of $Zr(B, Si)_{1.89}$. The $ZrB_{1.97}$ and ZrC were prepared by fluid-energy-milling. These powders were handled by procedures which were found to be appropriate for $ZrB_{1.89}$. No chemical analyses were determined since it was assumed that the contaminations would have been equivalent for $ZrB_{1.89}$, as given in Table 8. The hafnium diboride was used as received.

2. Pressing

Samples were pressed with a binder of polyvinyl alcohol in water solution; the procedure for incorporating the binder has been described previously (8). Samples were pressed at 24,000 and 70,000 psi. The green density of the pellets pressed at 70,000 psi varied from 3.75 to 4.03 g/cm^3, giving approximate relative densities of 62% for the initial density of the majority of the sintering experiments.

3. Sintering

All samples were sintered in a vacuum furnace which consists of a rolled tungsten sheet clamped into water-cooled electrodes. The furnace has been described in a previous report (8). Samples were either suspended through an upper opening of the tungsten sleeve or supported on a pedestal. The temperature of the specimen was read through a slot in the rolled sheet with an optical pyrometer. Furnace pressure was typically 5×10^{-5} mm of Hg at the firing temperatures.

C. Results

Data sheets for the sintered specimens presented in Table 9 show forming pressure, the as-pressed density, fired density, weight changes, firing times, firing temperatures, grain size, and porosity (determined by point counts and lineal analysis of photomicrographs). The relative density of samples of $ZrB_{1.89}$ sintered at temperatures from 2000° to $2300^\circ C$ is plotted linearly against logarithms of sintering time in Figure 13. The points include the densities measured by displacement in xylene as well as those determined by lineal analysis. The data scatter can be attributed to delamination which produces erroneous measurements in displacement densities, and to pullouts which are difficult to distinguish from pores (in low density specimens) and produce errors in the point count measurements.

TABLE 8

ANALYSIS OF ZrB_2 POWDER SAMPLES AND FIRED SPECIMENS

Constituent	A.R.	Fired at 2300°C 25 min. A.R.*	F.E.M.*	Fired at 2300°C 25 min. F.E.M.*	Fired at 2100°C 6 hrs.	Fired at 2200°C 2 hrs.
Zr	80.67	71.9	79.8	73.9	80.4*	79.5*
B	18.05	16.5	17.8	16.5	17.8*	17.8*
W	0.00	5.6	0.02	6.9	---	---
C	0.33	0.06	0.38	0.09	0.09+	0.09+
O	0.53	0.051	0.43	0.16	0.09+	0.09+
N	0.19	0.10	0.16	0.11	0.08+	0.07+
Fe					0.04+	0.03+
B/Zr ratio	1.89	1.94	1.88	1.89++	1.87++	1.88++

* Analysis by D. Guernsey, Metallurgy Department, M.I.T.

\+ Analysis by Jarrell-Ash Company, Waltham, Mass.

++ These values can be compared to the congruently vaporizing composition which is calculated as 1.94 at 2100°C and 1.91 at 2200°C from Figure 71.

TABLE 9

PROPERTIES OF DIBORIDE SINTERING SPECIMENS*

Specimen	Forming Press. (kpsi)	Green Density (g/cm^3)	Weight (grams)	Fired Density (g/cm^3)	Weight Change (grams)	Firing Time	Temp. (^oC)	Grain Size (μ)
TM-1 FEM	24	3.80		4.60		10 min.	2200	10.3
2 FEM	24	3.82		4.72		10 min.	2200	
3 FEM	24	3.80		4.57		10 min.	2200	
4 FEM	24	3.81		4.81		10 min.	2200	
II-2 AR	70	4.05	1.68	6.41	-0.01	25 min.	2310	16.6
III-2 FEM	70	3.84	1.71	6.44	+0.044	25 min.	2310	14.3
I-4 FEM	70		1.635	4.68	-0.0019	1 min.	2300	
II-4 FEM	70		1.603	4.67	+0.001	1 min.	2300	
III-4 FEM	70		1.635	4.65	-0.040	1 min.	2300	13.3
IV-4 FEM	70		1.470	4.50	-0.0475	1 min.	2300	
A FEM	70	4.03	1.0153	7.43	+0.0109	32 min.	2300	30.2
8A FEM	70	3.75	1.7491	5.81	-0.2322	6 hrs.	2100	35.4
8B FEM	70	3.82	1.5036	5.91	-0.2418	6 hrs.	2100	
X-1 FEM	70	3.84	1.4874	5.30	-0.0357	1 hr.	2100	
X1-1 FEM	70	3.94	1.7147	4.91	-0.0485	1 hr.	2100	13
X111-1 FEM	70	3.90	1.3176	4.24	-0.0267	1/2 hr.	2100	7.8
X111-2 FEM	70	3.92	1.7248	4.27	-0.0321	1/2 hr.	2100	
X-1 FEM	70	3.84	1.4874	5.39	-0.2257	2 hrs.	2100	15.4
X1-1 FEM	70	3.94	1.7147	5.08	-0.0548	2 hrs.	2100	13
XV-5 FEM	70	3.82	1.2208	5.26	-0.0405	1 hr.	2100	14
XV-6 FEM	70	3.83	1.4179	5.18	-0.0461	1 hr.	2100	
XV-7 FEM	70	3.78	1.1435	5.90	-0.2663	30 min.	2200	

TABLE 9 (CONTINUED)

PROPERTIES OF DIBORIDE SINTERING SPECIMENS*

Specimen	Forming Press. (kpsi)	Green Density (g/cm^3)	Weight (grams)	Fired Density (g/cm^3)	Weight Change (grams)	Firing Time	Temp. (^{o}C)	Grain Size (μ)
X11-1 FEM	70	3.89	1.5780	5.67	(broke)	1 hr.	2200	15.2
X11-2 FEM	70	3.83	1.5486	5.85	-0.0908	1 hr.	2200	
XV-1 FEM	70	3.86	1.5752	5.90	-0.0784	2 hrs.	2200	
XV-2 FEM	70	3.84	1.3953	5.96	-0.1123	2 hrs.	2200	19.7
XV-8 FEM	70	3.80	1.5041	6.01		4 hrs.	2200	41.4
LX-1 AR	50	3.85	2.1545	5.65	-0.0381	4 hrs.	2100	19.2
LX-2 AR	50	3.84	1.8983	5.75	-0.0116	4 hrs.	2100	
LX-3 AR	50	3.79	1.9832	4.37	-0.0369	1 hr.	2000	
LX-4 AR	50	3.88	2.0604	4.24	-0.0361	1 hr.	2000	9.6
LX-9 AR	50	3.84	2.1382	4.20	-0.0525	2 hrs.	2000	11
LX-10 AR	50	3.98	2.6230	4.36	-0.0503	2 hrs.	2000	
LX-11 AR	50	3.83	2.0227	4.43	-0.0361	4 hrs.	2000	11.6
LX-12 AR	50	3.78	2.1118	4.67	-0.0277	4 hrs.	2000	
LX-5 AR	50	3.78	2.2623	5.39	-0.0519	8-1/2 hrs.	2000	
LX-6 AR	50	3.80	2.0070	5.56	-0.0340	8-1/2 hrs.	2000	12.4
LXV-1 AR	50	3.92	1.1071	5.73	-0.1006	16 hrs.	2000	15.4
LXV-2 AR	50	3.91	1.1068	5.79	-0.0990	16 hrs.	2000	
PR-1 ($ZrB_{1.96}$)	50	3.79	0.6873	5.46	-0.0341	2 hrs.	2100	18.2
PR-2 ($ZrB_{1.96}$)	50	3.80	0.7482	5.49	-0.0390	2 hrs.	2100	

TABLE 9 (CONTINUED)

PROPERTIES OF DIBORIDE SINTERING SPECIMENS*

Specimen	Forming Press. (kpsi)	Green Density (g/cm^3)	Weight (grams)	Fired Density (g/cm^3)	Weight Change (grams)	Firing Time	Temp. (^oC)	Grain Size (μ)
PR-3 ($ZrB_{1.96}$)	50	3.78	0.7372	5.78	-0.0423	4 hrs.	2100	26.1
PR-4 ($ZrB_{1.96}$)	50	3.86	0.7331	5.78	-0.0414	4 hrs.	2100	
PR-5 ($ZrB_{1.96}$)	50	3.85	0.6314	5.50	-0.0500	6 hrs.	2100	
PR-6 ($ZrB_{1.96}$)	50	3.84	0.8411	5.82	-0.0602	6 hrs.	2100	50.4
OS-5	50	3.82	0.6851	6.01	-0.0434	6 hrs.	2100	
OS-6	50	3.86	0.7097	6.03	-0.0334	6 hrs.	2100	
OS-7	50	3.91	0.7605	6.00	-0.0355	6 hrs.	2100	
OS-8	50	3.84	0.6928	5.99	-0.0384	6 hrs.	2100	
OSS-1**	50	3.62	0.6221	4.90	(broke)	2 hrs.	1500	
OSS-2**	50	3.64	0.6917	4.91	-0.0088	2 hrs.	1500	
OSS-3**	50	3.72	0.8610	4.90	-0.0270	2 hrs.	1500	
OSS-4**	50	3.76	0.8037	4.82	-0.0336	2 hrs.	1500	
OSS-5**	50	3.80	0.8801	4.97	-0.0391	4 hrs.	1700	
OSS-6**	50	3.74	0.7702	5.03	-0.0380	4 hrs.	1700	
OSZ-1 ($ZrB_{1.7}$)	50	3.82	0.7212	5.95	(broke)	2 hrs.	1800	
OSZ-2 ($ZrB_{1.7}$)	50	3.86	0.7610	5.93	-0.0576	2 hrs.	1800	
OSZ-3 ($ZrB_{1.7}$)	50	3.80	0.7681	5.91	-0.0605	2 hrs.	1800	15.4
Hf-1 (HfB_2)	70	6.44	2.5314	8.66	-0.0648	4 hrs.	2100	

TABLE 9 (CONTINUED)

PROPERTIES OF DIBORIDE SINTERING SPECIMENS

Specimen	Forming Press. (kpsi)	Green Density (g/cm^3)	Weight (grams)	Fired Density (g/cm^3)	Weight Change (grams)	Firing Time	Temp. (°C)	Grain Size (μ)
Hf-2 (HfB_2)	70	6.55	2.5271	9.13	-0.0306	4 hrs.	2100	
Hf-3 (HfB_2)	70	6.29	2.5930	9.73	-0.0654	6 hrs.	2100	
Hf-4 (HfB_2)	70	6.27	2.4887	9.40	-0.0694	5 min.	2300	
ZrC-1+	70	3.87	0.9763	6.01	-0.0537	4 hrs.	2200	30
ZrC-5++	70	3.80	0.8627	5.83	-0.0326	4 hrs.	2200	
ZrC-10+++	70	3.77	0.9007	4.74	-0.0137	4 hrs.	2200	
ZrC-15++++	70	3.79	0.7503	4.48	-0.0034	4 hrs.	2200	

* The metallographic analysis of the more dense samples which appeared to lose a considerable amount of weight during firing did not reveal any contamination. Unless otherwise noted, samples are $ZrB_{1.89}$.

** [$Zr(B, Si)_{1.89}$]

\+ ZrB_2 + 1wt % ZrC

++ ZrB_2 + 5wt % ZrC

+++ ZrB_2 + 10wt % ZrC

++++ ZrB_2 + 15wt % ZrC

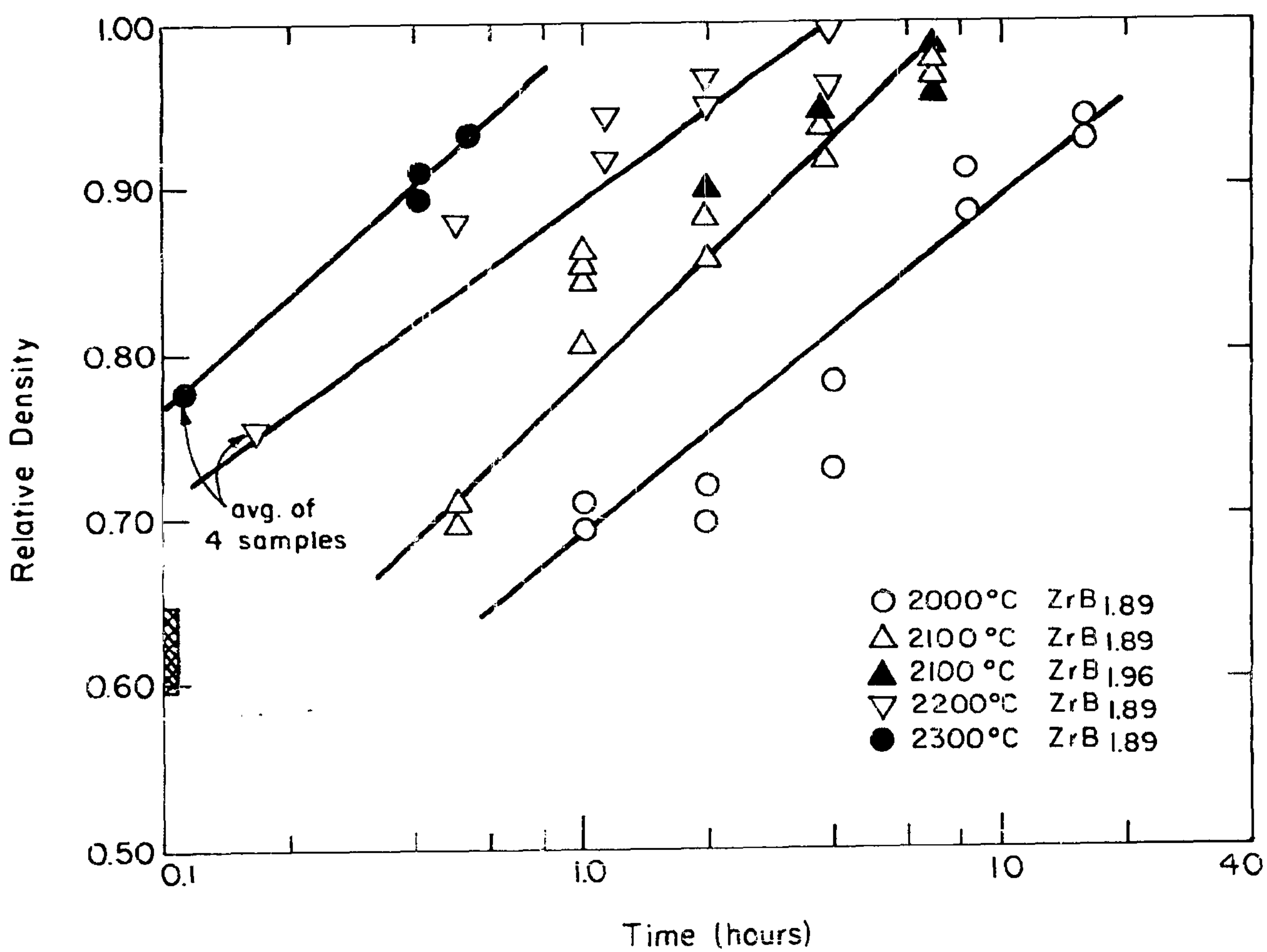

Figure 13. Relative Density vs. Time for $ZrB_{1.89}$ as a Function of Temperature and for $ZrB_{1.96}$ at 2100°C.

The relative density of other samples is plotted in Figure 14. The $ZrB_{1.89}$ samples sintered at 2300°C (Figure 13) contained tungsten. The chemical analysis of two samples are given in Table 8 . The relative densities presented in Figure 13 for specimens fired at the higher temperatures are corrected for the volume fraction and density of tungsten by assuming a contamination of 6 weight per cent tungsten. Grain size data determined by point counting are presented in Figure 15. Polished sections of samples containing tungsten are shown in Figures 16a and 16b in the as-polished and etched conditions, respectively. The etched sample reveals the structure of eutectic solidification. The pores occur inside the grains and provide evidence for discontinuous grain growth in this sintering cycle. Photomicrographs of sintered specimens are presented in Figures 17 through 27 for various samples, and for sintering temperatures and times.

For samples with the shortest sintering times, large grains (25 microns) exist in a much finer grained matrix, as in Figures 17a and 17b There is little evidence that pores have been trapped inside grains. In the etched sample (Figure 17b), the grain boundaries appear to intersect the majority of the small pores.

In $ZrB_{1.89}$ samples fired at 2100°C for one hour, 2200°C for 4 hours, and 2000°C for 16 hours, the presence of a second phase appears in the as-polished photomicrographs, (18a, 21a, 22a, and 23a). In a sample which had been fired for 6 hours and etched (Figure 20b), the presence of a second phase is denoted by the corrugations and marked changes in the etching characteristics of given boundaries. The large increase in average grain size in this sample and the presence of a duplex structure (Figure 20) show that the sample experienced discontinuous grain growth.

In Figure 15, the minimum grain size (17 microns) for the 6 hour sample was measured in the fine grained matrix, and the maximum grain size for secondary grains was of the order of 80 microns. For the $ZrB_{1.89}$ sample sintered two hours, the majority of pores were intersected by grain boundaries, however, for the 6 hour specimen pores were entraped in larger secondary grains. The behavior of samples fired at 2000°C was essentially identical to that observed at 2100°C. The change in the time at which discontinuous grain growth occurred was consistent with the change in the kinetics due to temperature. The general features of the microstructures at equivalent densities remain the same and are independent of temperature.

It is concluded that a second phase was present at all sintering temperatures. The grain structure shown in Figure 20b (linear boundaries of larger grains are intersected by boundaries of other grains without an observable deviation in the intersected boundaries) would require that a liquid phase be present at the sintering temperature. If no additional phase were present, the included angle of intersection must be less than 180°. Therefore, there is evidence that a second phase exists in the structure and that the second phase was present as a liquid at the sintering temperatures.

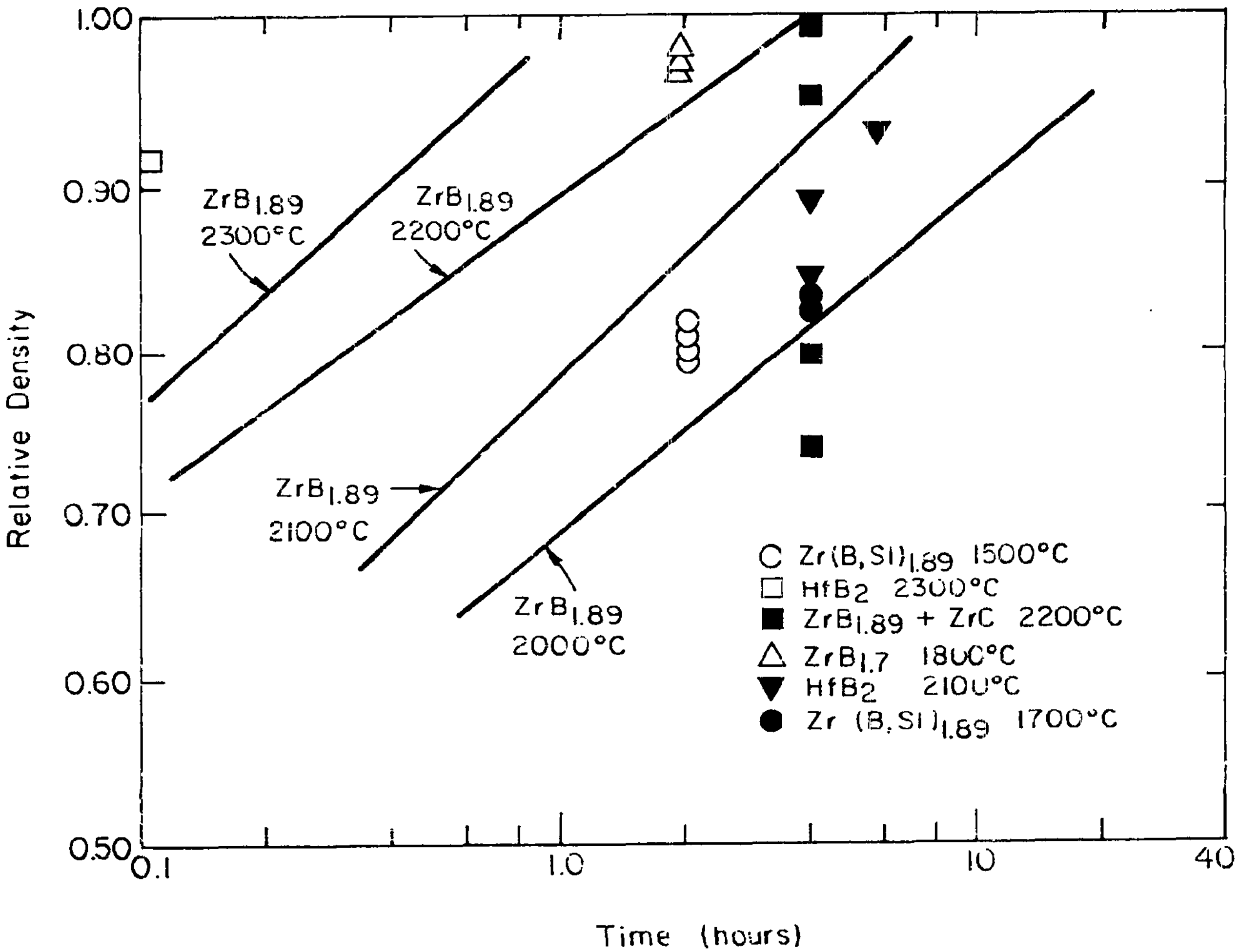

Figure 14. Relative Density vs. Time for Various Materials Compared with $ZrB_{1.89}$ at 2000° to 2300°C.

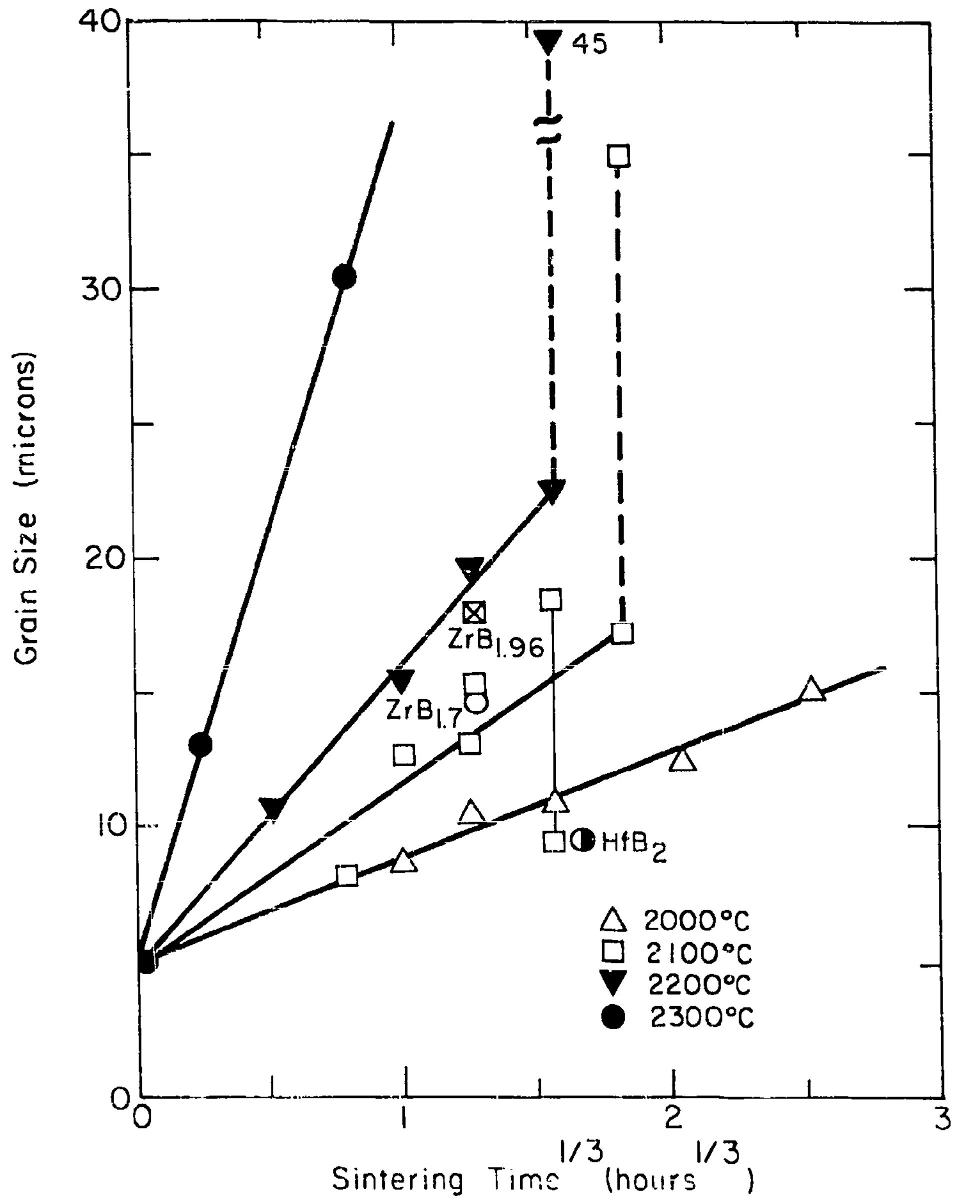

Figure 15. Grain Size vs. Time $^{1/3}$ for $ZrB_{1.89}$.

Figure 16a. FEM $ZrB_{1.89}$ Fired at 2300°C for 32 Minutes; (400X, Unetched).

Figure 16b. FEM $ZrB_{1.89}$ Fired at 2300°C for 32 Minutes; (400X, Etched 1 Hf, 1 HNO_3, 3 Lactic).

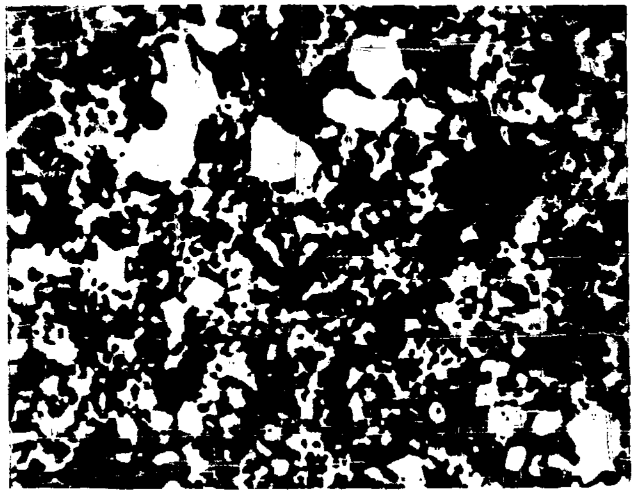

Figure 17a. FEM $ZrB_{1.89}$ Fired at 2100°C for 1/2 Hour, 400X, Unetched.

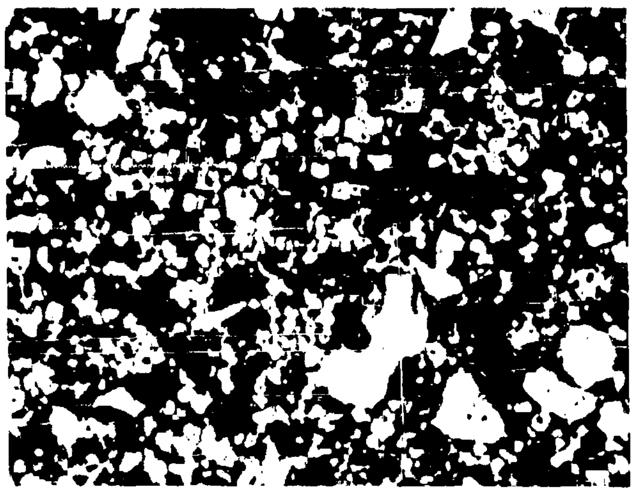

Figure 17b. FEM $ZrB_{1.89}$ Fired at 2100°C for 1/2 Hour, 400X, Etched 1 HF: 2 HNO_3: 2 H_2O.

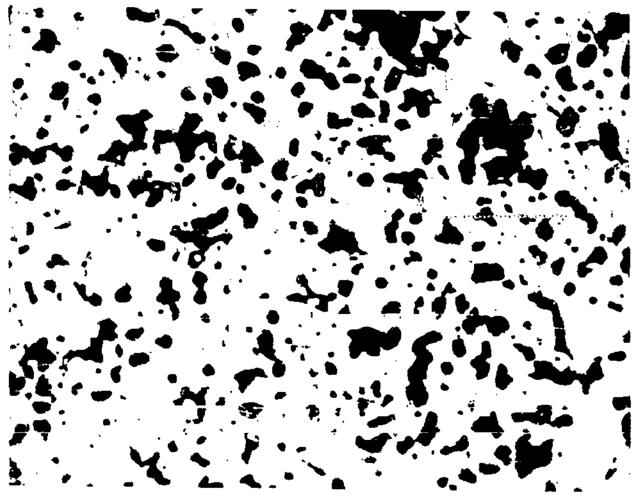

Figure 18a. FEM $ZrB_{1.89}$ Fired at 2100°C 1 Hour, 400X, Unetched.

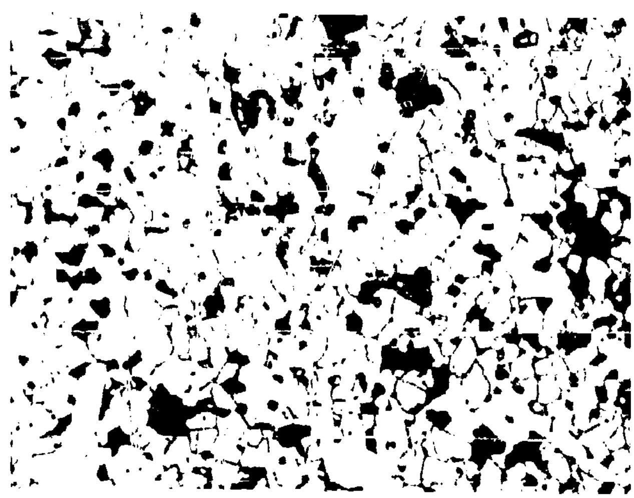

Figure 18b. FEM $ZrB_{1.89}$ Fired at 2100°C 1 Hour, 400X, Etched 1 HF: $2HNO_3$: $2H_2O$.

Figure 19a. FEM $ZrB_{1.89}$ Fired at 2100°C 2 Hours, 400X, Unetched.

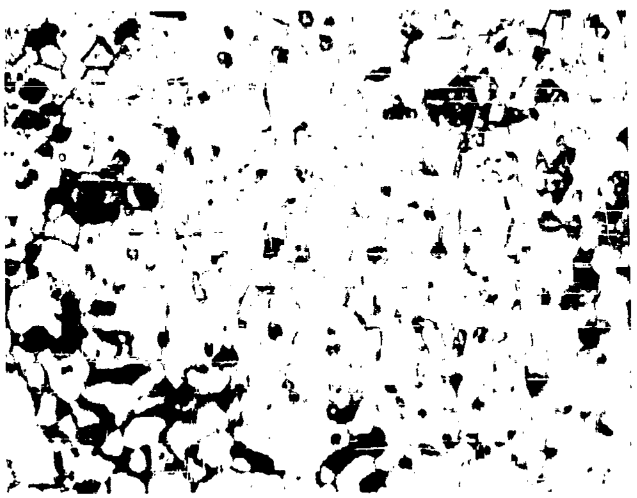

Figure 19b. FEM $ZrB_{1.89}$ Fired at 2100°C 2 Hours, 400X, Etched 1HF : $2HNO_3$: $2H_2O$.

Figure 20a. FEM $ZrB_{1.89}$ Fired at 2100°C 6 Hours, 400X, Unetched.

Figure 20b. FEM $ZrB_{1.89}$ Fired at 2100°C 6 Hours, 400X, Etched 1 HF: 2 HNO_3: 2 H_2O.

Figure 21a. FEM $ZrB_{1.89}$ Fired at 2200°C for 4 hours 400X, Unetched.

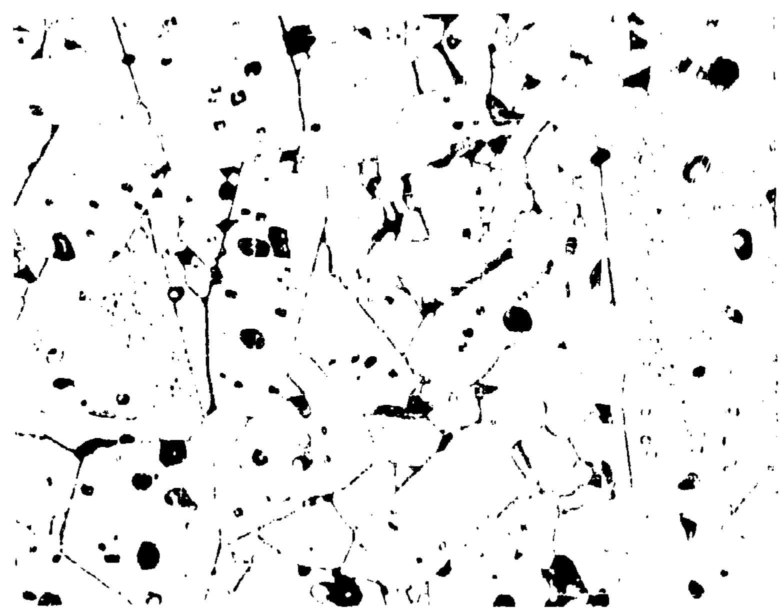

Figure 21b. FEM $ZrB_{1.89}$ Fired at 2200°C for 4 hours 400X, Etched 1HF: $2HNO_3$: $2H_2O$

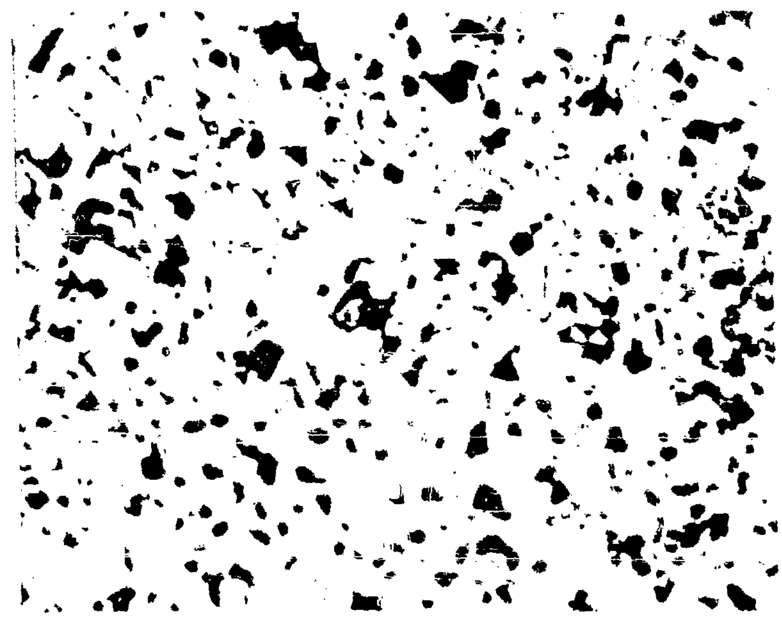

Figure 22a. FEM $ZrB_{1.89}$ Fired at 2000°C for 16 hrs. 400X, Unetched.

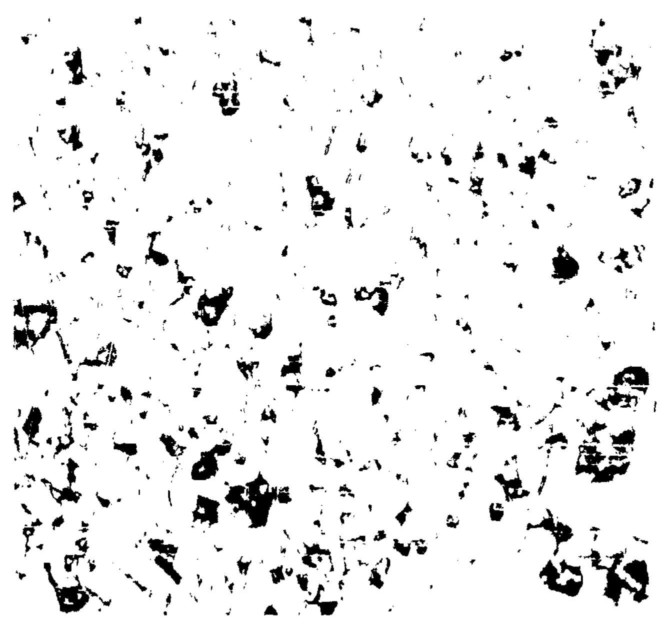

Figure 22b. FEM $ZrB_{1.89}$ Fired at 2000°C for 16 hrs. 400X, Etched $1HF:2HNO_3:2H_2O$

Figure 23a. A. R. $ZrB_{1.96}$ Fired at 2100°C for 6 hours
400X, Unetched.

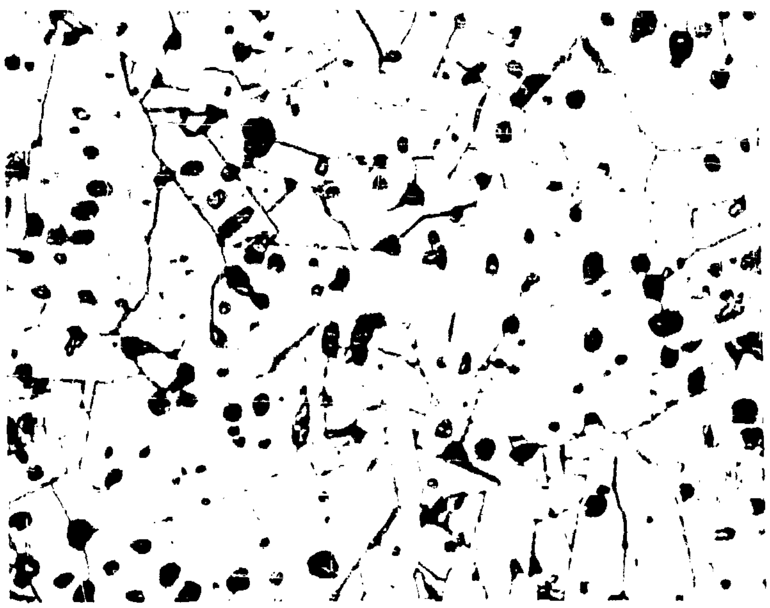

Figure 23b. A. R. $ZrB_{1.96}$ Fired at 2100°C for 6 hours
400X, Etched $1HF:2HNO_3:2H_2O$

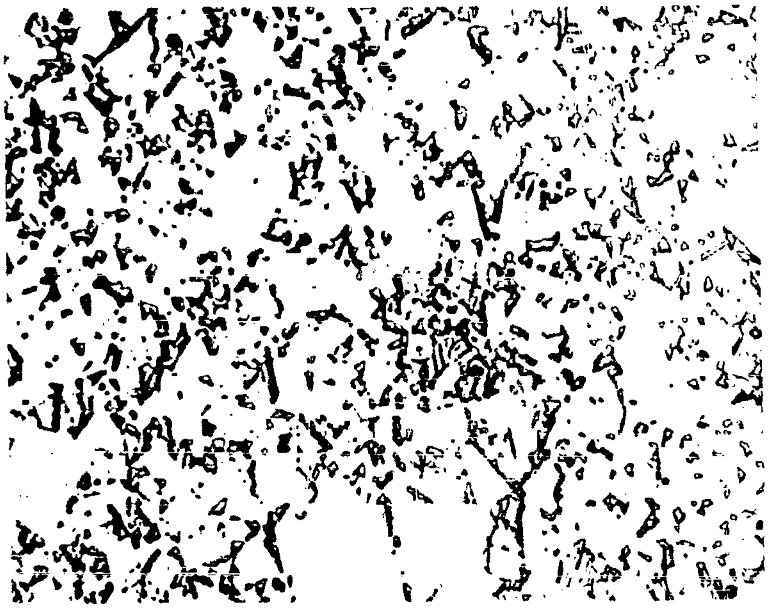

Figure 24a. $ZrB_{1.7}$ Fired at 1800°C for 2 hours
400X, Unetched.

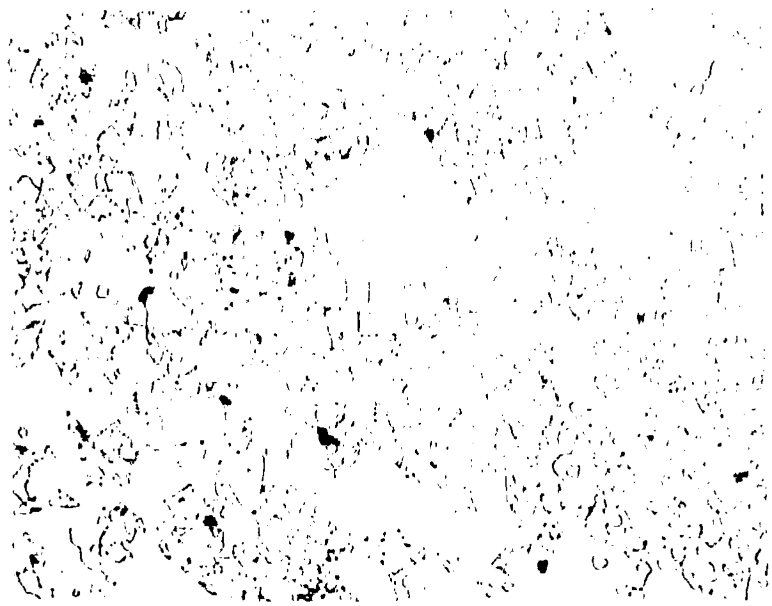

Figure 24b. $ZrB_{1.7}$ Fired at 1800°C for 2 hours
400X, Etched $1HNO_3$: $1H_2SO_4$: $2H_2O$

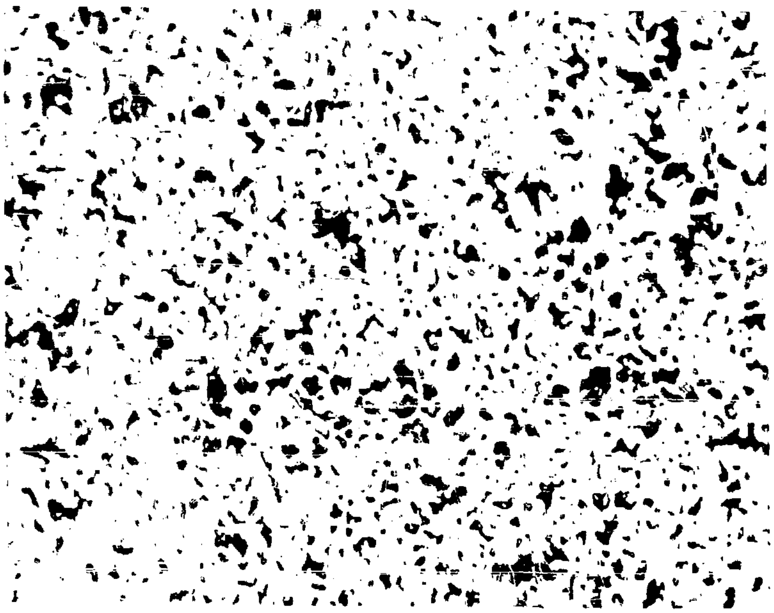

Figure 25a. A. R. HfB_2 Fired at 2100°C for 4 hours
400X, Unetched.

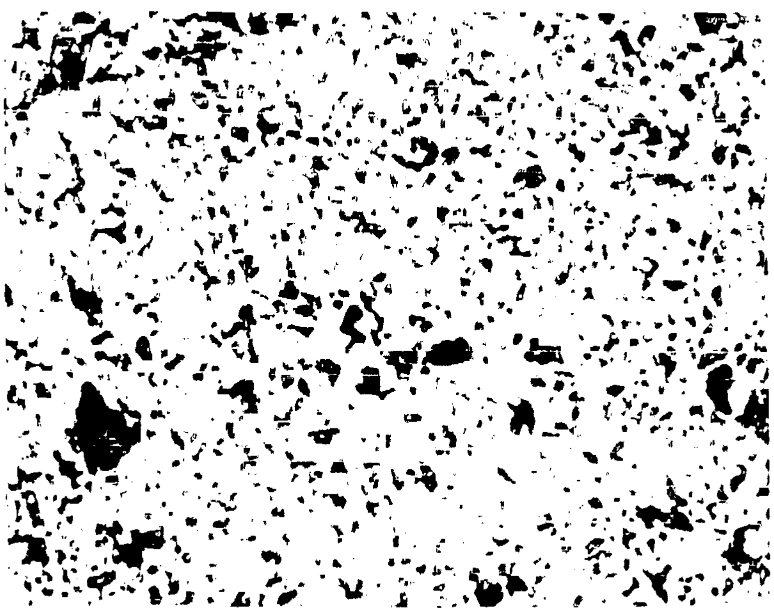

Figure 25b. A. R. HfB_2 Fired at 2100°C for 4 hours
400X, Etched $1HF:2HNO_3:2H_2O$

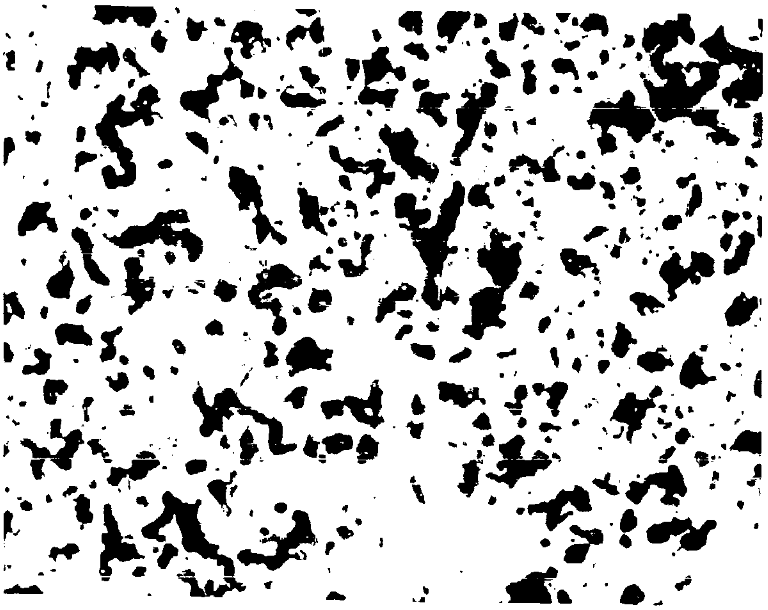

Figure 26a. $Zr(B, Si)_{1.89}$ Fired at 1500°C for 2 hours 400X, Unetched.

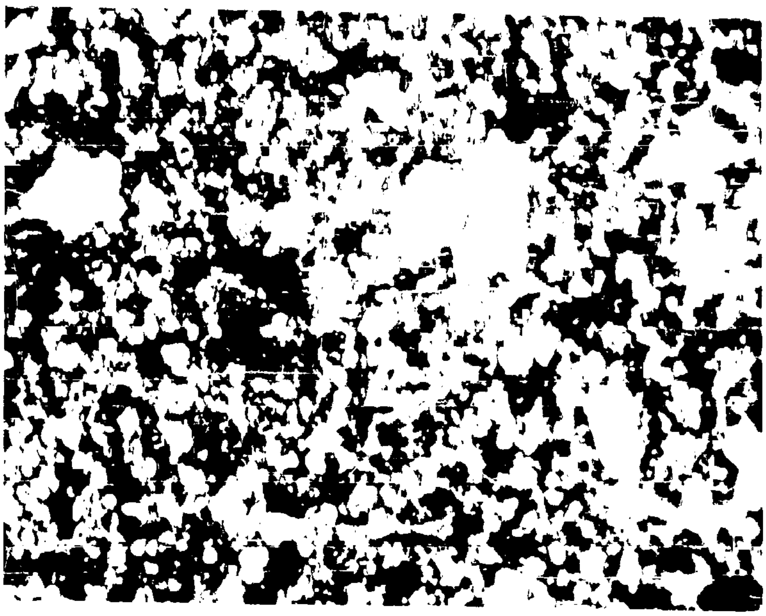

Figure 26b. $Zr(B, Si)_{1.89}$ Fired at 1500°C for 2 hours 400X, Etched $1HF:2HNO_3:2H_2O$

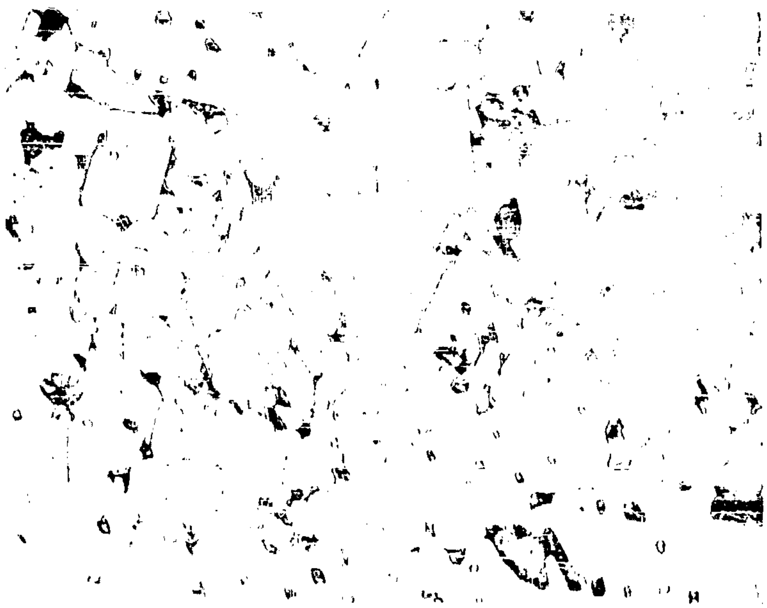

Figure 27. $ZrB_{1.89}$ + 1 wt. % -ZrC Fired at 2200°C for 4 hours, Etched 1HF:$2HNO_3$:$2H_2O$

The densities and grain sizes of $ZrB_{1.89}$ with zirconium, silicon and zirconium carbide additives, $ZrB_{1.96}$, and hafnium diboride are included on the data in Figures 14 and 15. These specimens were sintered at times and temperatures where the densities and grain size for $ZrB_{1.89}$ were known because a survey of their total sintering behavior was not planned. It can be concluded that for $ZrB_{1.96}$, HfB_2, and $ZrB_{1.89}$ + 1% ZrC the sintering behavior does not change significantly from that of $ZrB_{1.89}$, for samples containing more than 1% ZrC, the sintering rate was reduced in proportion to the content of zirconium carbide. Samples containing excess zirconium exhibited a sintering rate much higher than any observed for $ZrB_{1.89}$; these samples sintered to high density at 1800°C in 2 hours. Simultaneous additions of silicon and zirconium inhibited the sintering rate and resulted in low densities. Metallographic examination revealed a grossly inhomogeneous structure (Figure 26). Large particles were present and were separated from the general matrix by cracks and the included second phase.

D. Discussion

The mechanism of sintering in $ZrB_{1.89}$ may be assessed with the data now available. The change in relative density as a linear function of log time (Figure 14) appears to be analogous to the relation observed in aluminum oxide when the grain size increases linearly with time to the 1/3 power. In $ZrB_{1.89}$ the grain size increases from the initial or starting particle size as time to the 1/3 power. It was shown that the linear change in density with logarithm of time can be expected only if the grain size extrapolates through zero at time zero on a linear G vs. $t^{1/3}$ plot (9). An expression derived from a lattice diffusion sintering mechanism during the intermediate stage of the process is given as Eq. (1).

$$d\rho = \left\{\frac{N\, D_L\, \gamma\, \Omega}{G^3\, kT}\right\} dt \qquad (1)$$

where ρ = relative density
N = constant = 1.2×10^{-3}*
D_L = lattice diffusion coefficient of the rate controlling species
γ = the surface energy
Ω = the volume of a molecule of ZrB_2 (in the lattice)
k = Boltzmann's constant
T = Temperature
t = time
G = the grain size = $(G_o + k_1 t^{1/3})$
G_o = initial particle size
k_1 = the growth rate constant

*The constant was given in (9) as 10; the indicated value in this report was calculated by converting to equivalent spherical grain diameters, G, obtained metallographically.

Values of G observed from Figure 15 do not change significantly from the value of G_o in the region where discontinuous grain growth does not occur; therefore, the equation cannot be simplified for integration. For example, the grain sizes observed prior to discontinuous grain growth increase up to approximately 20 microns, with G_o at five microns. Values of k_1 were evaluated from Figure 15. For three temperatures, 2000°-2200°C an exponential relation exists with an activation energy of 154 kcal/mole. The higher growth rates at 2300°C (where tungsten contamination led to rapid densification and growth) give a higher k_1 value than would be given by the extrapolation of the behavior observed at lower temperatures. The activation energy observed for growth is in a range observed for other typical refractories.

For sintering by a liquid phase or grain boundary diffusion mechanism, the expression for densification during the intermediate stage of the process is:

$$d\left(\rho^{3/2}\right) = \frac{2.5\times10^3 D_b W \gamma \Omega}{G^4 \, kT} \, dt \qquad (2)$$

where D_b is the boundary diffusion coefficient and W is the boundary width.

Because of the dependence of the rate on grain size, temperature and time data were selected at three grain sizes (Figure 15) and the relative densities were taken from Figure 13 for analysis. These data are collected in Table 10. In order to test the applicability of Eq. (2), relative density (to the 3/2 power) was plotted versus time over grain size (to the fourth power) in Figure 28. The observed linear relation supports the boundary diffusion model. It is noteworthy that the grain size and density do not vary independently with temperature (Table 10). This could be related to control of grain growth by porosity, or to the fact that both are controlled by diffusion at the boundary region.

Diffusion coefficients calculated from both models are presented in Table 11. The calculated lattice diffusion coefficients are approximately equal to the value (10^{-10} cm^2/sec) observed for most refractories at sintering temperatures. The calculated boundary diffusion coefficients are dependent on the assumed value for the boundary width. The value for the boundary width (10 Å) is based on the results for the nickel activated sintering of tungsten (10) in which a monolayer is sufficient for rapid sintering. The D_b values should refer to diffusion in the liquid at the boundaries. A magnitude of 10^{-5} cm^2/sec is in the range for diffusion in low viscosity liquids (11). The temperature dependence observed is difficult to interpret because the solubility of ZrB_2 in the liquid changes with temperature. In addition to a change in the diffusion coefficient in the liquid, the change in solubility would also affect the rate variation with temperature. The D_o value is $\sim 10^{11}$ cm^2/sec for lattice diffusion and the $(D_b W)_o$ product is $\sim 10^7$ cm^3/sec. The D_o value for

TABLE 10

SELECTED DATA FROM SINTERING AND GRAIN GROWTH CURVES FOR $ZrB_{1.89}$

Temp. °C	Grain Size (μ)	Time (hours)	Relative Density
2000	10.2	1.74	0.71
	12	4.7	0.8
	15	14.7	0.92
2100	10.2	0.39	0.67
	12	0.94	0.79
	15	2.58	0.89
2200	10.2	0.125	0.72
	12	0.275	0.79
	15	0.714	0.89

TABLE 11

DIFFUSION COEFFICIENTS CALCULATED FROM SINTERING DATA ON $ZrB_{1.89}$

Temp. (°C)	D_L (cm^2/sec.)	$D_b W$ (cm^3/sec.)	D_b (cm^2/sec.)*
2000	1.6×10^{-10}	5.4×10^{-14}	5.4×10^{-7}
2100	9.7×10^{-10}	3.4×10^{-13}	3.4×10^{-6}
2200	3×10^{-9}	1.05×10^{-12}	1.05×10^{-5}

*Calculated for $W = 10^{-7}$ cm.

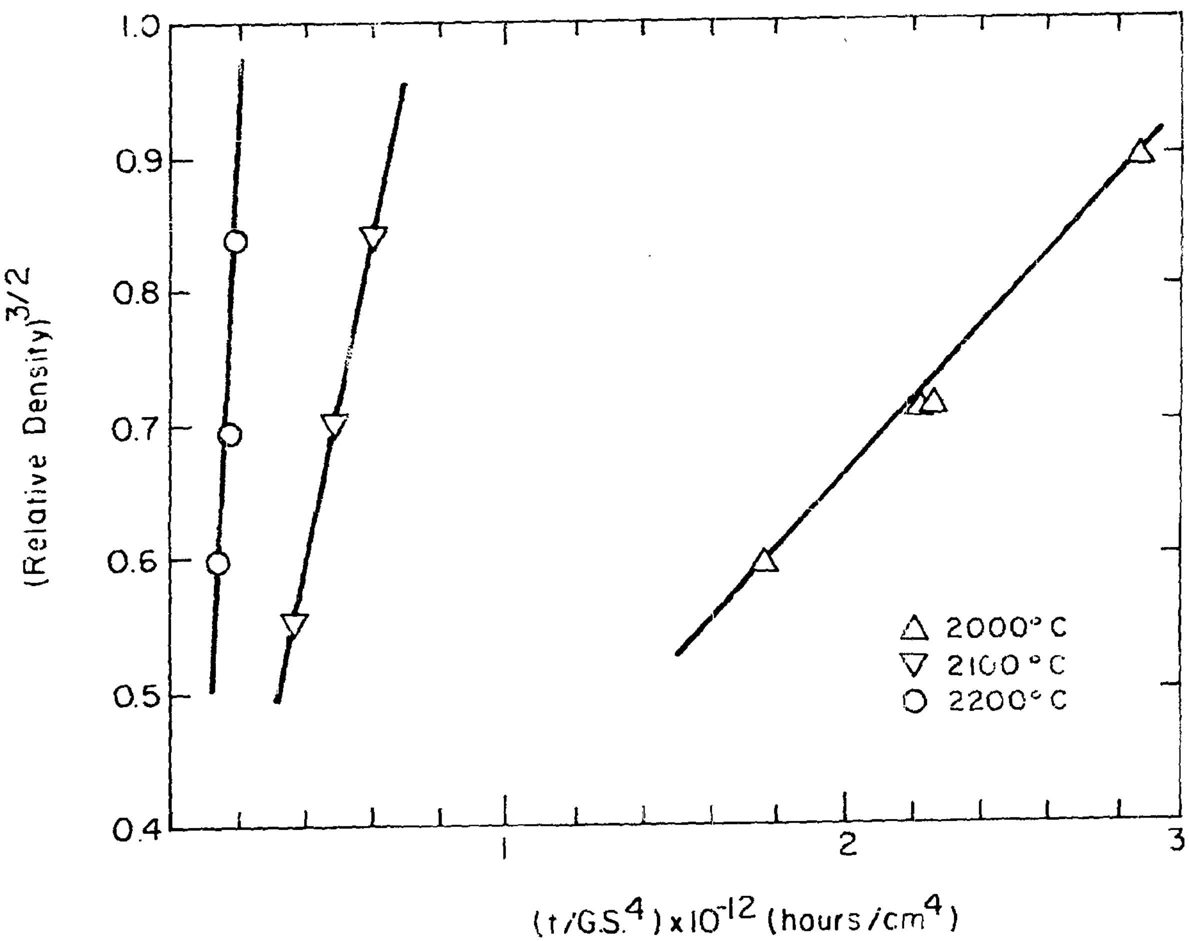

Figure 28. (Relative Density)$^{3/2}$ vs. $t/G.S.^4$ for $ZrB_{1.89}$.

lattice diffusion is unreasonably high; again this mechanism is rejected. The value for $(D_bW)_o$ is also high, but the unknown change in solubility with temperature would increase this quantity.

The sintering of ZrB_2 is tentatively concluded to occur by a process in which the rate-controlling step is diffusion of material through a film of liquid at the grain boundaries. The magnitudes of either the lattice diffusion coefficients or the boundary diffusion coefficients at the sintering temperatures are in acceptable ranges; the process could occur by transport involving both diffusion paths. However, the time dependence for densification favors the boundary diffusion model, and the temperature dependence leads to a D_o value for lattice diffusion which is too high for an intrinsic diffusion process.

VI. OXIDATION CHARACTERISTICS*

A. Introduction

On the basis of the experimental work performed during Part I of this study (1), HfB_2 and ZrB_2 were selected as the most promising of the diborides for more detailed investigation. Section B below reports on the oxidation behavior of these materials as a function of stoichiometry and temperature. In addition, limited results are presented concerning the effect of oxygen pressure, gas composition and flow rate on the oxidation behavior. In section C, the principals that have been applied in the past to the selection of alloying elements for improvement of oxidation resistance are discussed in relation to HfB_2. Potential alloying elements include metals of higher valency (Nb, Ta, Mo, W, Re), metals with exceptionally stable oxides (Th, Y, La), and metals which might result in ternary oxides (Ca or Si). In Section D, thermodynamic calculations are presented for all of the diborides as a function of stoichiometry to evaluate the possible formation of $B_2O_3(g)$ with a vapor pressure above one atmosphere at the diboride/oxide interface. The available results on HfB_2, ZrB_2, and the Carborundum ZrB_2-$MoSi_2$ composite are summarized in Section E and the oxidation resistance of these materials as a function of temperature and other variables are compared.

B. Experimental Results

1. General Discussion

During this period previous findings (1, 12 and 13) and calculations on the oxidation of hafnium and zirconium diboride were confirmed and extended. Experiments were designed and executed to test (1) the applicability of the parabolic rate equation for HfB_2 over long time periods, (2) the effects of variable stoichiometry on the oxidation of both ZrB_2 and HfB_2, (3) the effects of alloying additions and homogenization treatments on oxidation, (4) the effects of gas flow rate, and (5) the effects of water vapor on the oxidation of HfB_2 at relatively low temperatures. The specimens used in most of the present experiments were prepared by high pressure hot pressing as described in Section IV, previous specimens had been zone-melted (1, 12, 13). In addition specimens of pyrolytic ZrB_2 prepared by J. Pappas of Raytheon and "Boride Z" prepared by Carborundum were studied.

---

*J.B. Berkowitz-Mattuck, Arthur D. Little, Inc; E. V. Clougherty and L. Kaufman, ManLabs, Inc.

2. Experimental Materials and Techniques

A summary of experimental data is given in Tables 12 and 13. The oxidation technique has been discussed in detail elsewhere (14, 15). In brief, cylindrical sample pellets, approximately 300 mils in diameter and 100 mils thick, are degassed in helium at a temperature 100° higher than that planned for the oxidation run. Degassing is continued until permanent gas evolution, as monitored by the thermal conductivity apparatus, has ceased (usually 20-30 minutes). The degassed pellet is inductively heated in a helium-oxygen mixture flowing at about 3 cm/sec in the neighborhood of the samples. The rate of oxygen consumption is monitored continuously by means of a thermal conductivity bridge that compares the oxygen concentration in the gas stream before and after reaction. The parabolic rate constants in the last column of Table 12 are given in terms of total oxygen consumption i.e., the amount of oxygen in all of the product oxides, volatile and non-volatile. The base line drift in experiment (1) on HfB_2 was traced to temperature fluctuation in the air bath surrounding the thermal conductivity cell. Modification of the insulation and temperature control circuit has rendered the apparatus more stable and easier to operate.

Table 13 contains a description of the specimen fabrication in addition to some measurements of the specimen dimensions after oxidation treatment. These measurements were obtained by post mortem metallography which will be described below. Details of the fabrication are given in Section IV.

3. Results

3.1 Long Term Oxidation of Hafnium Diboride

In experiment (2), HfB_2 was oxidized for six hours to test the applicability of the parabolic rate law for long term exposures. The results are plotted in Figure 29 as the square of the total oxygen consumption vs. time. The parabolic rate law holds to a good approximation. Some deviation is seen, in that the observed rate constant drops slightly with time. Hence, after long exposures the actual rate of oxygen consumption may be smaller than the extrapolated rate. From Figure 29, a parabolic rate constant of 1.12×10^{-6} g^2/cm^4-min is calculated; this is to be compared with 1.18×10^{-6} g^2/cm^4-min obtained previously (12) over a two-hour period. At the same temperature pure hafnium displays breakaway behavior after a few minutes (16).

Table 13 contains information on the initial and final dimensions of this specimen which indicate virtually no change in dimension.

TABLE 12

SUMMARY OF EXPERIMENTAL RESULTS

Boride	Source	Pellet Identification	Initial weight prior to degassing	Weight loss on degassing	Surface area, cm^2	T, ^oK	P_{O_2}, torr	Flow, cc/min	Exposure time, min	Net weight change on oxidation, g/cm^2	k_{pp}, g^2/cm^4-min
$HfB_{2.035}$	454-2	XVIII-12	0.9050	0.0002	1.223	1758	40.7	95	232	0.0006	Baseline drift
$HfB_{2.035}$	454-2	XVIII-16	0.8546	0.0003	1.133	1758	40.7	95	360	0.0014	1.12×10^{-6}
$HfB_{2.035}$	454-2	XVIII-24	0.9621	0.0001	1.252	1208	19.3 + H_2O(4.6)	95	120	-0.0001	5.01×10^{-9}
$ZrB_{1.89}$	30-3	XVIII-28	0.9810	0.0003	1.987	1321	37.5	95	67		0.96×10^{-8}
						1553			87		0.787×10^{-6}
						1781			95		3.50×10^{-5}
						1852			83	0.0266	0.97×10^{-4}
$ZrB_{1.89}$	30-2	XVIII-33	Cracked on heating during degassing in helium								-
$ZrB_{1.89}$	30-1	XVIII-35	0.7014	0.0004	1.721	1321	0.4	95	51		too low
						1553			60		4.35×10^{-8}
						1781			73		-
						1852			70	0.0013	-
$HfB_{1.38}$	38-1	XVIII-39	Decrepitated on degassing in helium								-
$HfB_{1.88}$	38-5	XVIII-41	1.4644	0.0042	1.734	1321	0.4	95	60		too low
						1553			60		3.01×10^{-8}
						1781			18	0.0004	-
$HfB_{2.12}$	29-2	XVIII-45	1.2365	0.0060	1.565	1321	0.4	95	56		-
						1553			60		-
						1781			32	-0.0006	-

TABLE 12 (Cont'd.)

SUMMARY OF EXPERIMENTAL RESULTS

Boride	Source	Pellet Identification	Initial weight prior to degassing	Weight loss on degassing	Surface area, cm^2	T, °K	P_{O_2}, torr	Flow, cc/min	Exposure time, min	Net weight change on oxidation, g/cm^2	k_{pp}, g^2/cm^4-min
$HfB_{1.88}$	38-4	XVIII-49	1.4716	0.0039	1.577	1321	39.0	95	60		4.25×10^{-9}
						1553			71		9.14×10^{-8}
						1781			89		1.01×10^{-6}
						1852			91	0.0020	1.89×10^{-6}
$HfB_{2.12}$	29-6	XIX-1	1.2617	0.0019	1.582	1321	39.0	95	60		5.67×10^{-9}
						1553			71		1.57×10^{-7}
						1781			85		3.77×10^{-6}
						1852			14		1.44×10^{-5}
$HfB_{2.12}$+ Hf	RA-3-251	XIX-9	1.3513	0.0008	1.351	1321	39.0	95	70		5.46×10^{-9}
						1553			77		1.64×10^{-7}
						1781			80		2.91×10^{-6}
						1852			88		9.68×10^{-6}
$HfB_{2.12}$+ Ta	RA-5-3	XIX-14	1.3410	0.0017	1.570	1321	39.0	95	62		1.16×10^{-8}
						1553			61		3.25×10^{-7}
						1781			70		1.25×10^{-5}
						1852			76		4.53×10^{-5}
$ZrB_{1.89}$	28-2	XIX-18	0.7707	0.0004	1.6005	Pellet dropped off the fingers during oxidation					
$HfB_{2.035}$	454-2-5	XIX-21	0.9191	0.0001	1.1955	1206	19.9	95	60	0.0007	1.88×10^{-9}
$HfB_{2.035}$	38-2	XIX-24	1.2646	0.0045	1.5703	Temperature dropped during oxidation; pellet fell off mount					

TABLE 12 (Cont'd.)

SUMMARY OF EXPERIMENTAL RESULTS

Boride	Source	Pellet Identification	Initial weight prior to degassing	Weight loss on degassing	Surface area, cm^2	T, °K	P_{O_2}, torr	Flow, cc/min	Exposure time, min	Net weight change on oxidation, g/cm^2	k_{pp}, g^2/cm^4-min
$HfB_{1.88}$	51-2	XIX-27	1.3111	0.0227	1.5890	2125	39.7	119	119	~0.0080	7.16×10^{-4}
$HfB_{1.88}$	51-3	XIX-31	1.4014	0.0051	1.5961	2179	39.7	119	55		1.13×10^{-3}
$ZrB_{1.89}$	28-4	XIX-34	0.7432	0.0002	1.5400	Dropped from 2100 to 2030	39.0		65	0.0848	-
$HfB_{2.0}$	A-4-1	XIX-38	1.1594	0.0078	1.4058	1795	39.7	119	60		3.0×10^{-6}
						1903			78		4.04×10^{-5}
						2015			75		1.62×10^{-4}
						2109			58	-	7.46×10^{-4}
$ZrB_{1.89}Si_{0.05}$	A-8-3	XIX-42	0.6477	0.0006	1.3948	1551	39.0	95	60		3.71×10^{-7}
						1666			59		1.57×10^{-5}
						1778			58		6.11×10^{-5}
						1867			54	0.0265	2.64×10^{-4}
$HfB_{2.0}$	A-4-2	XIX-47	1.1640	0.0068	1.4058	1903	39.7	119	111		5.46×10^{-5}
						2017			93		1.94×10^{-4}
						2191			27	-	8.6×10^{-4}
$ZrB_{1.89}$	28-5	XX-1	0.7185	0.0001	1.5213	Dropped as above	39.0		31	0.0312	-
$ZrB_{1.97}$	P-5-2	XX-4	0.7569	0.0071	1.5755	Dropped as above	39.7		42	-	-

TABLE 12 (Cont'd.)

SUMMARY OF EXPERIMENTAL RESULTS

Boride	Source	Pellet Identification	Initial weight prior to degassing	Weight loss on degassing	Surface area, cm^2	T, °K	P_{O_2}, torr	Flow, cc/min	Exposure time, min	Net weight change on oxidation, g/cm^2	k_{pp}, g^2/cm^4-min
$ZrB_{1.97}$	P-5-4	XX-9	0.7678	0.0160	1.5616	1572	39.7	119	56		2.05×10^{-6}
						1688			59		1.991×10^{-5}
						1795			58		6.49×10^{-5}
						1895			52		1.736×10^{-4}
						2018			60	0.0565	3.87×10^{-4}
$HfB_{1.88}$	51-4	XX-13	1.2828	0.0062	1.5406	2193	39.7	119	49	0.0742	1.11×10^{-3}
$ZrB_{1.97}$	P-5-5	XX-17	0.7401	0.0045	1.5800	2118	37.5	119	47	0.0677	1.3×10^{-3}*
$HfB_{2.12}$	49-4	XX-21	1.2236	0.0079	1.5284	Pellet fell off mount			5	0.0173	-
$HfB_{1.88}$	46-6	XX-32	1.1750	0.1126	1.5774	2194	37.5	95	71		1.02×10^{-3}
$HfB_{1.70}$	A-16-2	XX-36	1.2594	0.0076	1.5419	1332	37.5	95	58		1.308×10^{-8}
						1569			59		1.87×10^{-7}
						1795			55		2.35×10^{-6}
						1900			58	0.0067	5.95×10^{-6}
$HfB_{1.70}$	A-16-1	XX-40	1.1833	0.0065	1.4942	Pellet fell off mount			5		-
$ZrB_{1.75}$	A-17-1	XX-42	0.5391	0.0015	1.3542	1333	37.5	95	61		1.38×10^{-8}
						1570			57		6.38×10^{-7}
						1795			57		7.39×10^{-5}
						1898			60	0.0339	4.53×10^{-4}

* Specimen reacted with all of the oxygen supplied. Hence, these experiments were diffusion controlled and the k_{pp} values shown are lower limits.

TABLE 12 (Cont'd.)

SUMMARY OF EXPERIMENTAL RESULTS

Boride	Source	Pellet Identification	Initial weight prior to degassing	Weight loss on degassing	Surface area, cm^2	T, °K	P_{O_2}, torr	Flow, cc/min	Exposure time, min	Net weight change on oxidation, g/cm^2	k_{pp}, g^2/cm^4-min
$ZrB_{1.75}$	A-17-2	XX-47	0.6573	0.0023	1.5271	2176	37.5	95	44	~0.0596	1.47×10^{-3}*
$HfB_{1.7}Si_{0.25}$	A-19-5	XXI-1	1.1299	0.0034	1.4961	1321	41.3	95	58		1.70×10^{-9}
						1553			56		3.28×10^{-9}
						1779			59		6.2×10^{-6}
						1886			57	0.0158	2.23×10^{-5}
$HfB_{1.7}Si_{0.25}$	A-19-1	XXI-5	1.1486	-	1.5561	A low melting eutectic with the Ir fingers formed on degassing					
$ZrB_{1.7}Si_{0.25}$	A-21-2	XXI-7	0.6752	0.0031	1.5161	1332	37.5	119	67		1.97×10^{-8}
						1572			56		1.32×10^{-7}
						1794			12		-
$HfB_{1.70}$	A-16-3	XXI-11	1.2751	0.0056	1.5503	2178	37.5	119	45	-	8×10^{-4}
$HfB_{1.7}Si_{0.25}$	A-19-2	XXI-14	1.1386	0.0022	1.5290	-	37.5	Pellet slipped during oxidation			
$ZrB_{2.10}$	A-22-5	XXI-19	0.6925	0.0036	1.5781	1330	37.5	119	59		3.04×10^{-8}
						1570			60		6.77×10^{-7}
						1794			56		3.24×10^{-4}
						1895			61	0.0134	1.041×10^{-3}
$ZrB_{1.7}Si_{0.25}$	A-21-3	XXI-17	0.7151	0.0024	1.5413	1796	37.5	119	63		4.13×10^{-5}
						1899			57	0.0367	1.47×10^{-4}
$HfB_{2.12}$	29-2	XVIII-45	1.0530	0.0011	1.4355	1903	41.3	119	61		2.05×10^{-4}
		rerun				2017			59		4.04×10^{-4}

(continued on next page)

* Specimen reacted with all of the oxygen supplied. Hence, these experiments were diffusion controlled and the k_{pp} values shown are lower limits.

TABLE 12 (Cont'd.)

SUMMARY OF EXPERIMENTAL RESULTS

Boride	Source	Pellet Identification	Initial weight prior to degassing	Weight loss on degassing	Surface area, cm^2	T, °K	P_{O_2}, torr	Flow, cc/min	Exposure time, min	Net weight change on oxidation, g/cm^2	k_{pp}, g^2/cm^4-min
						2118			51	0.0417	7.39×10^{-4}
$HfB_{1.88}$	38-5	XVIII-41	1.4405	0.0002	1.7103	1330	41.3	119	56		3.16×10^{-9}
		rerun				1569			57		9.06×10^{-8}
						1793			58		1.18×10^{-6}
						1900			60	0.0038	3.09×10^{-6}
$HfB_{1.88}$	47-2	XXI-34	1.2754	0.0027	1.5456	Variable	41.3		31		-
$HfB_{1.88}$	47-3	XXI-37	1.3248	0.0064	1.5748	2164	41.3	240	43	0.0438	1.41×10^{-3}
$ZrB_{2.10}$	A-22-3	XXI-40	0.6965		1.5819	Pellet split on degassing					
$ZrB_{2.10}$	A-22-2	XXI-42	0.6857	0.0251	1.5633	Pellet became highly porous on degassing	41.3				
$HfB_{1.88}$	51-5	XXI-46	1.2829	0.0042	1.5323	2019	41.3	119	63		2.57×10^{-5}
						2121			60	-	7.52×10^{-4}
$ZrB_{1.7}Si_{0.25}$	A-21-1	XXI-50	0.6079	0.0040	1.4671	Pellet fell from mount	41.3		13		-
$HfB_{1.70}$	A-16-4	XXII-1	1.2213	0.0025	1.4877	2019	41.3	119	60		3.09×10^{-5}
						2018		240	73		4.30×10^{-5}
						2122		240	60		4.56×10^{-4}
						2120		119	51		5.32×10^{-4}
$ZrB_{2.10}$	A-22-4	XXII-6	0.6808	0.0203	1.5413	2455	41.3	240	21	Diffusion controlled	
$ZrB_{2.10}$	A-22-1	XXII-9	0.5628	0.0217	1.4503	2233	41.3	240	34	Diffusion controlled*	

* The lower limit for k_{pp} at this temperature is approximately 10^{-2} gm^2/cm^4-min.

TABLE 12 (Cont'd.)

SUMMARY OF EXPERIMENTAL RESULTS

Boride	Source	Pellet Identification	Initial weight prior to degassing	Weight loss on degassing	Surface area, cm^2	T, ^oK	P_{O_2}, torr	Flow, cc/min	Exposure time, min	Net weight change on oxidation, g/cm^2	k_{pp}, g^2/cm^4-min
$ZrB_{1.85}$	Raytheon	XXII-12	0.5958	0.0001	1.4200	2122	41.3	240	79	-	1.47×10^{-4}
ZrSi	ADL	XIV-35	0.5061	-	1.4093	1620	38.75	95	139	0.0681	2.28×10^{-5}
$ZrB_{1.85}$	Raytheon	XXII-16	0.5798	0.0004	1.3710	1332	41.3	119	57		3.22×10^{-9}
						1570			56		5.27×10^{-7}
						1795			61		4.45×10^{-5}
						1897			55	0.0215	1.31×10^{-4}
Boride Z	Carborundum	XXII-21	0.5059	0.0075	1.4300	1330	41.3	119	56		3.37×10^{-8}
						1570			60		5.27×10^{-7}
						1790			60		3.65×10^{-5}
						1900			55		4.41×10^{-5}
Boride Z	Carborundum	XXII-26	0.5509	0.0070	1.4350	2122	35.0	240	66		7.4×10^{-4}
Boride Z	Carborundum	XXII-30	0.5579	0.0076	1.4570	1331	7.5	119	63		6.34×10^{-9}
						1452			18		1.40×10^{-8}
						1570			60		3.23×10^{-7}
						1794			66		4.45×10^{-5}
						1898			75		1.27×10^{-4}

TABLE 13

IDENTIFICATION OF SPECIMENS AND SUMMARY OF DIMENSIONAL CHANGES DURING OXIDATION

Boride	Pellet	Fabrication	Initial height h_o (mils)	Final height h_f (mils)	Area Ratio (A_o/A_f)	Conversion* Meas. (mils)	Conversion* Calc. (mils)
$HfB_{2.035}$	XVIII-12	Zone Refined	-	-	-	-	-
$HfB_{2.035}$	XVIII-16	Zone Refined	112	112	1.00	0.0	1.8(1)
$HfB_{2.035}$	XVIII-24	Zone Refined	-	-	-	-	-
$ZrB_{1.89}$	XVIII-28	Hot Pressed from raw powder B/Me = 1.89	111	52	1.76	29.5	14.5(4)
$ZrB_{1.89}$	XVIII-33	Same as XVIII-28	-	-	-	-	-
$ZrB_{1.89}$	XVIII-35	Same as XVIII-28	-	-	-	-	-
$HfB_{1.88}$	XVIII-39	Same as XVIII-28	-	-	-	-	-
$HfB_{1.88}$	XVIII-41	Same as XVIII-28	-	-	-	-	-
$HfB_{2.12}$	XVIII-45	Same as XVIII-28	-	-	-	-	-
$HfB_{1.88}$	XVIII-49	Same as XVIII-28	110	99	1.11	5.5	2.4(4)
$HfB_{2.12}$	XIX-1	Same as XVIII-28	110	108	1.01	1.0	3.2(4)
$HfB_{2.12}$ + Hf	XIX-9	Hot Pressed from raw powder, Hf added for B/Me = 2.00 No Homogenization	-	-	-	-	-
$HfB_{2.12}$ + Ta	XIX-14	Same as XIX-9	-	-	-	-	-
$ZrB_{1.89}$	XIX-18	Hot Pressed from raw powder	-	-	-	-	-
$HfB_{2.035}$	XIX-21	Zone Refined	-	-	-	-	-
$HfB_{2.035}$	XIX-24	Zone Refined	-	-	-	-	-
$HfB_{1.88}$	XIX-27	Hot Pressed	110	39	2.21	35.5	25.9(1)
$HfB_{1.88}$	XIX-31	from raw powder	112	73	1.47	19.5	22.0(1)
$ZrB_{1.89}$	XIX-34	Same as XIX-18	-	-	-	-	-
$HfB_{2.0}$	XIX-38	Hot Pressed from 2.12 powder with Hf added for B/Me = 2.00 Homogenized	111	67	1.61	22.0	34.2(4)
$ZrB_{1.89}Si_{0.05}$	XIX-42	Hot Pressed from raw powder with B/Me = 1.89 with Si added. Homogenized	-	-	-	-	-
$HfB_{2.0}$	XIX-47	Same as XIX-38	111	61	1.72	25.0	32.2(3)
$ZrB_{1.89}$	XX-1	Same as XIX-18	-	-	-	-	-
$ZrB_{1.97}$	XX-4	Hot Pressed from purified powder	-	-	-	-	-
$ZrB_{1.97}$	XX-9	Same as XX-4	110	68	1.51	21.0	31.1(5)
$HfB_{1.88}$	XX-13	Same as XVIII-49	102	64	1.48	19.0	20.6(1)
$ZrB_{1.97}$	XX-17	Same as XX-4	110	59	1.71	25.5	21.8(1)

* The number in parentheses following d_c indicates the number of different conditions the specimen was exposed to. Details are given in Table (12).

TABLE 13 (CONT'D.)

IDENTIFICATION OF SPECIMENS AND SUMMARY OF DIMENSIONAL CHANGES DURING OXIDATION

Boride	Pellet	Fabrication	Initial height h_o (mils)	Final height h_f (mils)	Area Ratio (A_o/A_f)	Conversion* Meas. (mils)	Conversion* Calc. (mils)
$HfB_{2.12}$	XX-21	Hot Pressed	-	-	-	-	-
$HfB_{1.88}$	XX-32	from raw powder	-	-	-	-	-
$HfB_{1.70}$	XX-36	Hot Pressed from 2.12 powder, Hf added Homogenized	105	94	1.10	5.5	3.1(3)
$HfB_{1.70}$	XX-40	Same as XX-36	-	-	-	-	-
$ZrB_{1.75}$	XX-42	Hot Pressed from 1.89 powder, Zr added Homogenized	87	47	1.55	20.0	20.4(4)
$ZrB_{1.75}$	XX-47	Same as XX-42	101	37	2.04	32.0	22.3(1)
$HfB_{1.7}Si_{0.25}$	XXI-1	Si added to XX-36	-	-	-	-	-
$HfB_{1.7}Si_{0.25}$	XXI-5	Si added to XX-36	-	-	-	-	-
$ZrB_{1.7}Si_{0.25}$	XXI-7	Si added to XX-42	102	102	1.00	0.0	0.0(3)
$HfB_{1.70}$	XXI-11	Same as XX-36	106	68	1.47	19.0	16.4(1)
$HfB_{1.7}Si_{0.25}$	XXI-14	Same as XXI-1	-	-	-	-	-
$ZrB_{2.10}$	XXI-19	Hot Pressed from 1.89 powder, Boron added; Homogenized	110	55	1.80	27.5	36.5(4)
$ZrB_{1.7}Si_{0.25}$	XXI-17	Same as XIX-42	109	98	1.10	5.5	12.6(2)
$HfB_{2.12}$	XVIII-45	Same as XVIII-28	98	49	1.71	24.5	40.1(4)
$HfB_{1.88}$	XVIII-41	Same as XVIII-28	-	-	-	-	-
$HfB_{1.88}$	XXI-34	Same as XVIII-41	104	63	1.38	20.5	-
$HfB_{1.88}$	XXI-37	Same as XVIII-41	105	61	1.57	22.0	21.6(1)
$ZrB_{2.10}$	XXI-40	Same as XXI-19	-	-	-	-	-
$ZrB_{2.10}$	XXI-42	Same as XXI-19	-	-	-	-	-
$HfB_{1.88}$	XXI-46	Same as XXI-19	-	-	-	-	-
$ZrB_{1.7}Si_{0.25}$	XXI-50	Same as XXI-17	-	-	-	-	-
$HfB_{1.70}$	XXII-1	Same as XX-36	98	43	1.83	27.5	35.5(4)
$ZrB_{2.10}$	XXII-6	Same as XXI-19	-	-	-	-	-
$ZrB_{2.10}$	XXII-9	Same as XXI-19	-	-	-	-	-
$ZrB_{1.85}$	XXII-12	Pyrolytic Material prepared by Raytheon	87	57	1.37	15.0	9.5(1)
ZrSi	XIV-35	Zone Melted by ADL	-	-	-	-	-
$ZrB_{1.85}$	XXII-16	Same as XXII-12	86	70	1.11	8.0	28.7(4)

* The number in parentheses following d_c indicates the number of different conditions the specimen was exposed to. Details are given in Table (12).

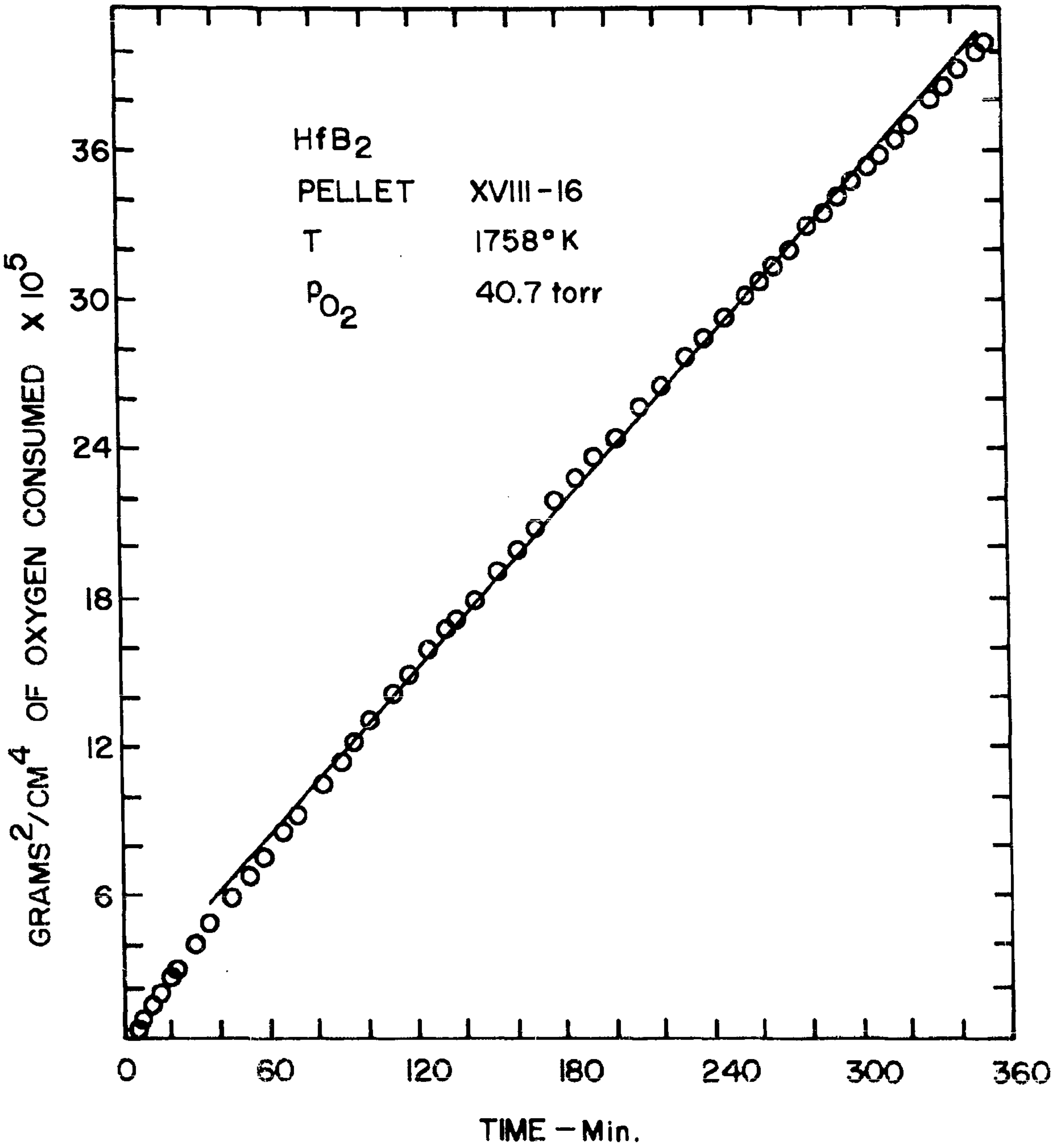

Figure 29 - Long Term Oxidation of HfB_2, 1758°K, p_{O_2} = 40.7 Torr.

3.2 The Effect of Water Vapor on the Oxidation of Diborides

As indicated in the last report, the effect of water vapor on the oxidation of borides should be to accelerate the rate of vaporization of B_2O_3(s or l) since $(HBO_2)_3$(g) is much more volatile than B_2O_3(g). If the temperature is sufficiently high so that B_2O_3 vaporizes as rapidly as it forms, then water vapor should not influence the over-all oxidation rate. If, on the other hand, the temperature is sufficiently low so that the rate of vaporization of B_2O_3 is negligible under normal oxidizing conditions, water vapor should enhance the vaporization of B_2O_3, and hence cause an increase in the observed net rate of oxidation. Comparing the results of pellet XVIII-24 and XIV-21 in Table 12 shows that at 1206°K with 19.9 torr oxygen gave $k_{pp} = 1.9 \times 10^{-9} g^2/cm^4 min$ whereas the same material at the same temperature and pressure of oxygen but with added water vapor (4.6 torr) gave $k_{pp} = 5.0 \times 10^{-9} g^2/cm^4 min$. These results provide direct experimental verification of the enhanced oxidation rate of HfB_2 in the presence of water vapor. Two additional experiments, not tabulated herein, showed the absence of a water vapor effect in the oxidation of HfB_2 at higher temperature. The rate of oxidation at 1760°K at 19 torr oxygen and 5 torr water in helium was identical to the rate of oxidation at 19 torr oxygen in helium.

3.3 The Effect of Stoichiometry on the Oxidation of HfB_2

The effect of boron to metal ratio on the oxidation characteristics of HfB_2 is shown graphically in Figures 30 and 31. The full curves for k_{pp} vs. T are based on the results obtained earlier (1) with zone refined specimens. The break occurs at about the monoclinic to tetragonal transition temperature for HfO_2. In the present study, specimens were prepared by hot pressing from two batches of "raw" hafnium diboride powders corresponding to B/Me = 1.88, batch 2A, and B/Me = 2.12, batch 2, (see Section IV). In addition, specimens were prepared by adding hafnium to batch 2 in order to adjust B/Me = 2.00. Pellets numbered XIX-38 and XIX-47 were homogenized to insure solution of the Hf addition by holding at 1500°C for twenty-four hours. Subsequent metallographic examination showed no evidence for pure hafnium. Pellets XIX-9 and XIX-14 which were not homogenized showed undissolved patches of Hf and Ta. Specimens corresponding to B/Me = 1.70 were also prepared by hafnium additions to B/Me = 2.12 powder (see Section IV for details).

The effect of stoichiometry on the oxidation of HfB_2 is shown quite clearly in Figures 31 and 32. On the average, the rate constants for metal rich hafnium diboride specimens lie below the lines drawn, while the rate constants for boron rich specimens lie above the lines. For example, at 1550°K, 1800°K, 1900°K, and 2000°K the value of k_{pp} for B/Me = 2.12 is larger than that for the B/Me = 1.88 specimens. Moreover, additions of hafnium to the 2.12 material are seen to lower the value of k_{pp}.

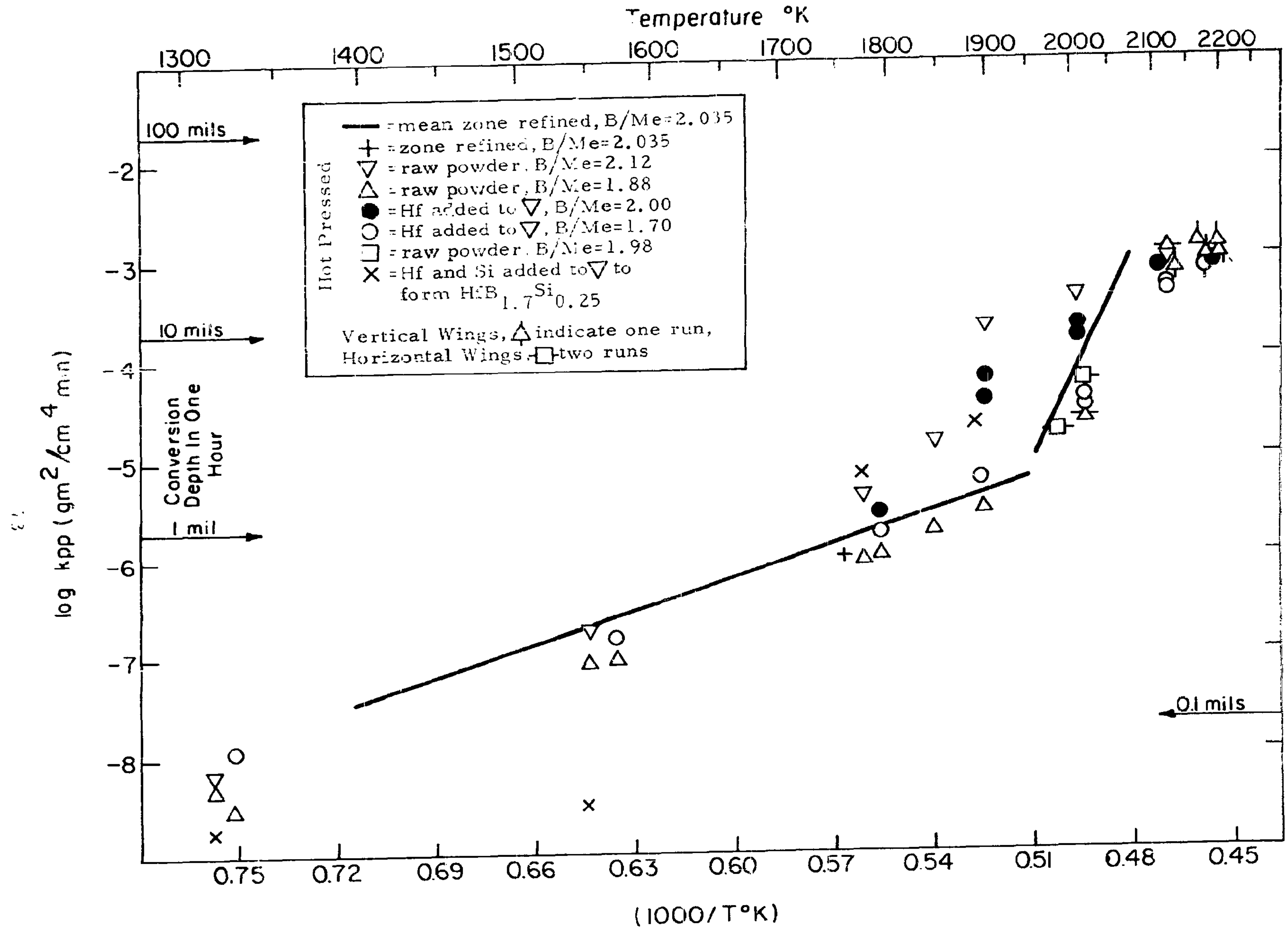

Figure 30 - Oxidation of HfB_2

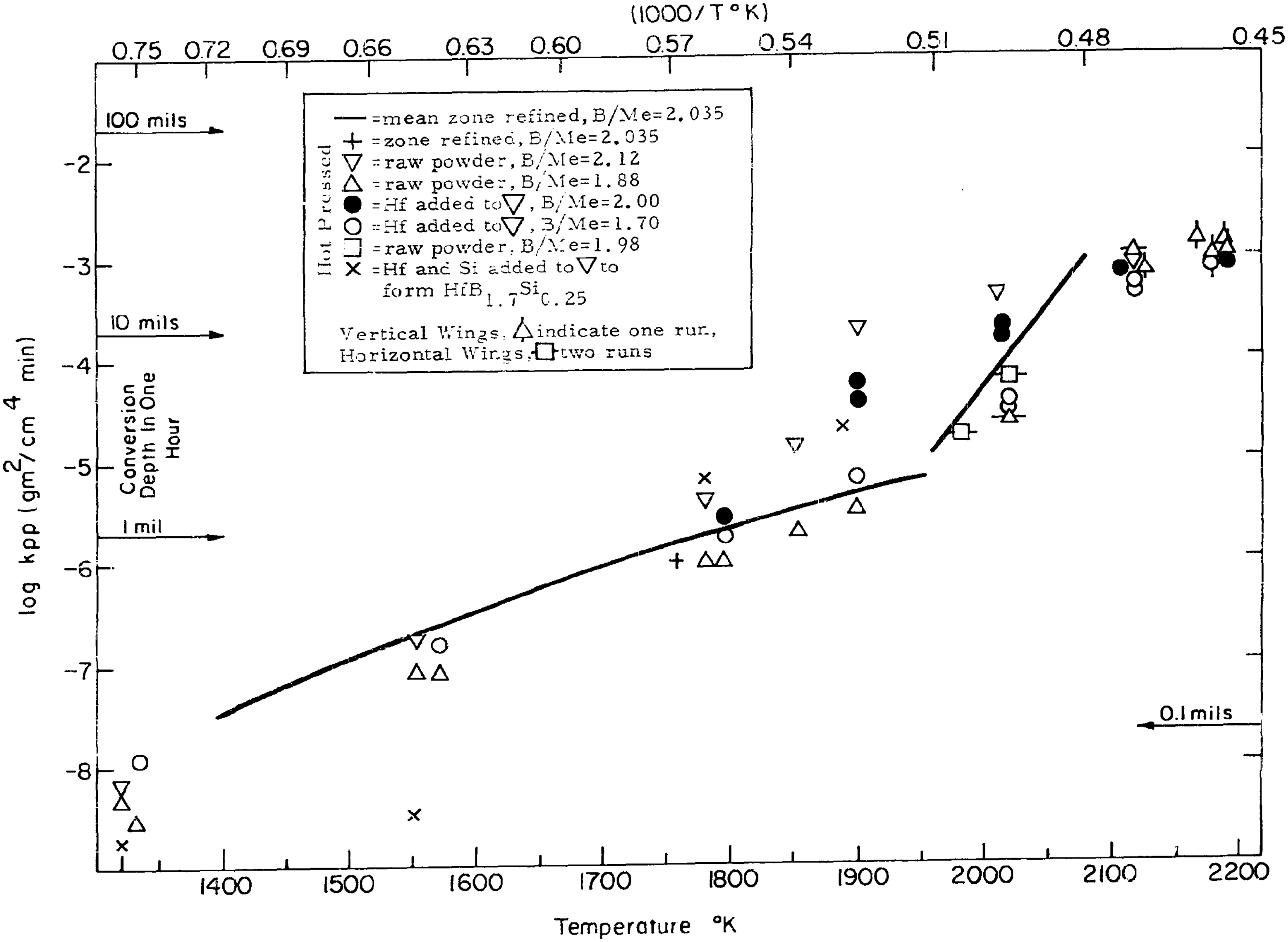

Figure 31 - Oxidation of HfB_2

The relation between oxygen consumption and conversion of the diboride to oxides has been discussed previously (1). Briefly, if the diborides of interest oxidize stoichiometrically according to a relationship of the form:

$$MeB_2 + \frac{5}{2} O_2 \rightarrow MeO_2 + B_2O_3 \tag{1}$$

where Me = Zr, Hf, the parabolic rate constant for oxygen consumption, k_{pp} g^2/cm^4-min is related to the parabolic rate constant for alloy consumption, k_{px} cm^2/min by the equation:

$$k_{pp} = (k_{px}) (\rho^2_{MeB_2}) \frac{25 M_O^2}{M^2_{MeB_2}} \tag{2}$$

where ρ_{MeB_2} is the density of the metal diboride and M_{MeB_2} is the molecular weight of MeB_2 and M_O is the molecular weight of oxygen. Thus, for both HfB_2 and ZrB_2

$$k_{pp} \; (gms^2/cm^4 min) = 20 \; k_{px} \; (cm^2/min) \tag{3}$$

based on the volumetric data given in Section IX. Thus Eqs. (1-3) imply that

$$d^2 = k_{px} t \tag{4}$$

where d is the average depth of boride converted to oxide in a time t. If d is in cm and t in minutes, then

$$d^2 \; (cm^2) = \frac{k_{pp} \; (gm^2/cm^4 min)}{20} \; t \; (min) \tag{5}$$

If, on the other hand, d is in mils and t in hours, then

$$d^2 \; (mils^2) = 4.8 \times 10^5 \; k_{pp} \; (gm^2/cm^4 min) \; t \; (hr) \tag{6}$$

Eq. (6) has been used to compute the k_{pp} levels corresponding to various conversion depths based on one hour parabolic oxidation shown on the ordinates of Figures 30 and 31. It is apparent that at the highest temperatures sufficient conversion to alter the area of the specimen will occur in one hour which corresponds to the time used in many experiments. In order to verify this fact and assess its influence on the k_{pp} values shown in Table 12 (which were computed on the basis of initial areas) the specimen disks were measured by macrophotographic techniques after oxidation exposure.

Figure 32 shows a cross section of pellet XXII-1. The initial thickness (see Table 13) was 98 mils, the thickness after oxidation 43 mils, corresponding to a total depth of diboride conversion of 27.5 mils on each surface. This conversion may be compared with a computed depth of conversion of 35.5 mils which is obtained by using Eq. (6) and the values of k_{pp} and time given in Table 12. The computation has been performed for approximately twenty different experiments shown in Table 13 with good agreement between measured conversion depths and depths computed on the basis of k_{pp} as tabulated. In some cases, it was possible to measure the change in height <u>and</u> the change in diameter. This is illustrated in Figures 33 and 34 showing pellet XXII-16 which was first ground to display the final height of 70 mils corresponding to an eight mil conversion, and then ground to display the final diameter of 275 mils corresponding to an 8.5 mil radial conversion depth. As anticipated, both radial and height conversions are equal. The measured initial and final height given in Table 13 yield values of d_m which in turn can be used to compute the ratio of final area A_f to initial area A_o. As expected, experiments performed at temperatures below 2000°K, where k_{pp} is less than 10^{-5} produce little or no change in area. At higher temperatures and higher values of k_{pp}, significant changes in area occur. For example, for a pellet having a diameter D_o and a height equal to h_o, the final area A_f is given by Eq. (7) as a function of time as

$$A_f = A_o - 2\pi\ (2D_o + h_o)\ (k_{px}t)^{1/2} + 6\pi\ k_{px}t \tag{7}$$

For D_o = 300 mils and h_o = 100 mils, this yields

$$A_f/A_o = 1 - 13\ (k_{pp}t)^{1/2} + 40\ k_{pp}t \tag{8}$$

Eq. (8) yields area ratios of 1.04, 1.14 and 1.56 at $k_{pp} = 10^{-5}$, 10^{-4} and 10^{-3} respectively after one hour. On this basis, the "area correction" to k_{pp} is negligible for values of k_{pp} less than or equal to 10^{-4} gm^2/cm^{4}min. For values of k_{pp} equal to 10^{-3} the correction might correspond to a factor of two at the most. Examination of the individual oxygen consumption vs. time curves recognizing the changes in area, does not indicate departures from parabolic behavior at levels of 10^{-3}.

Figures 30 and 31 show a transition in k_{pp} at about 2000°K which was previously associated (1) with the phase transformation temperature observed in HfO_2. While the slope of the high temperature log k_{pp} vs. 1/T curve shown in Figure 30 is probably too large there seems to be a definite change in behavior on crossing 2000°K. This change is also evident in the post-mortem metallographic appearance of the oxide. Figure 32 shows a specimen oxidized above the transition which exhibits a distinctly columnar oxide. Figure 35 shows an oxide layer formed on pellet XX-36 which is

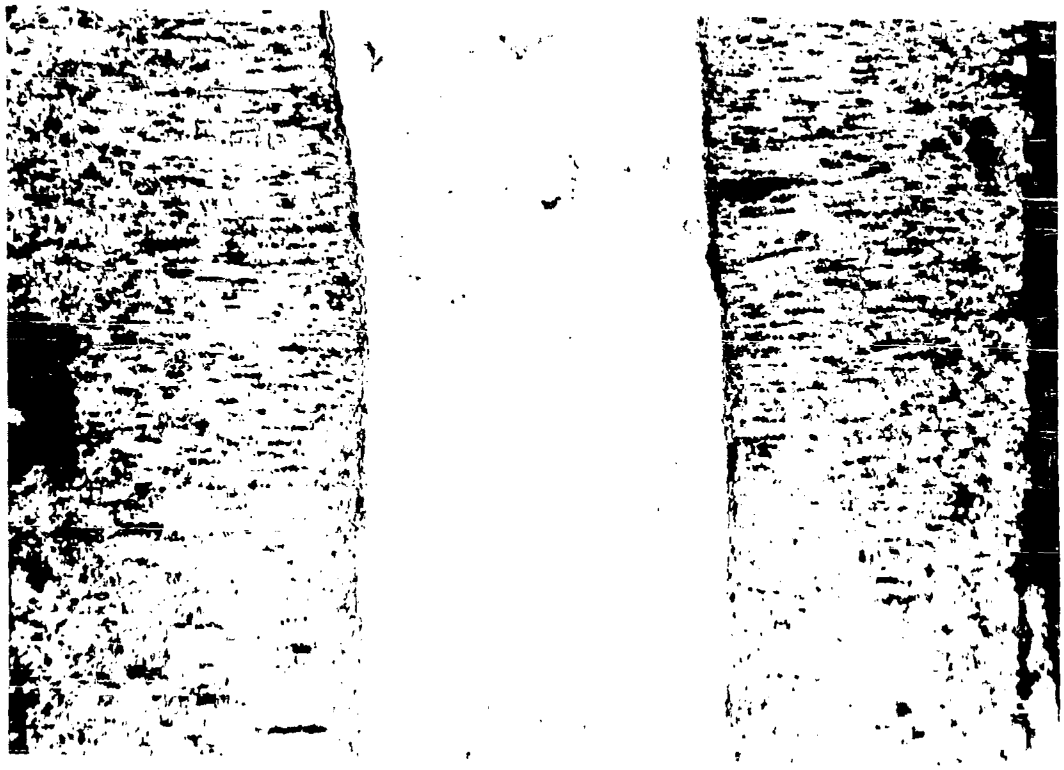

As polished X50

Figure 32 - Pellet XXII - 1, $HfB_{1.70}$, After Oxidation for 133 Minutes at $2020^{o}K$ and 111 Minutes at $2120^{o}K$. Initial Height = 98 Mils, Final Height = 43 Mils, Depth of Conversion 27.5 Mils.

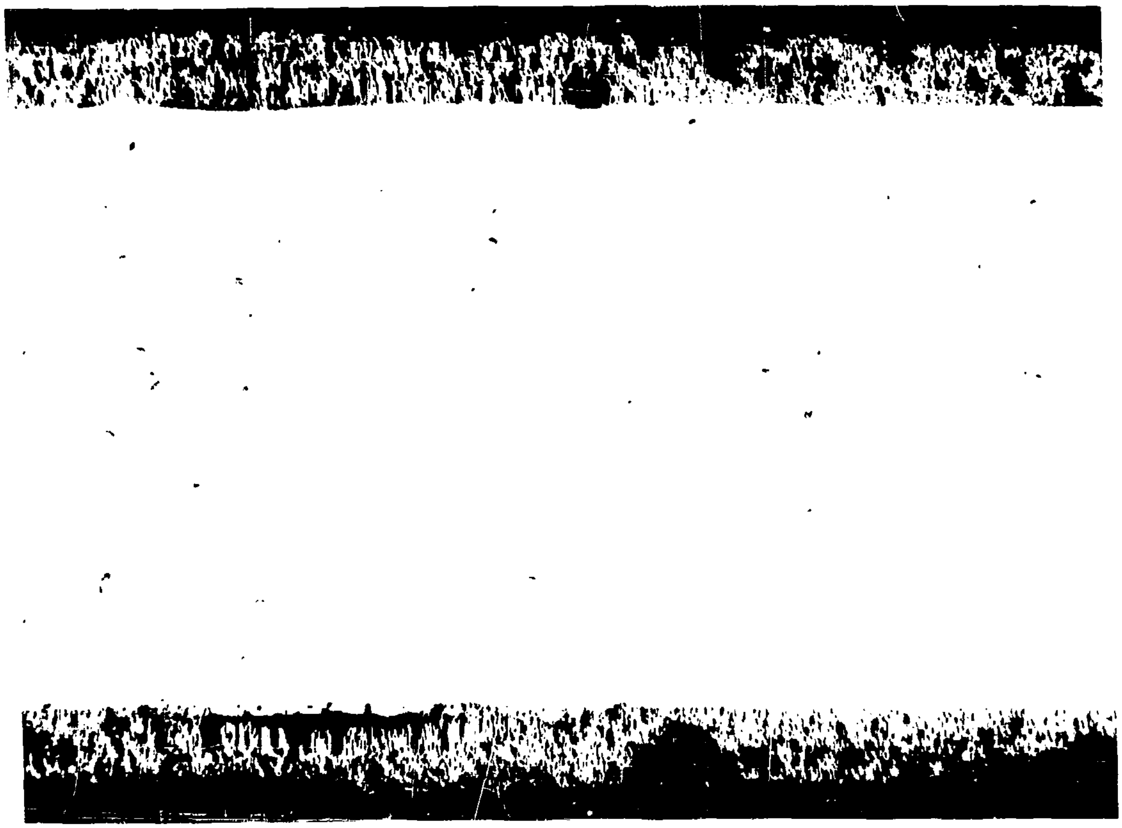

As polished X50

Figure 33 - Pellet XXII - 16, Pyrolytic $ZrB_{1.85}$, After Oxidation at $1897^{o}K$. Initial Height 86 Mils, Final Height 70 Mils, Depth of Conversion = 8 Mils.

As polished (polarized light) X20

Figure 34 - Pellet XXII - 16, Pyrolytic $ZrB_{1.85}$, After Oxidation at 1897°K. Initial Diameter 292 Mils, Final Diameter 275 Mils, Depth of Conversion = 8.5 Mils.

Etched X200

Etchant: 10cc glycerine, 10cc HNO_3
2cc HCl, 0.1cc HF

Figure 35 - Pellet XX - 36, $HfB_{1.70}$ After Oxidation at 1900°K.

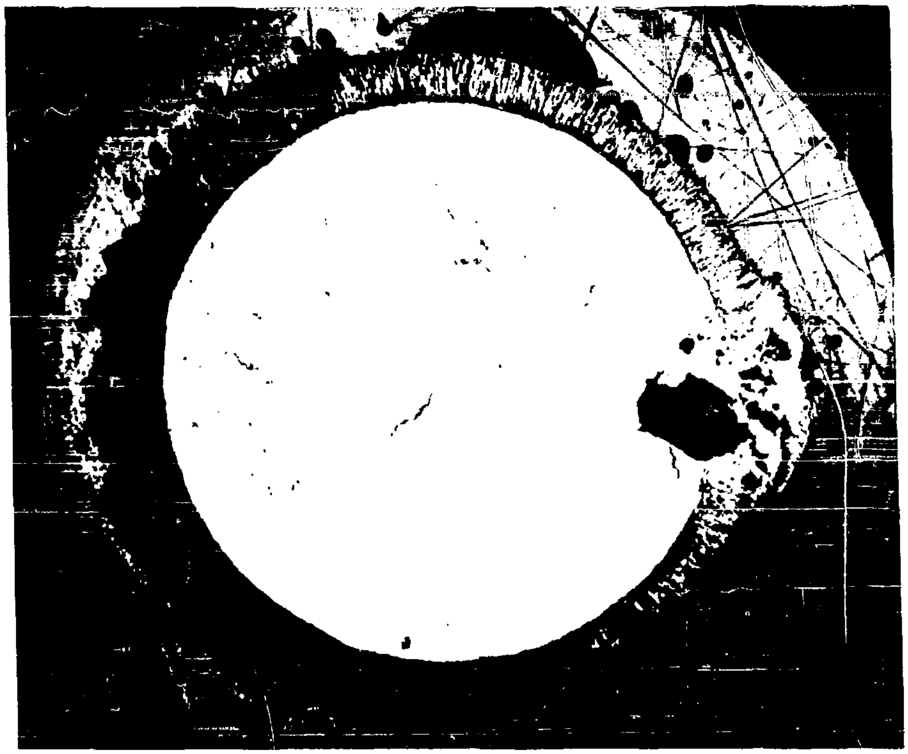

As polished X12.5

Figure 36 - Pellet XXI - 11, $HfB_{1.70}$ After Oxidation at 2178°K.

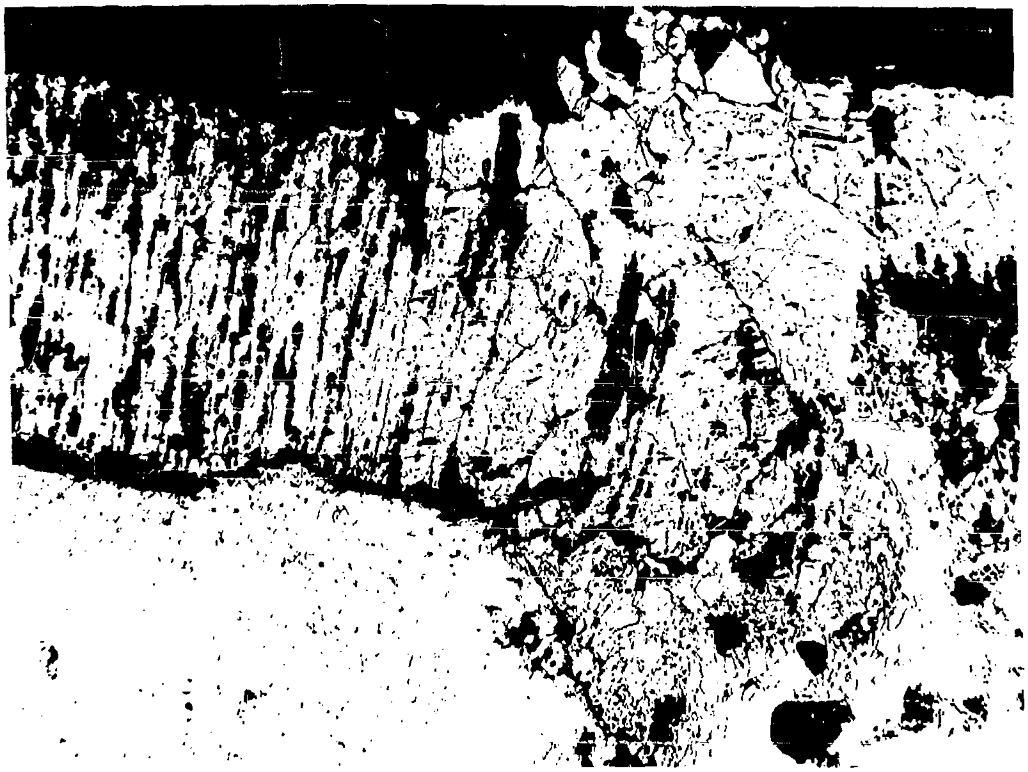

Etched X100

Etchant: 10cc glycerine, 10 cc HNO_3
2cc HCl, 0.1 cc HF

Figure 37 - Pellet XXI - 11, $HfB_{1.70}$ After Oxidation at 2178°K.

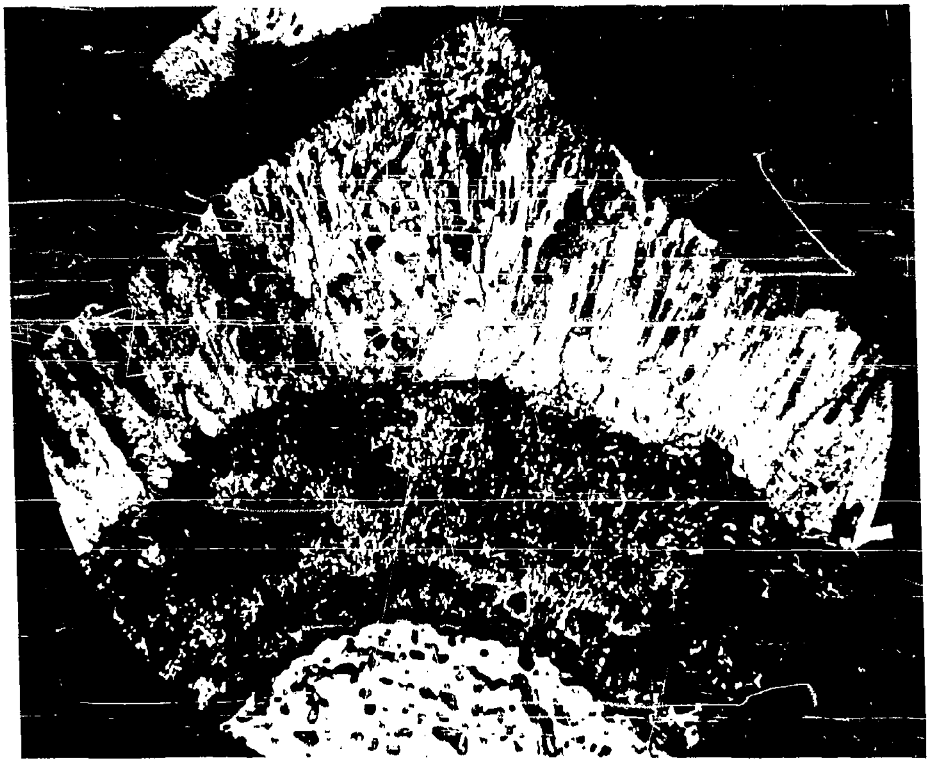

As polished X75

Figure 38 - Pellet XIX - 38, $HfB_{2.0}$ After Oxidation at 2109°K.

$HfB_{1.70}$ as was XXII-1 shown in Figure 32. However, this specimen was not oxidized above 1900°K. It shows a non-columnar oxide. Another illustration is shown in Figures 36 and 37 which are photomicrographs of pellet XXI-11 which was oxidized at 2178°K for 45 minutes. The oxide surrounding the sample is distinctly columnar except for one region in which a reaction occurred between the iridium finger holding the specimen and the diboride. Examination of Figure 37 shows a transition in the oxide from columnar to non-columnar. Figure 38 is particularly interesting since it shows the result of oxidizing a specimen (pellet XIX-38) at temperatures below the transition and subsequently above the transition. This sample shows a columnar "outer oxide" on a non-columnar inner oxide. This may imply formation of the non-columnar oxide by outward diffusion of hafnium.

Figures 39-45 show metallographic comparisons of the matrix areas of HfB_2 specimens before and after oxidation. Figures 39 and 40 show pellet XXI-11, $HfB_{1.70}$ before and after oxidation at 2178°K. Pellet XX-36 which was oxidized at 1900°K exhibits a microstructure similar to Figure 40 which illustrates non-uniform grain growth and no porosity. The microstructural changes which occurred in the $HfB_{1.88}$ specimens are shown in Figures 41-44. Pellet XVIII-49, $HfB_{1.88}$, is shown before and after oxidation at 1850°K. Little change in microstructure occurs at this temperature. However, heating $HfB_{1.88}$ to higher temperatures was found to result in grain growth and void formation or porosity in some cases. For example, Figures 43 and 44 show the microstructure of pellet XIX-31 before and after oxidation at 2179°K. This sample had a finer grain size than did pellet XVIII-49. The microstructure resulting from high temperature oxidation exhibits grain growth and void formation. Figure 45 on the other hand which reveals the microstructure of pellet XXI-37 after oxidation at 2164°K does not indicate extensive void formation. The initial microstructure (prior to oxidation) was similar to Figure 43. Consequently this specimen also exhibited grain growth. The microstructural changes which occurred in the boron rich material are illustrated in Figures 46 and 47 which show a pellet XVIII-45 before and after oxidation at 2118°K. No gross changes in grain size or porosity appear to be evident.

3.4 The Effect of Stoichiometry on the Oxidation of ZrB_2

The effect of boron to metal ratio on the oxidation characteristics of ZrB_2 is shown graphically in Figures 47 and 48. The full curve is based on results obtained earlier with zone refined material (1). The break in the parabolic rate constant occurs at about 1450°K where the monoclinic/tetragonal transition occurs in ZrO_2. In addition, the rate of vaporization of B_2O_3 changes rapidly with temperature in this range (see discussion below). The specimens of ZrB_2 were prepared from raw powder with a boron/metal ratio of 1.89. Additions of zirconium to form B/Me = 1.75 or boron to form 2.10 were also tested (see Section IV for details). In addition to the raw 1.89 powder, a purified batch of ZrB_2 powder with B/Me = 1.97 was also employed for fabricating specimens. The results are shown in Table 12 and 13 and in Figures 47 and 48. With ZrB_2, as discussed above for HfB_2,

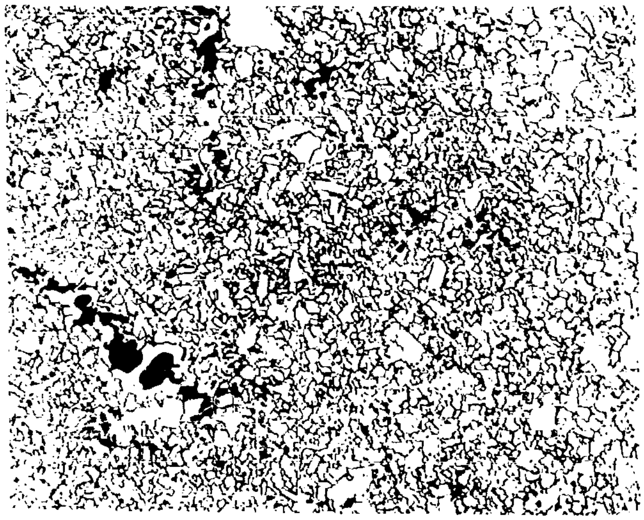

Etched X500
Etchant; 10cc glycerine, 10cc HNO_3
2cc HCl, 0.1cc HF

Figure 39 - Pellet XXI - 11, $HfB_{1.70}$, Matrix Structure.

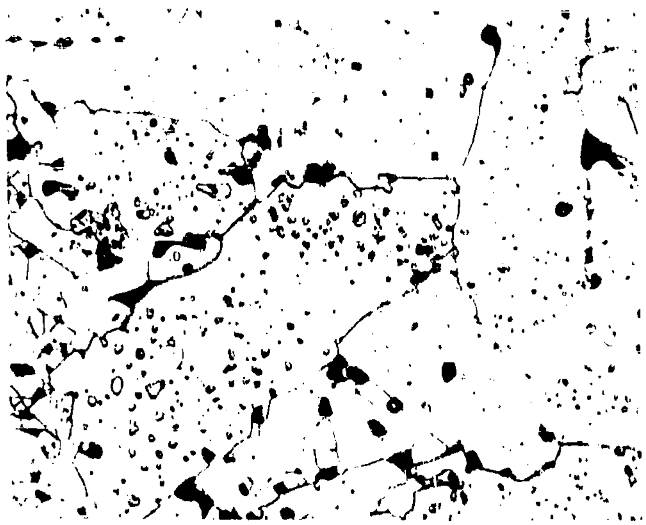

Etched X500
Etchant: 10cc glycerine, 10cc HNO_3
2cc HCl, 0.1cc HF

Figure 40 - Pellet XXI - 11, $HfB_{1.70}$, Matrix Structure, After Oxidation at 2178°K.

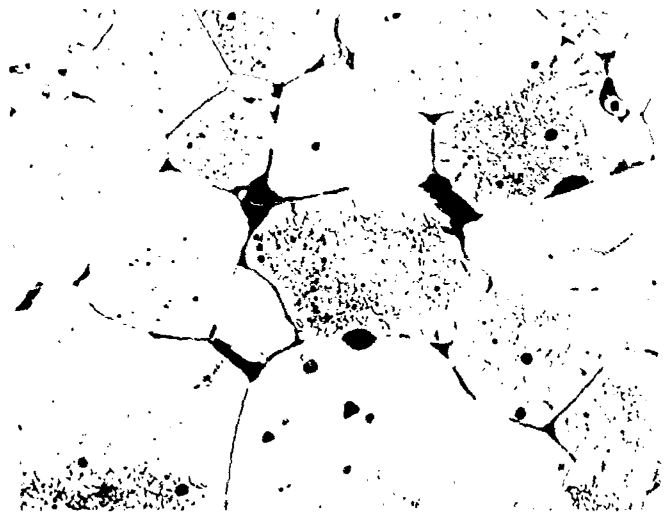

Etched X500
Etchant: Modified Aqua Regia

Figure 41 - Pellet XVIII - 49, $HfB_{1.88}$, Matrix Structure.

Etched X500
Etchant: 10cc glycerine, 10cc HNO_3
2cc HCl, 0.1cc HF

Figure 42 - Pellet XVIII - 49, $HfB_{1.88}$, Matrix Structure, After Oxidation at 1852°K.

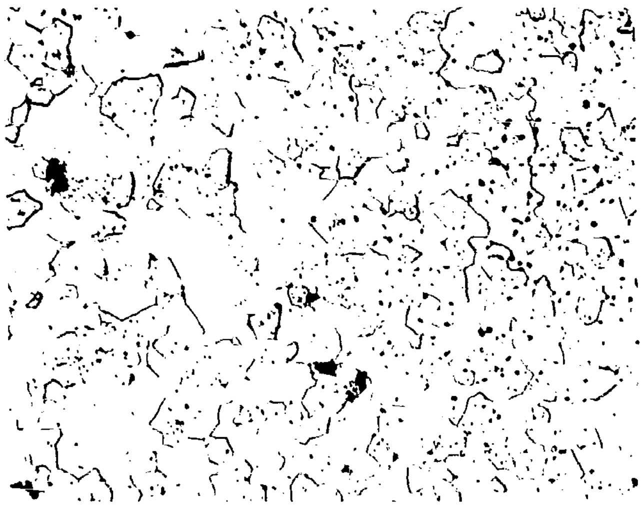

Etched X500
Etchant: Modified Aqua Regia

Figure 43 - Pellet XIX - 31, $HfB_{1.88}$, Matrix Structure.

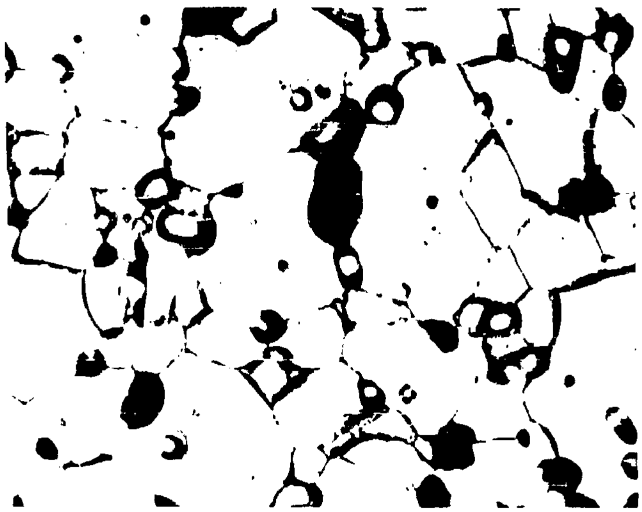

Etched X500
Etchant: 10cc glycerine, 10cc HNO_3
2cc HCl, 0.1cc HF

Figure 44 - Pellet XIX - 31, $HfB_{1.88}$, Matrix Structure After Oxidation at 2179°K.

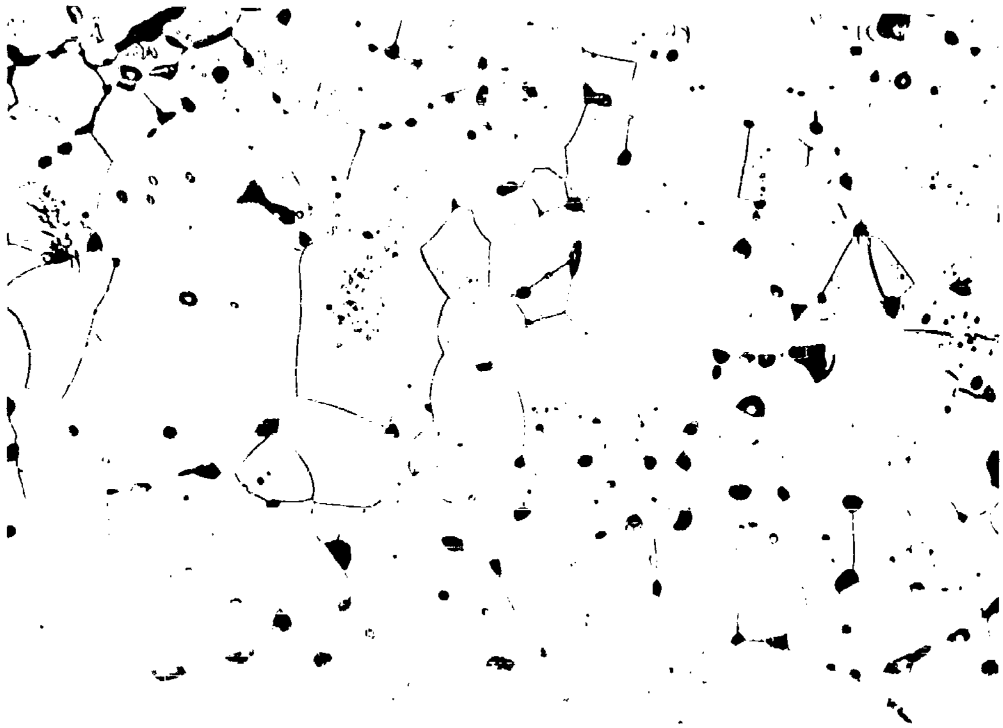

Etched X500
Etchant: 10cc glycerine, 10cc HNO_3
2cc HCl, 0.1cc HF

Figure 45 - Pellet XXI - 37, $HfB_{1.88}$, Matrix Structure After Oxidation at 2164°K.

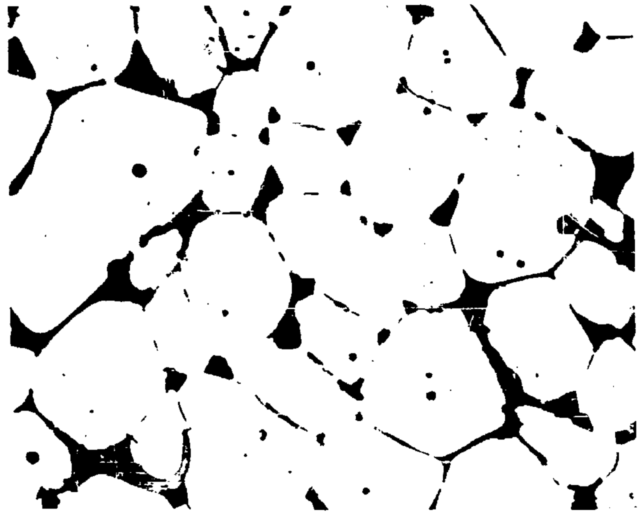

Etched X500
Etchant: Modified Aqua Regia

Figure 46 - Pellet XVIII - 45, $HfB_{2.10}$, Matrix Structure.

Etched X500
Etchant: 10cc glycerine, 10cc HNO_3
2cc HCl, 0.1 cc HF

Figure 47 - Pellet XVIII - 45, $HfB_{2.10}$, Matrix Structure After Oxidation at 2118°K.

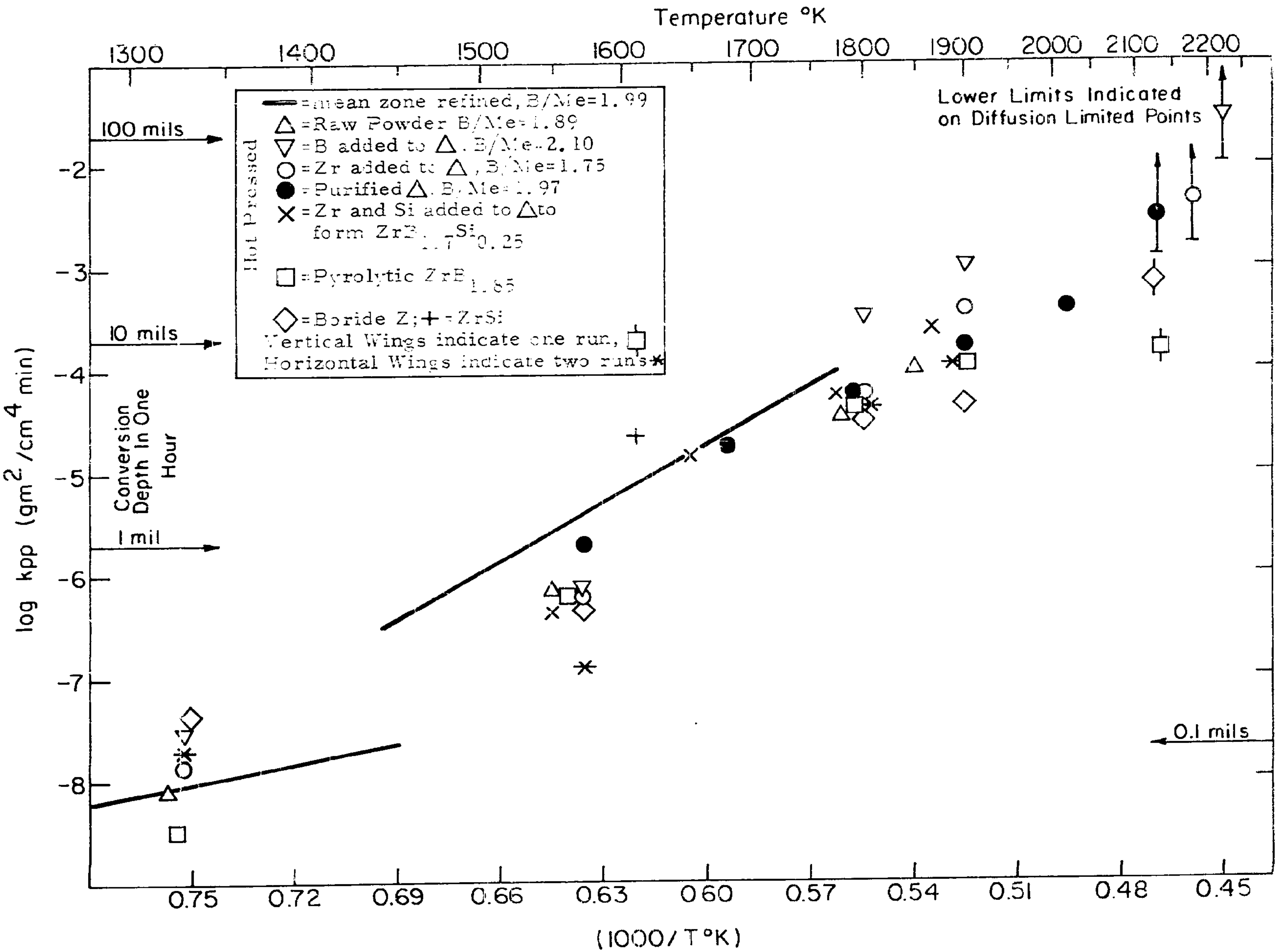

Figure 48 - Oxidation of ZrB_2

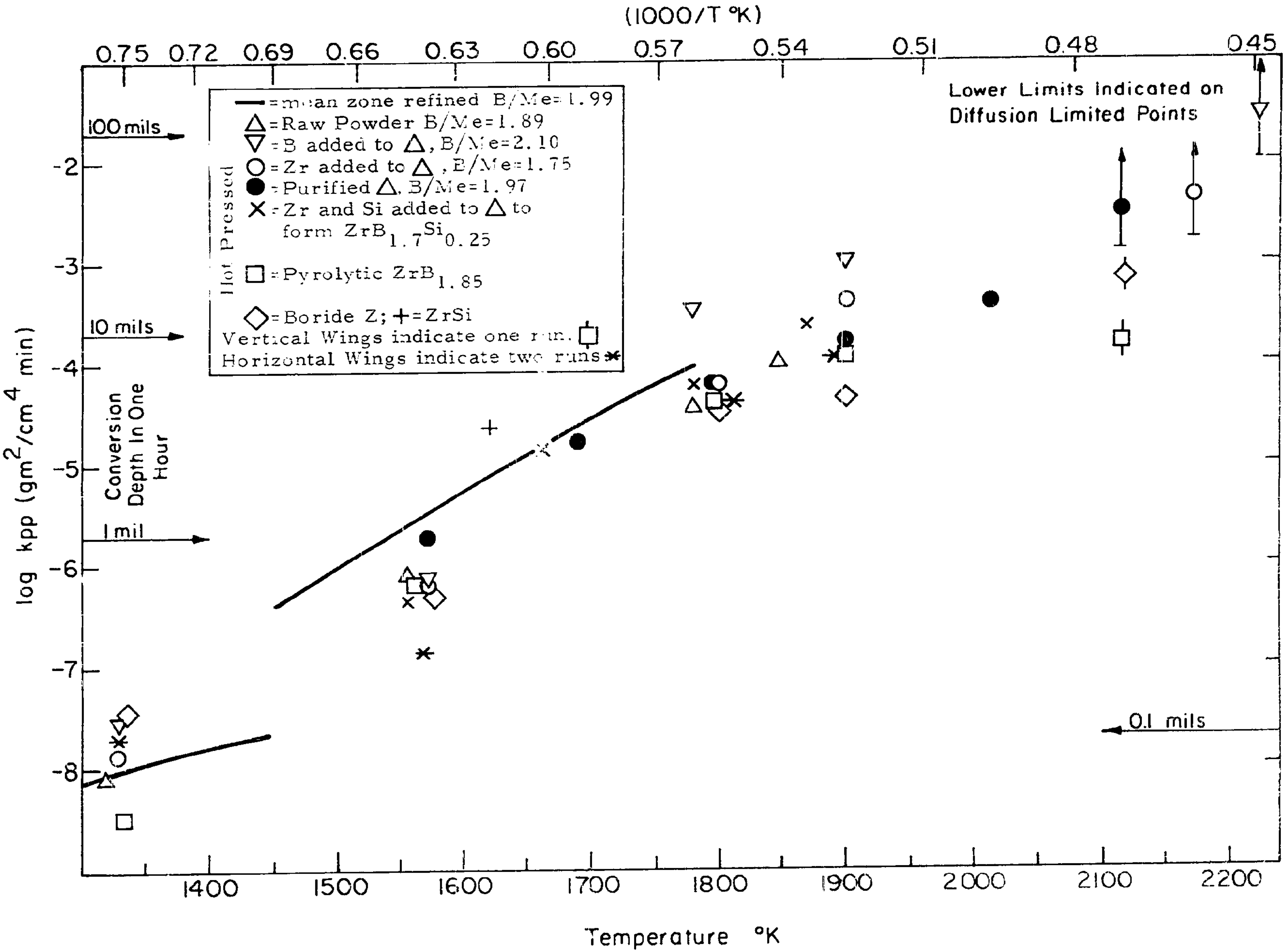

Figure 49 - Oxidation of ZrB_2

the rates of oxidation are lower on the metal rich side than on the boron rich side of stoichiometry. However, ZrB_2 is generally less resistant to oxidation over the temperature range explored than is HfB_2. The metallographic examination of the oxide formed on ZrB_2 specimens above 1450°K indicated a columnar oxide as expected (1, 12, 13).

Figures 50-56 show matrix structures of ZrB_2 before and after oxidation. Figure 50 is characteristic of the metal rich diboride $ZrB_{1.75}$ which is shown in Figure 51 (pellet XX-42) after oxidation at 1898°K and Figure 52 (pellet XX-47) after oxidation at 2176°K. Surprisingly, the former specimen shows some non-uniform grain growth, while the latter does not. No porosity or void formation is indicated in either Figure 51 or Figure 52. Figures 53-56 show matrix areas of the $ZrB_{1.97}$ and $ZrB_{2.10}$ material before and after oxidation. In both cases grain growth and void formation is not evident.

3.5 Gas Phase Diffusion Limited Oxidation and Effects of Flow Rate on Oxidation of HfB_2 and ZrB_2

When the value of the rate of oxide becomes sufficiently fast, the oxidation is controlled by the rate at which oxygen molecules arrive at the surface. Under these conditions every oxygen molecule striking the surface reacts with the diboride. Pellets XX-17 and XX-47 which are $ZrB_{1.97}$ and $ZrB_{1.75}$ respectively were observed to react with essentially all of the oxygen supplied in the gas flow. In addition, pellet XXII-2, $ZrB_{2.1}$, was also observed to exhibit diffusion limited oxidation at 2233°K. Thus in the temperature range between 2100°K and 2200°K, ZrB_2 appears to show diffusion limited oxidation. By contrast, HfB_2 does not. Pellet XXII-1 shows that doubling the flow rate at 2100°K produces no appreciable effect on k_{pp}.

3.6 Effect of Silicon Additions on the Oxidation of ZrB_2 and HfB_2

Since silicon forms a glass on oxidation and is likely to substitute on the boron sublattice in the diboride (see Section IX) an investigation of the effects of silicon on the oxidation of ZrB_2 and HfB_2 has been initiated. Samples of $HfB_{1.70}Si_{0.25}$ were prepared by hot pressing raw $HfB_{2.12}$ powder with suitable additions of hafnium and silicon. Similarly samples of $ZrB_{1.70}Si_{0.25}$ were prepared by alloying raw $ZrB_{1.89}$ powder. Homogenization treatments were performed after hot pressing. The preliminary results of this study are shown in Tables 12 and 13 and in Figures 30, 31, 48 and 49. These results indicate that at low temperatures (below 1550°K) rather pronounced improvement is afforded by silicon additions. For example, the $HfB_{1.70}Si_{0.25}$ specimen exhibited a value of k_{pp} which was more than 50 times smaller than the rate constant of the raw B/Me = 2.12 powder from which it was prepared. At higher temperatures i.e., 1800°K and 1900°K, the beneficial effect appears to be lost. At present, it is not clear if this is due to loss of silicon via evaporation of some other factor. Additional experiments with specimens containing higher levels of silicon are presently in process. As an additional comparison, Figures 48 and 49 show k_{pp} for ZrSi which is comparable to $ZrB_{1.70}Si_{0.25}$ at about 1650°K. Figures 57-60 show some photomicrographs

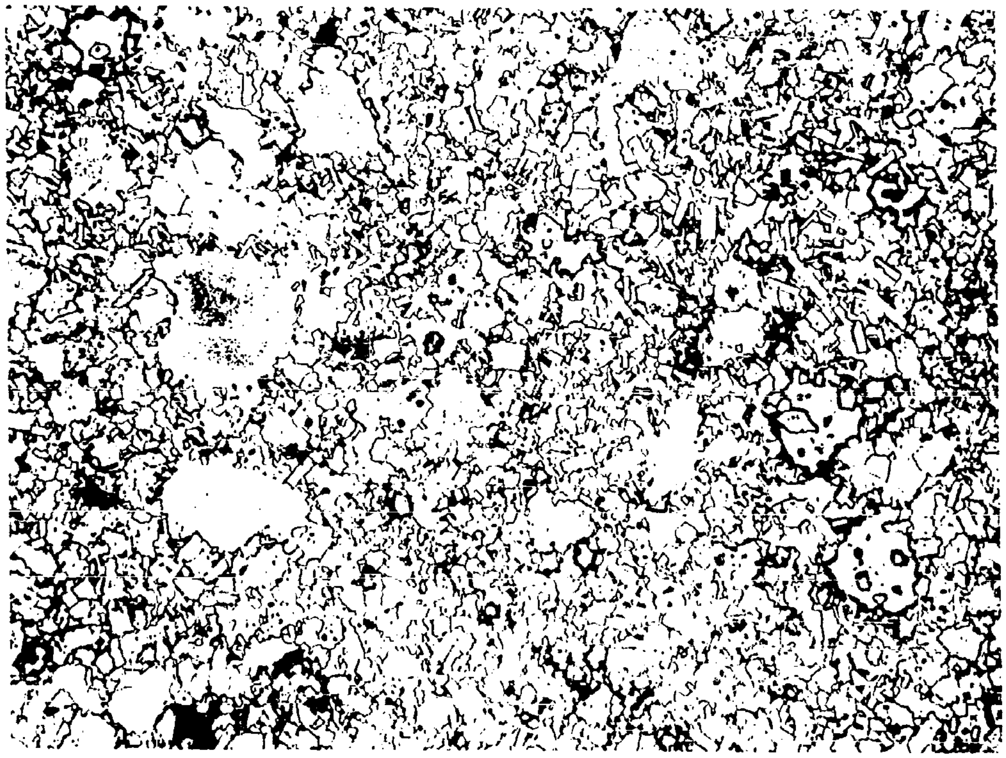

Etched X500
Etchant: 10cc glycerine, 10cc HNO_3
2cc HCl, 0.1cc HF

Figure 50 - Pellet XX - 42, $ZrB_{1.75}$, Matrix Structure.

Etched X500
Etchant: 10cc glycerine, 10cc HNO_3
2cc HCl, 0.1cc HF

Figure 51 - Pellet XX - 42, $ZrB_{1.75}$, Matrix Structure After Oxidation at 1898°K.

Etched X500
Etchant: 10cc glycerine, 10cc HNO_3
2cc HCl, 0.1cc HF

Figure 52 - Pellet XX - 47, $ZrB_{1.75}$, Matrix Structure After Oxidation at 2170°K.

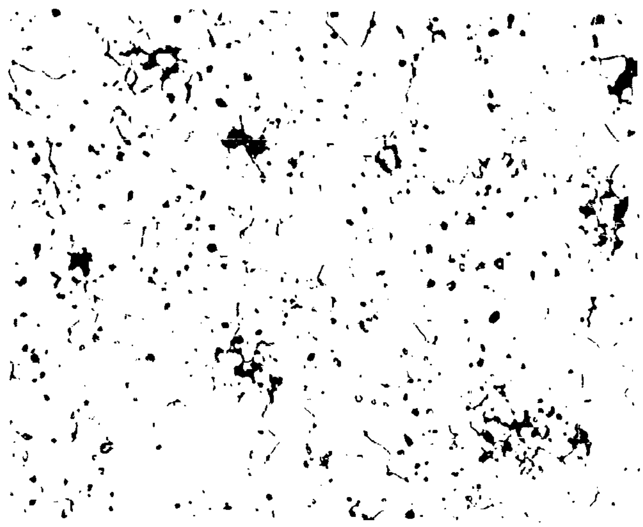

Etched X500
Etchant: Modified Aqua Regia

Figure 53 - Pellet XX - 17, $ZrB_{1.97}$, Matrix Structure.

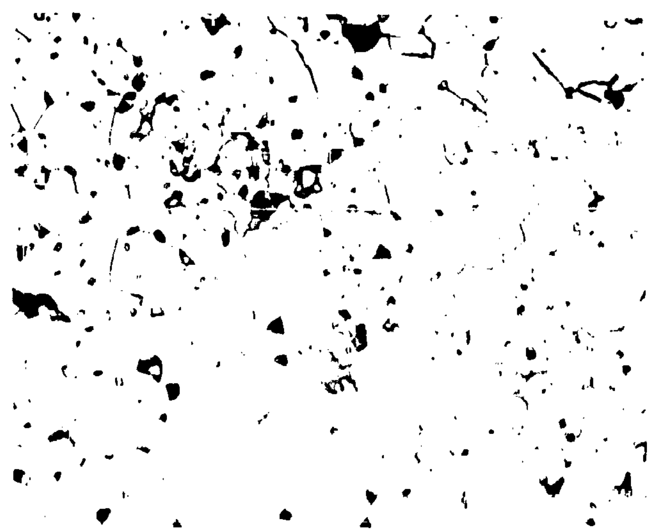

Etched X500
Etchant: 10cc glycerine, 10cc HNO_3
2cc HCl, 0.1cc HF

Figure 54 - Pellet XX - 17, $ZrB_{1.97}$, Matrix Structure After Oxidation at $2118^{\circ}K$.

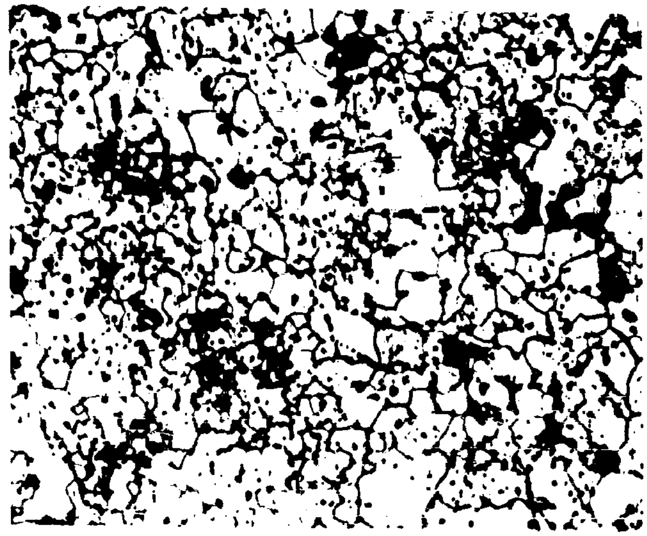

Etched X500
Etchant: Modified Aqua Regia

Figure 55 - Pellet XXI - 19, $ZrB_{2.10}$, Matrix Structure.

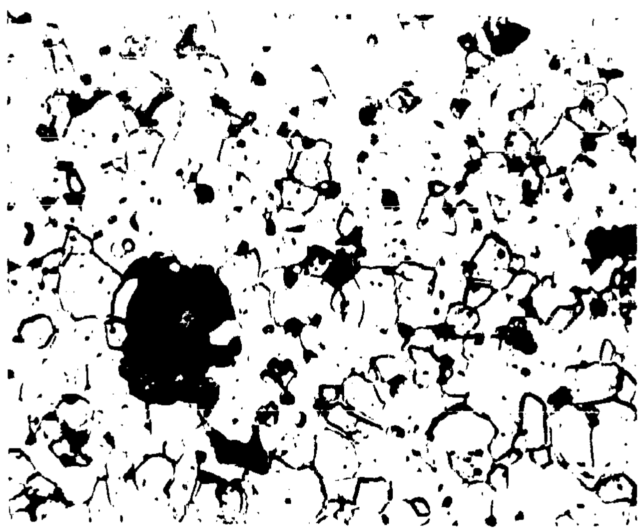

Etched X500
Etchant: 10cc glycerine, 10cc HNO_3
2cc HCl, 0.1cc HF

Figure 56 - Pellet XXI - 19, $ZrB_{2.10}$, Matrix Structure After Oxidation at 1898°K.

Etched X20
Etchant: Modified Aqua Regia
Polaroized Light

Figure 57 - Pellet XXI - 17, $ZrB_{1.7}Si_{0.25}$, After Oxidation at 1899°K.

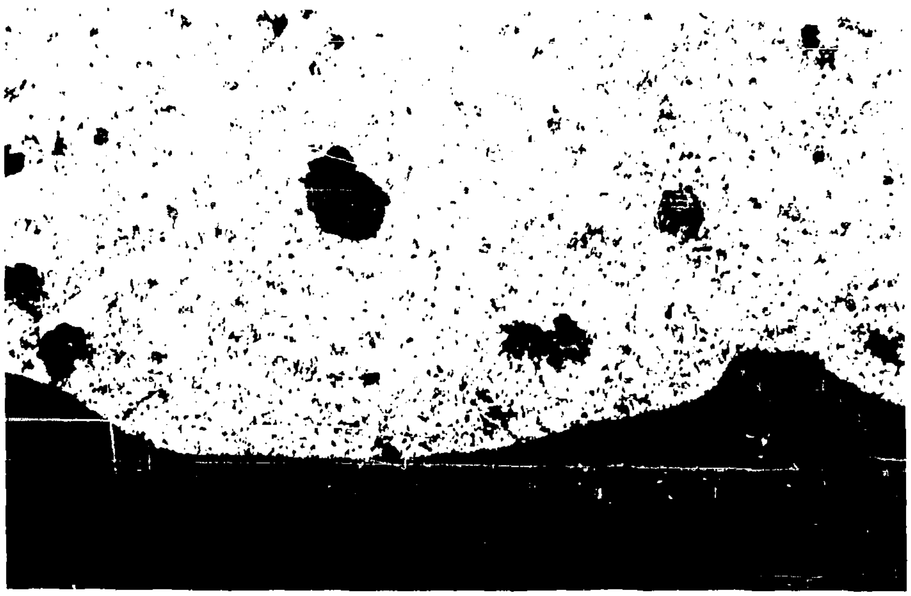

Etched X 100
Etchant: 10cc glycerine, 10cc HNO_3
2cc HCl, 0.1cc HF

Figure 58 - Pellet XXI - 17, $ZrB_{1.7}Si_{0.25}$, After Oxidation at 1899°K.

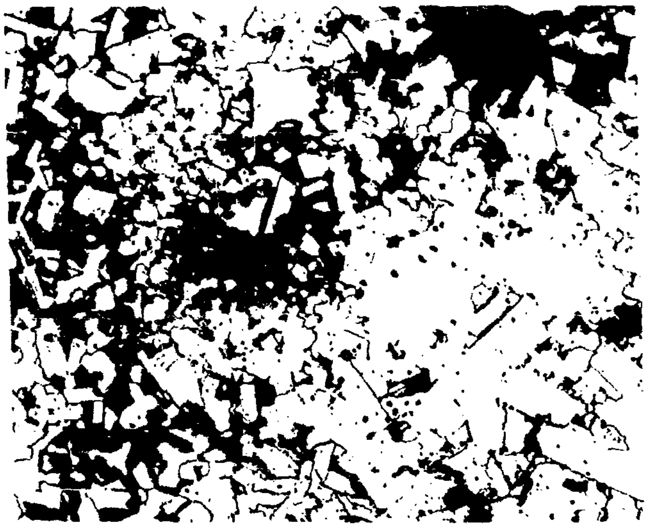

Etched X500
Etchant: Modified Aqua Regia

Figure 59 - Pellet XXI - 17, $ZrB_{1.7}Si_{0.25}$, Matrix Structure.

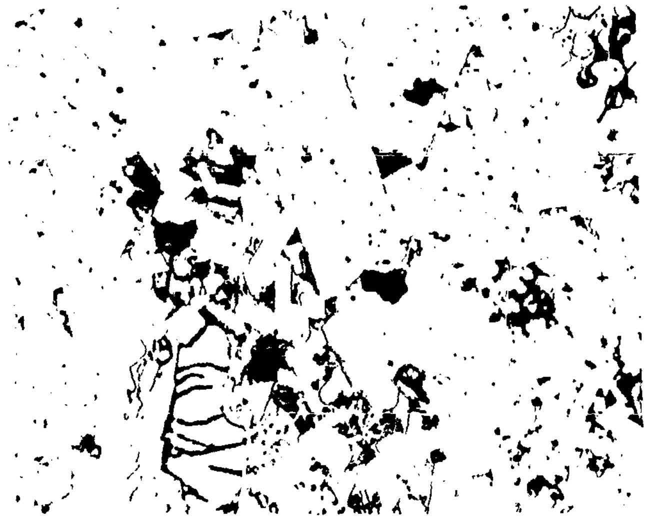

Etched X500
Etchant: 10cc glycerine, 10cc HNO_3
2cc HCl, 0.1cc HF

Figure 60 - Pellet XXI - 17, $ZrB_{1.7}Si_{0.25}$, Matrix Structure After Oxidation at 1899°K.

of $ZrB_{1.70}Si_{0.25}$ pellet XXI-17 before and after oxidation at 1899°K. The low magnification photographs i.e., Figures 57 and 58 show a fairly adherent oxide layer, while the matrix photomicrographs do not show any radical changes.

3.7 Oxidation of Boride Z and Pyrolytic $ZrB_{1.85}$

Several specimens of "Boride Z", a ZrB_2-$MoSi_2$ composite material prepared by Carborundum were studied in addition to two specimens of $ZrB_{1.85}$ prepared at Raytheon Co. by J. Pappas by means of vapor deposition. The results are shown in Tables 12 and 13 and in Figures 33, 34, 48 and 49. At temperatures up to 1900°K both materials compare with metal rich $ZrB_{1.70}$ prepared by high pressure hot pressing. However, at higher temperatures, both "Boride Z" and the vapor deposited material are more oxidation resistant than the hot pressed specimens. Additional work on both "Boride Z" and pyrolytically deposited material is in progress.

C. The Effects of Alloying Additions on Oxidation Behavior

In a comprehensive talk entitled "Alloying for Oxidation Protection", Stringer (17) summarized the principals which have been applied in the past to the selection of alloying elements for oxidation protection. These are:

(1) Wagner-Hauffe theory.

(2) Preferential formation of the oxide of the alloying element.

(3) Formation of a compound oxide.

(4) Stabilization of a more protective oxide.

(5) Formation of a metal or internal oxide barrier.

A discussion of each of these principals, with particular emphasis on potential applications for improving the oxidation resistance of HfB_2 follows.

1. Applications of the Wagner-Hauffe Theory

1.1 The Parabolic Rate Law

In cases where a parabolic rate law is observed in the oxidation of metals and alloys, the Wagner mechanism is frequently applicable, and the rate of oxide growth (dx/dt) can be written as follows in terms of the specific conductivity (κ_o) of the oxide film at an oxygen pressure of 1 atm., the transport numbers of cations, anions, and electrons (τ_C, τ_A, τ_e) in the oxide, and the oxygen pressures p_x and p_o at the oxide/gas and oxide/metal interfaces respectively:

$$\frac{dx}{dt} = \frac{\Omega RT}{x} (\tau_A + \tau_C)\, \tau_e\, \kappa_o \,(p_x^{1/n} - p_o^{1/n}) \qquad (9)$$

In (1), x is the oxide film thickness at time t, Ω and n are constants for any given system and R is the gas constant.

The conductivity of most oxides is predominantly electronic. Hence, $\tau_e \approx 1$, and the ionic conductivity of the oxide $(\tau_A + \tau_C)\,\kappa_o$ determines the oxidation rate. Since ions migrate via vacancies or interstitials, it should be possible to reduce the oxidation rate by reducing the defect concentration in the growing oxide film. In p-type oxides, this means reducing the number of negatively charged defects, cation vacancies or anion interstitials. In n-type oxides, it means reducing the number of positively charged defects, anion vacancies or cation interstitials. Thus where p-type oxides are formed, the substitution of cations of lower valency or anions of higher valency should improve oxidation resistance. Where n-type oxides are formed, the substitution of higher valent cations or lower valent anions should prove beneficial.

1.2 Wagner-Hauffe Mechanism - General Considerations

In summary, to improve the oxidation resistance of a metal, Me, which oxidizes parabolically to an oxide, MeO_y, choose an alloying element, Mt, of higher valence than Me, if MeO_y is an n-type semi-conductor, and of lower valence than Me, if MeO_y is p-type. Similar arguments can be applied to additions to the anion lattice.

In many cases (18), the alloy Me-Mt, chosen as above, will indeed oxidize less rapidly than pure Me. In other cases, there will be either no improvement or an adverse effect. Even in instances where oxidation resistance has been improved by application of the Wagner-Hauffe principals, the extent of the improvement is often not given quantitatively by the theory (18). The reasons for possible failure are manifold. In order to fulfill the Wagner-Hauffe conditions, Mt ions must be substituted for Me ions in the oxide. If one simply prepares an alloy Me-Mt, and oxidizes it, there is no guarantee that the oxide which forms will have the desired structure. Mt ions may not be soluble in the oxide MeO_y. They might for example be too large to substitute for Me ions. The stability of the two oxides might be so different that one or the other metal could be oxidized preferentially. Furthermore, it is conceivable that a homogeneous alloy Me-Mt will not form in the first phase.

A particular reason for possible failure of the Wagner-Hauffe theory in high temperature systems is that the intrinsic defect concentration of the oxide may already be so high that the addition of a small concentration of ions of different valency will make very little difference.

1.3 Wagner-Hauffe Mechanism - Derivation of Equations

If the principal diffusing species in a growing oxide film of MeO_y is an ion defect $I^{\pm z}$, then the addition of a cation $Mt^{+\omega}$ to the oxide should change the oxidation rate approximately as follows. The bulk of the oxide must be electrically neutral, thus

$$C(e^{\mp}) = |z| C \; (I^{\pm z}) \pm (\omega - \nu) \; C \; (Mt^{+\omega}) \tag{10}$$

where $C(e^{\mp})$ is the concentration of free electrons or positive holes in the oxide, and ν is the valence of $Me^{+\nu}$ ions in the oxide. If equilibrium is established at the oxide/metal and oxide/gas phase boundaries, then throughout the oxide, the product $[C(e^{\mp})]^{|z|} C \; (I^{\pm z})$ is a constant K at a given oxygen pressure:

$$[C(e^{\mp})]^{|z|} C \; (I^{\pm z}) = K \tag{11}$$

If the subscript o is used to refer to the pure metal Me,

$$K = [C_o(e^{\mp})]^{|z|} C_o(I^{\pm z}) = [C_o(I^{\pm z})]^{(1 + |z|)} \left(|z|^{|z|}\right) \tag{12}$$

Substituting (10) into (11) affords:

$$[|z| C(I^{\pm z}) \pm (\omega - \nu) \; C \; (Mt^{+\omega})]^{|z|} C \; (I^{\pm z}) = K \tag{13}$$

Equating (12) and (13), provides an expression that defines $\dfrac{C(I^{\pm z})}{C_o(I^{\pm z})}$ in terms of measurable parameters

$$\left[|z| \frac{C(I^{\pm z})}{C_o(I^{\pm z})} \pm (\omega - \nu) \frac{C(Mt^{+\omega})}{C_o(I^{\pm z})} \right]^{(|z|)} \left(\frac{C(I^{\pm z})}{C_o(I^{\pm z})} \right) = (|z|)^{|z|} \tag{14}$$

The ratio of the ion defects in the alloy oxide and in the pure oxide, $C(I^{\pm z})/C_o(I^{\pm z})$ is equal to the ratio of the parabolic rate constants for oxidation of alloy and pure metal, k/k_o. Therefore, from (14)

$$\left(\frac{k}{k_o}\right)^{(1 + (1/|z|))} = 1 \mp \frac{(\omega - \nu)}{z} \left(\frac{C(Mt^{+\omega})}{C_o(I^{\pm z})}\right) \left(\frac{k}{k_o}\right)^{(1/|z|)} \tag{15}$$

where the negative sign is associated with I^{+z} ($z > 0$) and the positive sign with I^{-z}($z < 0$).

Equation (15) can be solved approximately for the ratio (k/k_o) under given experimental conditions. In general, the concentration of added ions $C(Mt^{+\omega})$ will be very large compared to the equilibrium defect concentration in the pure oxide $C_o(I^{\pm z})$, i.e.

$$\frac{C(Mt^{+\omega})}{C_o(I^{\pm z})} \gg 1 \tag{16}$$

Two cases will be considered: (1) the addition of ions of lower valence ($\omega < \nu$) to oxides with cation interstitials or anion vacancies ($z > 0$) or the addition of ions of higher valency ($\omega > \nu$) to oxides with cation vacancies or anion interstitials ($z < 0$) and (2) the addition of ions of higher valency ($\omega > \nu$) to oxides with cation interstitials or anion vacancies ($z > 0$) or the addition of ions of lower valency ($\omega < \nu$) to oxides with cation vacancies or anion interstitials ($z < 0$).

Case (1): $(\omega - \nu) < 0$ and $z > 0$ or $(\omega - \nu) > 0$ and $z < 0$

For case (1), equation (15) becomes:

$$\left(\frac{k}{k_o}\right)^{(1 + (1/|z|))} = 1 + \left(\frac{|\omega - \nu|}{|z|}\right)\left(\frac{C(Mt^{+\omega})}{C_o(I^{\pm z})}\right)\left(\frac{k}{k_o}\right)^{(1/|z|)} \tag{17}$$

Making use of the inequality in (16) generates

$$\frac{k}{k_o} \approx \left(\frac{|\omega - \nu|}{|z|}\right)\frac{C(Mt^{+\omega})}{C_o(I^{\pm z})} \tag{18}$$

Physically, then the addition of cations of lower valency than the lattice cations to n-type oxides or the addition of cations of higher valency to p-type oxides will result in an increase in the rate of oxidation. The ratio of the parabolic rate constant for the alloy to the parabolic rate constant for the pure base metal will be proportional to the ratio of the concentration of additive cations in the oxide to the equilibrium defect concentration in the pure oxide.

Case (2): $(\omega - \nu) > 0$ and $z > 0$ or $(\omega - \nu) < 0$ and $z < 0$

For case (2), equation (15) becomes:

$$\left(\frac{k}{k_o}\right)^{(1 + 1/|z|)} = 1 - \left(\frac{|\omega - \nu|}{|z|}\right)\frac{C(Mt^{+\omega})}{C_o(I^{\pm z})}\left(\frac{k}{k_o}\right)^{(1/|z|)} \tag{19}$$

Dividing by $\left(\frac{k}{k_o}\right)^{(1+(1/|z|))}$, (11) can be rewritten in the form:

$$1+\left(\frac{|\omega - \nu|}{|z|}\right)\frac{C(Mt^{+\omega})}{C_o(I^{\pm z})}\left(\frac{k_o}{k}\right) = \left(\frac{k_o}{k}\right)^{(1+(1/|z|))} \qquad (20)$$

Again using the inequality (3), the ratio k/ko becomes

$$\frac{k}{k_o} \approx \left(\frac{|z|^{|z|}}{(|\omega - \nu|)^{|z|}}\right)\left[\frac{C_o(I^{\pm z})}{C(Mt^{+\omega})}\right]^{|z|} \qquad (21)$$

Case (2) is then characterized by $k < k_o$; i.e. case (2) alloy additions result in a decreased oxidation rate. The magnitude of the decrease is given by (14) and again depends on the ratio of added metal ions to the equilibrium defect concentration in the pure oxide. If $C(Mt^{+\omega})$ cannot be made very much larger than $C_o(I^{\pm z})$, then very little change in oxidation rate can be anticipated.

1.4 Wagner-Hauffe Mechanism Applied to HfB_2

If the Wagner theory applies to the oxidation of HfB_2 under conditions where HfO_2 is the only condensed oxide formed, and if the growing oxide film is anion deficient, then the addition of ions with valence greater than +4, such as Ta^{+5}, W^{+6}, should improve the oxidation resistance, while addition of ions with valence less than +4, such as Al^{+3} or Be^{+2}, should have a deleterious effect. If the experimental results fail to confirm the theoretical conclusions, several reasons might be sought. As discussed above, the intrinsic defect concentration in the oxide could be so high as to be influenced only negligibly by addition of foreign cations. Furthermore, the growing $HfO_2(c)$ film might not be anion deficit. On the basis of recent work on the conductivity of $ZrO_2(c)$ (13,19) it might be surmized that the conduction mechanism is a great deal more complicated.

2. Preferential Formation of the Oxide of the Alloying Element

If the free energy of formation of the oxide of the alloying element is very much smaller (more negative) than the free energy of formation of the oxide of the basis metal, then it is possible that the oxide of the alloying element will form exclusively. If in addition, the defect concentration of the alloying element oxide is less than that of the basis metal oxide, the alloy may oxidize to a smaller extent than the pure basis metal.

Here it is difficult to predict the results that might be expected in any given case, because kinetic factors may override thermodynamic stability, and because defect concentrations are largely unknown.

Furthermore, even if the oxide of the alloying element is formed preferentially, it will be saturated with ions of the basis metal and the defect structure might be very different from that of the pure oxide in equilibrium with a pure metal. In addition, the alloy oxide might be mechanically incompatible with the substrate.

To apply the above considerations to improving the oxidation resistance of HfB_2, it is necessary to find an oxide with a lower free energy of formation than $HfO_2(c)$ in the temperature range of interest. Hafnium dioxide is a highly stable oxide with $\Delta F_{f,\ HfO_2,\ 2000^oK} = -180.1$ kcal/mole of O_2. Oxides with greater stability are ThO_2 with $\Delta F_{f,\ ThO_2,\ 2000^oK} = -203.2$ kcal/mole of O_2, Y_2O_3 with $\Delta F_{f,\ Y_2O_3,\ 2000^oK} = -206.6$ kcal/mole of O_2, and La_2O_3 with $\Delta F_{f,\ La_2O_3,\ 2000^oK} = -191.3$ kcal/mole of O_2. The question of the defect concentration in the oxide which actually forms must defer to experiment.

The elements Y and La, on the basis of the Wagner theory, would increase the rate of oxidation of HfB_2. However, on the basis of thermodynamic stabilities, a decrease in oxidation rate becomes possible. This should have no effect on the rate of oxidation of HfB_2, if the Wagner mechanism is valid for the system, but might be beneficial if a continuous coherent layer of ThO_2 should form.

3. Formation of a Ternary Oxide

The oxidation of an alloy may produce two single phase oxides, or a ternary oxide which confers greater oxidation resistance than the oxide of either the basis metal or the alloying element. This principal is difficult to apply to the protection of HfB_2, since virtually no information is available on mixed oxides of hafnium. A $CaO.HfO_2$ phase melting at about 2470°C has been reported (20) and might form on oxidation of HfB_2 with calcium additions. A hafnium silicate analogous to zircon might be formed from a HfB_2-Si alloy.

4. Stabilization of a More Protective Oxide

Frequently an alloying element may serve to improve the plasticity of an oxide film so that any stresses created by a mismatch between the oxide and alloy lattice may be more easily accommodated. In the oxidation of HfB_2, a large increase in oxidation rate occurs at the monoclinic to tetragonal transition temperature of HfO_2. It seems unlikely that any alloying element will serve to stabilize the monoclinic oxide at higher temperatures.

5. Formation of a Metal or Internal Oxide Barrier

In the oxidation of molybdenum silicides, the preferential oxidation of silicon eventually results in the formation of a terminal solid solution of silicon in molybdenum at the alloy-oxide interface. The low silicon activity in this region contributes to the oxidation resistance of the silicides. A comparable mechanism does not apply to the oxidation of HfB_2.

Rapp (21), by careful temperature-time programming, was able to deposit a very narrow protective band of $In_2O_3(c)$ at a predetermined depth in Ag-In alloys. Since oxygen dissolves in silver, and silver oxide is unstable, Ag-In alloys undergo internal oxidation. Again, this method of protection is not obviously applicable to HfB_2.

D. Thermodynamics of Oxidation

1. The Influence of B_2O_3 Volatility on Diboride Oxidation

The appreciable volatility of B_2O_3 in the temperature range of the present oxidation experiments has been discussed previously (1). On the assumptions (1) that the metal diborides MeB_2 oxidize non-preferentially and parabolically to solid $MeO_2(c)$ and liquid $B_2O_3(l)$, and (2) that $B_2O_3(l)$ vaporizes linearly at 0.01 the equilibrium rate of vaporization into vacuum, G, as long as liquid is present, we were able to define an experimental time t_o after which boron oxide would vaporize as rapidly as it formed. The time t_o was given by the equation:

$$t_o = 0.1894 \times 10^4 \frac{k_{pp}}{G^2} \tag{22}$$

We showed in a previous report, that for HfB_2 above 1488°K, essentially no condensed phase boron oxide should be present after about the first five minutes of oxidation. In the current program, measurements were made on HfB_2 at a temperature of 1330°K where rate constants of 1.32×10^{-7} g^2/cm^4-min for $HfB_{2.12}$ and 1.31×10^{-8} for $HfB_{1.7}$ were obtained. For the boron rich material, we would have

$$t_o = \frac{0.1894 \times 10^4 \times 1.31 \times 10^{-7}}{(2.6 \times 10^{-4})^2} \simeq 3700 \text{ min} \tag{23}$$

For the metal rich material A_o = 370 min. Hence, at the lowest temperature for the hour long experimental runs described here, the rate of formation of liquid $B_2O_3(l)$ should be much greater than the rate of loss $B_2O_3(g)$. That is, essentially all of the boron oxide formed will remain in the surface. For ZrB_2, the situation would of course be similar.

2. Calculation of the Pressure of B_2O_3 at the Oxide/Boride Interface

In the final report (1), the problem of whether the metal oxide $MeO_y(c)$ would be thermodynamically stable in contact with the boride $Me_{1-x}B_x$ with respect to decomposition to $B_2O_3(g)$ and the metal was considered. Results were given for $x = 2/3$. Here the calculation is extended to the metal and boron rich side of stoichiometry $x = 0.660$ and 0.674 and the results are compared to those obtained previously. The results for each metal are given in Table 14. The pressure of $B_2O_3(g)$ was calculated for the equilibrium:

$$MeO_y\,(c) + \frac{2y}{3}\,B(a_B^{\eta}) \rightarrow \frac{y}{3}\,B_2O_3(g) + Me(a_{Me}^{\eta}) \tag{24}$$

where a_B^{η} and a_{Me}^{η} are the activities of boron and metal respectively in the boride $Me_{1-x}B_x$. The standard free energy of reaction (14) may be written in terms of the free energy of formation of the oxides:

$$\Delta F^{o}_{(14)} = \frac{y}{3}\,\Delta F_{f,B_2O_3(g)} - \Delta F_{f,MeO_y(c)} \tag{25}$$

or in terms of the pressure of B_2O_3 and the activities of metal and boron:

$$\Delta F^{o}_{(14)} = -RT\,\ln \frac{a_{Me}^{\eta}\;P_{B_2O_3(g)}^{\,y/3}}{(a_B^{\eta})^{2y/3}} \tag{26}$$

From (25) and (26), one can calculate the pressure of $B_2O_3(g)$ in equilibrium with $MeO_y(c)$ and $Me_{1-x}B_x(c)$:

$$\ln\,p_{B_2O_3} = 2\,\ln\,a_B^{\eta} - \frac{3}{y}\,\ln\,a_{Me}^{\eta} - \frac{\Delta F_{f,B_2O_3(g)}}{RT} + \frac{3}{y}\,\frac{\Delta F_{f,MeO_y(c)}}{RT} \tag{27}$$

Activities of boron and metal were calculated from the formulas given in the final report;(1) free energies of formation were taken from the JANAF Tables and the AVCO Tables.

If the calculated $\log p_{B_2O_3} \geq 0$, then a coherent metal oxide film is not thermodynamically stable on the surface of the metal diboride. The film would be ruptured by evolution of $B_2O_3(g)$. If this mechanism is a significant cause of material failure during oxidation, then it would be advantageous to remain on the metal-rich side of the range of homogeneity of the diboride. For the stoichiometric compounds, the equilibrium pressure of B_2O_3 at the boride/oxide interface exceeds an atmosphere at 2000°K for TiO_2 on TiB_2, NbO_2 on NbB_2, and Ta_2O_5 on TaB_2, at 1500°K for NbO_2 on NbB_2 and for Ta_2O_5 on TaB_2, and at 1000°K for NbO_2 on NbB_2 and Ta_2O_5 on TaB_2. On the metal-rich side of stoichiometry, the vapor pressure of B_2O_3 remains below an atmosphere for all of the diborides. Thus, the relative order of oxidation resistance based on B_2O_3 pressure is HfB_2 (best) followed by ZrB_2, TiB_2, TaB2 and NbB_2 for stoichiometric diborides. In addition, metal rich diborides are more resistant to oxidation than boron rich diborides. These conclusions are similar to those reached in Section IX based on "boron activity gradient" computations.

Table 14 indicates that for zirconium diboride the equilibrium pressure of $B_2O_3(g)$ calculated from Eq. (1) at 2000°K is about 10^{-14} atm over $ZrB_{1.94}$, 10^{-4} atm over stoichiometric ZrB_2, and almost 10 atm over $ZrB_{2.08}$. This means that a protective film of ZrO_2 formed on a metal rich ZrB_2 should be stable over any pressures encountered in practice. Stoichiometric ZrB_2 might exhibit low pressure oxidative failure at 2000°K at ambient pressures near 0.1 torr. Boron rich ZrB_2 might not exhibit protective oxidation at all at 2000°K, even at oxygen pressures of an atmosphere. For hafnium diborides at 2000°K, the calculated pressures of $B_2O_3(g)$ in equilibrium with $HfO_2(c)$ and $HfB_2 \pm x$ are respectively 10^{-22} atm for $HfB_{1.94}$, 10^{-5} atm for HfB_2, and 10^{-1} atm for $HfB_{2.08}$. Thus, at ambient pressures of the order of 0.1 atm, a protective layer of $HfO_2(c)$ might fail to form on the surface of a boron rich hafnium diboride, while in equilibrium with a metal rich HfB_2, the dioxide should be perfectly stable.

One therefore predicts on thermodynamic grounds that, other things being equal, the range of temperature and pressure over which HfB_2 and ZrB_2 can be used in an oxidative environment should be greater on the metal rich side of the region of homogeneity than on the boron rich side. Factors that might override the thermodynamic conclusions are (1) an effect of stoichiometry on the adherence between oxide and substrate, and (2) failure to achieve the equilibrium described by Eq. (1) at the interface, either for kinetic reasons or because the oxide formed in immediate contact with the alloy is not the dioxide, but the monoxide or a ternary Me-B-O mixture.

Thus from a thermodynamic point of view, the minimum rate of oxidation of refractory diborides at low pressures and temperatures above 2000°K should be achieved on the metal rich side of the single phase diboride region. On the basis of the experimental results of Section B, and the earlier results of this study (1), the metal rich diborides are superior in oxidation resistance at pressures of an atmosphere and temperatures up to 2000°K. Since no unexpected adverse effects are introduced on the metal rich side of the homogeneity range, it should be advantageous for most practical applications to use metal rich material.

TABLE 14

PRESSURES OF $B_2O_3(g)$ IN EQUILIBRIUM WITH $MeO_y(c)$ AND $Me_{1-x}B_x$

T = 2000°K

x	Ti	Zr	Hf	Nb	Ta
0.660	- 7.20	-14.29	-15.0	- 0.10	- 3.12
0.666	1.15	- 4.23	- 5.16	7.25	+ 4.58
0.674	+ 5.3	0.96	- 0.13	10.58	*

T = 1500°K

x	Ti	Zr	Hf	Nb	Ta
0.660	-15.11	*	*	- 6.14	- 6.50
0.666	- 1.00	- 8.28	- 8.58	7.81	3.64
0.674	*	*	*	*	*

T = 1000°K

x	Ti	Zr	Hf	Nb	Ta
0.660	*	*	*	-17.2	-18.0
0.666	- 1.99	-17.25	-18.9	6.11	1.28
0.674	*	*	*	*	*

* Outside of the single phase diboride region

E. Conclusions

The following conclusions can be drawn from these results:

(a) In the lower temperature range where $B_2O_3(l)$ is present, the effect of varying the stoichiometry of HfB_2 from metal rich to boron rich and the comparison of the magnitude of k_{pp} for HfB_2 vs. ZrB_2 are masked by the oxidation resistance enhancement conferred by the protective layer of $B_2O_3(l)$. The apparent decreased oxidation resistance of ZrB_2 at temperatures above the monoclinic to tetragonal transition in ZrO_2 is also masked by the rapidly decreasing oxidation resistance of $B_2O_3(l)$ (as a consequence of its own vaporization) in the same temperature range.

(b) Measurements of the effect of oxygen pressure on zone melted specimens of ZrB_2 and HfB_2 performed earlier (12) and in the present study (see Table 12) indicate that the k_{pp} for HfB_2 varies directly as the square root of the oxygen partial pressure between 0.4 and 700 torr at about 1700°K. These results and the calculations presented above do not indicate catastrophic low pressure failure for HfB_2. The k_{pp} for ZrB_2 was found (12) to vary directly with oxygen partial pressure at about 1300°K and to be independent of oxygen partial pressure at about 1800°K. Consequently, the experiments and above calculations do not indicate catastrophic low pressure failure of ZrB_2.

(c) The addition of water vapor to the oxidizing gas enhances the rate of oxidation at low temperatures where liquid B_2O_3 would normally be present. This effect is probably due to increased vaporization of B_2O_3 which would protect the diboride. At higher temperatures additions of water vapor appear to have no effect.

(d) The oxidation of ZrB_2 is gas diffusion limited at temperatures near 2100°K at an oxygen partial pressure of 37 torr and a gas flow rate of about 100 cm^3/min (linear velocity of 3 cm/sec.). Hafnium diboride does not exhibit gas diffusion limited oxidation at 2200°K and flow rates of about 100 cm^3/min. Doubling the flow rate at 2100°K did not result in higher values of k_{pp} at 40 torr oxygen pressure.

(e) Oxidation studies on HfB_2 at 1760°K for six hours indicates that the rate remains parabolic over this time period.

(f) The mechanism of oxidation of HfB_2 changes at about 1950°K. This change is probably caused by the phase change in HfO_2 which takes place at this temperature. The oxide which forms below this temperature appears non-columnar while the high temperature oxide appears columnar. The rate constant increases more rapidly with increasing temperature above 2000°K than at low temperatures.

(g) Studies of the effect of stoichiometry on the oxidation resistance of HfB_2 and ZrB_2 indicate that metal rich samples exhibit superior oxidation properties at temperatures up to 2000°K.

(h) Silicon additions have been found to confer added oxidation resistance below 1600°K. However, at higher temperatures this advantage is lost.

(i) Hafnium diboride is more oxidation resistant than ZrB_2 at temperatures up to 2200°K.

(j) Metal rich HfB_2 appears superior to Boride Z over the temperature range investigated.

(k) The total depth of diboride conversion computed from the measured rate constants is in reasonable agreement with that observed metallographically, indicating that the reaction is probably stoichiometric.

Reference to Figures 30, 31, 47 and 48 as well as to Table 13 indicate that the best results obtained thus far correspond to a conversion depth of about 20 mils in one hour at 2200°K. If the diborides are to be seriously considered in this temperature range, one hour conversion depths of 1-10 mils must be achieved. This would require depression of the present k_{pp} values by a factor of 5 to 500. The silicon additions at low temperatures have produced a depression in k_{pp} of about 50 times. Consequently our future efforts will be directed towards varying the silicon levels in order to retain this advantage to higher temperatures.

Additions of Y and Ta have been previously considered as a means of slowing oxygen diffusion through the oxides. However, recent studies at General Telephone (2, 3) have shown that additions of Y to hafnium and zirconium actually increase the oxidation rate. These studies indicate that the diffusion of oxygen through Al_2O_3 proceeds more slowly than the diffusion through ZrO_2 or HfO_2. During the next phase of this study Al additions to the diborides will be investigated.

The preliminary results obtained with vapor deposited $ZrB_{1.85}$ are quite interesting and will be pursued during the next phase of our study.

VII. PHYSICAL PROPERTIES*

A. Introduction

In accordance with the principal objectives of the present program, physical and mechanical property data are of interest for all the diborides up to 1000°C and for ZrB_2 and HfB_2 up to 1500°C and possibly to higher temperatures where feasible. The previous report (1) contains linear thermal expansion data (25°-1000°C), X-ray thermal expansion data (800°-1500°C), electrical resistivity data (25°-1050°C), and hot hardness data (25°-1050°C); these results were obtained on the then available well characterized specimens. The present report contains new experimental results on the electrical resistivity of polycrystalline ZrB_2 (25°-1400°C) and polycrystalline HfB_2 (25°-1500°C). In addition, thermal conductivity and emissivity results obtained on polycrystalline materials prepared and characterized in this program are presented; these measurements were performed in the temperature range from 1173° to 2242°K for dense specimens of TiB_2, ZrB_2, HfB_2, and NbB_2.

B. Thermal Conductivity**

One of the problems associated with measuring high temperature thermal conductivity is that it is difficult to obtain specimens which do not crack and break apart during the thermal treatment associated with the experimental procedure. During this phase of the investigation dense, homogenous materials were fabricated; these materials provided test specimens which remained intact throughout the experimental procedure.

The experimental procedure described below provides data from which the thermal conductivity can be calculated. In practice this technique requires an independent measure of the total emissivity of the sample material. In this investigation, the latter was obtained from the experimentally determined time-temperature cooling data and the high temperature heat capacity data presented in the previous compilation (1).

1. Experimental Procedure

Short, cylindrical specimens of the diborides were induction heated in a vacuum furnace. The equipment was operated so as to confine the heating to the cylindrical surface of the specimen.

During steady state conditions, assuming that the cylindrical surface is isothermal, heat flows radially inward by conduction and then radiates away from the ends of the specimen. By setting the conductive heat flow equal to the radiative heat loss, Hoch, et. al. (23) developed Eq. (1) which relates the thermal conductivity, K, and

$$K = \frac{\epsilon \sigma T_o^4 \alpha L}{4\Delta T L K_o + 2\pi K_o \alpha \Delta T} \qquad (1)$$

*E. V. Clougherty and R. L. Pober, ManLabs, Inc., Cambridge, Mass.

**Taken in part from a report submitted by M. Hoch, University of Cincinnati and presented at a recent symposium (22).

ϵ, the total emissivity; σ, the Stefan-Boltzman radiation constant; T_o, the temperature (°K) at the center of the end surface; a, the radius (cm) of the specimen at the end surface; L, half the height (cm) of the specimen; ΔT, the temperature difference (°K) between the center and the edge of the end surface; and K_o and K_o', constants defined by the length to diameter ratio of the specimen. Temperatures were measured with an optical pyrometer and dimensions were measured by conventional methods. Total emissivity was determined by another experimental technique in which the specimen was heated in vacuum to the maximum desired temperature and then allowed to cool by radiation. During cooling, the time-temperature relationship was automatically recorded. By equating the radiative heat loss to the enthalpy change of the specimen and solving for total emissivity, ϵ, Hoch and Narasimhamurty (24) derived Eq. (2) which relates the differential cooling term, $\frac{d(T^{-3})}{dt}$; C_P, the specific heat (cal/gram °K) at T°K,

$$\frac{C_P}{\epsilon} \quad \frac{d(T^{-3})}{dt} = \frac{3\ \sigma A}{m} \tag{2}$$

ϵ, the total emissivity; t, time (sec.); A, area (cm^2) of the specimen; and m, the mass (gram) of the sample. The area and mass of the specimen were measured by conventional methods. Temperature and time were obtained from the cooling data. Specific heat was obtained from previously reported results (1).

2. Characterization of Specimens

All the thermal conductivity measurements reported herein were performed on polycrystalline specimens fabricated by high pressure hot pressing. The available single crystal material (NbB_2, ZrB_2, and HfB_2) did not remain intact during the measurement. The characterization data provided for the specimens in Table 15 and Figures 61 through 64 include: (1) The pycnometric density measured on the fabricated bars and percentage of the powder density obtained directly from the measured powder densities of HfB_2(2) and ZrB_2(1) as given in Section III and TiB_2 as measured in another study (7) and NbB_2 as estimated from Figure 64. (2) The metallographic analyses before and after thermal conductivity measurement. The former were obtained on samples of the same bar from which the test specimens were prepared; the latter were obtained directly from the test specimens. The percentage porosity and the amount of the second phase were determined by point counting techniques for TiB_2, ZrB_2, and HfB_2 and by visual estimation for NbB_2. The fine grain structure of the NbB_2 specimen and the extremely fine porosity significantly reduce the accuracy of the point counting techniques. The grain size data were obtained by lineal analysis. (3) The chemical analyses tabulated under "before" were obtained on the starting powders; the detailed results are presented in Section III and in a previous report (1). The analyses tabulated under "after" were obtained on the test specimens. Additional analytical results comparing as received powders and fabricated bars are presented in the Appendix.

TABLE 15

CHARACTERIZATION* OF THERMAL CONDUCTIVITY SPECIMENS

Material	TiB_2		ZrB_2		HfB_2		NbB_2	
Characterization No.	75		7		28		5	
Geometric								
Mass (gram)	0.5010		0.5552		1.1094		0.5735	
Radius (cm)	0.4521		0.4480		0.4276		0.4360	
Height (cm)	0.1905		0.1480		0.1852		0.158	
Area (cm^2)	1.8245		1.7098		1.6456		1.6359	
Densitometry								
Density (g/cc.)	4.30		5.92		10.4		6.47	
% Powder Density	95		99		100		(99)	
Metallographic	Before	After	Before	After	Before	After	Before	After
% Porosity	5.5	5.4	0.5	0.5	0.5		(1)	(1)
% Second Phase	none	none	2	2	7	10	(9)	(9)
Grain Size (μ)	13	19	6	15	25	50	fine	fine
Figure No.	61		62		63		64	
Chemical								
B	31.0	30.6	18.1	17.5	11.2	--	18.6	18.1
Me	68.7	67.5	80.7	79.9	87.3	86.7	80.7	81.5
B/Me	1.98	2.00	1.89	1.84	2.12	--	1.98	1.90

*Qualitative spectroscopic analyses for metallic impurities of all materials after completion of the measurements showed no significant contamination.

Etched X500
Etchant: Modified Aqua Regia
High Pressure Hot Pressed, R-75
Fabricated from U.S. Borax TiB_2(1).

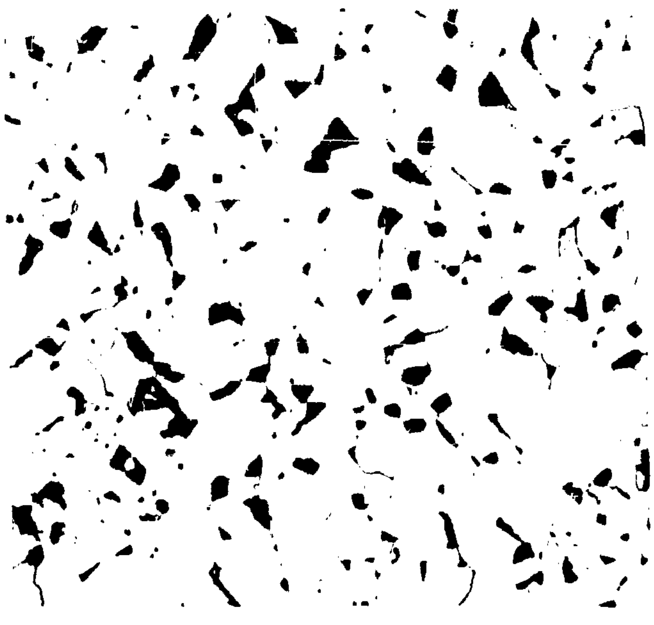

Etched X500
Etchant: Modified Aqua Regia
Thermal Conductivity Specimen After
Measurement.

Figure 61 - Titanium Diboride Thermal Conductivity Material.

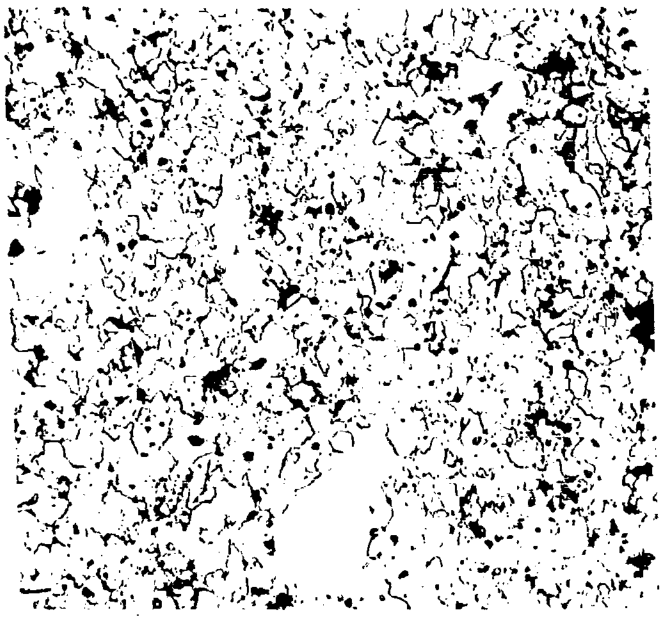

Etched X500
Etchant: Modified Aqua Regia
High Pressure Hot Pressed, R-7
Fabricated from U.S. Borax ZrB_2(1).

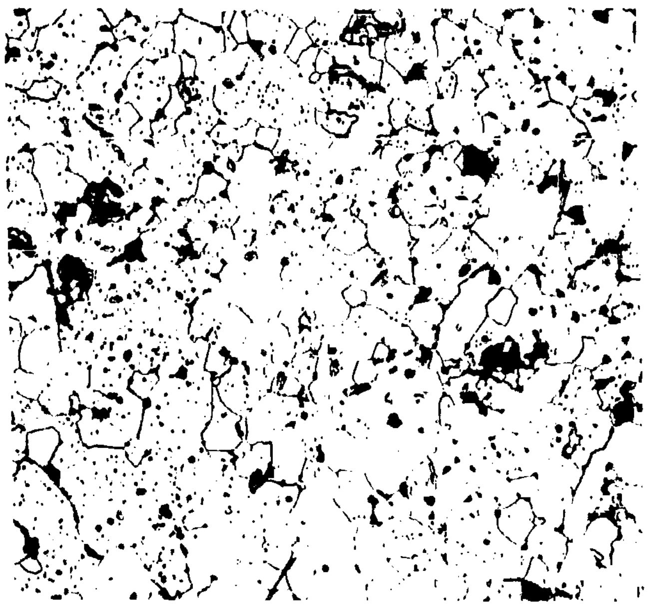

Etched X500
Etchant: Modified Aqua Regia
Thermal Conductivity Specimen After
Measurement.

Figure 62 - Zirconium Diboride Thermal Conductivity Material.

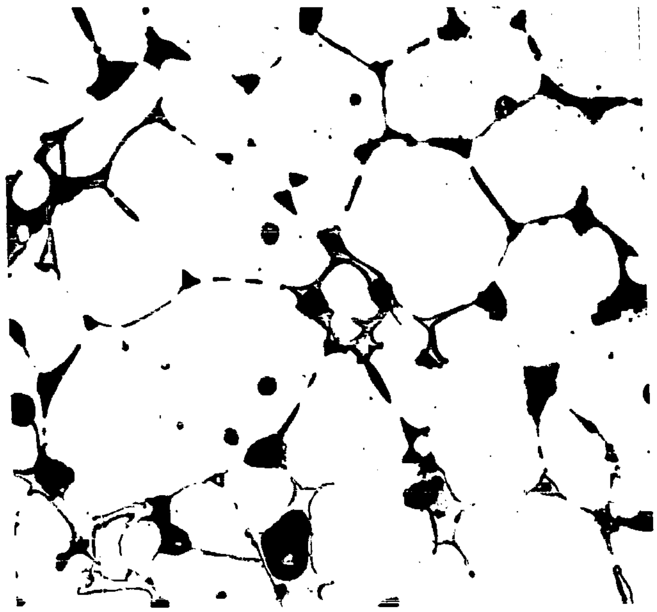

Etched X500
Etchant: Modified Aqua Regia
High Pressure Hot Pressed, R-28
Fabricated from Wah Chang HfB_2(2).

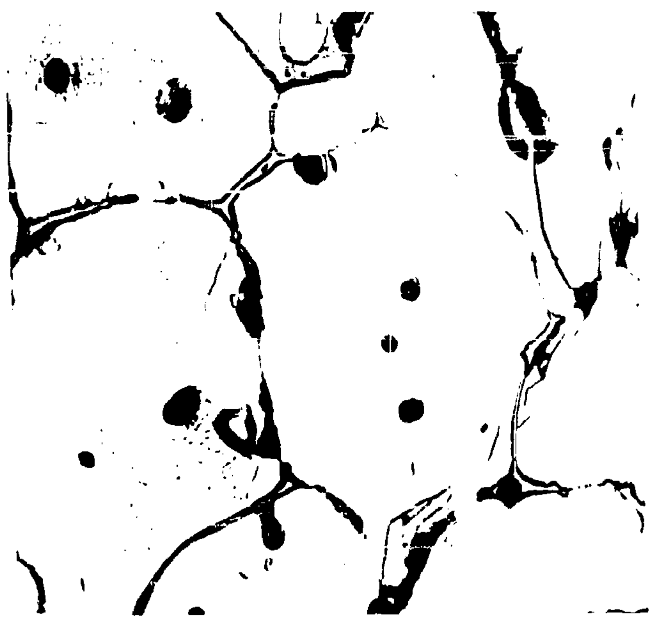

Etched X500
Etchant: Modified Aqua Regia
Thermal Conductivity Specimen After
Measurement.

Figure 63 - Hafnium Diboride Thermal Conductivity Material.

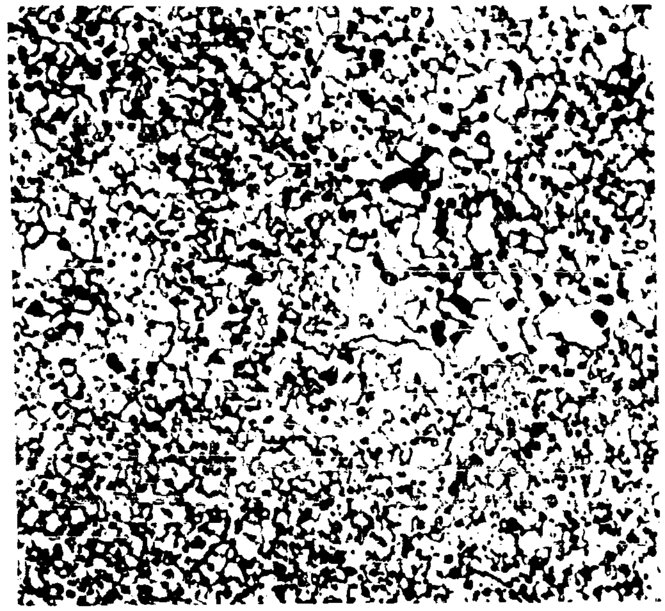

Etched X1500
Etchant: Modified Aqua Regia
High Pressure Hot Pressed, R-5
Fabricated from U.S. Borax NbB_2(2).

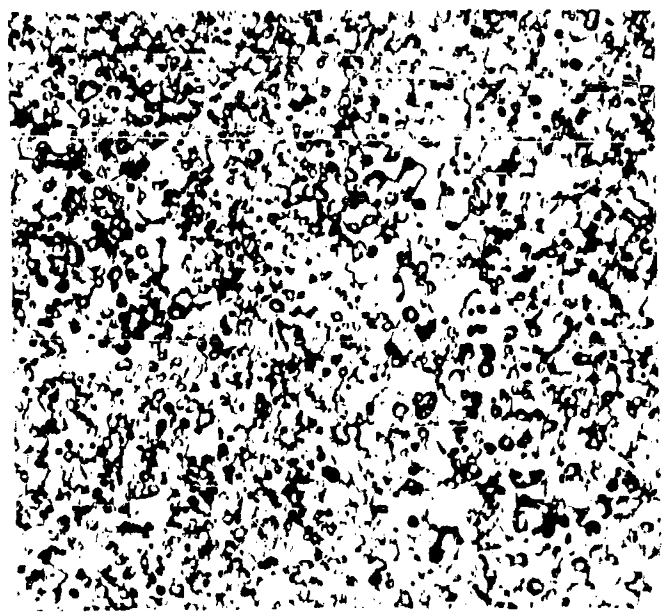

Etched X1500
Etchant: 25 cc Lactic Acid, 5 cc HNO_3, 5 cc HCL, 0.25 cc Hf
Thermal Conductivity Specimen After Measurement.

Figure 64 - Niobium Diboride Thermal Conductivity Material.

Inspection of the specimens after completion of the measurements revealed crack-free surfaces on the TiB_2 and the HfB_2; small circumferential cracks were observed on the surface of the ZrB_2 near the outer edges; and radial cracks were observed on the face of the NbB_2.

3. Results

The measured quantities were converted to total emissivity and thermal conductivity; the results are expressed as a linear function of temperature in Table 16. The slopes and intercepts were determined by the method of least squares; the report limits are probable errors.

TABLE 16

THERMAL CONDUCTIVITY* AND TOTAL EMISSIVITY* OF POLYCRYSTALLINE TiB_2, ZrB_2, HfB_2, AND NbB_2

Material	Temp.Range (°K)	Thermal Conductivity (cal/sec.cm.°K)	Total Emissivity Range†
TiB_2	1268-1886	$(8.34 \pm 0.77)\ 10^{-5}T$	0.461-0.495
ZrB_2	1173-1905	$(-1.15 \pm 0.11)\ 10^{-2}$ $+(8.24 \mp 0.53)\ 10^{-5}T$	0.533-0.588
HfB_2	1375-1896	$(-2.32 \pm 0.07)\ 10^{-2}$ $+(7.73 \mp 0.38)\ 10^{-5}T$	0.328-0.349
NbB_2	1263-2242	$(1.51 \pm 0.08)\ 10^{-2}$ $+(2.00 \mp 0.33)\ 10^{-5}T$	0.199-0.226

* Raw data uncorrected for porosity and/or second phase.
† Emissivity range increases linearly from the lower temperature to the higher.

A comparison of the present results with data available in the literature must take into account the variation of thermal conductivity with the physical state of aggregation of the matrix material and the presence of extraneous phases. The thermal conductivity decreases approximately linearly with porosity as long as the solid phase is continuous. Thus, for a first approximation, data can be corrected for porosity by assuming that heat transfer by radiation across pore volumes is negligible compared to heat transfer through the solid matrix by conduction. The correction for the amount and the distribution of the second phase material is a more difficult task but since heat transfer will proceed by conduction across the second phase, this correction is second order and can be neglected. The effect of grain size has not been thoroughly investigated for ceramic type materials; virtually no data of this type are available for the diborides.

The thermal conductivity of TiB_2, ZrB_2, and HfB_2 was measured at elevated temperatures at Southern Research Institute (25). The measurements were made with an absolute radial heat flow device; the specimens were heated in carbon tube furnace. Some characterization data are presented for typical sample material; examination after measurements showed numerous cracks in all specimens. Additional data for TiB_2 were reported by Mandorf (26) in the range 800°-$1400^{\circ}C$. Other results have been reported (27, 28) at much lower temperatures. The results of the present investigation are shown graphically in Figure 65 along with the above high temperature data.

In order to discuss the significance of the combined results in Figure 65 it is important to note that higher purity starting materials were used in the present investigation than in either of the above studies and that the specimens were essentially unchanged physically and chemically after completion of the measurements. Accordingly the data reported herein as measured by Professor Hoch at the University of Cincinnati are considered representative of the pure dense diborides.

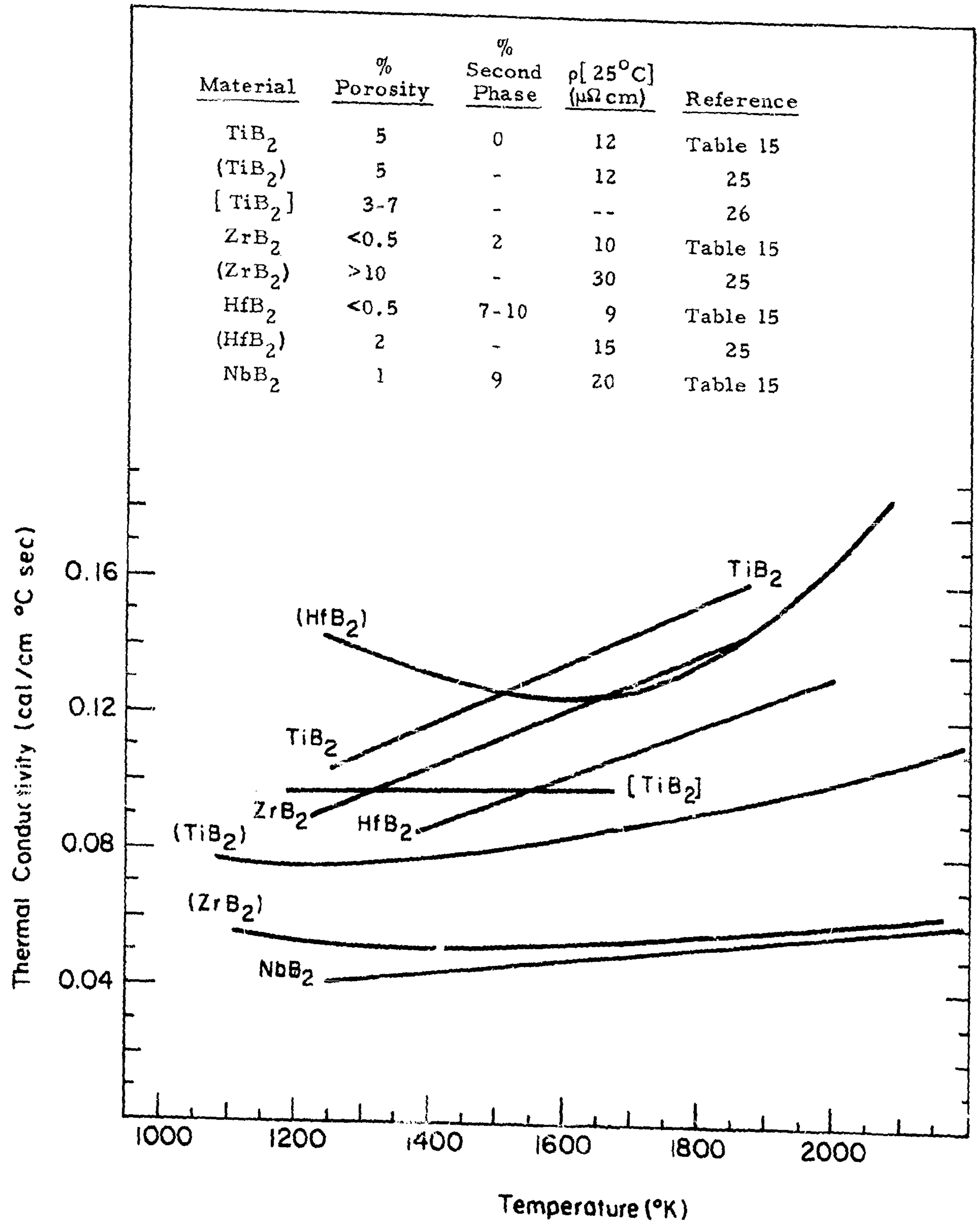

Material	% Porosity	% Second Phase	ρ[25°C] ($\mu\Omega$ cm)	Reference
TiB_2	5	0	12	Table 15
(TiB_2)	5	-	12	25
[TiB_2]	3-7	-	--	26
ZrB_2	<0.5	2	10	Table 15
(ZrB_2)	>10	-	30	25
HfB_2	<0.5	7-10	9	Table 15
(HfB_2)	2	-	15	25
NbB_2	1	9	20	Table 15

Figure 65. Variation of Thermal Conductivity of Polycrystalline Diborides with Temperature.

C. Electrical Resistivity

The primary purpose of the present investigation was to obtain reliable data on the variation of the resistivity of HfB_2 and ZrB_2 up to 1500°C. The previous report (1) contains a discussion of the technique for measuring resistivity as a function of temperature for brittle, metallic alloys and compounds. The variation of the room temperature resistivity of all the diborides of interest with porosity and the variation of the resistivity of TiB_2, ZrB_2, and HfB_2 with temperature to 1050°C were measured and reported. In this investigation the resistivity measurements were extended to 1400°C for ZrB_2 and to 1500°C for HfB_2. The experimental procedure is very similar to that previously used except that (1) the housing material in the specimen holder was changed from boron nitride to tantalum and (2) alumina discs were employed to insulate the leads from the metallic housing. In the course of the development of the techniques which lead to the extension of the upper temperature limit to 1500°C, several sets of measurements were performed on specimens of ZrB_2 and HfB_2 with different characteristics. These data combined with results in the literature provide a reasonably complete description of the variation of the resistivity of ZrB_2 and HfB_2 and to a lesser extent of TiB_2 with temperature and physical structure.

1. Experimental Procedures

The development of a technique suitable for measuring the resistivity of brittle intermetallic compounds with electrical properties similar to metals was presented in the first technical report (1). In this investigation the components of the measureing apparatus were changed to provide higher temperature capability. In particular, the boron nitride housing (see Figure 51 in Reference 1) which supports the specimen was replaced by a tantalum housing and alumina discs were used to insulate the specimen from the housing. The sample was heated in a platinum tube furnace in a gas tight alumina tube under a positive pressure of dry argon. Contact resistance commenced in the vicinity of 1500°C and prohibited measurements at higher temperatures.

2. Sample Characterization

The available characterization data pertaining to specimens for which the resistivity has been measured at elevated temperatures is summarized in Table 17 along with the measured temperature coefficients of resistivity. The density of each bar was measured and percentage porosity was calculated from the known powder density. Since it was known that the fabricating conditions do not introduce significant contamination (see Section IV and VI, and the Appendix) only selected samples were examined metallographically (Figures 66 and 67) and a limited number of chemical and spectroscopic analyses were obtained. The room temperature resistivity is a sensitive measure of porosity of a specimen which is known to be principally single phase material.

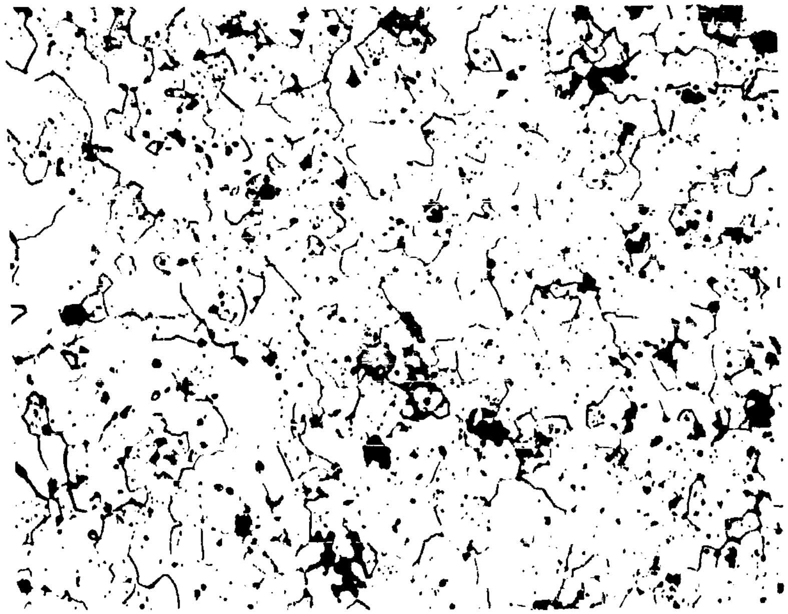

Etched X500

Etchant: Modified Aqua Regia

High Pressure Hot Pressed
Fabricated from $ZrB_2(1)$, $B/Zr = 1.89$
Run 31, d = 6.01 g/cc., $\rho\,[25^{\circ}C] = 7.9\mu\Omega$ cm

Figure 66. Zirconium Diboride Resistivity Specimen

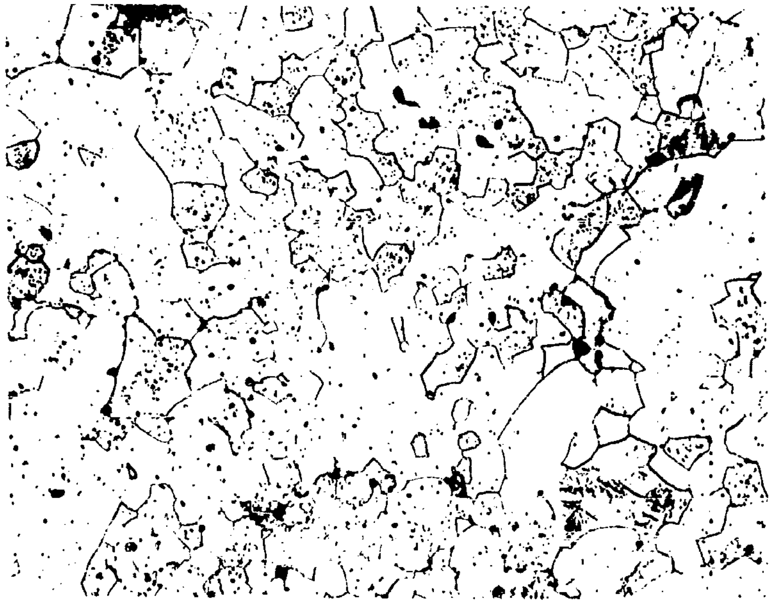

Etched X500

Etchant: Modified Aqua Regia

High Pressure Hot Pressed
Fabricated from HfB_2(2A), B/Hf = 1.88
Run 47, d = 10.70 g/cc., ρ[25°C] = 10.3 $\mu\Omega$ cm

Figure 67. Hafnium Diboride Resistivity Specimen

TABLE 17

SPECIMEN CHARACTERIZATION AND RESISTIVITY RESULTS

Material	B/Me	Origin*	Density (g/cc.)	% Porosity	% Second Phase	$\rho[25^oC]$ ($\mu\Omega$ m)	$\alpha . 10^3 = \frac{\Delta\rho}{\rho[25^oC]\,\Delta T}$ ($^oC^{-1}$) 10^3	$\Delta\rho\,\Delta T\,10^2$ ($\mu\Omega$ cm/^oC)	Miscellaneous Remarks
TiB_2	1.98	H.p.h.p. (R-46)	4.35	5	0	11.9	4.76	5.7	Ref. 1
	--	H.P. (N.C.)	--	20	0	20	2.5	5.0	Ref. 26
	--	H.P. (S.R.I.)	--	3	0	10	4.5	4.5	Ref. 25
ZrB_2	--	H.P. (S.R.I.)	--	>10	-	30	1.5	4.5	Ref. 25
	1.89	H.p.h.p. (R-12)	6.00	< 0.5	2	10.3	3.8	3.9	
	1.89	H.p.h.p. (R-31)	6.01	< 0.5	2	7.9	4.5	3.6	Figure 66
	1.99	Zone Refined	--	0	< 0.5	5.0	6.3	3.2	Ref. 1
HfB_2	1.88	H.p.h.p. (R-53)	9.80	9	-	17.9	5.0	8.9	
	1.97	H.p.h.p. (R-6)	9.58	10	-	18.3	4.2	7.6	Ref. 1
	1.88	H.p.h.p. (R-47)	10.70	0.5	2	10.3	4.8	4.9	Figure 67
	2.12	H.p.h.p. (R-50)	10.39	0.5	7	9.0	4.8	5.3	Qual. Spec.: No Contamination
	--	H.P. (S.R.I.)	--	2	-	10	4.5	4.5	Ref. 25

* The letters H.p.h.p. indicate high pressure hot pressing as carried out at ManLabs; H.P., conventional hot pressing. The numbers in the parentheses are sample identification numbers and the letters S.R.I. and N.C. refer to Southern Research Institute and National Carbon Co., respectively.

3. Results

The resistivity for several different samples of ZrB_2 and HfB_2 is shown graphically as a function of temperature in Figures 68 and 69. The new high temperature results are shown explicitly. The ZrB_2 data in Figure 68 are representative of dense zone refined, dense polycrystalline and porous polycrystalline specimens. The data for HfB_2 in Figure 69 are representative of dense and porous polycrystalline specimens. All measurements indicate that the resistivity is a linear function of temperature. This type of data is generally expressed by a linear coefficient of resistivity defined as

$$\alpha = \frac{1}{\rho[25^{o}C]} \frac{\Delta \rho}{\Delta T} \qquad (3)$$

In addition the differential quantity $\Delta \rho / \Delta T$ was also tabulated. The latter is less sensitive to the physical state of aggregation, i.e., porosity, grain boundary precipitates, cracks, etc., and should be more characteristic of the matrix material. Available data from the literature also indicate linear behavior; these linear coefficients are also provided in Table 17. The combined results for the dense materials i.e., with five per cent or less porosity, indicate that both α and $\Delta \rho / \Delta T$ are the same within experimental error for TiB_2, ZrB_2, and HfB_2.

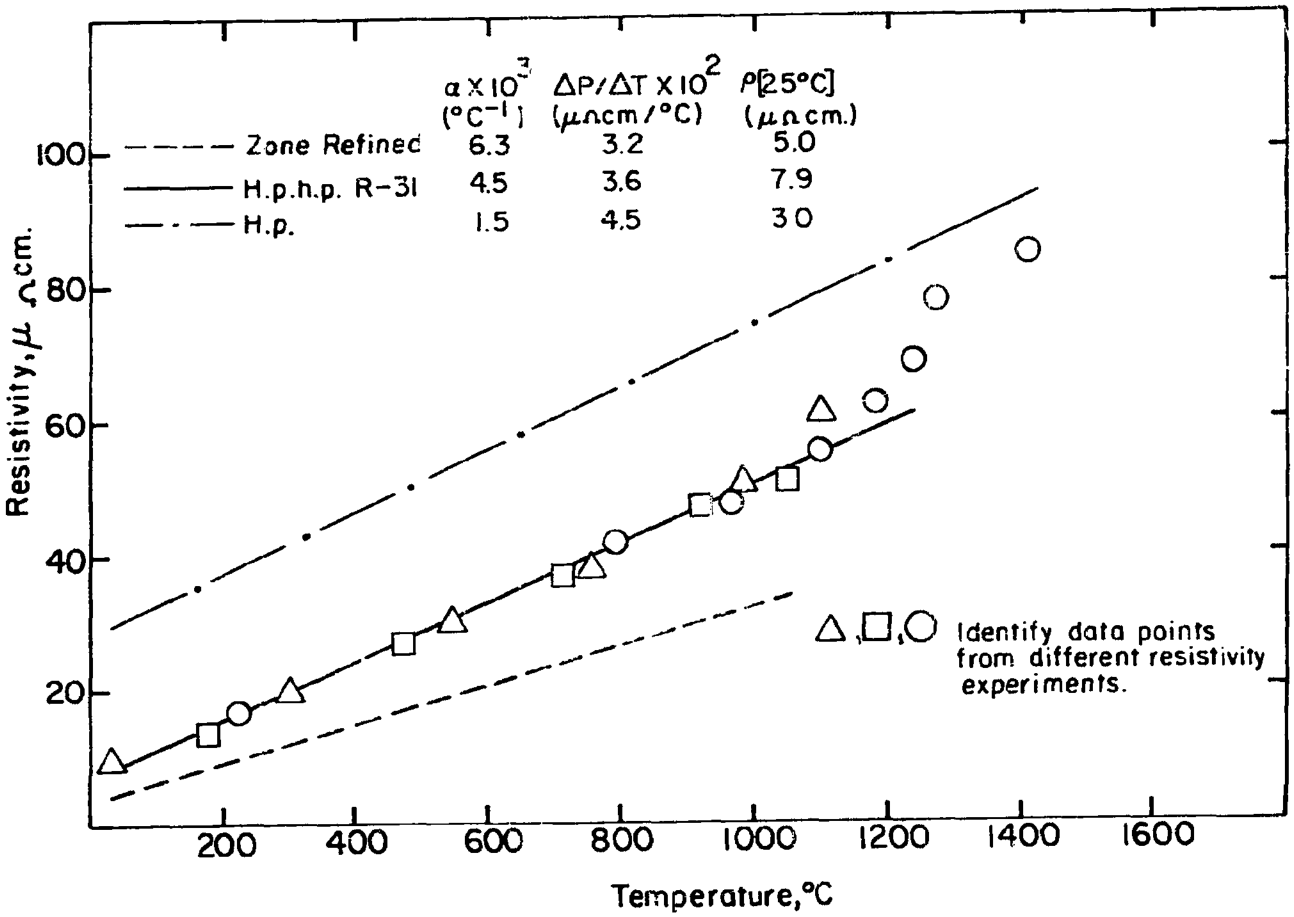

Figure 68. Resistivity of Zone Refined, Dense Polycrystalline, and Porous Polycrystalline Zirconium Diboride as a Function of Temperature.

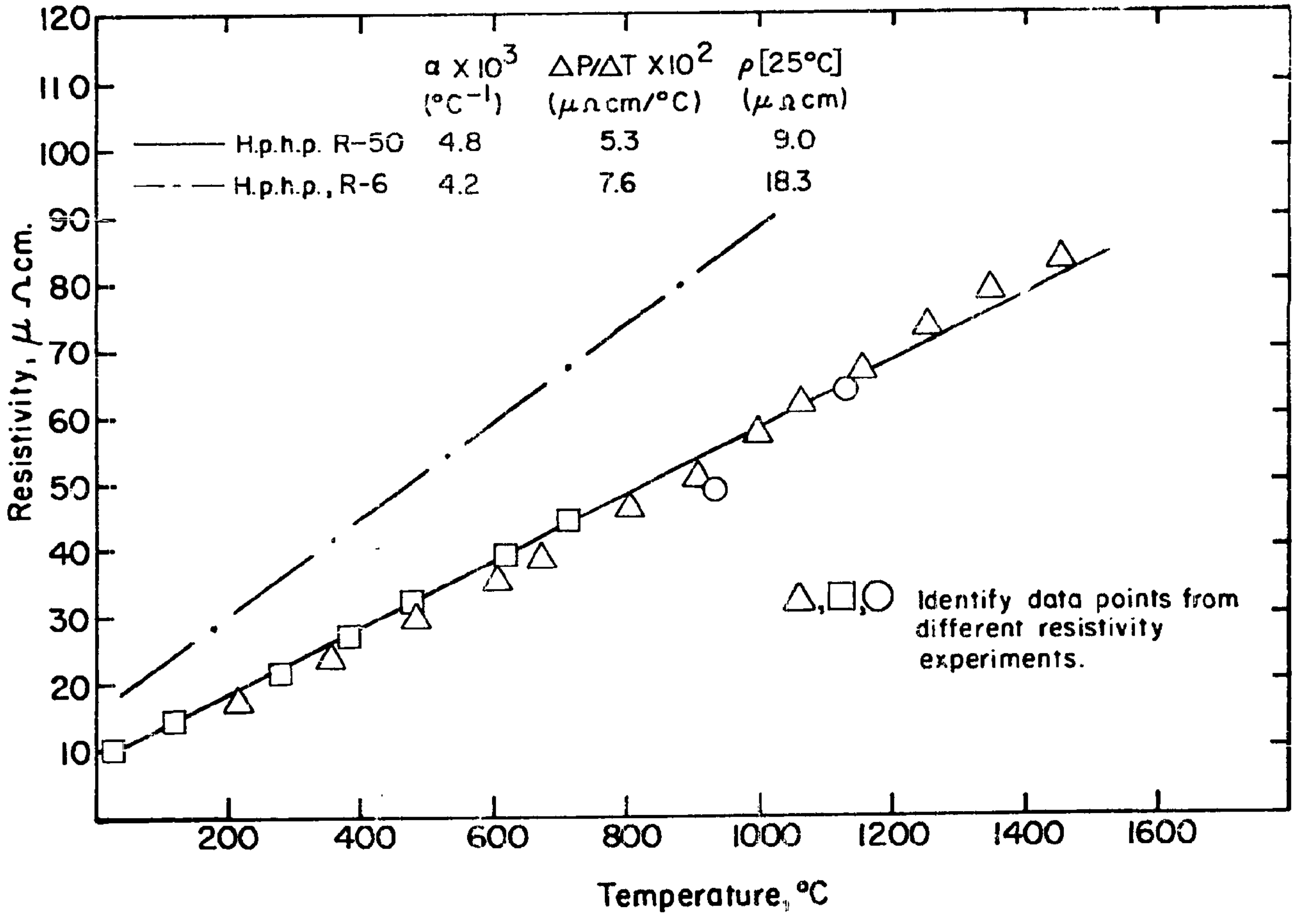

Figure 69. Resistivity of Dense and Porous Polycrystalline Hafnium Diboride as a Function of Temperature.

VIII. PHASE EQUILIBRIA*

A. Introduction

The original purpose of the phase equilibria investigation was to determine the range of stability of the single phase diborides of titanium, zirconium, hafnium, niobium, and tantalum. Zone refined diborides were considered as ideal specimen materials because it was anticipated that phase equilibria data obtained from such high purity material would be truly representative of the binary system. Satisfactory samples of TiB_2 and TaB_2 could not however be produced by the zone refining technique. Diffusion couples were prepared with a metal/diboride interface to examine the metal rich side of stoichiometry for ZrB_2; the poor mechanical properties of NbB_2 and the non-availability of zirconium-free hafnium metal prohibited the study of phase boundaries in the Hf-B and Nb-B systems by this technique. An early attempt to circumvent the materials problem as regards the diboride involved the preparation of a metal/boron diffusion couple. High purity Ti, Zr (Hf-free), Nb, and Ta and zone refined B were available and it was anticipated that this technique would provide additional information about these metal-boron systems. Unfortunately, the relatively high vapor pressure of elemental boron lead to the development of a vapor deposited metal diboride on the surface of the metal. The intermediate phases did not form. Quantitative data were obtained for Zr/ZrB_2 diffusion couples at 1000° and 1400°C; the metal rich boundaries at these temperatures are at a B/Me = 1.99 and 1.97 respectively. The zone refining subtask also provided some high purity two phase material with B/Me ratios slightly less than, and slightly greater than, 2.00. Quantitative data in the boron rich boundary of ZrB_2 was obtained by equilibration of two phase boron rich ZrB_2 at 1730°C; this boundary is at a B/Me = 2.02.

This report contains calculated phase diagrams for the Hf-B and the Zr-B systems. These calculated diagrams are based on the thermodynamic description of the diboride phase (1, 29) and the previously developed techniques (30) which have proved satisfactory for the Ti-C, Zr-C, and Ta-C systems. The limits of the diboride phase calculated herein are based on a more realistic model than those previously reported.(1)

Experimental techniques have been employed to define the metal rich and the boron rich boundaries of ZrB_2 and HfB_2 and to provide new data on the solidities of the metal - "metal rich boride" and the "metal rich boride"-metal rich diboride in the Zr-B and Hf-B systems. The materials used for equilibration experiments included (1) Arc-melted mixtures with B/Me = 1.5 and 6.0, (2) Cold pressed compacts of Me + B with compositions of B/Me < 1.0, (3) Two phase zone refined alloys in the Zr-B system and (4) High pressure hot pressed specimens fabricated from as-received powder, ZrB_2(1) with Zr added to adjust the B/Me = 1.5.

---

* E. V. Clougherty, R. L. Pober, and L. Kaufman, ManLabs, Inc., Cambridge, Mass.

B. Calculation of Phase Diagrams

Binary Zr - B and Hf - B phase diagrams have been computed using the thermodynamic description of the diboride phases generated previously (1, 29) and the techniques previously utilized in computing binary Ti-C, Zr-C, and Ta-C phase diagrams (30). As in the latter cases, the computations are not intended as a replacement for experimental observation but rather as a guide for meaningful experimentation and a vehicle for correlating thermodynamic information with phase equilibria. The results of the computations are given in Figures 70 through 73. Details of the calculation are given below.

1. Computation of Diboride/Liquid Equilibria

In line with the carbide calculations(30), it is assumed that the diboride phase melts congruently at stoichiometry and that the liquid phase can be approximated by a regular solution. Thus the free energy of the liquid phase F^L is approximated by

$$F^L = (1-x)F_{Me}^L + x\,F_B^L + Lx(1-x) + RT[x\ln x + (1-x)\ln(1-x)] \qquad (1)$$

Since the free energy of the diboride phase at stoichiometry is defined as

$$F^{\eta}[\tfrac{2}{3}, T] = \tfrac{1}{3}\,F_{Me}^{o} + \tfrac{2}{3}\,F_B^{o} + \Delta F^{\eta}[\tfrac{2}{3}, T] \qquad (2)$$

and the liquid forms of metal and boron are stable at the melting point of the diboride phase,

$$L = 4.5\,(\Delta F^{\eta}[\tfrac{2}{3}, \overline{T}^{\eta}] + \tfrac{1}{3}RT\ln 6.75) \qquad (3)$$

where $\overline{T}^{\eta}$ is the melting point and $\Delta F^{\eta}[\frac{2}{3}, \overline{T}^{\eta}]$ is the free energy of formation (per gram atom) of the stoichiometric diboride.

Values of $\Delta F^{\eta}[\frac{2}{3}, T]$ are given in Table 61 of reference 1 thus L = -51.8 k cal/g.at for Zr-B and -47.0 k cal/g. at. for Hf-B. Thus the free energy of the liquid phase can be specified as an explicit function of temperature and composition (subject to the errors introduced by the regular solution approximation).

The next step is the location of the $L/(L+\eta)$ boundary, $x_{L\eta}$, in equilibrium with metal rich diboride at the $(L+\eta)/\eta$ boundary (i. e. $x_{\eta L}$). Similarly, the boron rich boundary $\overline{x}_{\eta L}$ and the corresponding liquid composition $\overline{x}_{L\eta}$ must be computed.* This procedure is performed by equilibrating partial molar free energies as follows:

---

* The symbolism $x_{L\eta}$, $\overline{x}_{L\eta}$, $x_{\eta L}$ and $\overline{x}_{\eta L}$ is used(30) merely to distinguish between metal rich (without bars) and boron rich (with bars) compositions in η/L equilibrium.

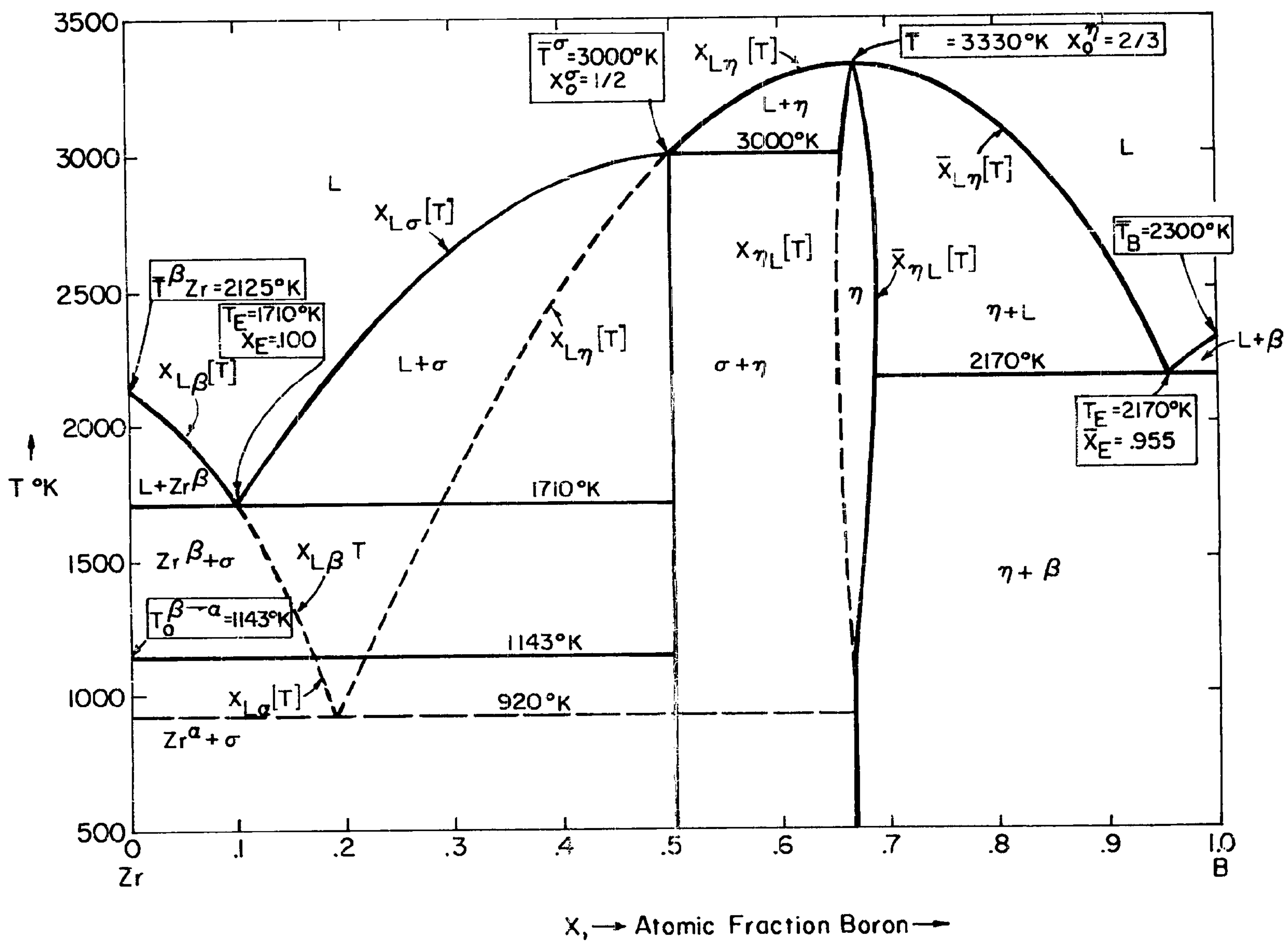

Figure 70. Calculated Zr-B Phase Diagram.

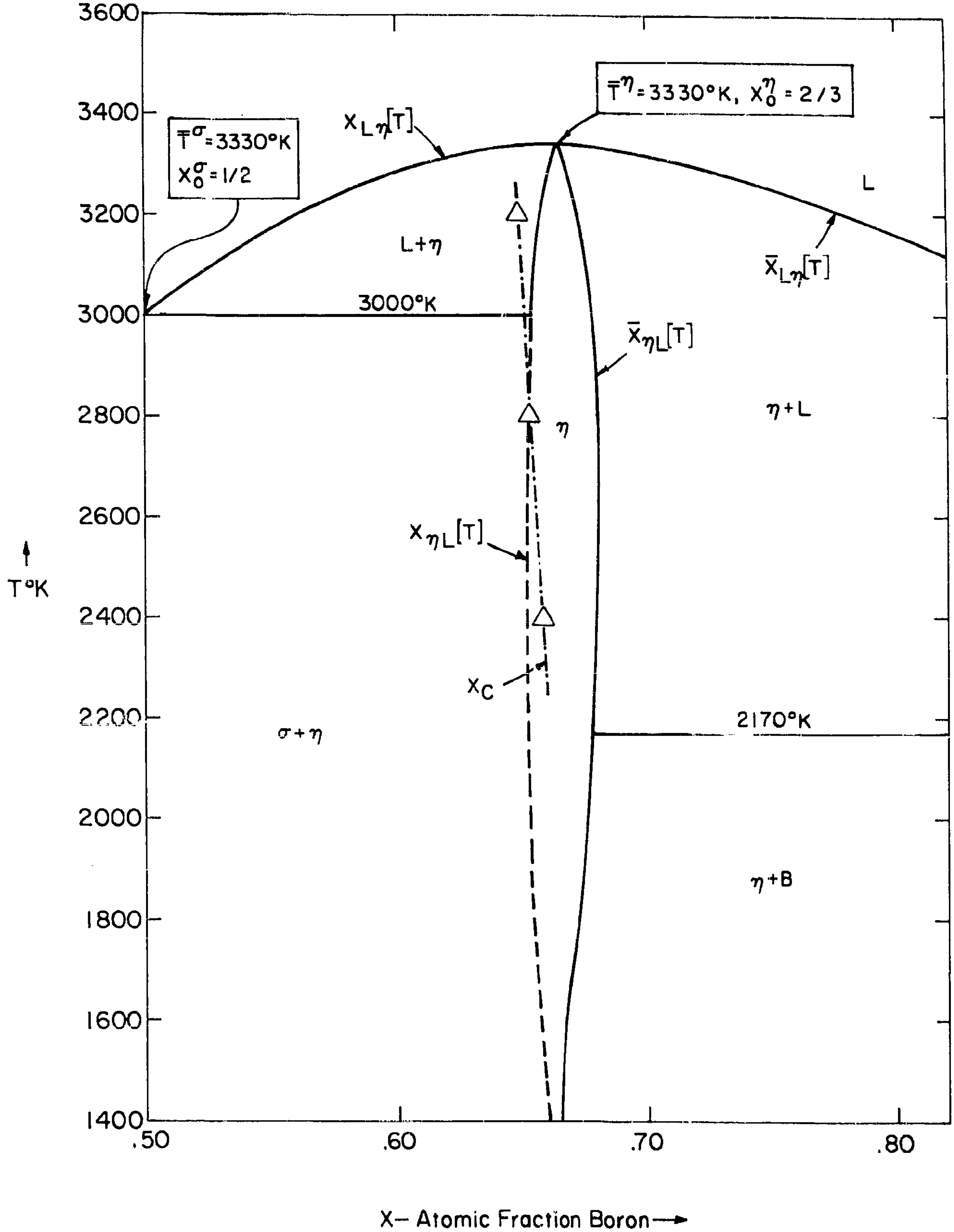

Figure 71. Calculated "ZrB_2" Phase Field.

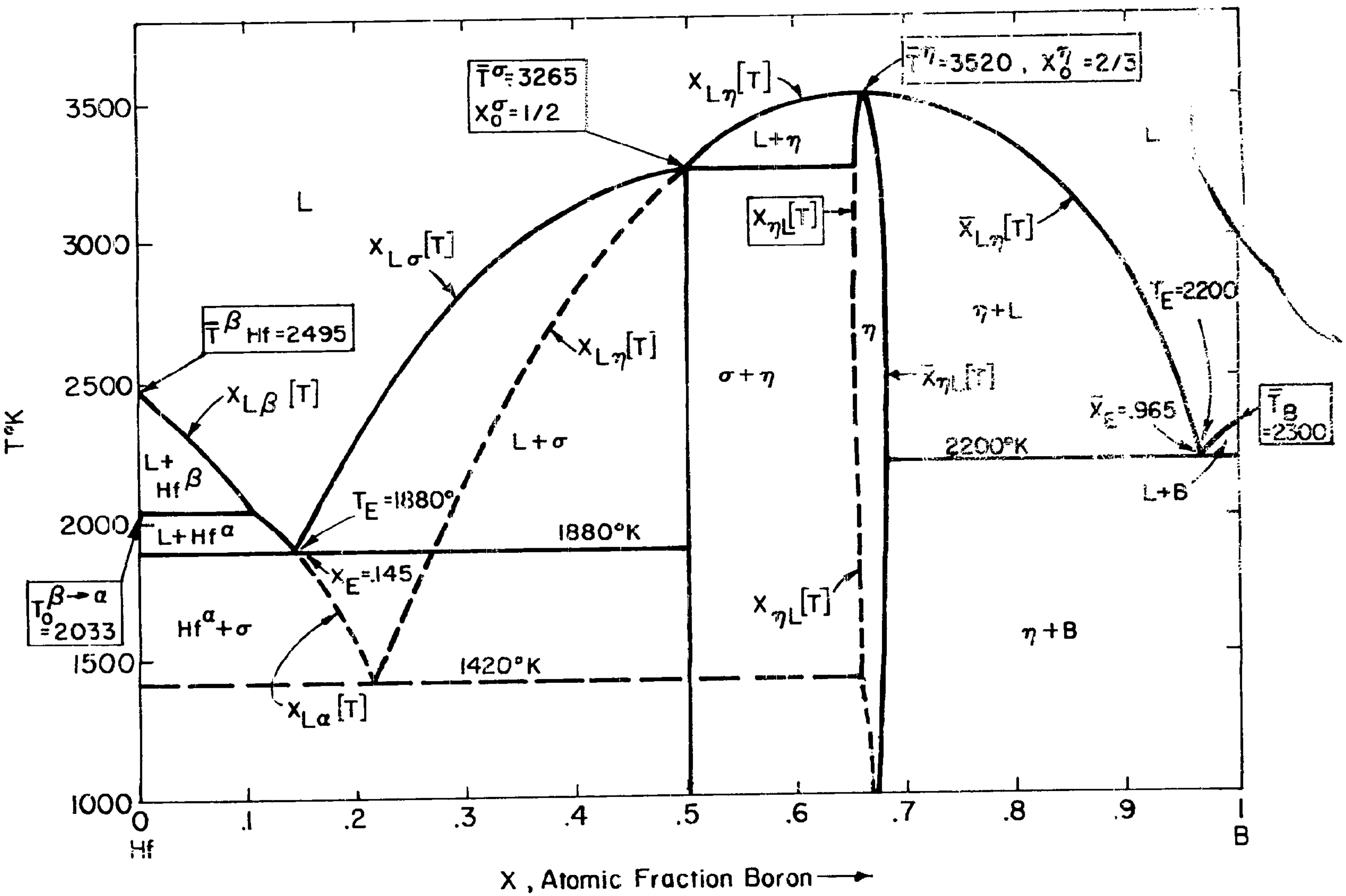

Figure 72. Calculated Hf-B Phase Diagram.

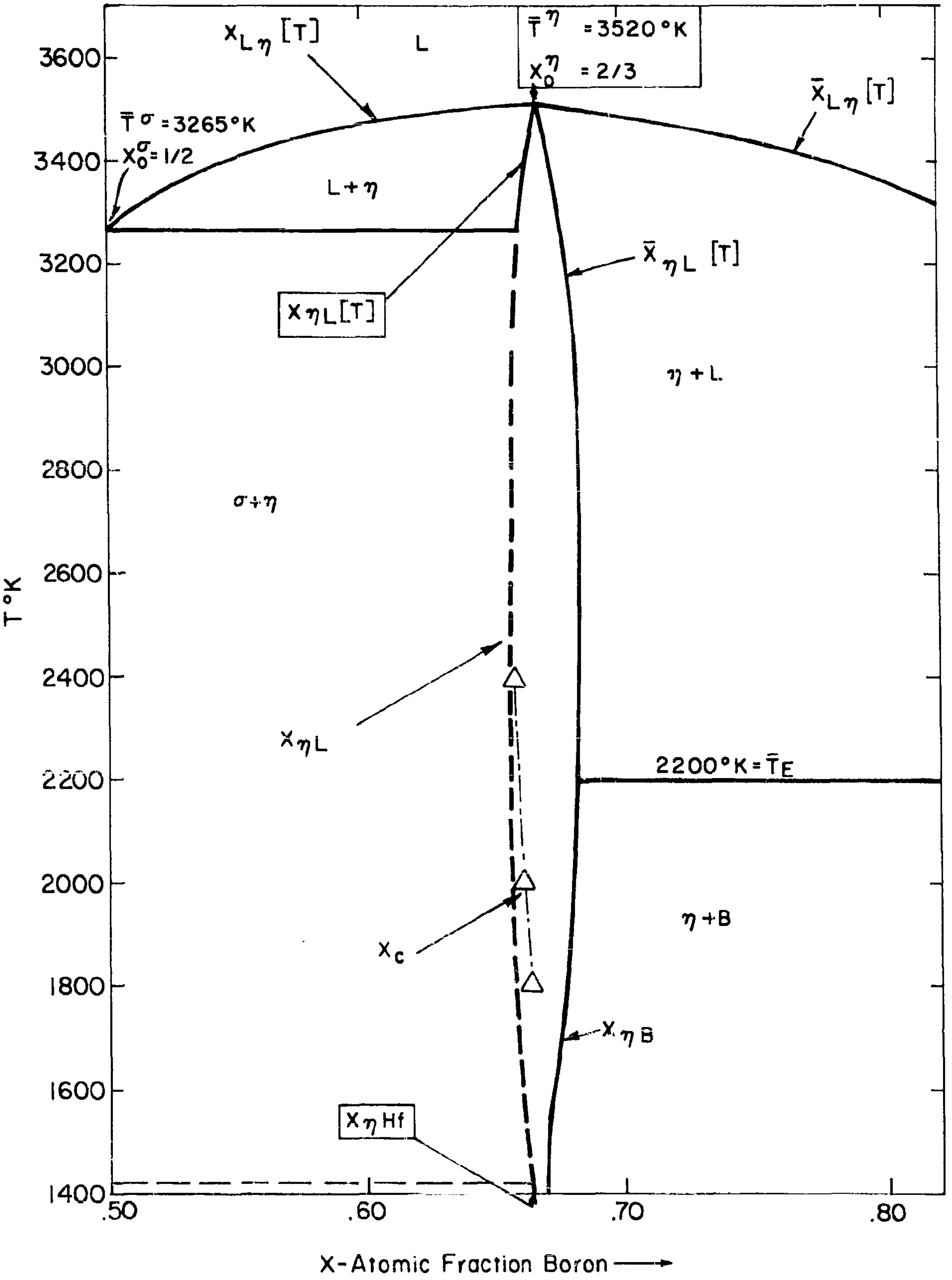

Figure 73. Calculated "HfB_2" Phase Field.

$$\bar{F}^{L}_{Me}\Big|\, x_{L\eta} = \bar{F}^{\eta}_{Me}\Big|\, x_{\eta L} \tag{4}$$

and

$$\bar{F}^{L}_{B}\Big|\, x_{L\eta} = \bar{F}^{\eta}_{B}\Big|\, x_{\eta L} \tag{5}$$

Since the partial molar free energies of Me and B in the liquid phase are defined by Eq. (1) and the corresponding diboride partials have been defined earlier (1, 29) Eqs. (4) and (5) yield

$$F^{L}_{Me} + L\, x^{2}_{L\eta} + RT \ln (1-x_{L\eta}) = F^{o}_{Me} - F_{Me+} + RT \ln (2-3x_{\eta L})^{2}\, 27^{-1} \alpha^{-3} (1-x_{\eta L})^{-2} \tag{6}$$

and

$$F^{L}_{B} + L(1-x_{L\eta})^{2} + RT \ln x_{L\eta} = F^{o}_{B} - F_{B+} + RT \ln x_{\eta L} (2-3x_{\eta L})^{-1} \tag{7}$$

where F_{Me+} and F_{B+} refer to the free energies of metal and boron vacancies in the diboride phases. Since all of the quantities in Eqs. (6) and (7) are known, (1, 29) with the exception of $x_{L\eta}$ and $x_{\eta L}$, these phase boundary compositions can be computed by solving Eqs. (6) and (7) as a function of temperature. Repeating the equilibration on the boron rich side yields Eqs. (8) and (9)

$$F^{L}_{Me} + L\bar{x}^{2}_{L\eta} + RT \ln (1-\bar{x}_{L\eta}) = F^{o}_{Me} - F_{Me+} + RT \ln 2(1-\bar{x}_{\eta L})^{-1} (3\bar{x}_{\eta L}-2)^{-1} \tag{8}$$

and

$$F^{L}_{B} + L(1-\bar{x}_{L\eta})^{2} + RT \ln \bar{x}_{L\eta} = F^{o}_{B} - F_{B+} + 2^{-1} RT \ln 4(3\bar{x}_{\eta L}-2)\, 27^{-1} (\bar{x}_{\eta L})^{-1} \alpha^{-3} \tag{9}$$

Eqs. (8) and (9) yield the $\bar{x}_{L\eta}[T]$ and $\bar{x}_{\eta L}[T]$ curves shown as functions of temperature in Figures 70 and 71.

2. Computation of the Pure Metal/Liquid and Pure Boron/Liquid Equilibria

In line with the Me-C calculations, the assumption of no solubility of B in Me or Me in B was made. This restriction is imposed in order to simplify the calculations and can be lifted if relaxation is required. Equilibrating the partial molar free energy of Me in the liquid phase with that of pure Me yields the $x_{L\beta}[T]$ and $x_{L\alpha}[T]$ curves which derive from Eqs. (10) and (11)

$$\Delta F_{Me}^{L\rightarrow\beta}[T] = RT \ln (1-x_{L\beta}) + L\, x_{L\beta}^{2} \tag{10}$$

for $T > To^{\alpha\rightarrow\beta}$, and

$$\Delta F_{Me}^{L\rightarrow\alpha}[T] = RT \ln (1-x_{L\alpha}) + L\, x_{L\alpha}^{2} \tag{11}$$

for $T < To^{\alpha\rightarrow\beta}$.

Similarly, the equilibration of partial free energies of boron in the liquid phase with pure boron yields the $x_{LB}[T]$ curve which is calculated directly from Eq. (12).

$$\Delta F_{B}^{L\rightarrow S} = RT \ln x_{LB} + L(1-x_{LB})^{2} \tag{12}$$

3. Location of the Diboride/Boron and (Metastable) Diboride/Metal Eutectics

The diboride-boron eutectic is located at the intersection of the $\bar{x}_{L\eta}[T]$ and $x_{LB}[T]$ curves. These intersections result in values of $\bar{T}_E = 2170^{o}K$ and $\bar{x}_E = 0.955$ for the Zr-B system and $2200^{o}K$ and 0.965 in the Hf-B case. These results neglect the possible existence of intermediate boride compounds between MeB_2 and boron. If such phases are stable (i.e. dodecaborides) at high temperatures, then $\bar{T}_E$ would be elevated and $\bar{x}_E$ shifted to higher boron concentrations.

The metal rich eutectics result in similar fashion from the intersection of the $x_{L\eta}[T]$ curve with the $x_{L\alpha}[T]$ curve (Zr-B). These eutectics are metastable since the monoboride phase displaces the stable eutectics to higher temperatures and lower concentrations.

4. Computation of Monoboride/Liquid Equilibria

Monoborides of hafnium and zirconium have been reported to exist as stable phases in the Hf-B and Zr-B systems. Although virtually no thermodynamic data for either compound is available, the compilation of phase diagrams presented earlier (1) suggests that both monoborides decompose peritectically to liquid and diboride at high temperatures. These "suggested" decomposition temperatures(1) are approximately $2700^{o}K$ for ZrB and $3200^{o}K$ for HfB.

Schissel and Trulson(31) determined the free energy of formation* of TiB at $2340^{o}K$ to be -17 k cal/g.at. by means of mass spectrometric vapor pressure studies. Krikorian(32) estimated the enthalpy of formation of HfB to be -24 k cal/g.at. at $298^{o}K$.

* This value was originally reported as an enthalpy of formation assuming $\Delta C_p = 0$

The free energy of formation of the stoichiometric monoboride phase, σ, can be represented[1] by Eq. (13) at high temperatures

$$\Delta F^{\sigma}[0.5, T] = \Delta H^{\sigma}[0.5, 0^{o}K] + 1.5\ RT\ \ln\ \theta_{Me}^{\sigma}\ \theta_{B}^{\sigma}\ \theta_{Me}^{-1}\ \theta_{B}^{-1} - 0.5\gamma^{\sigma}T^{2}$$

$$-0.5\ \phi_{Me}^{o} - 0.5\phi_{B}^{o} \qquad \text{cal/g. at.} \qquad (13)$$

Where[1] $\Delta H^{\sigma}[0.5, 0^{o}K]$ is the enthalpy of formation of the stoichiometric monoboride phase at $0^{o}K$, γ^{σ} is the electronic specific heat coefficient, and ϕ_{Me}^{o} and ϕ_{B}^{o} are the non-vibrational, temperature-dependent free energies terms for the pure metals[1] (the latter include electronic specific heat free energies, free energies of transformation and fusion, etc.). The second term on the right of Eq. (13) is the high temperature approximation to the Debye free energy of formation, thus θ_{Me} and θ_B are the Debye temperatures of pure metal and boron while θ_{Me}^{σ} and θ_{B}^{σ} correspond to the value for the components in the monoboride phase. Eq. 13 contains three unknown terms, $\Delta H^{\sigma}[0.5, 0^{o}K]$, θ_{Me}^{σ}, and θ_{B}^{σ}. Analysis of the low temperature ($5^{o}K$ - $350^{o}K$) specific heat of the diborides on the basis of the Two-Debye Temperature method[6] indicated (page 270 ref 1) that a Lindemann type relation could be written for the Debye temperatures of TiB_2, ZrB_2, HfB_2, NbB_2 and TaB_2. Writing a similar relation for the monoborides yields

$$\theta_{Me}^{\sigma} \approx 130\ V^{-\frac{1}{3}}\ (\overline{T}^{\sigma})^{\frac{1}{2}}\ (M_{Me})^{-\frac{1}{2}} \qquad (14)$$

where $\overline{T}^{\sigma}$ is the melting point of the σ phase, V is the volume of the σ phase in cm^3/g. at and M_{Me} is the atomic weight of the metallic component. In addition, the Debye temperatures of the metal and boron components of the σ phase can be interrelated[1] as follows

$$(\theta_{Me}^{\sigma})^{2}\ M_{Me} = (\theta_{B}^{\sigma})^{2}\ M_{B} \qquad (15)$$

Thus application of Eqs. (14) and (15), reduce the number of unknowns to two, $\Delta H^{\sigma}[0.5, 0^{o}K]$ and $\overline{T}^{\sigma}$.

If the melting of the monoboride phase is considered (as a first approximation) as the temperature at which $x_{L\eta} = 0.5$, then $\overline{T}^{\sigma}$ is defined as being equal to $3000^{o}K$ for the Zr-B case and 3265 for the Hf-B case*. Under these circumstances θ_{Me}^{σ} and θ_{B}^{σ} are fixed by Eqs. (14) and (15) and since

* Relaxing this assumption will not result in large differences in this calculated value of $\Delta H^{\sigma}[0.5, 0^{o}K]$ and the θ values. For example if the HfB^{σ} phase is assumed to decompose at $3000^{o}K$ into liquid ($x_{L\eta}$ 0.43) and diboride phase, then the computed $\Delta H^{\sigma}[0.5, 0^{o}K]$ turns out to be -21.5 k cal/g. at. rather than the present value of -22.8 k cal/g. at.

$F^L[0.5, \bar{T}^\sigma] = F^\sigma[0.5, \bar{T}^\sigma]$ then $\Delta H^\sigma[0.5, 0^oK]$ is specified. The results of this calculation, yielding $\Delta F^\sigma[T]$ for the ZrB and HfB phases are given in Table 18.

Equilibrating the metal and boron partial molar free energies across the liquid plus σ fields yields (30)

$$F_{Me}^L + RT\ \ln(1-x_{L\sigma}) + Lx_{L\sigma}^2 = F_{Me}^o - F_{Me+} + RT\ \ln(1-2x_{\sigma L})/4\alpha^2(1-x_{\sigma L}) \quad (15)$$

$$F_B^L + RT\ \ln x_{L\sigma} + L(1-x_{L\sigma})^2 = F_B^o - F_{B+} + RT\ \ln x_{\sigma L}/(1-2x_{\sigma L}) \quad (16)$$

where

$$2\,\Delta F^\sigma[0.5,\ T] = -F_{Me+} - F_{B+} - 2RT\ln 2\alpha \quad (17)$$

In Eqs. (16) and (17) the free energy of metal and boron vacancies, F_{Me+} and F_{B+}, and the vacancy parameter, α, refer to the monoboride phase and are not presently known. Consequently both $x_{L\sigma}$ and $x_{\sigma L}$ which are specified by Eqs. (16) and (17) cannot be computed. However if Eqs. (16) and (17) are added, the sum,

$$RT\ \ln x_{L\sigma}(1-x_{L\sigma}) + L\ (1-2x_{L\sigma} + 2\,x_{L\sigma}^2) = 2\Delta F^\sigma[0.5, T] + (F_{Me}^o - F_{Me}^L) + (F_B^o - F_B^L) + RT\ \ln x_{\sigma L}(1-x_{\sigma L})^{-1} \quad (18)$$

Eq.(18) exhibits two unknowns, $x_{L\sigma}$ and $x_{\sigma L}$. However, if the solubility of metal in the monoboride is neglected as a first approximation, then $x_{\sigma L} \approx (1-x_{\sigma L})$ and Eq. (18) can be solved for $x_{L\sigma}[T]$. The results are shown in Figures 70 and 72.

5. Location of the Monoboride/Metal Eutectics

Intersection of the $x_{L\beta}[T]$ and $x_{L\sigma}[T]$ curves at x_E and T_E defines the monoboride - metal eutectics. These invariant temperatures are computed to be 1710°K in the Zr-B system and 1880°K in the Hf-B system. Relaxation of the idealizations involved in the calculations of the $x_{L\beta}[T]$ (no solubility of boron in Me) and $x_{L\sigma}[T]$ ($x_{\sigma L} \approx (1-x_{\sigma L})$) curves would both tend to raise the calculated value of T_E.

6. Location of the Congruently Vaporizing Composition within Diboride Phase Field

The composition at which congruent vaporization occurs (1), x_c,

TABLE 18

SUMMARY OF COMPUTED THERMODYNAMIC PROPERTIES OF HfB AND ZrB

	$\overline{T}^{\sigma}[0.5]$ °K	V^{σ} $cm^3/g.at$	θ_{Me}^{σ} °K	θ_{Me} °K	θ_B^{σ} °K	θ_B °K	$\Delta H^{\sigma}[0.5, 0°K]$ k cal/g. at
ZrB^{σ}	3000	7.57	320	260	930	1270	-20.1
HfB^{σ}	3265	7.43	285	200	1155	1270	-22.8

$\Delta F^{\sigma}[0.5, T]$ k cal/g. at.

T°K	ZrB	HfB
1400	-20.0	-21.5
1600	-19.9	-21.2
1800	-19.8	-20.9
2000	-19.7	-20.6
2200	-19.4	-20.3
2400	-18.9	-19.9
2600	-18.3	-19.1
2800	-17.7	-18.2
3000	-17.1	-17.4
3200	-16.5	-16.4

Note: The electronic specific heat coefficients of the monoborides are assumed to be less than 1×10^{-4} cal/g.at.$°K^2$ as in the case of the diborides and ZrC(1). Consequently, the corresponding contribution to the free energy of formation (i.e., $-0.5\gamma^{0}T^2$ in Eq. 13) is neglected.

is defined by Eq. (19).

$$-3\ln(2-3x_c) = 0.5\ln M_B M_{Me}^{-1} + \ln p_{Me}^{o}(p_B^{o})^{-1} + 3\ln\theta_{Me}^{\eta}\theta_{Me}^{-1}\theta_B(\theta_B^{\eta})^{-1}$$

$$-\frac{(39,000+4.5\Delta H^{\eta}[0^{o}K] - \phi_B^{o} + \phi_{Me}^{o} - 1.5\gamma^{\eta}T^2)}{RT} \qquad (19)$$

Applying this expression to the ZrB_2 and HfB_2 cases yields $x_c[T]$ curves which cross the $x_{\eta L}[T]$ curve at 2800°K for the ZrB_2 case and at 2400°K in the HfB_2 case. Unfortunately, these computations do not provide a clear definition of the temperature at which x_c leaves the single phase η field. The reason for the present lack of definition is that $x_{\eta L}[T]$ is a metastable boundary. The pertinent equilibrium boundary, $x_{\eta\sigma}[T]$, cannot be calculated at present and will lie to the right of $x_{\eta L}[T]$ curve suggesting exiting of x_c from the single phase field at lower temperatures. However, the comparison of observed and computed values of x_c at 2400°K for ZrB_2 and HfB_2 indicated that the computed values were lower than those observed (1.92 vs 1.97 for ZrB_2 and 1.89 vs 1.96 for HfB_2). This factor would counteract the effect of the $x_{\sigma\eta}$ displacement and raise the exit temperature.*

C. Experimental

Numerous experimental difficulties have hampered the phase boundary program from its inception. However, the results of the several different types of experiments completed in the present investigation of the Zr-B and the Hf-B systems combined with the calculated phase equilibria and the previously described (1) diffusion couple data for the Zr-B system provide sufficient information to redefine certain aspects of the previously reported (1) phase diagrams for these systems.

In order to provide adequate background information, the principal features of different types of experiments are reviewed and the advantages and limitations of each as applied to the systems of interest are stated.

1. Diffusion Couples

The previous report contains a complete description of the experimental techniques. The diffusion couple materials were high porosity Zr metal and zone refined ZrB_2. The experiments were carried out inside a molybdenum sample holder in the carbon tube furnace with an argon atmosphere. The initial temperatures for equilibration were selected

---

* The computed values for ZrB_2 are in good agreement with the results indicated in Table 8 and with a value of B/Me = 1.93 ± 0.02 obtained by G.M. Kibler, T.F. Lyon and M.J. Linevsky, G.E., Cincinnati and reported in WADD-TR-60-646, Part 4, August 1964.

from the phase diagrams reported by Glaser and Post (34) and by Schedler (35). The attempted experiments at 1850°, 1770°, 1750°, and 1650°C failed because a liquid phase formed; the reported (34, 35, 1) solidus was 1780°C. Successful couples were heat treated at 1500°, 1400°, and 1000°C; no evidence of an intermediate phase between Zr and ZrB_2 was found. Thus, these experiments indicated that the solidus temperature for the metal plus metal-rich boride phase field is less than 1650°C but higher than 1500°C. The phase diagram proposed by Glaser and Post (34) indicated a cubic monoboride stable from 800° to 1250°C; the results of the diffusion couple at 1000°C show no evidence of an intermediate phase. In addition the apparent unsuccessful couples above 1650°C did produce a solid intermediate compound, ZrB (cubic) at the diboride interface. Again, the diagram of Glase and Post (34) shows no phase at these temperatures but the diagram of Schedler (35) does show a monoboride (orthorhombic, B-27) above the solidus between the metal and the diborides. In the diffusion couple experiments, the presence of a small amount of carbon could have stabilized the cubic monoboride relative to the orthorhombic structure.

2. Equilibration Experiments

In the original planning of the phase boundary program it was anticipated that equilibration of two phase alloys would complement the data obtained from the diffusion couples. The zone refining subtask (1) was considered an ideal source of high purity samples because many attempts to prepare single phase material produced two phase samples. Metal rich and boron rich specimens were equilibrated at temperatures from 1000° to 1850°C. In practice it is better to have a larger amount of the second phase in such samples; thus these high purity materials have some disadvantages. In comparing the two types of experiments the two phase alloys can provide phase boundary data on the diborides to much higher temperatures because the metal/diboride couple cannot be used above the metal-solidus. In practice (1) diffusion couples between boron and the diboride where not feasible as the relatively higher vapor pressure of boron, lead to vaporization and a diffusion bind was formed. The characteristics of the various types of specimens used for equilibration experiments are provided below.

2.1 Zone Refined Specimens

The zone refining subtask in Part I of this investigation (1) provided several high purity bars which were either metal rich or boron rich and which contained ZrB_2 as the major component and a small amount of a second phase. The relatively small amount and the difficulty in the identification of the second phase impose a limitation on the usefulness of this material. The amount of the second phase in the metal rich material is considerably less than in the boron rich material. A metal rich sample was equilibrated at 1850°C and boron rich samples were equilibrated at

1730°, 1400°, and 1000°C. The phases in the sample equilibrated at 1730°C were analyzed by the electron microprobe; the results gave B/Me = 2.02 for the boron rich boundary of ZrB_2 and since the second phase contained < 0.1 per cent Zr, it was concluded that the reported (34, 35) ZrB_{12} was not stable at, or below, this temperature.

2.2 High Pressure Hot Pressed Specimens

Since the high pressure hot pressing procedure had proven capable of fabricating dense samples of the diboride powders, an attempt was made to prepare two phase alloys by fabricating a mixture of Zr metal and ZrB_2(1) powder starting material; the powders were mixed with an overall composition of B/Zr = 1.5. The hot pressing was performed at 1750°C for 5 minutes at 200 kpsi. One limitation on the conclusions drawn from data on specimens prepared from this mixture is the uncertainty of effects from impurity materials in the original ZrB_2(1) powder. For example, it is known that the cubic monoboride is stabilized by carbon; ZrB_2(1) powder has 0.33 weight per cent carbon. Equilibrations at 1500° and 1550°C produced a mixture of the cubic monoboride and ZrB_2.

2.3 Cold Pressed Compacts of Zirconium and Boron

Mixtures of metallic zirconium powder and crystalline boron were prepared with B/Me in the region of the reported metal-"metal rich boride" eutectic compositions for the Zr-B and Hf-B systems and other compositions with increasing amounts of boron up to B/Me = 1.5. The mixtures were pressed at 100 ksi at room temperature. This procedure produced compacts which were mechanically sound but quite porous. The excessive porosity in some of these specimens complicates the metallographic analyses. However, these specimens were successfully equilibrated at elevated temperatures and the solidus temperature of the metal-metal rich boride was determined for the Zr-B and the Hf-B systems. In addition, specimens with B/Me = 0.67 to 1.50 were used to show the presence of a metal rich boride between the metal and the diboride which is stable above the metal eutectic temperature.

2.4 Arc Melted Specimens

Mixtures of zirconium plus boron and hafnium plus boron were successfully arc melted into dense buttons. The arc melting was carried out in argon with thoriated-tungsten electrodes; the specimen was contained in a water cooled copper hearth. Spectroscopic analysis did reveal metallic contamination. Specimens were prepared with B/Me = 1.5 to investigate the metal rich diboride boundary and with B/Me = 6.0 to investigate the boron rich diboride boundary. These specimens contain from 50 to 75 per cent diboride. Accordingly, the additional phase(s) can be easily identified and analyzed. Equilibrations were performed up to 2200°C; the analyses of the heat treated specimens provided qualitative and quantitative results on the equilibrium structures at elevated temperatures.

3. Heating Procedures

The diffusion couples were heated in a molybdenum sample holder which was designed to provide sufficient pressure between the couple components to insure interdiffusion without cracking the diboride. The holder was heated in argon inside a carbon tube furnace. The completed details were provided in the previous report (1).

Two phase alloys provided from the zone refining program in Part I and those prepared by high pressure hot pressing from ZrB_2(1) powder and Zr metal were equilibrated in an argon atmosphere in either a resistance wound furnace or a Glo-Bar type tube furnace. Alloys equilibrated in this way could be quenched to ambient temperatures in a relatively short time.

The compacted mixtures of metal and boron powders (0.40 in. diameter by 0.20 in. long) were heated in vacuo (1×10^{-5} torr) in a resistance furnace. Two furnaces were used; one consisted of a BeO muffle with Ta wire windings and ZrO_2 powder insulation; the other was a Ta resistance furnace of vertical split tube design with Ta radiation shields. The pellets were set on pressed and sintered ZrO_2 discs. The furnace was enclosed in a water cooled jacket and the entire assembly was contained in a metal vacuum bell jar. Temperatures were measured with calibrated W-3% Re vs. W-25% Re thermocouples and with an optical pyrometer. Cooling was accomplished by backfilling the vacuum system with He to about 75 mm Hg pressure. The latter furnace was also used for the arc melted specimens.

4. Heating Conditions and Evaluations

The experimental conditions for the diffusion couples and the equilibration experiments and the evaluations obtained for these specimens are collected in Table 19. Representative photomicrographs of each type of specimen are provided in Figures 74 through 79.

5. Results and Discussion

The results presented in Table 19 are summarized and compared with the previously reported (35, 36) phase diagrams and the calculated phase diagrams in Figures 80 and 81.

The salient features of the present investigation are:

(a) The metal-"metal rich boride" solidus temperatures for the Zr-B and Hf-B systems are 1660° and 1960°C respectively.

(b) There is a solid phase stable at elevated temperatures in the composition region near 50 a/o B. This is presumably the previously reported monoboride. For the Zr-B system, this phase is not stable below 1500°C as evidenced by the diffusion couple experiments. The experiments with B/Zr = 1.0 and 1.5 show this phase to be stable from 1625° up to 2360°C.

TABLE 19

HEATING CONDITIONS AND EVALUATIONS FOR PHASE DIAGRAM STUDY

Exp. No.	Composition	Furnace (atm.)	Temp. (°C)	Time (Hrs.)	Post Heating Analyses: X-Ray	Post Heating Analyses: Metallographic Comments
Diffusion Couples Zr/ZrB_2						
		Carbon				
D-2	-	Argon	1850	3	-	Zr Melted
D-5	-	Argon	1770	12	$ZrB(\sigma)$ ZrB_2	Zr Melted, Eutectic
D-4	-	Argon	1750	8		Zr Melted
D-6	-	Argon	1650	11	$ZrB(\sigma)$ ZrB_2	Zr Melted, Eutectic
		Globar				
D-7	-	Argon	1500	24	Zr, ZrB_2	Sound couple No intermediate phase
D-8	-	Argon	1400	24		Sound couple No intermediate phase
D-9	-	Argon	1000	116		Sound couple No intermediate phase
Zone Refined Two Phase Alloy Specimens						
		Carbon				
D-2	Metal Rich	Argon	1850	3	ZrB_2	No Liquid Phase
D-3	Boron Rich	Argon	1730	12	ZrB_2	No Liquid Phase
		Globar				
D-6	Boron Rich	Argon	1400	24	ZrB_2	No Liquid Phase, Figure 74
D-7	Boron Rich	Argon	1000	350	ZrB_2	No Liquid Phase
D-8	Metal Rich	Argon	1000	350	ZrB_2	No Liquid Phase

TABLE 19 (CONT.)

HEATING CONDITIONS AND EVALUATIONS FOR PHASE DIAGRAM STUDY

Exp. No.	Composition	Furnace Atmos.	Temp. (°C)	Time (Hrs.)	Post Heating Analyses: X-Ray	Post Heating Analyses: Metallographic Comments
High Pressure Hot Pressed Specimens: ZrB_2(1) + Zr						
D-9	B/Zr = 1.5	Globar Argon	1500	40		No Liquid Phase
D-10	B/Zr = 1.5	Argon	1550	36	ZrB(J) ZrB_2	No Liquid Phase, Figure 75
Cold Pressed Compacts: Zr + B or Hf + B						
D-11	$Zr_{0.93}B_{0.07}$	Globar Argon	1600	2.0	Zr, ZrB_2	No Eutectic
	$Zr_{0.75}B_{0.25}$	Argon	1600	2.0	Zr, ZrB_2	No Eutectic
VHT-1	$Hf_{0.93}B_{0.07}$	Mo vacuum	1650	0.5	Hf, HfB(B-27)	No Eutectic
	$Hf_{0.84}B_{0.16}$	vacuum	1650	0.5	Hf, HfB(B-27)	No Eutectic
VHT-2	$Hf_{0.4}B_{0.6}$	vacuum	1625	0.8	HfB(B-27), HfB_2	No Liquid
	$Zr_{0.4}B_{0.6}$	vacuum	1625	0.8	Zr, ZrB_2	No Liquid
VHT-5	$Zr_{0.75}B_{0.25}$	vacuum	1700	1.5	Zr, ZrB_2	Hard Area Single Phase + Two Phase
	$Zr_{0.4}B_{0.6}$	vacuum	1700	1.5	Zr, ZrB_2	No Eutectic
VHT-6	$Hf_{0.93}B_{0.07}$	vacuum	1850	0.5	Hf, HfB(B-27)	Two Phase One Phase was Liquid, Figure 76
	$Hf_{0.4}B_{0.6}$	vacuum	1850	0.5	HfB(B-27), HfB_2	No Liquid
VHT-11	$Zr_{0.6}B_{0.4}$	Ta vacuum	1660	-	Zr, ZrB_2	Compact Liquified at 1660°C
VHT-14	$Hf_{0.93}B_{0.07}$	vacuum	1960	-		Compact Liquified at 1960°C
VHT-10	$Hf_{0.6}B_{0.4}$	vacuum	2040	0.2		No Evidence of Liquid
VHT-13	$Hf_{0.6}B_{0.4}$	vacuum	2200	0.2	Hf, HfB_2	No Evidence of Liquid
VHT-16	$Hf_{0.6}B_{0.4}$	vacuum	2250	0.2		Edges of compact rounded at 2250°C

TABLE 19 (CONT.)

HEATING CONDITIONS AND EVALUATIONS FOR PHASE DIAGRAM STUDY

Exp. No.	Composition	Furnace Atmos.	Temp. (°C)	Time (Hrs.)	Post Heating Analyses: X-Ray	Post Heating Analyses: Metallographic Comments
Arc Melted Specimens: Zr + B or Hf + B before melting						
		Ta				
VHT-15	$Hf_{0.4}B_{0.6}$	vacuum	2000	1.2	Hf, HfB_2	Remained Solid, Figure 78
	$Zr_{0.4}B_{0.6}$	vacuum	2000	1.2	Zr, ZrB_2	Remained Solid
VHT-19	$Zr_{0.4}B_{0.6}$	vacuum	2330	1.0	-	Remained Solid, Figure 79
VHT-9	$Zr_{0.5}B_{0.5}$	vacuum	1625	1.0	Zr, ZrB_2	Remained Solid
VHT-8	$Zr_{0.5}B_{0.5}$	vacuum	1900	0.25	Zr, ZrB_2	Remained Solid
VHT-17	$Zr_{0.5}B_{0.5}$	vacuum	2360	1.0	Zr, ZrB_2	Remained Solid
VHT-18	$Hf_{0.14}B_{0.86}$	vacuum	2015	1.0	HfB_2	Remained Solid
	$Zr_{0.14}B_{0.86}$	vacuum	2015	1.0	ZrB_2, ZrB_{12}	Remained Solid, Figure 77
VHT-20	$Zr_{0.14}B_{0.86}$	vacuum	2170	0.2	-	Remained Solid

As Zone Refined Unetched - X500

Exp. No. d-6
1400°C - 24 Hours - Argon Unetched - X500

Figure 74 - Zone Refined Two Phase Alloy Specimen: Boron Rich ZrB_2 + 2nd Phase

As Hot Pressed Unetched - X500

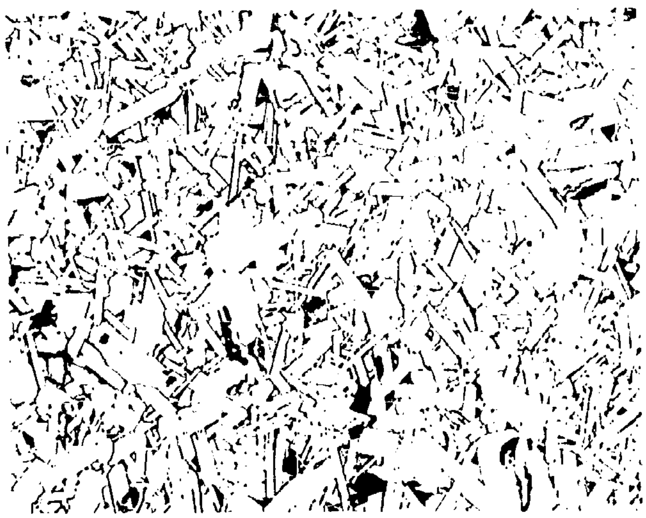

Exp. No. d-10
1500°C - 18 Hours - Argon, followed by
1550°C - 36 Hours - Argon
Etched X500
Etchant: Modified Aqua Regia

Figure 75 - High Pressure Hot Pressed Specimen: ZrB_2 (1) Powder and Zr Metal, B/Zr = 1.5.

Exp. No. VHT-6
1850°C 30 Minutes Argon
Etched
Etchant: Modified Aqua Regia

X250

Figure 76 - Cold Pressed Compact Specimen: $Hf_{0.93}B_{0.07}$

Etched X50
Etchant: 10 cc Glycerine, 10 cc HNO_3,
2 cc HCL, 0.1 cc HF

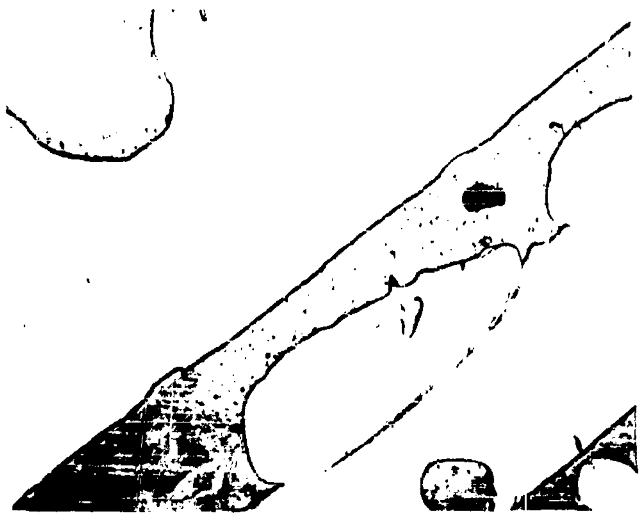

Etched X500
Etchant: 10 cc Glycerine, 10 cc HNO_3, 2 cc HCL, 0.1 cc HF
Exp. No. VHT-18
2015°C 1 Hour Vacuum

Figure 77 - Arc Melted Specimen: $Zr_{0.14}B_{0.86}$

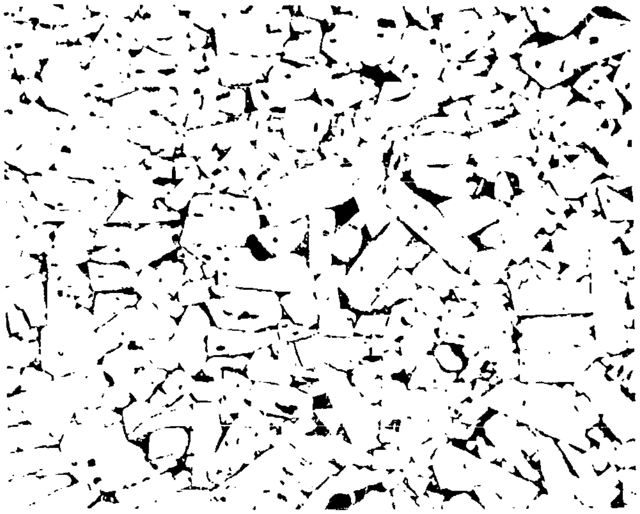

Etched X50
Etchant: 10 cc Glycerine, 10 cc HNO_3,
2 cc HCL, 0.1 cc HF

Etched X500
Etchant: 10 cc Glycerine, 10 cc HNO_3,
2 cc HCL, 0.1 cc HF
Exp. No. VHT-15
2000°C 1.2 Hours Vacuum

Figure 78 - Arc Melted Specimen: $Hf_{0.4}B_{0.6}$

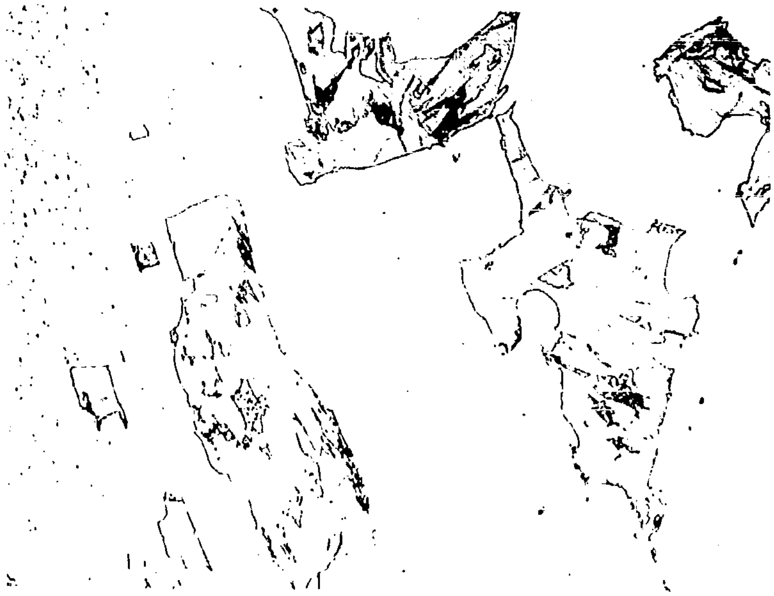

Etched X500
Etchant: 10 cc Glycerine, 10 cc HNO_3, 2 cc HCL, 0.1 cc HF
Exp. No. VHT-19
2330°C 1 Hour Vacuum

Figure 79 - Arc Melted Specimen: $Zr_{0.4}B_{0.6}$

The monoboride could not be quenched to ambient temperatures unless a carbon impurity was present to stabilize the "cubic" monoboride. No X-ray evidence for an orthorhombic monoboride was found in this investigation for the Zr-B system. For the Hf-B system, the reported orthorhombic monoboride was formed and retained in cold compacted powder mixtures of Hf and B heated at 1625°, 1650°, and 1850°C for times from 30 to 45 minutes. Similar mixtures heated to 2000°-2250°C for shorter times showed only Hf and HfB_2 in the heat treated specimens. Arc melted specimens heated at 2000°C for 1.2 hours did show the orthorhombic monoboride in the heat treated specimen. The results of Exp. Nos. VHT-10, -13, and -16 show that the so-called monoboride or the metal-rich boride in the Hf-B system is stable at a composition of 40 a/o B. There has been no previous evidence of a significant range of composition for the stability of hafnium monoboride. The subject of the effect of carbon on the relative stabilities of the monoborides of zirconium and hafnium has been reviewed by Nowotny, Rudy, and Benesovsky (37).

(c) The solidus temperature for metal rich ZrB_2 and HfB_2 are above 2360°C and above 2250°C respectively.

(d) The solidus temperatures for boron rich ZrB_2 and HfB_2 are both above the melting point of elemental boron (2030°C). In the Hf-B system, equilibration of a composition $Hf_{0.14}B_{0.86}$ at 2015°C for 1 hour did not produce a liquid phase but only HfB_2 was identified in the sample after cooling. In the Zr-B system, equilibrations were carried out at 2015° and 2170°C. The dodecaboride, ZrB_{12}, was identified by X-ray diffraction in a sample after heating. The previously reported (1) electron probe analysis of a boron rich ZrB_2 two phase alloy specimen equilibrated at 1730°C showed <0.1 a/o Zr in the second phase. Thus, both systems have solid phases present at elevated temperatures. The phases probably have the MeB_{12} composition.

(e) Several samples were selected for electron microprobe analysis of both metal rich and boron rich compositions in the Zr-B and Hf-B systems. The results of these analyses and the previously reported data (1) are summarized along with calculated phase boundaries in Table 20. The metallographic analyses of some of the heat treated arc melted specimens indicated evidence that a phase decomposition had occurred during cooling. In some of the latter specimens the overall composition of the apparent two phase region was scanned for average composition of the equilibrium phase at elevated temperature. The electron probe results confirm the very narrow range of the single phase fields; the composition limits of HfB_2 are undistinguishable by this technique. The composition of the dodecaboride indicates a boron deficiency, that is, $ZrB_{10.5}$. The dark grey phase in the boron rich Zr-B alloys at high temperatures has a considerable amount of Zr. The average composition of 94.2 w/o Hf for the 2nd phase in VHT-6 agrees with the composition calculated for the monoboride.

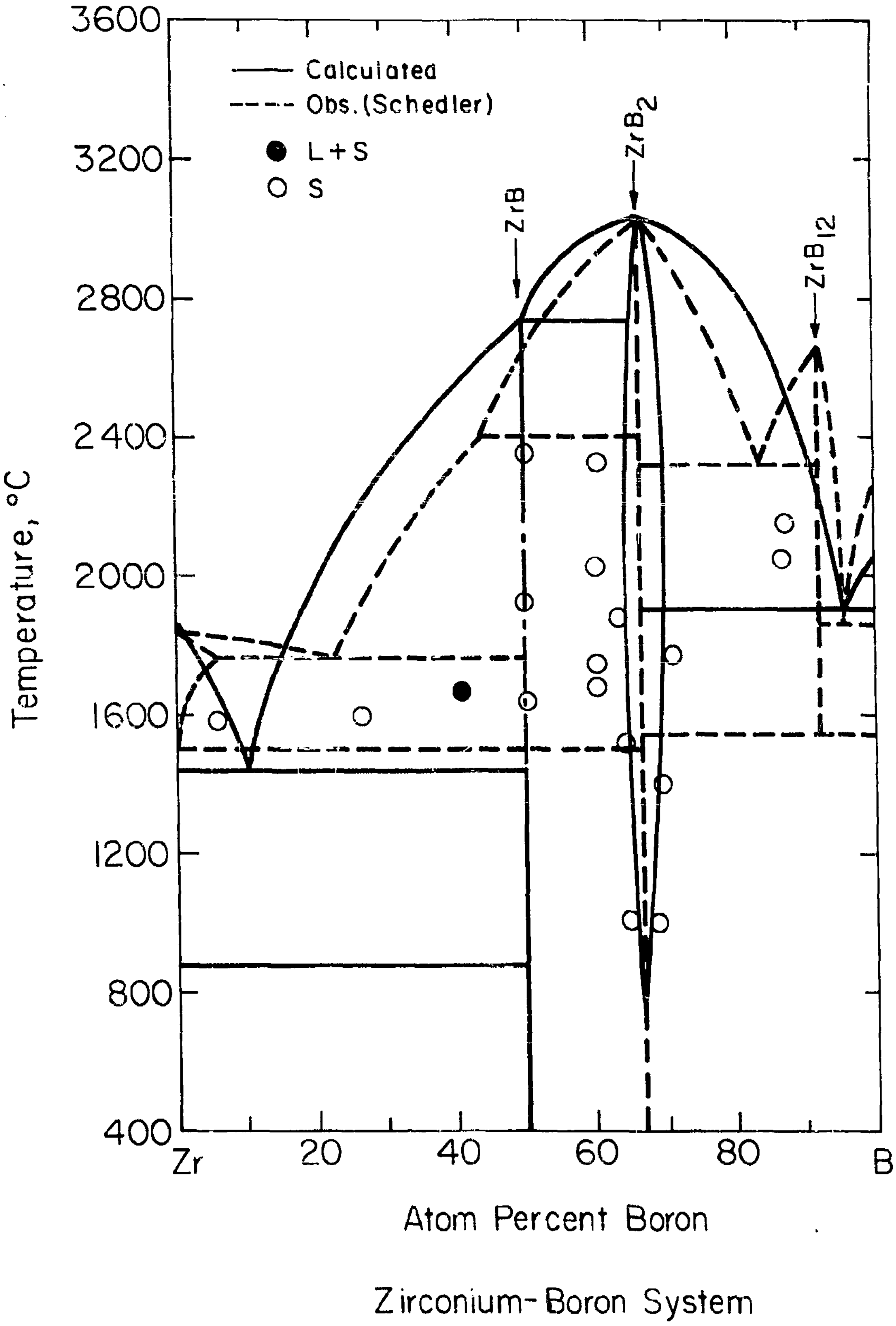

Figure 80. Zirconium-Boron System.

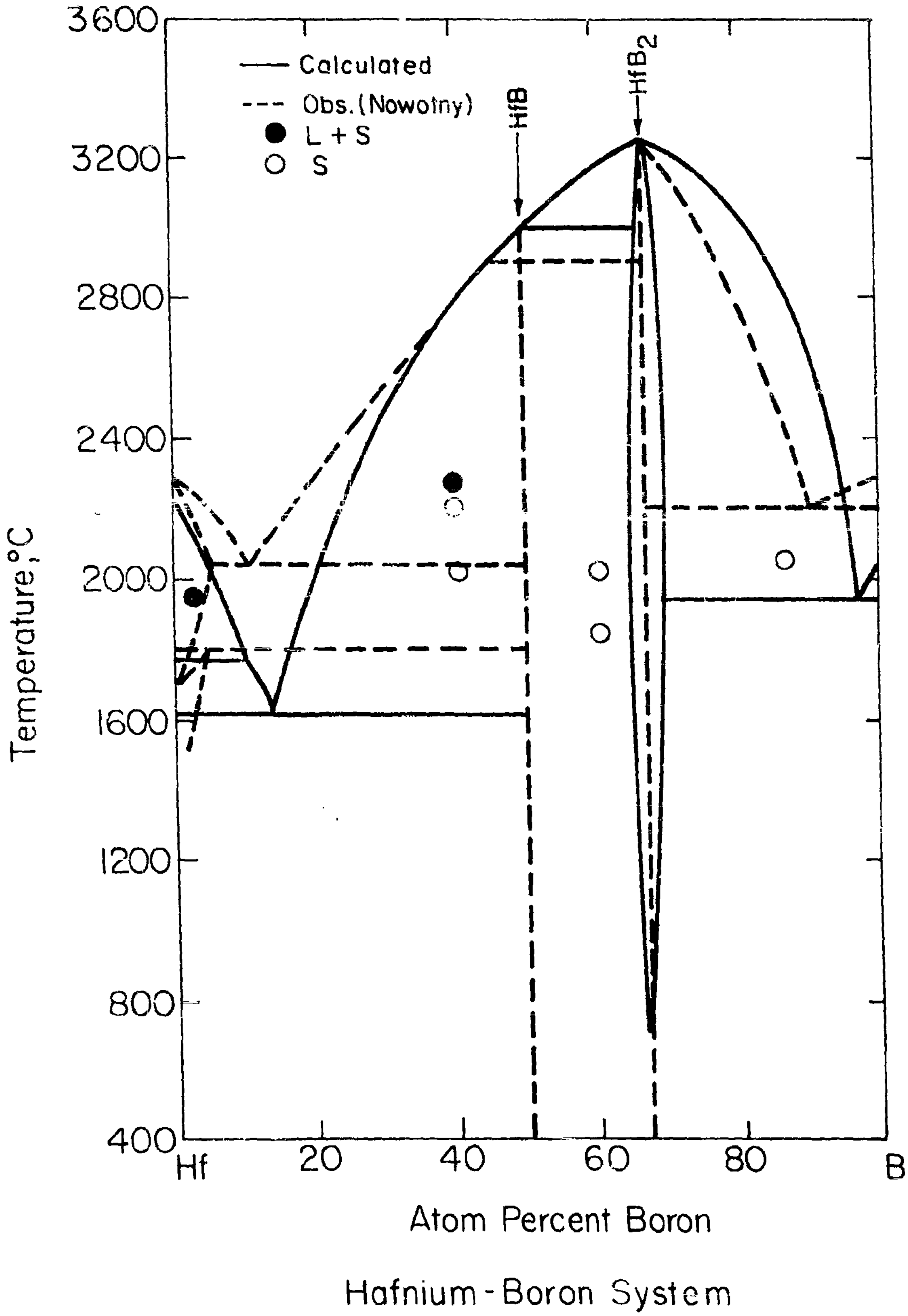

Figure 81. Hafnium-Boron System.

TABLE 20

COMPARISON OF OBSERVED AND CALCULATED PHASE BOUNDARIES IN THE Zr-B AND Hf-B SYSTEMS

Temp. (°K)	Calculated ZrB_2 Boundaries, Atom Fraction Metal		Calculated HfB_2 Boundaries, Atom Fraction Metal	
	Metal Rich	Boron Rich	Metal Rich	Boron Rich
1400	0.659	0.665	0.663	0.669
1600	0.657	0.667	0.659	0.671
1700	0.655	0.669	0.658	0.675
1800	0.654	0.672	0.657	0.677
2000	0.653	0.675	0.655	0.679
2100	0.652	0.677	0.655	0.680
2200	0.652	0.678	0.655	0.681
2300	0.652	0.679	0.655	0.681
2400	0.652	0.680	0.655	0.682

Results of Electron Probe Analyses

Material	Experimental Conditions	Results
Zone refined boron rich two phase alloy	1730° C-12 hrs. -argon	Matrix: 80.8 w/o Zr B/Zr 2.02 2nd Phase: < 0.1 w/o Zr
Zr/ZrB_2 Diffusion Couple	1400° C-24 hrs. -argon	Diboride Phase: 81.1 w/o Zr, B/Zr = 1.97
Zr/ZrB_2 Diffusion Couple	1000° C-116 hrs. -argon	Diboride Phase: 80.9 w/o Zr, B/Zr = 1.99
Arc melted $Zr_{0.14}B_{0.86}$	2015° C-1 hr. -vacuum (VHT-18)	$ZrB_2 + ZrB_{12}$ by X-ray Diffraction White Phase: 80.3 w/o Zr; B/Zr = 2.08 Purple Phase: 44.8 w/o Zr; B/Zr = 10.5 Grey Phase: 16.5 w/o Zr; B/Zr = 43
Arc melted $Hf_{0.4}B_{0.6}$	VHT-6	Composition of diboride phase indistinguishable from B/Hf = 2.0
Arc melted $Hf_{0.14}B_{0.86}$	VHT-18	
Arc melted $Hf_{0.4}B_{0.6}$	VHT-16	Grey Phase region of VHT-6 showed 94.2 w/o Hf, B/Hf = 1.0

IX THERMODYNAMICS OF STABILITY*

A. Introduction

The description of the thermodynamic and oxidation properties of the transition metal diborides generated during the past two years, "indicates that metal-rich deviations from stoichiometry in these compounds will probably result in additional enhancement of the oxidation resistance". (ref 1 p iii and p 7). Present efforts in the preparation and oxidation characterization of HfB_2 and ZrB_2 reported in Section IV and VI of this report have provided substantial support for this prediction. Since the purpose of the stability study is to provide a rational basis for guiding the development of oxidation resistant diboride compounds, current interest has been centered on the description of a model which can predict the relative oxidation resistance of the pure stoichiometric diborides and the effects of composition on the oxidation resistance. In addition, a description of the effects of ternary additions on the thermodynamic properties of the diborides has been generated in order to gain some insight in selecting candidate third component additions. Finally, available volumetric data on oxide/diboride have been collected in order to present a graphical description of the degree of coherencybetween the oxide and diboride.

It should be emphasized that the general problem is quite complex and that the consideration presented below are idealized and not necessarily unique. However, on the basis of present information, these areas appear most fruitful.

B. Consideration of the Boron Activity Gradient Across the Metal Oxide Formed During Diboride Oxidation

On the basis of the observed oxidation behavior of the diborides, we consider a system described by Eq. (1)

$$\eta \text{ (Diboride [} x, T \text{]} \overset{1}{\Big|} \; \Upsilon \text{ (Oxide)} \overset{2}{\Big|} \; \lambda \; (B_2O_3) \qquad (1)$$

As a first approximation we consider a case where the activity of metal atoms in the diboride phase (η), which has a composition x, is equal to the activity of metal atoms in the oxide phase (Υ). Secondly we assume that the activity of oxygen in the oxide is equal to the activity of oxygen in the (λ) B_2O_3 phase. These assumptions are gross idealizations since no gradients in composition are considered within the η or λ phases nor are Me and O gradients considered between the η/Υ interface, 1, or the Υ/λ interface at point 2. Thus, no diffusion limitation is considered.

We can now compute the ratio of the activity of boron in the η phase to that in the oxide.

---

* L. Kaufman, ManLabs, Inc.

The calculation is illustrated schematically in Figure 82 which starts with a metal rich diboride and graphically illustrates metal activity equilibration across interface 1, oxygen equilibration across interface 2 and computation of the boron activity gradient. The activity composition curves drawn in Figure 82 are schematic but it can be shown that the cross-over point is associated with the minimum in the free energy-composition curve which is taken to be close to stoichiometry.

In order to compute the boron activity gradient between points 1 and 2, the following procedure is utilized. The free energy of formation (per gram atom) of diboride phase is given by

$$\Delta F^{\eta}[x,T] = (1-x)\ RT \ln a_{Me}^{\eta}[x,T] + x\ RT \ln a_B^{\eta}[x,T] \tag{2}$$

where x is the atom fraction of boron. Similarly, we approximate the free energy of formation of the τ phase (HfO_2, ZrO_2, TiO_2 and NbO_2) by

$$\Delta F^{\tau}[T] = (\tfrac{1}{3})\ RT \ln a_{Me}^{\tau} + (\tfrac{2}{3})\ RT \ln a_O^{\tau} \tag{3}$$

while the free energy of the B_2O_3 (λ) phase is

$$\Delta F^{\lambda}[T] = (\tfrac{2}{5})\ RT \ln a_B^{\lambda} + (\tfrac{3}{5})\ RT \ln a_O^{\lambda} \tag{4}$$

In the TaB_2/Ta_2O_5 calculations the coefficients (1/3) and (2/3) in Eq. (3) are simply replaced by (2/7) and (5/7). Equating the metal activities across interface 1 yields

$$a_{Me}^{\eta}[x,T] = a_{Me}^{\tau} \tag{5}$$

Substitution into (2) and (3) yields

$$\Delta F^{\eta}[x,T] = (1-x)\ (3.5\Delta F^{\tau} - 2.5\ RT \ln a_O^{\tau}) + xRT \ln a_B^{\eta}[x] \tag{6a}$$

for the TaB_2/Ta_2O_5 case, and

$$\Delta F^{\eta}[x,T] = (1-x)\ (3\Delta F^{\tau} - 2\ RT \ln a_O^{\tau}) + xRT \ln a_B^{\eta}[x] \tag{6b}$$

for the other diborides. Equating

$$a_O^{\tau} = a_O^{\lambda} \tag{7}$$

across the interface at point 2 and substituting Eqs. (7) and (4) into Eqs. (6a) and (6b) yields

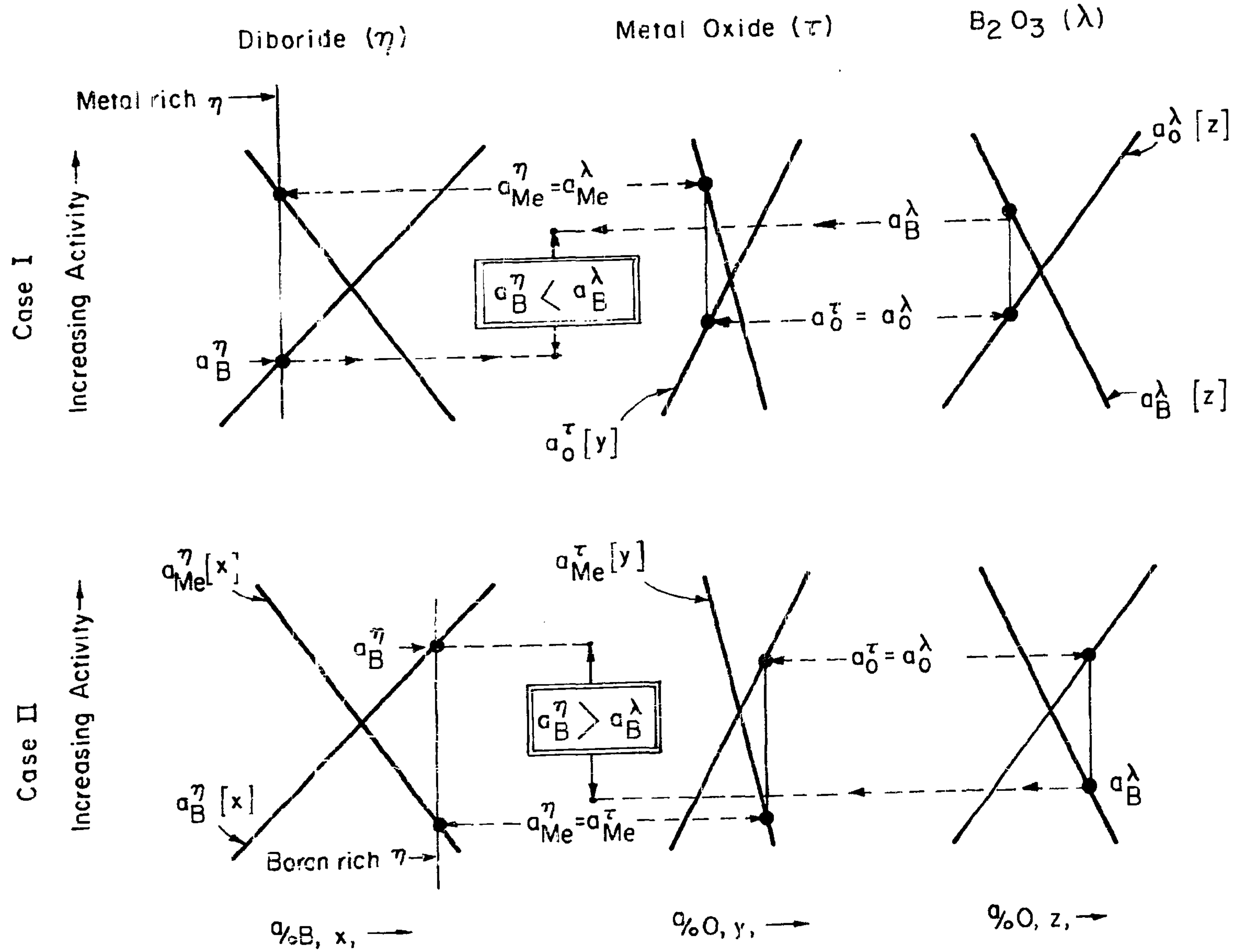

Figure 82. Schematic Illustration of the Effect of Diboride Composition on the Boron Activity Gradient Between MeB_2 and B_2O_3.

$$RT \ln a_B^{\eta}[x]/a_B^{\lambda} = 2.1\Delta F^{\tau} - 2.5\Delta F^{\lambda} - 0.6(1-x)\Delta F^{\eta}[x,T]$$
$$+0.1(10-4x)(1-x)^{-1} RT \ln a_B^{\eta}[x,T] \quad (8a)$$

for the TaB_2/Ta_2O_5 case, and

$$RT \ln a_B^{\eta}[x]/a_B^{\lambda} = 2.25\Delta F^{\tau} - 2.5\Delta F^{\lambda} - 0.75(1-x)\Delta F^{\eta}[x,T] \quad (8b)$$
$$+0.25(4-x)(1-x)^{-1} RT \ln a_B^{\eta}[x,T]$$

for the other diborides. Thus Eqs. (8a) and (8b) specify the boron activity gradient as a function of x, and T. The calculation neglects the change in stoichiometry of the τ and λ phases as a second order effect.

Substitution of the appropriate values for ΔF^{τ}, ΔF^{λ} (Table 21), $\Delta F^{\eta}[x,T]$(1, 29) and $RT \ln a_B^{\eta}[x,T]$(1, 29) into Eqs. (8a) and (8b) for the case $x = 2/3$ yields Figure 83. The activity gradient - temperature curves of Figure 83 indicate that on the basis of this model HfB_2 and ZrB_2 are superior to TiB_2 which is superior to TaB_2 and NbB_2. The compositional dependence of the activity gradients predicted by Eqs. (8a) and (8b) indicate that the dominant compositional dependent term is $RT \ln a_B^{\eta}[x,T]$ which decreases with decreasing x. Thus the boron activity gradient will become more negative as the activity of boron in the η is decreased or as x is decreased. Hence metal rich diborides, $x < 2/3$, should yield more negative boron activity gradients and better oxidation resistance than boron rich diborides. This is the same conclusion as that reached in Section VI on the basis of minimizing the pressure of B_2O_3''.

C. Calculation of the Effects of Ternary Additions on the Thermodynamic Properties of Diborides

In addition to the conclusion (1) that metal rich HfB_2 and ZrB_2 would afford superior oxidation behavior, it was suggested that ternary alloying additions such as tantalum, yttrium and silicon might also provide beneficial results(1). The former two elements might diffuse into the oxide and, if the Wagner mechanism were operative, impede diffusion of oxygen. Moreover, these elements are known to stabilize the cubic and tetragonal forms of the oxide. Silicon was chosen because of its glass forming tendency and ability to substitute for boron on the boron sublattice within the η phase. Presently, additions of Ta, Y, and Si are being made to metal rich HfB_2 and ZrB_2 in small quantities. The following thermodynamic analysis which is designed to deliniate the thermodynamic effects of these additions is an extension of the Schottky-Wagner model of non-stoichiometric binary phases developed earlier (30) to the ternary case. Thus two situations are treated, the first considers additions of a third element which substitutes on the metal lattice. In the second case, an element which substitutes on the boron lattice in the η phase is considered.

TABLE 21

TABULATION OF FREE ENERGIES OF FORMATION
REQUIRED IN MODEL CALCULATIONS

T^oK	$(-\Delta F^{\lambda})$	$(-\Delta F^{T})$				
	(B_2O_3)*	(HfO_2)o	(ZrO_2)+	(TiO_2)†	(Ta_2O_5)**	(NbO_2)oo
	k cal/g. at.			k cal/g. at.		
1400	44.8	68.3	66.1	53.9	49.1	43.5
1600	42.8	65.5	63.2	52.4	46.4	41.0
1800	40.8	62.7	60.3	49.6	43.8	38.5
2000	38.8	60.0	57.5	46.8	41.0	36.0
2200	36.8	57.4	54.6	44.0	38.4	33.5
2400	34.8	54.8	51.6	41.6	36.4	31.3
2600	33.4	52.1	48.6	39.2	34.3	29.3
2800	32.4	49.4	45.7	36.7	32.3	27.3
3000	31.4	46.8	42.8	34.3	30.2	25.1
	$x_o^{\lambda}=0.6$	$x_o^{T}=\frac{2}{3}$	$x_o^{T}=\frac{2}{3}$	$x_o^{T}=\frac{2}{3}$	$x_o^{T}=\frac{5}{7}$	$x_o^{T}=\frac{2}{3}$

Notes

* JANAF Thermochemical Tables (March 1961) Dow Chemical Co. Midland, Michigan

o Schick, H.L., Anthrop, D.F., Dreikorn, R.E., Hanst, P.L. and Panish.M.B. "Thermodynamics of Certain Refractory Compounds" Quarterly Progress Report #4,15 June 1963 Contract AF 33(657)-8223 AVCO RAD Wilmington, Mass., p 171

\+ Ibid QPR #5, 15 Sept. 1963 p 233

† Ibid p 221

** Ibid p 241

oo Ibid p 193

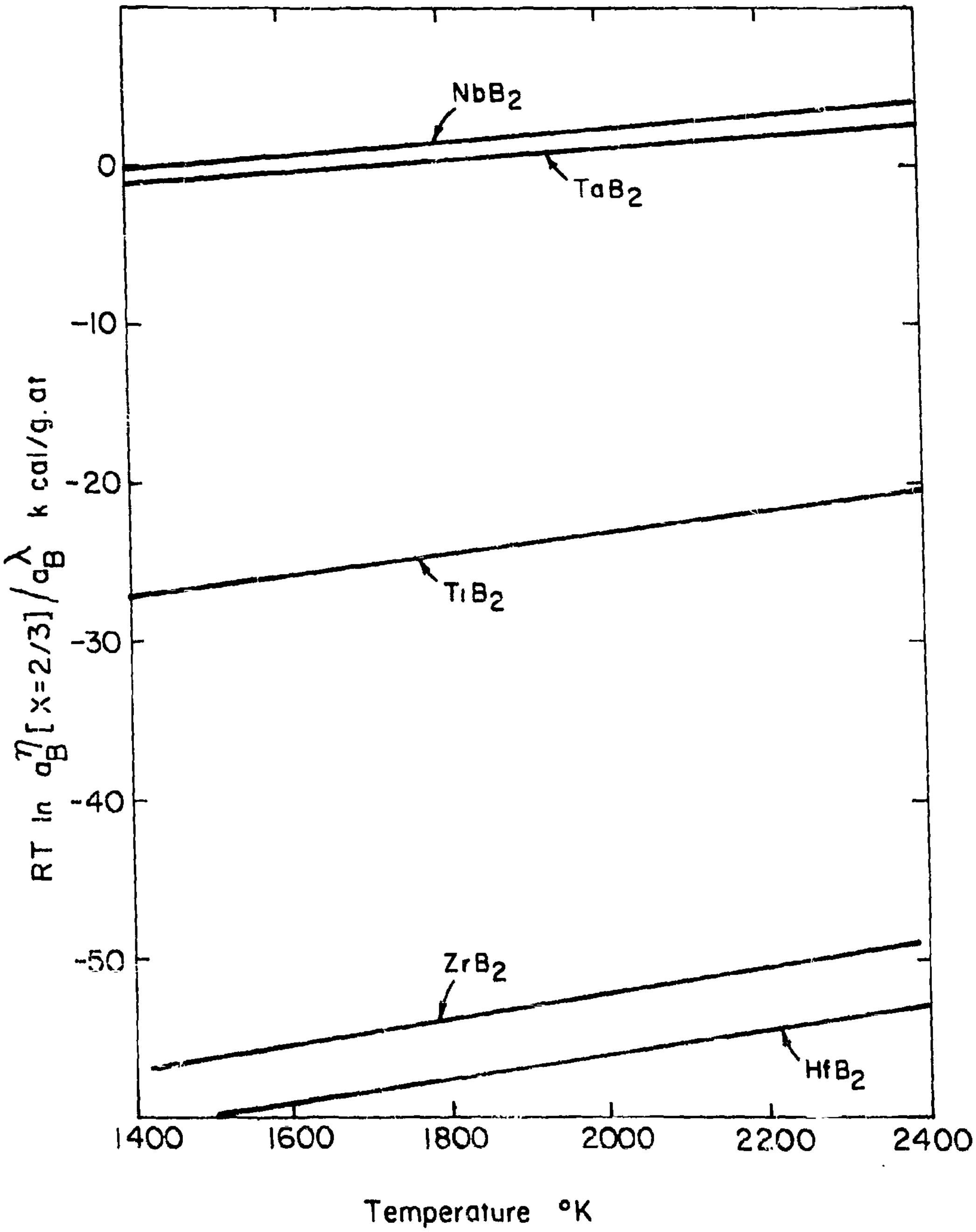

Figure 83. Computed Ratio of Boron Activity in Stoichiometric Diborides, (a_B^η [x = 2/3]) and B_2O_3 (a_B^λ) as a Function of Temperature.

1. Ternary (Me, Mé) B_2 Diborides

In order to extend the treatment of binary diborides (1, 29, 30) to the ternary case where two of the elemental components occupy the metal lattice, we consider a system A-B-C containing a ternary compound having the η crystal structure. The composition is specified by setting (1-x-y) equal to the atom fraction of A, x equal to the atom fraction of B, and y equal to the atom fraction of C. We consider a case where two sublattices exist, the A and B atoms occupying one sublattice, while the C atoms occupy the other (i.e. A = hafnium, B = tantalum, C = boron). If stoichiometry corresponds to $y = y_o$ and the total number of sites, filled and unfilled, is N_s then,

$$N_{sA} = \text{Number of A sites} = (1-x-y)\,(1-y_o)\,(1-y)^{-1}N_s$$
$$N_{sB} = \text{Number of B sites} = x(1-y_o)(1-y)^{-1}N_s$$
$$N_{sC} = \text{Number of C sites} = y_oN_s$$

while

$$N_A = \text{Number of A atoms} = (1-x-y)N$$
$$N_B = \text{Number of B atoms} = xN$$
$$N_C = \text{Number of C atoms} = yN$$

where N is Avogardro's number.

If the ratio of A atoms on A sites, N_{A1}, to A atoms on B sites, N_{A0}, is equal to the ratio of A sites to B sites (ditto for the B atoms) then

$$N_{A0} = \text{Number of A atoms on B sites} = x(1-x-y)\,N(1-y)^{-1}$$
$$N_{A1} = \text{Number of A atoms on A sites} = (1-x-y)^2N(1-y)^{-1}$$

and

$$N_{B0} = \text{Number of B atoms on A sites} = x(1-x-y)N(1-y)^{-1}$$
$$N_{B1} = \text{Number of B atoms on B sites} = x^2N(1-y)^{-1}$$

In line with the standard state convention adopted earlier,(3-5) the free-energy per gram atom F^σ is given by Eq. (9)

$$F^\eta = (1-x-y)F_A^{\,o} + xF_B^{\,o} + yF_C^{\,o} + \left(\frac{N_s}{N}\right)\Delta F^\eta + \frac{N_{A1}}{N}F_{A1} + \frac{N_{B1}}{N}F_{B1} + \frac{N_{C1}}{N}F_{C1}$$
$$+ \frac{N_{A0}}{N}F_{A0} + \frac{N_{B0}}{N}F_{B0} - kT\ \ln W_p \qquad (9)$$

In Eq. 1, $F_A^{\,o}$, $F_B^{\,o}$, and $F_C^{\,o}$ are the free energies of pure A, B, and C at the temperature in question, where

$$F_A^o[0^oK] = F_B^o[0^oK] = F_C^o[0^oK] = 0 \text{ at one atmosphere} \qquad (10)$$

is the reference state. Moreover, ΔF^η is the free energy of formation of the ternary compound for a given value of x and y_o. The free energies of A atoms on B sites and B atoms on A sites are given by F_{A0} and F_{B0}, while F_{A+}, F_{B+}, and F_{C+} are the free energies of formation for A, B, and C vacancies. The numbers of A, B, and C vacancies, which appear in Eq. (9) are given as follows:

$$N_{A+} = \text{Number of vacant A sites} = (1-x-y)(1-y_o)N_s(1-y)^{-1}-(1-x-y)N$$
$$N_{B+} = \text{Number of vacant B sites} = x(1-y_o)N_s(1-y)^{-1}-xN$$
$$N_{C+} = \text{Number of vacant C sites} = y_oN_s - yN$$

The final term to be evaluated in Eq. (9) is the thermodynamic probability factor Wp which is given by,

$$Wp = \frac{N_{sC}!}{N_{C+}!\,N_C!} \quad \frac{N_{sA}!}{N_{A+}!\,N_{A1}!\,N_{B0}!} \cdot \frac{N_{sB}!}{N_{B+}!\,N_{B1}!\,N_{A0}!} \qquad (11)$$

Making the appropriate substitutions for the N_s and applying Stirling's formula and substitution into Eq. (9) yields for the case $y_o = 2/3$

$$\begin{aligned} F^\eta = {} & (1-x-y)F_A^o + xF_B^o + yF_C^o + z\,(\Delta F^\eta_{AC_2} + x(1-y)^{-1}(\Delta F^\eta_{BC_2} - \Delta F^\eta_{AC_2})) \\ & + (\tfrac{1}{3} \quad + y-1)\,(1-y)^{-1}((1-x-y)F_{A+} + xF_{B+}) + (\tfrac{2}{3}z \quad -y)F_{C+} + x(1-x-y)(1-y)^{-1}W \\ & + RT(-\tfrac{z}{3}\ln\frac{4z^3}{27} + y\ln y + x\ln x + (1-x-y)\ln(1-x-y) \\ & + (\tfrac{2}{3}z - y)\ln(\tfrac{2}{3}z - y) + (\tfrac{1}{3}z + y - 1)\ln(\tfrac{1}{3}z + y - 1)) \end{aligned} \qquad (12)$$

where z = ratio of sites to atoms = N_s/N, $W = F_{A0} + F_{B0}$, and the free energy of formation of the ternary compound $\Delta F^\eta[x, y_o]$ has been approximated by a linear combination of the free energies of formation of stoichiometric AC_2 and BC_2 which might represent TaB_2 and HfB_2. Under these conditions Eq. (12) reduces to

$$\begin{aligned} F^\eta = {} & (1-x)F_A^o + xF_B^o + 3\,(\Delta F^\eta_{AC_2} + x(\Delta F^\eta_{BC_2} - \Delta F^\eta_{AC_2})) + 2\,F_{C+} + W\,x(1-x) \\ & + RT\,(x\ln x + (1-x)\ln(1-x)) \end{aligned} \qquad (13)$$

for the case where $y = 0$ and $N_s/N = 3$ which corresponds to a substitutional solid solution of A in B with the C sublattice empty. Eq. (13) is recognizable as being the regular solution approximation for substitutional solid solutions. In the other limits where $x = 0$ or $1-x-y = 0$ (i.e. no B or A atoms are present), Eq. (12) reduces to the equation for the binary compound identical with the expression derived earlier (1, 29, 30).

The next step in the derivation is to fix the composition and minimize the free energy at constant temperature and pressure by letting the volume (i.e. the total number of sites) vary. This procedure is performed by setting the derivative of F^η (Eq. 12) with respect to z at constant x, y, and T equal to 0. The result is

$$3(\Delta F^{\eta}_{AC_2} + x(1-y)^{-1}(\Delta F^{\eta}_{BC_2} - \Delta F^{\eta}_{AC_2})) + (F_{A+} + x(1-y)^{-1}(F_{B+} - F_{A+})) + F_{C+}$$
$$= -3RT \ln 3\,\alpha\, 4^{-1/3} \qquad (14)$$

where

$$-3RT \ln 3\,\alpha\, 4^{-1/3} = RT \ln (4z^3\, 27^{-1})\,(\tfrac{2}{3} z - y)^{-2}(\tfrac{1}{3} z + y - 1)^{-1} \qquad (15)$$

when $y = y_o = 2/3$, $\alpha = 4^{1/3}(z-1)/3z = 0.4^{1/3}(N_s - N)/3N_s$. Thus, as in the binary case,[4] α is the fractional number of vacant sites at stoichiometry. Substitution of Eq. 14 and 15 into Eq. (12), i.e. minimization of the free energy with respect to volume, at constant composition, temperature, and pressure, yields

$$F^{\eta} = (1-x-y)(F^{o}_{A} - F_{A+}) + x(F^{o}_{B} - F_{B+}) + y(F^{o}_{C} - F_{C+}) + x(1-x-y)(1-y)^{-1}W$$
$$+RT(x \ln x + y \ln y + (1-x-y)\ln(1-x-y) - y \ln(\tfrac{2}{3}z - y)$$
$$-(1-y)\ln(\tfrac{1}{3}z + y - 1)) \qquad (16)$$

Eqs. 14, 15 and 16 completely define the temperature and compositional dependence of the free energy in terms of the parameters F_{A+}, F_{B+}, F_{C+}, α and W.

The final step in the present analysis is the derivation of the partial molar free energies. For the case of a binary system (i.e. if y were equal to zero) these relations are well known.

$$\overline{F}_A = F - x\frac{\partial F}{\partial x} \qquad (17)$$

and

$$\overline{F}_B = F + (1-x)\frac{\partial F}{\partial x} \qquad (18)$$

where $\bar{F}_A$ and $\bar{F}_B$ are the partial molar free energies of A and B and x is the atom fraction of B and (1-x) is the atom fraction of A. The analogous expressions for the ternary case are:

$$\bar{F}_A = F - x\left(\frac{\partial F}{\partial x}\right)_y - y\left(\frac{\partial F}{\partial y}\right)_x \tag{19}$$

$$\bar{F}_B = F + (1-x)\left(\frac{\partial F}{\partial x}\right)_y - y\left(\frac{\partial F}{\partial y}\right)_x \tag{20}$$

$$\bar{F}_C = F - x\left(\frac{\partial F}{\partial x}\right)_y + (1-y)\left(\frac{\partial F}{\partial y}\right)_x \tag{21}$$

Since Eqs., 14, 15 and 16 yield:

$$\left(\frac{\partial F}{\partial x}\right)_y = -(F_A^o - F_{A+}) + (F_B^o - F_{B+}) + W(1-2x-y)(1-y)^{-1} + RT\ \ln x(1-x-y)^{-1}$$
$$+ \frac{1}{3} z(1-y)^{-1}(F_{B+} - F_{A+} + 3(\Delta F^\eta_{BC_2} - \Delta F^\eta_{AC_2})) \tag{22}$$

and

$$\left(\frac{\partial F}{\partial y}\right)_x = -(F_A^o - F_{A+}) + (F_C^o - F_{C+}) - Wx^2(1-y)^{-2} + \frac{1}{3}zx(1-y)^{-2}(F_{B+} - F_{A+}$$
$$+ 3(\Delta F^\eta_{BC_2} - \Delta F^\eta_{AC_2})) + RT\ \ln y\left(\frac{1}{3}z + y - 1\right)(1-x-y)^{-1}\left(\frac{2}{3}z - y\right)^{-1} \tag{23}$$

Substitution into Eqs., 19, 20 and 21 yields the expression for the partial molar free energies as follows:

$$\bar{F}_A^\eta - F_A^o = -F_{A+} + Wx^2(1-y)^{-2} - \frac{1}{3}xz(1-y)^{-2}(F_{B+} - F_{A+} + 3(\Delta F^\eta_{BC_2} - \Delta F^\eta_{AC_2}))$$
$$+ RT\ \ln(1-x-y)\left(\frac{1}{3}z + y - 1\right)^{-1} \tag{24}$$

$$\bar{F}_B^\eta - F_B^o = -F_{B+} + W(1-x-y)^2(1-y)^{-2} + \frac{1}{3}(1-x-y)z(1-y)^{-2}(F_{B+} - F_{A+}$$
$$+ 3(\Delta F^\eta_{BC_2} - \Delta F^\eta_{AC_2})) + RT\ \ln x\left(\frac{1}{3}z + y - 1\right)^{-1} \tag{25}$$

$$\bar{F}_C^\eta - F_C^o = -F_{C+} + RT\ \ln y\left(\frac{2}{3}z - y\right)^{-1} \tag{26}$$

Since

$$\bar{F}_A^\eta - F_A^o = RT\ \ln p_A^\eta[x,y]/p_A^o \tag{27}$$

$$\bar{F}_B^\eta - F_B^o = RT\ \ln p_B^\eta[x,y]/p_B^o \tag{28}$$

and

$$\overline{F}_C^{\eta} - F_C^{o} = RT \ln p_C^{\eta}[x,y]/p_C^{o} \tag{29}$$

where $p_A^{\sigma}[x,y]$, $p_B^{\sigma}[x,y]$, and $p_C^{\sigma}[x,y]$ are the pressures of A, B, and C respectively over the alloys and p_A^{o}, p_B^{o}, and p_C^{o} are the corresponding vapor pressures of the pure elements, Eqs. 25 through 29 can be used to compute the vapor pressures of the elements over the alloys.

In particular when $y = y_o = 2/3$

$$\overline{F}_A^{\eta} - F_A^{o} = -F_{A+} + 9Wx^2 - 3x(F_{B+} - F_{A+} + 3(\Delta F_{BC_2}^{\eta} - \Delta F_{AC_2}^{\eta}))$$
$$+ RT \ln \left(\tfrac{1}{3} - x\right)(1 - 3\alpha 4^{-1/3})\, 4^{1/3} \alpha^{-1} \tag{30}$$

$$\overline{F}_B^{\eta} - F_B^{o} = -F_{B+} + 9W\left(\tfrac{2}{3} - x\right)^2 + 2(0.5 - x)(F_{B+} - F_{A+} + 2(\Delta F_{BC}^{\eta} - \Delta F_{AC}^{\eta}))$$
$$+ RT \ln x(1 - 3\alpha 4^{-1/3})\, 4^{1/3} \alpha^{-1} \tag{31}$$

and

$$\overline{F}_C^{\eta} - F_C^{o} = -F_{C+} + RT \ln 4^{1/3}(1 - 3\alpha 4^{-1/3})\, 3^{-1} \alpha^{-1} \tag{32}$$

where z can be approximated by unity.

When y is less than 2/3, $z \approx 3(1-y)$ and $(\frac{1}{3}z + y - 1)$ is approximately equal to $27\alpha^3(1-y)^3(2-3y)^{-2}$. Under these conditions Eqs. 24 through 26 reduce to

$$\overline{F}_A^{\eta} - F_A^{o} = -F_{A+} + Wx^2(1-y)^{-2} - x(1-y)^{-1}(F_{B+} - F_{A+} + 3(\Delta F_{BC_2}^{\eta} - \Delta F_{AC_2}^{\eta}))$$
$$+ RT \ln (1-x-y)(2-3y)^2\, 27^{-1} \alpha^{-3}(1-y)^{-3} \tag{33}$$

$$\overline{F}_B^{\eta} - F_B^{o} = -F_{B+} + W(1-x-y)^2(1-y)^{-2} + (1-x-y)(1-y)^{-1}(F_{B+} - F_{A+} + 3(\Delta F_{BC_2}^{\eta} - \Delta F_{AC_2}^{\eta}))$$
$$+ RT \ln x(2-3y)^2\, 27^{-1} \alpha^{-3}(1-y)^{-3} \tag{34}$$

and

$$\overline{F}_C^{\eta} - F_C^{o} = -F_{C+} + RT \ln y(2-3y)^{-1} \tag{35}$$

When y is greater than 2/3, $z \approx \frac{3}{2}y$, and $(\frac{2}{3}z - y)^2$ is approximately $27\alpha^3 y^3 4^{-1}(3y-2)^{-1}$ and

$$\overline{F}_A^{\eta} - F_A^{o} = -F_{A+} + Wx^2(1-y)^{-2} - \frac{1}{2}xy(1-y)^{-2}(F_{B+} - F_{A+} + 3(\Delta F^{\eta}_{BC_2} - \Delta F^{\eta}_{AC_2}))$$
$$+RT\ \ln(1-x-y)\ 2(3y-2)^{-1} \qquad (36)$$

$$\overline{F}_B^{\eta} - F_B^{o} = -F_{B+} + W(1-x-y)^2(1-y)^{-2} + \frac{1}{2}(1-x-y)y(1-y)^{-2}(F_{B+} - F_{A+} + 3(\Delta F^{\eta}_{BC} - \Delta F^{\eta}_{AC}))$$
$$+RT\ \ln x\ 2(3y-2)^{-1} \qquad (37)$$

$$\overline{F}_C^{\eta} - F_C^{o} = -F_{C+} + \frac{1}{2}RT\ \ln 4(3y-2)\ 27^{-1}y^{-1}\alpha^{-3} \qquad (38)$$

It should be noted that equations (30-38) reduce exactly to those derived previously for binary diborides (1, 29, 30) when $x = 0$.

2. Ternary Me $(B,X)_2$ Diborides

In the case where two of the elemental components occupy the boron lattice (i.e. additions of Si or Al to the metal diboride are possible examples), the development is similar to Section C-1 with the following changes. We consider a system A-B-C containing a ternary compound having the η crystal structure with $(1-x-y)$ atom fractions of A, x atom fractions of B, and y atom fractions of C. Here A and B atoms occupy the "boron" lattice and C is the metal atom (i.e. A = silicon, B = boron, and C = hafnium). In this case $y_o = 1/3$ since y is the atom fraction of metal and y_o is the value of y at stoichiometry. Thus the development of Section C-1 through Eq.(11) is directly applicable. However, in the present case the value $y_o = 1/3$ must be used (rather than $y_o = 2/3$) in order to obtain the analogue of Eq. (12).

Making the appropriate substitutions for the N_s and applying Stirling's formula and substitution into Eq. (11) yields for the case $y_o = 1/3$

$$F^{\eta} = (1-x-y)F_A^{o} + xF_B^{o} + yF_C^{o} + z(\Delta F^{\eta}_{CA_2} + x(1-y)^{-1}(\Delta F^{\eta}_{CB_2} - \Delta F^{\eta}_{CA_2}))$$
$$+(\frac{2}{3}z + y - 1)(1-y)^{-1}((1-x-y)F_{A+} + xF_{B+}) + (\frac{1}{3}z - y)F_{C+} + x(1-x-y)(1-y)^{-1}W$$
$$+RT(-\frac{z}{3}\ln\frac{4z^3}{27} + y\ln y + x\ln x + (1-x-y)\ln(1-x-y)$$
$$+(\frac{1}{3}z - y)\ln(\frac{1}{3}z - y) + (\frac{2}{3}z + y - 1)\ln(\frac{2}{3}z + y - 1)) \qquad (39)$$

where z = ratio of sites to atoms = N_s/N, $W = F_{A0} + F_{B0}$, and the free energy of formation of the ternary compound $\Delta F^{\eta}[x, y_o]$ has been approximated by a linear combination of the free energies of formation of stoichiometric CB_2 and CA_2 which might represent HfB_2 and a $HfSi_2$ "η type" compound. Under these conditions Eq. (39) reduces to

$$F^{\eta} = (1-x)F_A^o + F_B^o + \frac{3}{2}(\Delta F^{\eta}_{CA_2} + x(\Delta F^{\eta}_{CB_2} - \Delta F^{\eta}_{CA_2}) + \frac{1}{2}F_{C+}) + W\,x(1-x)$$

$$+RT\,(x \ln x + (1-x)\ln(1-x)) \qquad (40)$$

for the case where $y = 0$ and $N_s/N = \frac{3}{2}$ which corresponds to a substitutional solid solution of A in B with the C sublattice empty. Eq. (40) is recognizable as being the regular solution approximation for substitutional solid solutions. In the other limits where $x = 0$ or $1-x-y = 0$ (i.e. no B or A atoms are present), Eq. (39) reduces to the equation for the binary compound identical with the expression derived earlier (1, 29, 30).

Fixing the composition and minimizing the free energy at constant temperature and pressure by letting the volume (i.e. the total number of sites) vary as before yields:

$$3(\Delta F^{\eta}_{CA_2} + x(1-y)^{-1}(\Delta F^{\eta}_{CB_2} - \Delta F^{\eta}_{CA_2})) + 2(F_{A+} + x(1-y)^{-1}(F_{B+} - F_{A+})) + F_{C+}$$

$$= -3RT \ln 3\alpha 4^{-\frac{1}{3}} \qquad (41)$$

where

$$-3RT \ln 3\alpha\, 4^{-\frac{1}{3}} = RT \ln \frac{z^3 4}{27}\left(\frac{2}{3}z + y - 1\right)^{-2}\left(\frac{1}{3}z - y\right)^{-1} \qquad (42)$$

when $y = y_o = \frac{1}{3}$, $\alpha = 4^{\frac{1}{3}}(z-1)/3z = 4^{\frac{1}{3}}(N_s - N)/3N_s$. Thus, as in the binary case, α is the fractional number of vacant sites at stoichiometry. Substitution of Eqs. 41 and 42 into Eq. (39), i.e. minimization of the free energy with respect to volume, at constant composition, temperature, and pressure, yields

$$F^{\eta} = (1-x-y)(F_A^o - F_{A+}) + x(F_B^o - F_{B+}) + y(F_C^o - F_{C+}) + x(1-x-y)(1-y)^{-1}W$$

$$+RT(x \ln x + y \ln y + (1-x-y)\ln(1-x-y) - y \ln(\frac{1}{3}z - y) - (1-y)\ln(\frac{2}{3}z + y - 1)) \quad (43)$$

Eqs. 41, 42 and 43 define the temperature and compositional dependence of the free energy in terms of the parameters F_{A+}, F_{B+}, F_{C+}, α and W.

Eqs., 41-43 yield

$$\left(\frac{\partial F}{\partial x}\right)_y = -(F_A^o - F_{A+}) + (F_B^o - F_{B+}) + W(1-2x-y)(1-y)^{-1} + RT \ln x(1-x-y)^{-1}$$

$$+\frac{1}{3}z\,(1-y)^{-1}(2(F_{B+} - F_{A+}) + 3(\Delta F^{\eta}_{CB_2} - \Delta F^{\eta}_{CA_2})) \qquad (44)$$

and

$$\left(\frac{\partial F}{\partial x}\right)_y = -(F_A^o - F_{A+}) + (F_C^o - F_{C+}) - Wx^2(1-y)^{-2} + \frac{1}{3}zx(1-y)^{-2}(2(F_{B+} - F_{A+})$$

$$+3(\Delta F^\eta_{CB_2} - \Delta F^\eta_{CA_2})) + RT \ln y\left(\frac{2}{3}z + y - 1\right)(1-x-y)^{-1}\left(\frac{1}{3}z - y\right)^{-1} \qquad (45)$$

Substitution of 43-45 into Eqs., 19, 20 and 21 yields the following expressions for the partial molar free energies:

$$\overline{F}^\eta_A - F_A^o = -F_{A+} + Wx^2(1-y)^{-2} - \frac{1}{3}xz(1-y)^{-2}(2(F_{B+} - F_{A+}) + 3(\Delta F^\eta_{CB_2} - \Delta F^\eta_{CA_2}))$$

$$+ RT \ln (1-x-y)\left(\frac{2}{3}z + y - 1\right)^{-1} \qquad (46)$$

$$\overline{F}^\eta_B - F_B^o = -F_{B+} + W(1-x-y)^2(1-y)^{-2} + \frac{1}{3}(1-x-y)z(1-y)^{-2}(2(F_{B+} - F_{A+})$$

$$+3(\Delta F^\eta_{CB_2} - \Delta F^\eta_{CA_2})) + RT \ln x\left(\frac{2}{3}z + y - 1\right)^{-1} \qquad (47)$$

$$\overline{F}^\eta_C - F_C^o = -F_{C+} + RT \ln y\left(\frac{1}{3}z - y\right)^{-1} \qquad (48)$$

Since

$$\overline{F}^\eta_A - F_A^o = RT \ln p^\eta_A[x,y]/p_A^o \qquad (49)$$

$$\overline{F}^\eta_B - F_B^o = RT \ln p^\eta_B[x,y]/p_B^o \qquad (50)$$

and

$$\overline{F}^\eta_C - F_C^o = RT \ln p^\eta_C[x,y]/p_C^o \qquad (51)$$

where $p^\eta_A[x,y]$, $p^\eta_B[x,y]$, and $p^\eta_C[x,y]_o$ are the pressures of A, B, and C respectively over the alloys and p_A^o, p_B, and p_C^o are the corresponding vapor pressures of the pure elements, Eqs. 49 through 51 can be used to compute the vapor pressures of the elements over the alloys.

In particular when $y = y_o = \frac{1}{3}$

$$\overline{F}^\eta_A - F_A^o = F_{A+} + \frac{9}{4}Wx^2 - \frac{3}{4}x(2(F_{B+} - F_{A+}) + 3(\Delta F_{CB_2}^\eta - \Delta F_{CA_2}^\eta))$$

$$+ RT \ln \left(\frac{2}{3} - x\right)\left(1 - 3\alpha 4^{-\frac{1}{3}}\right)\alpha^{-1} 2^{-\frac{1}{3}} \qquad (52)$$

$$\overline{F}_B^{\eta} - F_B^o = - F_{B+} + \frac{9}{4} W \left(\frac{2}{3} - x\right)^2 + \frac{3}{4}\left(\frac{2}{3} - x\right) (2(F_{B+} - F_{A+}) + 3 (\Delta F^{\eta}_{CB_2} - \Delta F^{\eta}_{CA_2}))$$

$$+RT \ln x (1 - 3 \alpha 4^{-1/3}) \alpha^{-1} 2^{-1/3} \qquad (53)$$

and

$$\overline{F}_C^{\eta} - F_C^o = - F_{C+} + RT \ln 4^{1/3} (1 - 3 \alpha 4^{-1/3}) 3^{-1} \alpha^{-1} \qquad (54)$$

where z can be approximated by unity.

When y is less than $\frac{1}{3}$, $z \approx 1.5 (1-y)$ and $(2z3^{-1} + y - 1)^2$ is approximately equal to $4 \alpha^2 (1-y)^2 (1-2y)^{-1}$. Under these conditions Eqs. 27 through 29 reduce to

$$\overline{F}_A^{\eta} - F_A^o = - F_{A+} + W x^2 (1-y)^{-2} - 2^{-1} x (1-y)^{-1} (2(F_{B+} - F_{A+}) + 3(\Delta F^{\eta}_{CB_2} - \Delta F^{\eta}_{CA_2}))$$

$$+2^{-1} RT \ln (1-x-y)^2 (1-3y) 4 \alpha^{-3} (1-y)^{-3} 27^{-1} \qquad (55)$$

$$\overline{F}_B^{\eta} - F_B^o = - F_{B+} + W(1-x-y)^2 (1-y)^{-2} + 2^{-1} (1-x-y)(1-y)^{-1} (2(F_{B+} - F_{A+})$$

$$3(\Delta F^{\eta}_{CB_2} - \Delta F^{\eta}_{CA_2})) + 2^{-1} RT \ln x^2 (1-3y) 4 \alpha^{-3} (1-y)^{-3} 27^{-1} \qquad (56)$$

and

$$\overline{F}_C^{\eta} - F_C^o = - F_{C+} + RT \ln 2y (1-3y)^{-1} \qquad (57)$$

When y is greater than $\frac{1}{3}$, $z \approx 3y$, and $(3^{-1}z - y)$ is approximately $27 \alpha^3 y^3 (3y-1)^{-2}$. Thus,

$$\overline{F}_A^{\eta} - F_A^o = - F_{A+} + W x^2 (1-y)^{-2} - xy(1-y)^{-2} (2(F_{B+} - F_{A+}) + 3(\Delta F^{\eta}_{CB_2} - \Delta F^{\eta}_{CA_2}))$$

$$+RT \ln (1-x-y) (3y-1)^{-1} \qquad (58)$$

$$\overline{F}_B^{\eta} - F_B^o = - F_{B+} + W(1-x-y)^2 (1-y)^{-2} + (1-x-y) y (1-y)^{-2} (2(F_{B+} - F_{A+}) + 3(\Delta F^{\eta}_{CB_2} - \Delta F^{\eta}_{CA_2}))$$

$$+RT \ln x (3y-1)^{-1} \qquad (59)$$

$$\overline{F}_C^{\eta} - F_C^o = - F_{C+} + RT \ln (3y-1)^2 27^{-1} \alpha^{-3} y^{-2} \qquad (60)$$

These equations are explicit if W is known or approximated by zero.

3. <u>Evaluation of the Calculated Thermodynamic Effect of Ternary Additions on the Boron Activity</u>

It is now appropriate to consider the results of the formal calculations for the metal rich case where the third element enters the η phase on the metal lattice (Eqs. 33-35) and for the metal rich case where the third element enters the η phase on the boron lattice (Eqs. 58-60). Taking the former case first. Eq. 35 gives the activity of boron as

$$RT \ln a_B^{\eta} = - F_{B+}^{\eta} + RT \ln B\ (2-3B)^{-1} \qquad (61)$$

where F_{B+}^{η} is the free energy of formation of boron vacancies in the ternary (Hf, Me) B_2 or (Zr, Me) B_2 diboride which is metal rich. In this equation, B represents the atomic fraction of boron in the ternary compound. The free energy of formation of boron vacancies is known [3,4] for the case where the atom fraction of metal is zero (i.e. for the pure diboride). If the fraction of Me is small, one can assume that the change in F_{B+}^{η} due to Me additions might be small. The corresponding expression for metal rich Hf $(B,X)_2$ or $Zr(B,X)_2$ is given by Eq. 59. Approximating W = 0 and the atom fraction of X = A small (i.e. 1-x-y small) yields

$$RT \ln a_B^{\eta} = - F_{B+}^{\eta} + RT \ln B\ (2-3B-3X)^{-1} \qquad (62)$$

where X is the atom fraction of element X. Thus if we neglect the effects of Me and X on F_{B+}, we find that for <u>metal-rich</u> ternary diborides

$$a_B^{\eta}\,[Hf(B,X)_2]/a_B^{\eta}[(Hf,\ Me)B_2] \simeq 1-(3X)/(2-3B) \qquad (63)$$

where B + X must be less than 2/3 to preserve the metal rich condition (hence $3X < 2-3B$). Reference to Eq. (63) indicates that

a) additions of a third element which enters the boron sublattice to metal rich diborides is likely to produce a greater lowering of the boron activity than the addition of a third element which enters the metal sublattice in metal-rich diborides

b) as the atomic fraction of X increases the activity of Boron decreases.

The total quantity of X which can be substituted into the η phase will be limited by the ternary phase relations (i.e. how much X can be substituted into the η phase before an alternate Me-X. B-X or ternary Me-B-X compound precipitates)and by the vaporization of X. Thus, according to Eq. 58.

$$RT \ln p_X^{\eta} / p_X^{o} \approx - F_{X+}^{\eta} + RT \ln X\,(2-3B-3X)^{-1} \tag{64}$$

where F_{X+}^{η} is the free energy of formation of X vacancies in the η phase. This quantity is usually a positive number. Since the vapor pressure of pure silicon is of the order of 10^{-2} atm. at 2500°K, then if X is silicon, reduction of the silicon pressure over the η phase to 10^{-6} (comparable to boron in metal rich HfB_2 or ZrB_2 [3,4]) at this temperature would require the right side of Eq. (64) to be -46 k cal/g at. At 2500°K, F_{B+}^{η} is about 44 k cal/g. at. Thus, if F_{Si+}^{η} was equal to F_{B+}^{η}, values of p_{Si}^{η} equal to or less than 10^{-6} atmospheres could be obtained if

$$Si\,(2-3B-3Si)^{-1} \leq \frac{2}{3} \tag{65}$$

Defining the ratio of B+ Si to Hf by R (where R is less than 2)

$$3\,R\,Hf = 3(B + Si) \tag{66}$$

or

$$\frac{Si}{(2 - 3\,R\,Hf)} \leq \frac{2}{3} \tag{67}$$

with Hf near $\frac{1}{3}$ yields

$$\frac{Si}{(2 - R)} \leq \frac{2}{3} \tag{68}$$

Thus, if the boron + silicon to metal ratio is about 1.9 then silicon additions up to 0.066 atomic fraction or 6.6% should not produce vapor pressures of silicon in excess of 10^{-6} atmospheres at 2500°K. Reference to Eq. (63) shows that the addition of the maximum amount of Si allowed by Eq. (68) would lower the boron activity by a factor of three.

D. Comparison of the Volumes of HfB_2 vs. HfO_2 and ZrB_2 - ZrO_2

In order to compare the volumetric constraints at the oxide/ diboride interface, the volumes of HfO_2, ZrO_2, TiO_2, NbO_2 and Ta_2O_5 were computed at 25°C(38). These volumes are compared with corresponding values for the diborides (39) in Table 22. The results indicate that the "matching order" corresponds to the order of oxidation resistance except that ZrB_2 and HfB_2 are interchanged. It is difficult to make this comparison at high temperatures due to the lack of accurate data on the volume of the oxides. However, the following computations were performed for the HfB_2/ HfO_2 and ZrB_2/ ZrO_2. For ZrB_2 and HfB_2, the results of this study (1, 40) yield

TABLE 22

COMPARISON OF DIBORIDE AND OXIDE VOLUMES AT 25°C

Diboride	Volume[9] $cm^3/g.$ at	MeO_2 Volume[8] $cm^3/g.$ at	Percentage Difference
ZrB_2	6.17	7.05	13.3
HfB_2	5.97	6.86	13.9
TiB_2	5.15	6.26	19.5
NbB_2	5.48	7.03	24.8
		Ta_2O_5 Volume	
TaB_2	5.32	7.35	32.0
		(7/6)Ta_2O_5 Volume* 8.57	46.7

* One gm. atom of TaB_2 contains (1/3) N tantalum atoms. One gm. atom of Ta_2O_5 contains (2/7) N tantalum atoms. Hence (7/6) gm. atoms of Ta_2O_5 contains the same number of tantalum atoms as one gm. atom of TaB_2.

$$V^{\eta}[ZrB_2, T] \approx 6.17 + 1.18 \times 10^{-4}\, T(^{\circ}C) \quad cm^3/g.at \tag{69}$$

and

$$V^{\eta}[HfB_2, T] \approx 5.97 + 1.22 \times 10^{-4}\, T(^{\circ}C) \quad cm^3/g.at \tag{70}$$

for $25^{\circ}C \leq T \leq 1600^{\circ}C$.

For the oxides, the following procedure was used. The expansion coefficient of monoclinic ZrO_2 was taken from dilatometric measurements (41) yielding

$$V^{\mu}[ZrO_2, T] \approx 7.05 + 1.70 \times 10^{-4}\, T(^{\circ}C) \; cm^3/g.at \tag{71}$$

for $T < 1100^{\circ}C$. The volume of the tetragonal form of ZrO_2 (T) was computed from X-ray measurements at about $1200^{\circ}C$ (42, 43) and the assumption that the expansion coefficient of the μ and T phases were equal. Thus

$$V^{T}[ZrO_2, T] \approx 6.80 + 1.70 \times 10^{-4}\, T(^{\circ}C) \quad cm^3/g.\ at \tag{72}$$

for $T > 1200^{\circ}C$

The volumetric calculations for HfO_2 were performed using lattice parameter data at 25 (42, 44), 1640 (44) and $1920^{\circ}C$ (44), assuming that the expansion coefficients of the T and μ phases are equal. Thus

$$V^{\mu}[HfO_2, T] \approx 6.86 + 2.29 \times 10^{-4}\, T(^{\circ}C) \quad cm^3/g.at \tag{73}$$

for $T < 1700^{\circ}C$, and

$$V^{T}[HfO_2, T] \approx 6.52 + 2.29 \times 10^{-4}\, T(^{\circ}C) \quad cm^3/g.\ at \tag{74}$$

for $T > 1800^{\circ}C$. Figure 84 shows the volume temperature relations for the ZrB_2/ZrO_2 and HfB_2/HfO_2 cases as functions of temperature. Reference to Figure 84 and Eqs. (69-74) indicates that at $1800^{\circ}C$, $V^{\eta}[ZrB_2] \approx 6.38\ cm^3/g.at$ and $V^{T}[ZrO_2] \approx 7.11\ cm^3/g.at$, while $V^{\eta}[HfB_2] \approx 6.19\ cm^3/g.at.$ and $V^{T}[ZrO_2] \approx 6.93$. Thus at $1800^{\circ}C$ the percentage volume differences are about 11.4% for both cases.

On the basis of these considerations, stabilization of a cubic ZrO_2 or HfO_2 with a gram atomic volume nearer the diboride might provide enhanced oxidation resistance.

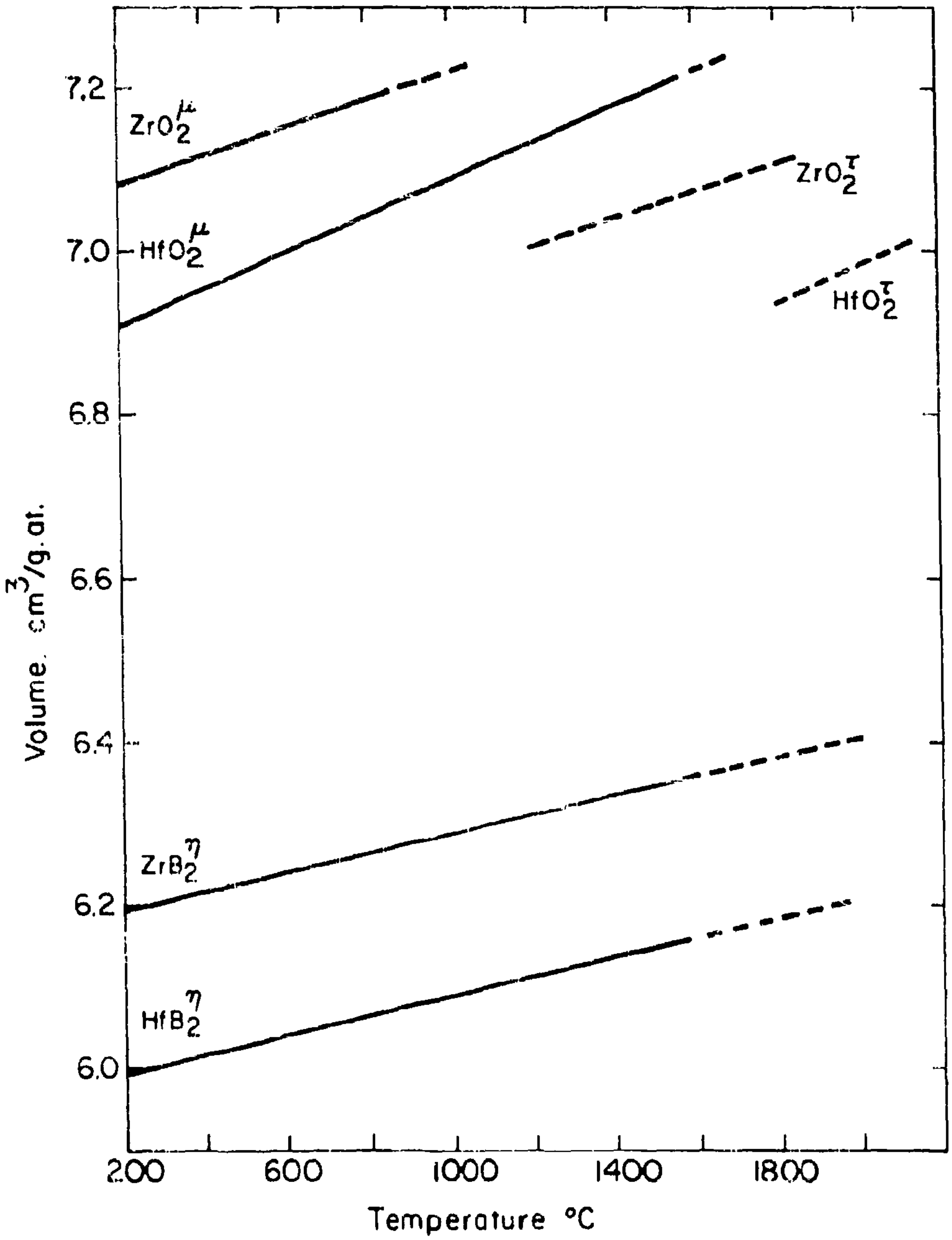

Figure 84. Comparison of ZrB_2/ZrO_2 and HfB_2/HfO_2 Volumes.

References

1. Kaufman, L. and Clougherty, E. V., "Investigation of Boride Compounds for Very High Temperature Applications", RTD-TDR-63-4096, December (1963).

2. Dickenson, C. D. and Siegle, L. L., "Experimental Studies of Factors Controlling the Effectiveness of High Temperature Protective Coatings for Tungsten", ASD-TDR-63-744, July (1963).

3. Siegle, L. L., et. al., "Experimental Studies of Factors Controlling the Effectiveness of High Temperature Protective Coatings for Tungsten", Fifth Progress Report AF33(657)-8787, 1 March 1964.

4. Boone, J. L. and Campbell, G. W., Jr., in Reference 1 pp. 19-46.

5. Bernstein, H., in Reference 1 pp. 121-155.

6. Kriege, O. H., "The Analysis of Refractory Borides, Carbides, Nitrides, and Silicides", LA-2306, Los Alamos Scientific Laboratory of the University of California.

7. Clougherty, E. V. and Kaufman, L., "Fundamental Study of Sintering Kinetics of Refractory Compound Phases at High Pressures and High Temperatures", Technical Report, Contract No. NONR-4262, ManLabs, Inc., Cambridge, Mass., October (1964).

8. Coble, R. L. and Hobbs, H. A., in Reference 1 pp. 82-119.

9. Coble, R. L., J. App. Phys., (1961) 32 787.

10. Brophy, J. H., Shepard, L. A., and Wulff, J., "The Nickel Activated Sintering of Tungsten", in Powder Metallurgy, W. Leszynski, Ed., Interscience Publishers, New York (1961), pp. 113-134.

11. Bird, R. B., Stewart, W. E. and Lightfoot, E. N., Transport Phenomena, John Wiley & Sons, Inc., New York (1960).

12. McClaine, L. A., "Thermodynamic and Kinetic Studies for a Refractory Materials Program", ASD-TDR-62-204, Part 2, Arthur D. Little, Inc., May (1963).

13. McClaine, L. A., "Thermodynamic and Kinetic Studies for a Refractory Materials Program", ASD-TDR-62-204, Part 3, Arthur D. Little, Inc., April (1964).

14. Berkowitz-Mattuck, J., "High Temperature Oxidation. I. A Thermal Conductivity Method for Oxidation Measurements", J. Electrochem. Soc., ADL (1964) 111 908.

15. Berkowitz-Mattuck, J., "Oxidation in the Mo-Si System", ASD-TDR-62-203, Part 2, Arthur D. Little, Inc., March (1963).

16. Dickenson, C. D. and Nicholas, M., General Telephone and Electronics ASD-TDR-62-205, Part 2, Figure 26.

17. Stringer, J., "Alloying for Oxidation Protection", a talk delivered at Grumman Aircraft Co., Bethpage, L. I., April 8, 1964.

18. Kubaschewski, O. and Hopkins, B.E., Oxidation of Metals and Alloys, sec. ed., Academic Press, N. Y. (1962).

19. Kofstad, P. and Ruzicka, D.J., J. Electrochem. Soc. (1963) 110 181.

20. Levin, E.M. and McMurdie, H.F., "Phase Diagrams for Ceramists", The Am. Ceram. Soc. (1959).

21. Armitage, J.V. and Rapp, R.A., SIAM Review (1963) 5 67.

22. Jun, C.K. and Hoch, M., "The Thermal Conductivity of Diborides at Elevated Temperatures", Conference on Thermal Conductivity, National Physical Laboratory, Teddington, Middlesex, England July (1964).

23. Hoch, M., et.al., "New Method for the Determination of Thermal Conductivity between 1000° and 3000°C" in Progress in International Research on Thermodynamic and Transport Properties, Edit. J.S. Mari and D.H. Tsai, Academic Press Inc., New York, (1962); Nitti, D.A., M. S. Thesis, University of Cincinnati, (1961).

24. Hoch, M., and Narasimhamurty, H.V.L., "Relation between Specific Heat and Emissivity of Tantalum at Elevated Temperature", ASD-TDR-63-371, University of Cincinnati, Cincinnati, Ohio.

25. Pears, C.D. and Oglesby, S., "The Thermal Properties of Twenty-Six Solid Materials to 5000°F or Their Destruction Temperature" ASD-TDR-62-765, Southern Research Institute, April (1962).

26. Mandorf, V., Hartwig, J., and Seldin, E.J., "High Temperature Properties of TiB_2", Fostoria Development Laboratory, National Carbon Company, Technical Memorandum TMC-49, Fostoria, Ohio, April (1961).

27. Norton, J.T., et.al., Trans. A.I.M.E. (1949) 185 749.

28. Glaser, F.W., J. Metals (1952) 4 391.

29. Kaufman, L., "Thermodynamic Properties of Transition Metal Diborides", Compounds of Interest in Nuclear Reactor Technology, Edited by J.T. Waber and P. Chiotti, Edwards Brothers, Ann Arbor, Michigan, (1964).

30. Kaufman, L. and Clougherty, E. V., "Thermodynamic Factors Controlling the Stability of Solid Phases at High Temperatures and Pressures", Metallurgy at High Pressures and Temperatures Edited by K. Gschneider, N. Parlee and M. T. Hepworth, Gordon and Breech, N. Y., N. Y. (1964).

31. Schissel, P. O. and Trulson, O. C., J. Phys. Chem. (1962) 66 1492.

32. Krikorian, O. H., University of California Radiation Laboratory Report No. UCRL-2888 (1955).

33. Kaufman, L., Tr. A.I.M.E. (1962) 224 1006.

34. Glaser, F. W., and Post, B., Trans. A.I.M.E. (1953) 197 1117.

35. Schedler, W., Dissert. Techn. Hochsch. Graz. (1952).

36. Nowotny, H., Braun, H., and Benesovsky, F., Radex-Rundschau (1960) 6 367.

37. Nowotny, H., Rudy, E., and Benesovsky, F., Monat. fur Chem. (1961) 92 393.

38. Pearson, W. B., Handbook of Lattice Spacings, Pergamon Press, London (1958).

39. Kaufman, L., in Reference 1 p. 287.

40. Bernstein, H., "Debye Temperature Measurements and Thermodynamic Properties of HfB_2, ZrB_2, HfC, and ZrC", Compounds of Interest in Nuclear Reactor Technology, Edited by J. T. Waber and P. Chiotti, Gordon and Breech Science Publishers, New York, N. Y. (1964).

41. Geller, R. F. and Yavorsky, J., J. of Research, N.B.S. (1945) 35 87, Research Paper RP1662.

42. Adam, J. and Rogers, M. D., Acta. Cryst. (1959) 12 951.

43. Teufer, G., Acta. Cryst. (1962) 15 1187.

44. Curtis, C. F., Doney, L. M., and Johnson, J. R., J. Am. Ceram. Soc. (1954) 37 458.

APPENDIX

CHEMICAL AND SPECTROSCOPIC ANALYSES OF SAMPLES FABRICATED BY HIGH PRESSURE HOT PRESSING

Powder Material*	Sample No.	Spectroscopic** Qualitative (Range w/o)	Spectroscopic** Quantitative (w/o)	Quantitative Chemical † Me (w/o)	B (w/o)	B/Me	Other
HfB_2(1)	R1	N. D.		88.3	10.5	1.96	
HfB_2(2A)	R38-3	Mn: .01-0.1		89.3	10.0	1.85	
		Fe: .01-0.1	.007				
	R45	N. D.		87.9	10.0		
				87.0	10.2	1.88	
	R51	Neg.		N.D.	N.D.		
HfB_2(2)	R32	Neg.		N.D.	N.D.		
	R21	Si: 0.1 -1.0	0.38	N.D.	N.D.		
		Al: .01-0.1	0.023				
	R29-4	Al: .01-0.1	0.036	87.5	10.5	1.98	
		Mn: .01-0.1	0.018				
	R28-6	Al: 0.1 -1.0	0.032	N.D.	N.D.		
		Si: 0.1 -1.0	0.18				
		Mn: .01-0.1	0.013				
	R30	N.D.		87.2	N.D.		
	R49	Neg.		N.D.	N.D.		
	R52	N.D.		N.D.	N.D.		N: 0.06
ZrB_2(1)	R1	N.D.		80.6	17.55	1.83	
	R26	N.D.		80.9	17.6	1.83	
	R28	Neg.		N.D.	N.D.		
	R30	Neg.		N.D.	N.D.		
	R43	N.D.		N.D.	N.D.		N: 0.19

APPENDIX (CONT.)

CHEMICAL AND SPECTROSCOPIC ANALYSES OF SAMPLES FABRICATED BY HIGH PRESSURE HOT PRESSING

Powder Material*	Sample No.	Spectroscopic** Qualitative (Range w/o)	Spectroscopic** Quantitative (w/o)	Quantitative Chemical † Me (w/o)	Quantitative Chemical † B (w/o)	Quantitative Chemical † B/Me	Quantitative Chemical † Other
ZrB_2(P)	R5	Si: 0.1 -1.0 Ti: 0.01-0.1 Mo: 0.01-0.1		N.D.	N.D.		
ZrB_2(1) + Zr+Si ($ZrB_{1.75}Si_{0.25}$)	A20	N.D.		N.D.	16.5		
HfB_2(2) + Hf ($HfB_{1.7}$)	A15	N.D.		89.2	-		
HfB_2(2)+ Hf+Si ($HfB_{1.7}Si_{0.25}$)	A19	N.D.		87.4	9.8		Si:3.7

* The powder materials are identified and described in Section III.

** The Spectroscopic analyses were performed by the Jarrell Ash Co., Newton, Mass. The letters N.D. signify "not determined"; Neg., negligible amounts of metallic impurities found.

† The chemical analyses which are not underscored were performed by the methods recommended by the Los Alamos Laboratory (see Reference) by Mr. Donald Gurnsey, Metallurgy Department, M.I.T. The underscored analyses were performed at ManLabs by the pyrohydrolysis method as described in the reports by Union Carbide Research Institute, Tarrytown, N.Y., on the program entitled "Research on Physical and Chemical Principles Affecting High Temperature Materials for Rocket Nozzles", Progress Reports from June 30, 1963 through Dec. 31, 1964.

DOCUMENT CONTROL DATA - R&D

(Security classification of title, body of abstract and indexing annotation must be entered when the overall report is classified)

1. ORIGINATING ACTIVITY (Corporate author) ManLabs, Inc. 21 Erie Street Cambridge, Massachusetts		2a. REPORT SECURITY CLASSIFICATION UNCLASSIFIED 2b. GROUP N/A
3. REPORT TITLE Investigation of Boride Compounds for Very High Temperature Applications		
4. DESCRIPTIVE NOTES (Type of report and inclusive dates) Technical Documentary Report, October 1963-November 1964		
5. AUTHOR(S) (Last name, first name, initial) Kaufman, Larry and Clougherty, Edward V.		
6. REPORT DATE February 1965	7a. TOTAL NO. OF PAGES 180	7b. NO. OF REFS 44
8a. CONTRACT OR GRANT NO. AF33(657)-8635 b. PROJECT NO. 7350 c. Task No. 735001 d.	9a. ORIGINATOR'S REPORT NUMBER(S) TRD-TDR-63-4096 Part II 9b. OTHER REPORT NO(S) (Any other numbers that may be assigned this report) N/A	
10. AVAILABILITY/LIMITATION NOTICES "Qualified requesters may obtain copies of this report from DDC" "(DDC release of this report to OTS NOT AUTHORIZED)"		
11. SUPPLEMENTARY NOTES N/A	12. SPONSORING MILITARY ACTIVITY R.T.D. AFML(MAMC), W-PAFB, Ohio	

13. ABSTRACT The earlier prediction of this program that metal rich diboride compounds would exhibit superior oxidation resistance was investigated and verified. Studies were made of high pressure hot pressed hafnium and zirconium diborides, which are the most oxidation resistant diborides, at boron/metal ratios between 1.7 and 2.1 Measurements between 1200 and 2200°K at partial pressures of 7 to 40 torr oxygen and flowrates of 100 to 200 cm^3/min. were performed. At 1900°K $HfB_{1.88}$ has a parabolic rate constant which is 50 times smaller than $HfB_{2.12}$. The parabolic rate constants for hafnium diboride oxidation are about ten times smaller than the corresponding zirconium diboride rate constants. Silicon additions were found to improve oxidation resistance below 1600°K but not at higher temperatures. Additional work is in progress to investigate larger silicon and aluminum additions. Measurements of vapor deposited $ZrB_{1.85}$ and Boride Z have been performed for comparison purposes. At present, our best "pure" diboride is $HfB_{1.7}$ which exhibits a parabolic rate constant for oxygen pickup of 10^{-3}gm^2/cm^{4}min. at 2200°K corresponding to a diboride/dioxide conversion of 20 mils in one hour at this temperature. Sintering studies on ZrB_2 indicate that densification proceeds by grain boundary diffusion and that $ZrB_{1.89}$ can be sintered to 96% theoretical density in four hours at 2100-2200°C without discontinuous grain growth. Additions of zirconium to $ZrB_{1.7}$ permitted densification at 1800°C. Silicon and ZrC additions did not inhibit discontinuous grain growth at high temperatures. Preliminary studies indicate that hafnium diboride sinters at slower rates than ZrB_2. Measurements

UNCLASSIFIED
Security Classification

14. KEY WORDS	LINK A		LINK B		LINK C	
	ROLE	WT	ROLE	WT	ROLE	WT
Borides						
Oxidation Resistant Materials						
Thermal Properties						
Phase Boundaries						
Sintering						
High Pressure Hot Pressing						
Evaluation of Oxidation Characteristics						
Thermodynamic Stability						

INSTRUCTIONS

1. ORIGINATING ACTIVITY: Enter the name and address of the contractor, subcontractor, grantee, Department of Defense activity or other organization (*corporate author*) issuing the report.

2a. REPORT SECURITY CLASSIFICATION: Enter the overall security classification of the report. Indicate whether "Restricted Data" is included. Marking is to be in accordance with appropriate security regulations.

2b. GROUP: Automatic downgrading is specified in DoD Directive 5200.10 and Armed Forces Industrial Manual. Enter the group number. Also, when applicable, show that optional markings have been used for Group 3 and Group 4 as authorized.

3. REPORT TITLE: Enter the complete report title in all capital letters. Titles in all cases should be unclassified. If a meaningful title cannot be selected without classification, show title classification in all capitals in parenthesis immediately following the title.

4. DESCRIPTIVE NOTES: If appropriate, enter the type of report, e.g., interim, progress, summary, annual, or final. Give the inclusive dates when a specific reporting period is covered.

5. AUTHOR(S): Enter the name(s) of author(s) as shown on or in the report. Enter last name, first name, middle initial. If military, show rank and branch of service. The name of the principal author is an absolute minimum requirement.

6. REPORT DATE: Enter the date of the report as day, month, year; or month, year. If more than one date appears on the report, use date of publication.

7a. TOTAL NUMBER OF PAGES: The total page count should follow normal pagination procedures, i.e., enter the number of pages containing information.

7b. NUMBER OF REFERENCES: Enter the total number of references cited in the report.

8a. CONTRACT OR GRANT NUMBER: If appropriate, enter the applicable number of the contract or grant under which the report was written.

8b, 8c, & 8d. PROJECT NUMBER: Enter the appropriate military department identification, such as project number, subproject number, system numbers, task number, etc.

9a. ORIGINATOR'S REPORT NUMBER(S): Enter the official report number by which the document will be identified and controlled by the originating activity. This number must be unique to this report.

9b. OTHER REPORT NUMBER(S): If the report has been assigned any other report numbers (*either by the originator or by the sponsor*), also enter this number(s).

10. AVAILABILITY/LIMITATION NOTICES: Enter any limitations on further dissemination of the report, other than those imposed by security classification, using standard statements such as:

(1) "Qualified requesters may obtain copies of this report from DDC."

(2) "Foreign announcement and dissemination of this report by DDC is not authorized."

(3) "U. S. Government agencies may obtain copies of this report directly from DDC. Other qualified DDC users shall request through

______________________________"

(4) "U. S. military agencies [illegible] report directly from DDC. [illegible] shall request through

______________________________"

(5) "All distribution of this report is [illegible] ified DDC users shall request through

______________________________"

If the report has been furnished to the Office of Technical Services, Department of Commerce, for sale to the public, indicate this fact and enter the price, if known.

11. SUPPLEMENTARY NOTES: Use for additional explanatory notes.

12. SPONSORING MILITARY ACTIVITY: Enter the name of the departmental project office or laboratory sponsoring (*paying for*) the research and development. Include address.

13. ABSTRACT: Enter an abstract giving a brief and factual summary of the document indicative of the report, even though it may also appear elsewhere in the body of the technical report. If additional space is required, a continuation sheet shall be attached.

It is highly desirable that the abstract of classified reports be unclassified. Each paragraph of the abstract shall end with an indication of the military security classification of the information in the paragraph, represented as (*TS*), (*S*), (*C*), or (*U*).

There is no limitation on the length of the abstract. However, the suggested length is from 150 to 225 words.

14. KEY WORDS: Key words are technically meaningful terms or short phrases that characterize a report and may be used as index entries for cataloging the report. Key words must be selected so that no security classification is required. Identifiers, such as equipment model designation, trade name, military project code name, geographic location, may be used as key words but will be followed by an indication of technical context. The assignment of links, roles, and weights is optional.

DD FORM 1 JAN 64 1473 (BACK)

UNCLASSIFIED
Security Classification

UNCLASSIFIED

Security Classification

DOCUMENT CONTROL DATA - R&D

(Security classification of title, body of abstract and indexing annotation must be entered when the overall report is classified)

1. ORIGINATING ACTIVITY (Corporate author)	2a. REPORT SECURITY CLASSIFICATION UNCLASSIFIED 2b. GROUP
3. REPORT TITLE	
4. DESCRIPTIVE NOTES (Type of report and inclusive dates)	
5. AUTHOR(S) (Last name, first name, initial)	
6. REPORT DATE	7a. TOTAL NO. OF PAGES / 7b. NO. OF REFS
8a. CONTRACT OR GRANT NO. b. PROJECT NO. c. d.	9a. ORIGINATOR'S REPORT NUMBER(S) 9b. OTHER REPORT NO(S) (Any other numbers that may be assigned this report)
10. AVAILABILITY/LIMITATION NOTICES	
11. SUPPLEMENTARY NOTES	12. SPONSORING MILITARY ACTIVITY

13. ABSTRACT

of the thermal conductivity and emissivity of TiB_2, ZrB_2, HfB_2 and TaB_2 on dense polycrystalline samples between 1200° and 2000°K are presented. Stu[dies] of the electrical resistivity of ZrB_2 and HfB_2 have been extended to 1500°C a[nd] are presented as a function of porosity and impurity phases. Comparisons have been made of computed Zr-B and Hf-B phase diagrams with experiment[al] phase equilibria in these systems and permit estimates to be made of the free energies of formation of the monoborides. Theoretical methods for predicting the relative oxidation resistance of the pure diborides, off-stoichiometric compounds and ternary diborides have been developed. This description predi[cts] the correct sequence of oxidation resistance and the enhanced oxidation resistance of metal rich diboride. An additional inference is that ternary alloy-ing elements substituting on the boron sublattice will enhance oxidation proper-ties.

This document contains blank pages that were not filmed

DD FORM 1 JAN 64 1473

UNCLASSIFIED

Security Classification